

Institutt for fysikk og teknologi



**Rapidity and transverse momentum spectra  
and the reaction dynamics in Au+Au  
collisions at RHIC**

by  
Jens Ivar Jørdre

a thesis submitted to Institutt for fysikk og teknologi,  
Universitetet i Bergen,  
in partial fulfillment of the requirements for  
the degree of Doctor Scientiarum

June 2005  
Universitetet i Bergen  
Bergen, Norway

ISBN 82-497-0285-9

# Acknowledgements

With this thesis I complete my studies at the Department of Physics and Technology, University of Bergen. During many years a multitude of people, at the department and elsewhere, have made my studies enjoyable and interesting. They all deserve my most honest gratitude as there would be no thesis without them.

First of all I would like to thank my supervisor Prof. Dieter Röhrich. His knowledge and insight never ceases to astonish me. In combination with his ability to convey this information to students his guidance has been no less than excellent.

I am indebted to everyone in the Experimental Nuclear Physics Group at the Department of Physics, University of Bergen. Thank you for countless discussions and a good social environment. I would like to mention Dr. Anders Strand Vestbø, my former office mate Dr. Zhongbao Yin, Gaute Øvrebekk, Kenneth Aamodt, Are Severin Martinsen, Hongyan Yang, Matthias Richter, Ketil Røed and Dr. Jørgen Lien. These and others have all contributed in making my years at the department most pleasurable. An equal amount of thanks goes to the research groups involved in experimental heavy ion physics at the Bergen University College and at the Department of Physics, University of Oslo. I would also like to thank Ola Kristoffer Øye for invaluable topical input.

Several stays at the Brookhaven National Laboratory have been made possible by Dr. Flemming Videbaek, Dr. Chellis Chasman and the Heavy Ion Research Group in the Physics Department. Thank you so much for letting me stay there most of 2001 as well as for shorter periods. In particular I would like to thank Dr. Hironori Ito for countless on-line discussions and good mood.

Finally I would express my gratitude for having a very supportive family. Foremost my father Lars Jørdre and his wife Helga Førner have encouraged me throughout my studies.

Bergen, April 2005  
Jens Ivar Jørdre



# Preface

In a regime of extreme energy density, which likely prevailed a few microseconds after the Big Bang, quantum chromo-dynamics (QCD) predicts the existence of quark gluon plasma (QGP). This state of bulk matter is characterized by the deconfinement of quarks and gluons.

At the Relativistic Heavy Ion Collider (RHIC) at Brookhaven National Laboratory, NY, USA, nuclei are accelerated up velocities above  $0.9999c$ . The energy density obtained in their collision is the highest ever created in the laboratory and exceeds typical lower limits for the creation of a short-lived QGP. The bulk of final state particles, however, consists of hadrons. Thus any QGP, if created at RHIC, must have hadronized during the short times span of the collision and the subsequent expansion.

This dissertation discusses characteristics of transverse mass spectra of pions, kaons and protons in the context of physics motivated blast-wave fits. The rapidity dependence of blast-wave fit parameters as well as rapidity densities are tested for hints of boost invariance. Transverse mass spectra are presented for  $\pi^\pm$ ,  $K^\pm$ ,  $p$  and  $\bar{p}$  obtained in a wide rapidity range. The data analyzed corresponds to the 10% most central Au+Au collisions at  $\sqrt{s_{NN}} = 200 \text{ GeV}$  recorded by the BRAHMS collaboration in 2001. Transverse spectra are fitted with a blast-wave parametrization. This method is applied consistently at all rapidities considered. By integrating the obtained blast-wave fit functions rapidity distributions of identified particles are deduced. These longitudinal distributions are screened for signs of boost invariance.

Chapter 1 presents an overview of the theoretical environment in which experimental heavy ion physics is carried out. Aspects of QCD and QGP characteristics and possible signatures of its existence are described. Chapter 2 addresses reaction dynamics in particular in the longitudinal direction. The setups of RHIC and the BRAMS experiment are laid out in Chapter 3. In Chapter 4 the analysis of the experimental data is presented and the obtained results shown in Chapter 5. Finally in Chapter 6 the results are discussed and conclusions drawn with respect to the theoretical model descriptions.



# Contents

<b>1 Ultra-Relativistic Heavy Ion Physics</b>	<b>1</b>
1.1 Nuclear matter and nuclear physics . . . . .	1
1.2 Quantum chromo-dynamics . . . . .	1
1.2.1 The constituents . . . . .	1
1.2.2 The strong interaction . . . . .	2
1.3 Quark gluon plasma . . . . .	3
1.3.1 Phases of the nuclear matter . . . . .	3
1.3.2 Theoretical descriptions . . . . .	5
1.4 Signatures of quark gluon plasma . . . . .	7
1.4.1 Thermalization and temperature . . . . .	7
1.4.2 Flow . . . . .	9
1.4.3 HBT . . . . .	11
1.4.4 Strangeness enhancement . . . . .	15
1.4.5 Electromagnetic probes . . . . .	19
1.4.6 Restoration of chiral symmetry . . . . .	21
1.4.7 Production of quarkonia . . . . .	23
1.4.8 High $p_T$ suppression . . . . .	24
<b>2 Collision scenarios</b>	<b>29</b>
2.1 Nuclear stopping . . . . .	29
2.2 Landau picture . . . . .	31
2.3 Bjorken picture . . . . .	32
2.4 CGC + hydro . . . . .	35
2.5 Experimental tests of collision scenarios . . . . .	37
<b>3 The Relativistic Heavy Ion Collider and the BRAHMS experiment</b>	<b>39</b>
3.1 The collider complex . . . . .	39
3.2 BRAHMS in general . . . . .	42
3.2.1 Forward Spectrometer . . . . .	43
3.2.2 Mid-rapidity Spectrometer . . . . .	44
3.3 Global detectors . . . . .	45
3.3.1 Multiplicity array . . . . .	45
3.3.2 Beam-beam counters . . . . .	45
3.3.3 Zero-degree calorimeters . . . . .	47
3.3.4 Trigger system . . . . .	50
3.4 Tracking detectors . . . . .	50

3.4.1	Time projection chambers . . . . .	51
3.4.2	Drift chambers . . . . .	52
3.5	Particle identification detectors . . . . .	53
3.5.1	Time-of-flight detectors . . . . .	53
3.5.2	Threshold Cherenkov detector . . . . .	54
3.5.3	Ring imaging Cherenkov detector . . . . .	54
<b>4</b>	<b>Data analysis</b>	<b>55</b>
4.1	Event selection . . . . .	55
4.2	Stepwise data reduction . . . . .	57
4.2.1	Local tracking . . . . .	57
4.2.2	Global tracking . . . . .	60
4.2.3	ID information . . . . .	63
4.3	Track selection . . . . .	66
4.4	Particle identification . . . . .	68
4.4.1	Momentum resolution . . . . .	68
4.4.2	Time of flight . . . . .	68
4.4.3	Cherenkov rings . . . . .	76
4.4.4	Combination of ID in the forward arm . . . . .	79
4.5	Corrections . . . . .	80
4.5.1	Acceptance correction . . . . .	80
4.5.2	Detector efficiency correction . . . . .	82
4.5.3	Multiple scattering correction . . . . .	86
4.5.4	Weak decay correction . . . . .	87
4.5.5	Absorption correction . . . . .	88
4.5.6	Feed-down correction . . . . .	88
4.6	Spectrum projection . . . . .	91
4.6.1	Correction and normalization . . . . .	92
4.6.2	Combination of vertex bins . . . . .	93
4.6.3	Combination of spectrometer settings . . . . .	94
4.6.4	Average over rapidity bins . . . . .	94
4.7	Systematic errors . . . . .	94
4.7.1	Setting dependent errors . . . . .	95
4.7.2	Errors from fits . . . . .	97
<b>5</b>	<b>Results</b>	<b>99</b>
5.1	Invariant spectra . . . . .	99
5.2	Fits to spectra . . . . .	102
5.3	Yields . . . . .	105
5.4	Temperature and transverse expansion . . . . .	112
5.5	Strangeness production . . . . .	115
<b>6</b>	<b>Discussion</b>	<b>117</b>
6.1	Transverse characteristics . . . . .	117
6.2	Longitudinal characteristics . . . . .	118
6.3	Conclusions . . . . .	119

<b>A Kinematics</b>	<b>123</b>
A.1 Lorentz transformations . . . . .	123
A.2 Coordinate systems . . . . .	124
A.3 Kinematic variables . . . . .	125
<b>B RICH correction for mis-identified particles</b>	<b>127</b>
<b>C Tabulated results</b>	<b>129</b>
<b>D Glossary</b>	<b>133</b>
<b>E List of publications</b>	<b>137</b>
E.1 Publications in refereed journals . . . . .	137
E.2 Conference contributions . . . . .	139
E.3 Publications as contributor or primary author . . . . .	140
<b>References</b>	<b>141</b>



# List of Figures

1.1	The quark potential . . . . .	2
1.2	Order of the phase transition for finite quark masses . . . . .	4
1.3	The QCD phase diagram . . . . .	4
1.4	Temperature and mean transverse velocity as a function of beam energy . .	8
1.5	STAR $m_T$ spectra for $\pi^\pm$ , $K^\pm$ , $p$ and $\bar{p}$ . . . . .	9
1.6	Flow in and out of plane . . . . .	10
1.7	Hydrodynamic prediction for excitation function of directed flow . . . . .	11
1.8	Experimental flow excitation function . . . . .	12
1.9	Experimental $v_2$ excitation function . . . . .	13
1.10	$\pi^-\pi^-$ correlation function at RHIC . . . . .	16
1.11	HBT excitation functions . . . . .	17
1.12	NA57 strangeness enhancement . . . . .	18
1.13	NA50 di-muon excess in Pb+Pb . . . . .	20
1.14	Enhancement of $\gamma/\pi^0$ in PHENIX. . . . .	20
1.15	Quark condensate with varying temperature and baryon density . . . . .	21
1.16	CERES/NA45 di-electron mass spectrum in Pb+Au at 40 AGeV . . . . .	22
1.17	Nuclear modification factor in Au+Au and d+Au collisions at RHIC . . . . .	25
1.18	Two-particle azimuthal distributions at RHIC . . . . .	26
2.1	Stopping in microscopic models. . . . .	30
2.2	Stopping as a function of energy . . . . .	31
2.3	Heavy ion collision in the Landau hydrodynamic picture . . . . .	32
2.4	Heavy ion collision in the Bjorken picture . . . . .	33
2.5	Space-time diagram according to Bjorken . . . . .	34
2.6	Initial conditions for hydrodynamics at RHIC . . . . .	36
2.7	Final (pseudo-)rapidity distributions after three-dimensional hydro . . . . .	36
3.1	RHIC complex layout . . . . .	40
3.2	RHIC complex stepwise acceleration . . . . .	41
3.3	BRAHMS experimental setup . . . . .	42
3.4	BRAHMS experimental acceptance . . . . .	43
3.5	Multiplicity correlation between silicon and tiles arrays . . . . .	46
3.6	Correlation of vertex determination from BB and TPM1 . . . . .	48
3.7	Correlation of vertex determination from ZDC and TPM1 . . . . .	49
3.8	Schematic layout of the proportional chamber region of TPCs . . . . .	52
4.1	Correlation of vertex determination from BB and ZDC . . . . .	56

4.2	Reconstructed track segments in T1 . . . . .	58
4.3	Hit finding in drift chamber module . . . . .	59
4.4	Matching in MRS . . . . .	62
4.5	Tracks intersecting slats in H1 . . . . .	64
4.6	A particle traversing the RICH . . . . .	65
4.7	RICH PMT hits and ring fitting result . . . . .	66
4.8	Data summary tree structure . . . . .	67
4.9	Correlation of $1/\beta_t$ and $p$ in the MRS . . . . .	70
4.10	Distribution of $\Delta(1/\beta)$ . . . . .	70
4.11	Time-of-flight resolution . . . . .	71
4.12	Low momentum particle identification . . . . .	72
4.13	Correlation of $1/\beta_t$ and $p$ for identified particles in the MRS . . . . .	73
4.14	Correlation of $1/\beta_t$ and $p$ for $0.9 \leq \eta \leq 1.1$ . . . . .	74
4.15	Distributions of $1/\beta_t$ for inclusive PID method in the MRS . . . . .	75
4.16	RICH ring radius correlated with particle momenta . . . . .	77
4.17	Distribution of $\Delta(r)$ . . . . .	78
4.18	Selected acceptance maps for $y \approx 1$ and $y \approx 3$ . . . . .	81
4.19	TPC tracking efficiency using embedded track method . . . . .	83
4.20	TPC tracking efficiency using reference track method . . . . .	84
4.21	DC tracking efficiency using reference track method . . . . .	85
4.22	Corrections for multiple scattering . . . . .	88
4.23	Corrections for weak decay . . . . .	89
4.24	Corrections for absorption . . . . .	89
4.25	Corrections for feed-down . . . . .	92
4.26	Invariant $p_T$ spectra for negative pions around $y=0$ . . . . .	95
4.27	Relative spectrum offset and statistical error for negative pions at mid-rapidity . . . . .	96
5.1	Two-dimensional differential yields . . . . .	100
5.2	Invariant $m_T$ spectra . . . . .	101
5.3	Invariant $m_T$ spectra with blast-wave fits . . . . .	104
5.4	Positive particle blast-wave fit functions with varying $n$ . . . . .	106
5.5	Blast-wave parametrization in comparison with other fit functions . . . . .	107
5.6	Rapidity distribution of identified particles . . . . .	109
5.7	Widths of Gaussian fits to rapidity distributions . . . . .	111
5.8	Rapidity distribution of net-protons . . . . .	112
5.9	Excitation function for $\langle\pi\rangle / \langle N_{part}\rangle$ . . . . .	113
5.10	Fitted temperatures and transverse surface velocities . . . . .	113
5.11	Mean transverse momentum as a function of rapidity . . . . .	114
5.12	$\langle K^+ \rangle / \langle \pi^+ \rangle$ and $\langle K^- \rangle / \langle \pi^- \rangle$ as a function of center-of-mass energy . . . . .	115
6.1	Rapidity distribution of identified particles overlaid with results from CGC+Hydro . . . . .	121
A.1	Choices of global and local coordinate systems in the BRAHMS experiment	124

# List of Tables

3.1	Trigger IDs and corresponding requirements . . . . .	50
4.1	Limits for low momentum particle identification using TOF . . . . .	73
4.2	Thresholds for high momentum particle identification using RICH . . . . .	76
5.1	Fit parameters obtained with blast-wave parametrization of $m_T$ spectra . .	103
5.2	Fit parameters obtained with blast-wave parametrization of $m_T$ spectra and fixed $n = 0.81$ . . . . .	105
5.3	Extrapolated yields for various fit functions at $y = 1.0$ . . . . .	110
5.4	Fraction of extrapolated yield within acceptance . . . . .	110
5.5	Integrated yields and width of rapidity distributions . . . . .	110
B.1	RICH efficiency corrections . . . . .	128
C.1	Extrapolated rapidity densities without cuts on momentum . . . . .	129
C.2	Extrapolated MRS rapidity densities with cuts on momentum . . . . .	129
C.3	Extrapolated yields for various fit functions at $y = 0.0$ . . . . .	130
C.4	Extrapolated yields for various fit functions at $y = 0.5$ . . . . .	130
C.5	Extrapolated yields for various fit functions at $y = 2.0$ . . . . .	131
C.6	Extrapolated yields for various fit functions at $y = 3.0$ . . . . .	131



# Chapter 1

## Ultra-Relativistic Heavy Ion Physics

### 1.1 Nuclear matter and nuclear physics

Our universe is a vast composition of matter and energy, which Albert Einstein showed are two sides of the same coin [1]. The matter itself has various ingredients, one of them being the ordinary nuclear matter that our earth and everything on it are made of. Nuclear physicists study the atomic nucleus to reveal its characteristics. As opposed to particle physics where single particle or simple particle systems are studied, nuclear physics also deals with collective effects among the nucleons and other particles produced in nuclear interactions. Nuclei are studied under a host of different conditions. Low energy nuclear structure physics tries to establish the conditions for nuclear stability, pushing the “drip line” forward and creating new nuclei by combining smaller ones. At the opposite end high energy nuclear physicists collide heavy nuclei in order to probe the matter under the most extreme conditions that can be achieved in the laboratory. This thesis deals exclusively with the high energy end of the spectrum.

### 1.2 Quantum chromo-dynamics

#### 1.2.1 The constituents

The building blocks of nucleons are called quarks. Each neutron and proton are built out of three constituent quarks. Particles carrying three quarks are called baryons. There are also particles called mesons that each carry one quark and one anti-quark. In addition to electric charge and mass quarks are characterized by flavor and color. Quarks of six different flavors, as well as six anti-flavors, have been found. The flavors are up ( $u$ ), down ( $d$ ), strange ( $s$ ), charm ( $c$ ), bottom ( $b$ ), top ( $t$ ) and their anti-flavor counterparts. The quark colors are *red*, *green*, *blue* and their respective anti-colors.

Quarks may interact electrically, weakly and strongly. Each kind of interaction is mitigated via a gauge boson. Electromagnetic interactions, whose gauge boson is the photon, are described in *quantum electro-dynamics (QED)*. Weak interactions that take place via exchange of the heavy  $W^\pm$  and  $Z$  bosons are described in the electro-weak theory. *Quantum chromo-dynamics (QCD)* describes the interaction of quarks via gluons, which

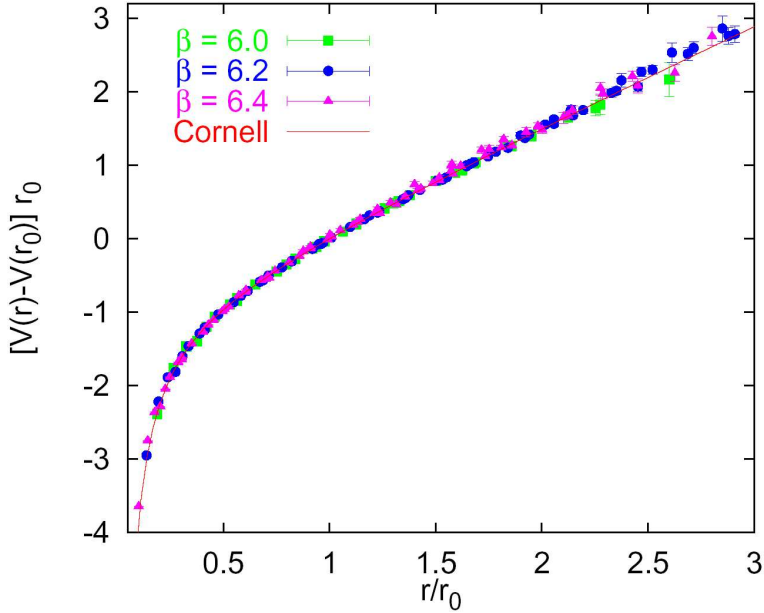


Figure 1.1: The potential between two quarks obtained in lattice QCD simulations and normalized to the potential at  $r_0 = 0.5$  fm [2].

like photons are massless. At the short distances of the nuclear scale ( $\sim 1$  fm/c) the strong interactions dominate.

### 1.2.2 The strong interaction

In QCD the potential between a heavy quark and its corresponding antiquark is described in its most simplistic form according to the Cornell potential [2]

$$V_{qq}(r) = -\frac{e}{r} + \sigma r \quad (1.1)$$

In fig. 1.1 the quark-antiquark potential as a function of the separation distance is shown as obtained in quenched lattice QCD simulations (sec. 1.3.2).

As one tries to separate the two quarks the second term in eq. 1.1 dominates and increases linearly with the separation distance. The linear increase is due to gluon self-interaction since gluons themselves carry color charge. The field lines between the two quarks can be described as a flux tube, also called a *color string*. This scenario describes color confinement of quarks and implies that single quarks can not exist. Instead, as the quarks are separated more and more, the potential reaches the limit where it becomes energetically favorable to create a quark-antiquark pair. The string is thus broken and total colorlessness is preserved.

Going to shorter separation distances, on the other hand, the linear term in eq. 1.1 goes to zero and hence the QCD potential is Coulomb like. Conditions in this regime are referred to as *asymptotic freedom*.

Alternatively the strength of strong interactions may be described by the strong cou-

pling constant,  $\alpha_s$ , which can be expressed as [3]

$$\alpha_s(q, T) = \frac{4\pi}{11\ln(-q^2/\Lambda^2) - 48G(q/T)} \quad (1.2)$$

Here  $q$  is momentum transfer in the interaction,  $T$  the temperature of the medium and  $\Lambda$  a dimensional parameter with value around 200 MeV. The medium contribution  $G$  decreases with increasing  $T$  while keeping of  $q$  constant<sup>1</sup>. Thus, as can be deduced from eq. 1.2  $\alpha_s$  is not a constant in the true meaning of the word. It decreases with increasing momentum transfer and temperature.

A characteristic difference exists between the low and high energy descriptions of the QCD vacuum. At low energies the density of quark-antiquark pairs, expressed in terms of the quark condensate  $\langle\bar{\psi}\psi\rangle$ , is non-zero. In [5] the condensate is estimated to  $\langle\bar{\psi}\psi\rangle \approx -(235 \text{ MeV})^3$ . Its non-vanishing value is attributed to chiral symmetry breaking in which quarks acquire dynamical masses of hundreds of MeV/c<sup>2</sup> as opposed to being almost massless where chiral symmetry prevails. At high energies the quark condensate approaches zero which is interpreted as restoration of chiral symmetry.

## 1.3 Quark gluon plasma

### 1.3.1 Phases of the nuclear matter

In ultra-relativistic heavy ion collisions the nuclear matter is believed to be compressed and heated sufficiently that partonic degrees of freedom describe the collision dynamics at least in a large significant fraction of the collision time span. In other words the matter is expected to go from an initial state described in terms of confined quarks with large masses to a state of (near) massless deconfined quarks. In addition, if this state is such that it may be described in terms of thermodynamics the matter is referred to as *Quark Gluon Plasma (QGP)*. Because of deconfinement the partons are free to roam around within the bulk of the matter.

The transition between these two regimes may be described as a phase transition, whose order may be first or second<sup>2</sup>. The order of the transition depends on the number of massless quark flavors. For 2 massless flavors a second order transition is predicted while a first order phase transition may be the case for 3 massless flavors [6, 7].

Nevertheless, the masses of the quarks are non-zero. It appears that this leads to phase transition being replaced by a rapid crossover in the low density range of the phase diagram. The order of the transition at the higher densities is still being investigated [8]. Fig. 1.2 shows recent constraints for the orders calculated on the lattice (sec. 1.3.2), while fig. 1.3 depicts the phases of the QCD matter as a function of chemical potential and temperature.

---

<sup>1</sup>The contribution to the strong coupling constant from the medium is expressed as  $G(\xi) = \int_0^\infty z dz \frac{f(z)}{e^{\xi z} - 1}$  where  $f(z) = (z - 1/2z + 1/8z^3) \ln\left(\frac{|1-2z|}{|1+2z|}\right) - 1 + 1/2z^2$ .

<sup>2</sup>A first order phase transition shows discontinuities in order parameters e.g. in temperature as a function of energy, while there is no such discontinuity for a second order phase transition. However, the order parameter has discontinuous derivative in second order transitions.

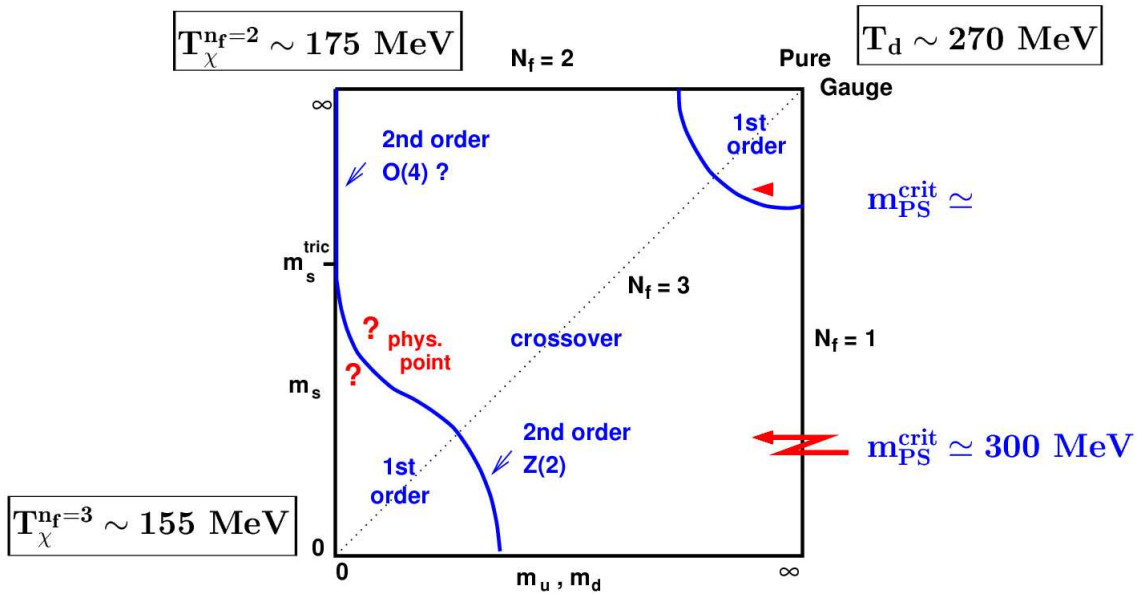


Figure 1.2: The order of the QGP phase transition as a function of light (u,d) and strange quark masses calculated on the lattice [8] with vanishing baryon number density.

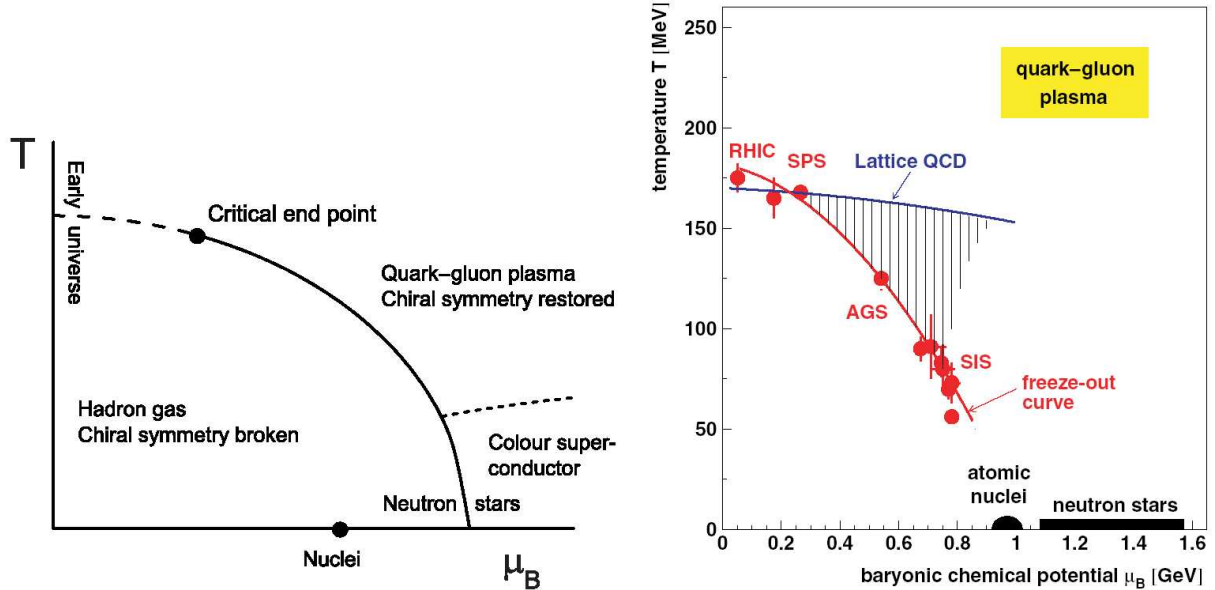


Figure 1.3: The phase diagram of QCD matter. In the left panel the solid line indicates model estimates for the first order phase transition, while the long-dashed line outlines the region for crossover. The short-dashed line shows the phase transition between normal and super-conducting QGP (not discussed in this analysis). On the right panel the lattice results are overlaid with data points and fitted curve indicating the experimental freeze-out conditions [9].

### 1.3.2 Theoretical descriptions

#### Perturbative QCD

As shown in sec. 1.2.2 the strong coupling is reduced with decreasing distances in space-time and high momentum transfers. This means that higher order terms in strong interactions can be treated as corrections, or *perturbations*, to the low order ones. Interactions at high energy may therefore be described in a manner similar to quantum electro-dynamics where the coupling is significantly smaller. This description of strong interactions is commonly referred to as *perturbative QCD (pQCD)*.

The onset of the regime where pQCD is a suitable description is disputed. It is commonly accepted that at AGS and SPS the momentum transfers in binary collisions are too low for a perturbative description only [10]. Still, perturbative components of various observables are calculated in this energy regime. The importance of perturbative components increases as we go to RHIC energies, and even more for the high energy LHC domain. Here hard reactions, such as jets and mini-jets, are so abundant that they can be used to probe the non-perturbative medium.

#### Lattice QCD

With the advent of high performance computers during the past decades simulation of QCD interactions on a grid, or *lattice*, has become a powerful tool. Here, both hadronic and partonic phases of QCD may be studied non-perturbatively. The fact that the lattice is a four dimensional regularized grid makes it especially suitable for parallel computer systems with ever increasing computing power. Lattices with sizes up to 64 points in each of the three spatial dimensions and also in the temporal dimension have been used [11], and typical lattice spacings are  $0.02 - 0.05 \text{ fm}$  [12, 13].

Since lattice QCD does not involve perturbative approximations it is in principle able to describe nuclear matter as well as QGP. This does, however, not mean that typical lattice QCD calculations are without approximations. Refined versions of lattice QCD have been developed to simplify the calculations where appropriate.

First of all, most calculations so far have been performed assuming zero net-baryon density. This may be an appropriate description of the Big Bang and possibly at LHC, but as can be seen in the right panel of fig. 1.3 it is not the case at the current collision energies. Yet, in the past years also lattice calculations with finite baryon chemical potential have come about thus probing also the horizontal dimension on the phase diagram.

In the *quenched* approximation the influence of quark-antiquark pairs on the QCD vacuum is neglected. Also, the nature of the grid being a regularized structure of finite size is an approximate description of nature. The *continuum limit* has to be found for values calculated on the lattice. By varying the grid spacing as well as the number of space-time points one can probe the dependence of these simulation parameters on calculated values to be compared with experimental results.

#### Parton cascade models

The above descriptions rely on the matter they depict being of infinite size at equilibrium. This may not be the case for the matter produced in high energy nuclear collisions, at

least not for the whole interaction time span. The collision fireball has a finite size, and it is naive to assume that e.g. the early stages of the collision are in thermal and chemical equilibrium. Also, effects of rapid expansion, resonance production and decay and collective dynamics makes equilibrium models unsuitable at certain stages of the collision. The non-equilibrium picture is addressed by various transport theories.

In the case of production of a QGP in heavy ion collisions the degrees of freedom are partonic. Microscopic models describing partonic degrees of freedom are commonly referred to as parton cascade models. These models evolve according to the following general picture [14]:

1. Initialization: Nucleons in the colliding nuclei dissolve into their partonic components according to measured nucleon structure functions producing the initial parton distributions.
2. Interaction: Incoherent interactions of partons according to pQCD.
3. Hadronization: Partons including those produced from fragmenting strings combine into hadrons.

Parton cascade models can address non-equilibrium issues such as stopping, expansion and thermalization. The latter results from scattering and radiative energy loss. Partonic models have predicted a.o. that  $\sim 50\%$  of the expected energy loss in RHIC collisions are due to partonic interactions, with an even higher fraction at LHC [15]. Also, timescales for thermalization and chemical equilibrium for heavy ion collisions at  $\sqrt{s_{NN}} = 200 \text{ GeV}$  are predicted to be  $\sim 0.7 \text{ fm/c}$  and a few fm/c, respectively [15, 16].

### **Hadronic transport models**

In hadronic transport models heavy ion collisions are depicted as a sequence of binary or multi-body collisions of hadrons, strings, di-quarks and single quarks. Even with the latter components considered in the models there are no explicit partonic degrees of freedom. Therefore the hadronic models do not include a phase transition. Yet, some of them do extend to high energies, where particles are produced from break-up of strings. Also, some models include effects that are strictly not hadronic, such as color-ropes [17] or decay of multi-quark droplets [18].

Hadronic models are often considered the baseline when searching for signatures of a phase transition in the most energetic collisions. They provide the means to subtract hadronic observables from the wide variety of potential signatures of the QGP.

### **Hydrodynamic models**

The term used to denote these models indicate that they are based on principles of fluid dynamics. Thus, hydrodynamic models describe the collision in terms of macroscopic parameters, as opposed to the two microscopic scenarios above. Macroscopic parameters are a.o. temperature, chemical potentials and flow velocity, relating to many-body concepts such as equilibrium and expansion. In general nuclear fluid models describe the collision in an idealized continuum limit based on local equilibrium and energy-momentum conservation [19]. These models are applicable when the density of particles is high, typically

when the distance between particles is smaller than the mean free path in the medium [5]. Also the size of the colliding system in terms of number of participants have to be large enough for applying statistical descriptions. Hence hydrodynamic models should not be used to describe very peripheral collisions.

Hydrodynamic models have as input an *equation of state (EoS)* which describes the pressure as a function of energy density. The EoS may or may not incorporate a phase transition. Thereby one can look for characteristic observables occurring as a result of partonic effects and which can not be accounted for in a hadronic scenario.

In sec. 2 three different hydrodynamic models are presented more in depth.

## 1.4 Signatures of quark gluon plasma

In the previous sections several theoretical approaches to describe heavy ion collisions have been discussed briefly. The models, each within its limits of applicability, can predict observables from collisions to be tested in the laboratory. Model pre- and postdictions are compared to the experimental outcome. In return results from experiments are used to tune the model parameters. Especially systematic studies of the collision outcome e.g. as a function of center of mass energy, system size and centrality, can reinforce or undermine a model description.

In the following various signatures of production of quark gluon plasma are presented and discussed along with experimental results.

### 1.4.1 Thermalization and temperature

Except for the relatively small intrinsic transverse momenta carried by partons in the incoming nucleons the transverse degrees of freedom detected after heavy ion interactions are produced during the collision. For a collision system or *fireball* of many components, whether they be partonic or hadronic, one can look for indications of thermal equilibrium in the transverse direction.

If the temperature in the fireball is beyond  $\sim 50$  MeV, the Fermi-Dirac or Bose-Einstein distributions of baryons or mesons in the hadronic scenario, or quarks and gluons in the partonic one can be approximated using the simpler Maxwell-Boltzmann distribution [20]. Experimental distributions in  $p_T$  or  $m_T$  may thus be fitted with distribution functions where the (effective) temperature and chemical potentials are fit parameters.

In the transverse momentum spectra of heavy ion collisions it is expected that a high temperature perturbative tail will show up at high  $p_T$  [21]. Also, in the case of a transition to a partonic phase a change in the equation of state is expected to show up in the rapidity density dependence on mean transverse momentum. For low and increasing  $dN/dy$  there is a corresponding steady increase in  $\langle p_T \rangle$ . But because of increased entropy at the transition a plateau in  $\langle p_T \rangle$  vs.  $dN/dy$  is anticipated, followed by a new increase above the transition density. Yet it is unlikely that this latter effect may be observed since most likely flow, described in sec. 1.4.2, will smear it out.

The raw experimental spectra have components from flow and decay products from resonances, and do therefore not show the pure thermal characteristics at kinetic freeze-out.

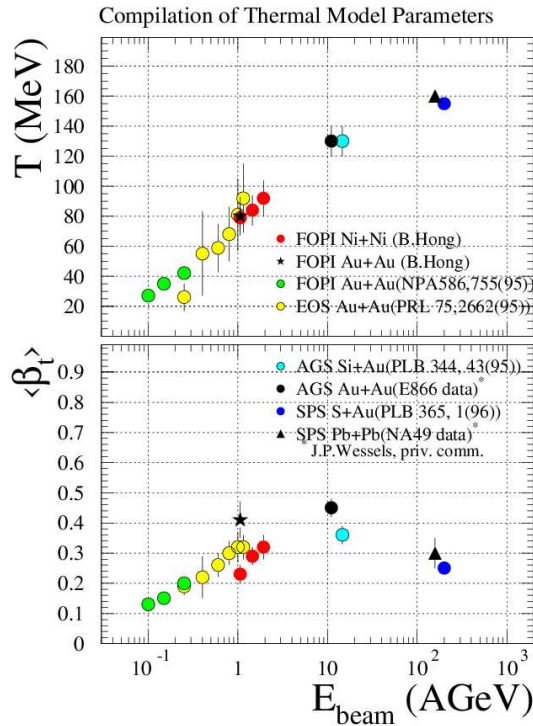


Figure 1.4: Excitation functions for temperature and mean transverse velocity as fitted with the Blast-Wave model [22]. The figure has been taken from [25].

In order to remedy the latter corrections for decay must be applied, either by the experimentalist to remove the decay part of the spectra, or by the theorist to include feed-down for the lighter particles. The flow component may in part be taken into account by fitting the experimental spectra depicting the freeze-out stage with functional parametrizations that include collective motion [22]. In these parametrizations the temperature  $T$  and the transverse flow velocity  $\beta_T$  are fit parameters. An even better solution is to describe the collision in the context of a full three-dimensional hydrodynamic model [23].

All the way from SIS energies to RHIC the particle spectra from heavy ion collisions show thermal-like behavior, with increasing temperature (and flow velocity) as a function of beam energy. The  $T$  and  $\langle \beta_T \rangle$  excitation functions up to SPS energies are shown in fig. 1.4. At RHIC the picture is also consistent with thermalization and flow, as shown for  $\pi^\pm$ ,  $K^\pm$ ,  $p$  and  $\bar{p}$  by the STAR experiment [24] in fig. 1.5.

It is a question how literally one should interpret the picture of a single freeze-out temperature. Some experimental data suggest that various particles are frozen out at different times and thus violates the picture of equilibrium at the later stages of the collision [26]. Also, as discussed in sec. 1.3.2, a certain amount of time is needed in the beginning of the collision for thermalization to occur. Hence the picture of a thermalized system should possibly rather be used in conjunction with some non-equilibrium description of the early and/or late stages of the collision.

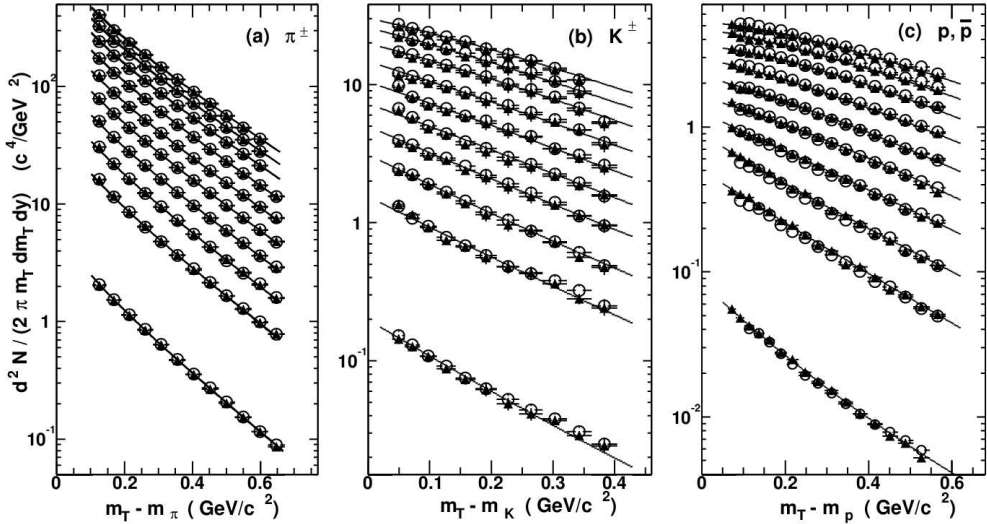


Figure 1.5:  $m_T$  spectra for  $\pi^\pm$ ,  $K^\pm$ ,  $p$  and  $\bar{p}$  in  $\sqrt{s_{NN}} = 200$  GeV Au+Au collisions at RHIC as measured by the STAR experiment [24]. The lower curve on each panel is p+p, while the other curves are Au+Au collisions at various centralities in the range 0 – 5% (top) to 70 – 80%. The pions are fitted with Bose-Einstein distribution  $\propto 1/(\exp(m_T/T) - 1)$  while the kaons and protons are fitted with Blast-Wave distributions [22].

### 1.4.2 Flow

In the range from central to semi-central collisions of heavy ions it is expected that pressure gradients within the fireball leads to collective motion or *flow*. The outgoing matter shows bulk properties such as collective velocity profiles. The typical theoretical description of these effects is hydrodynamics, although also in microscopic models such as QMD flow is predicted.

Systematical studies of flow as a function of collision energy may reveal its predicted strong dependence on the EoS [27]. In the hydro description flow is an effect of pressure gradients caused by initial spatial assymmetry of the matter in the reaction zone. The collective transverse momentum acquired from pressure can be deduced by the integral [19]

$$\mathbf{p}_T = \int_t \int_A P(\rho, S) d\mathbf{A} dt \quad (1.3)$$

where  $t$  is time and  $d\mathbf{A}$  is the surface element between the participant and spectator regions of the fireball.  $P$  is pressure depending on the density  $\rho$  and entropy  $S$ , i.e. an expression of the EoS.

Talking about flow it is common to distinguish two components, one being *in-plane* and the other being *out-of-plane* relative to the *reaction plane* as defined in fig. 1.6. The flow out-of-plane is a result of the rapidly expanding matter in the center of the fireball being squeezed out when it is obstructed by the spectator nucleons that have not decoupled. Going to higher energies it is thus expected that the spectators decouple earlier and the flow will mostly be in-plane [28, 29].

Flow can also be discussed in terms of *directed* and *radial* flow, where the former is related to the relative contributions from in- and out-of-plane components above and

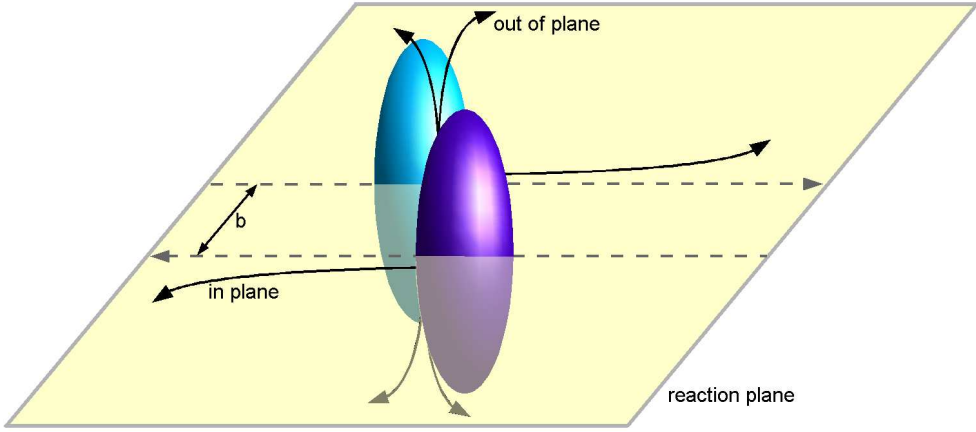


Figure 1.6: Simplified picture of a non-central heavy ion collision indicating the directions of in-plane and out-of-plane flow components.  $b$  denotes the impact parameter.

the latter term describes the azimuthally symmetric distribution [30]. In this language the overall azimuthal angular distribution of outgoing particles can be expressed as the Fourier series [31]

$$E \frac{d^3 N}{dp^3} = \frac{1}{2\pi} \frac{d^2 N}{p_T dp_T dy} \left( 1 + \sum_{n=1}^{\infty} 2v_n \cos[n(\phi - \Psi_r)] \right) \quad (1.4)$$

where  $\Psi_r$  is the azimuthal angle of the reaction plane in the lab frame and  $\phi$  is the azimuthal angle of the outgoing particles. The Fourier coefficients  $v_n$  can then be fitted from data and compared to model predictions. The factor of 2 is chosen so that the Fourier components can be evaluated as  $v_n = \langle \cos[n(\phi - \Psi_r)] \rangle$ , i.e. the mean over all particles in all events.

The value of flow as a probe of QGP lies a.o. in its predicted behavior in case of a first order phase transition. It is predicted that direct flow is modified at the transition [27, 32], and thus a signal in its excitation function has been searched for experimentally. In case that deconfinement is reached a local minimum is predicted, while a smooth decrease is predicted in the hadronic case as shown in fig. 1.7. The position of the QGP minimum and also its magnitude depends highly on the EoS and is therefore not well known.

The expansion depends highly on the pressure gradient  $\partial p / \partial \epsilon = c_s^2$ , where  $c_s$  is the speed of sound. In the mixed phase is  $c_s = 0$  making the expansion slow down or even stall. Even in the case of a rapid crossover, which limits the pressure gradients, this signal could be observed.

This decrease in the speed of sound is referred to as *softening* of the EoS. Unfortunately, this signal also may be difficult to detect from a fireball of finite size. It looks like fluctuations may reduce or wash out the separation of effects from a QGP and a hadronic phase [33].

Flow measurements at the SIS and BEVALAC energies show indeed that there is directed flow occurring in heavy ion collisions. In this beam energy range, from  $0.1 - \sim 2$  GeV/nucleon, the directed flow is increasing up to an asymptotic value around  $\sim 1.5$  GeV/nucleon [25, 34]. At the AGS the E895 and E866/E917 experiments have

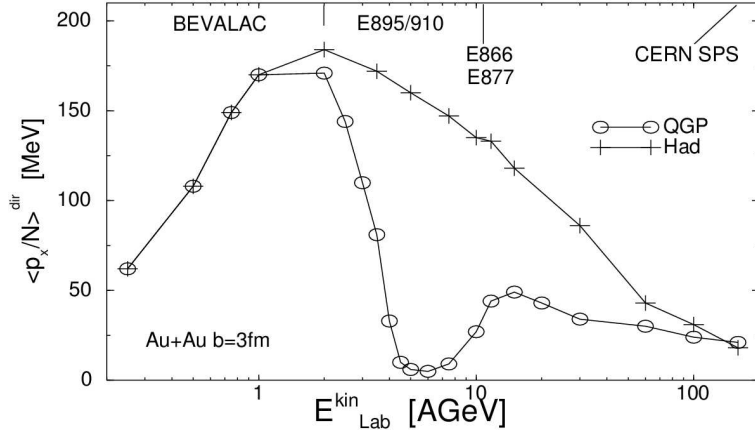


Figure 1.7: Directed transverse flow excitation function in a hydrodynamic picture with and without at QGP phase transition [19].

shown directed flow decreasing in the beam energy range from  $2 - 10$  GeV/nucleon [35, 36]. The SPS results show an even further decrease in the directed flow. In fig. 1.8 various results  $\langle p_x/N \rangle$ , i.e. mean collective transverse momentum per nucleon, from BEVALAC to SPS are compiled together with some model predictions. So far no local minimum is seen, but due to the minimum's dependence on the EoS and finite collision volume effects a phase transition can not be ruled out.

Fig. 1.9 illustrates the evolution of  $v_2/\epsilon$  as a function of the charged particle density from AGS to RHIC energies. The dependence on  $\frac{1}{S} \frac{dN}{dy}$ , where  $S$  is the transverse overlap area, indicate a linear increase within errors. Predicted QGP signatures such as a kink in the dependence curve [38] or a decrease in  $v_2/\epsilon$  with decreasing centrality (or charged particle density) [39] are not supported.

Yet, for the first time the  $v_2$  results in the most central collisions at RHIC energies are in agreement with hydrodynamic predictions. At lower energies hydro predicted too high values of  $v_2/\epsilon$  [40]. Furthermore, the EoS deduced for the matter produced in Au+Au collisions at RHIC is close to the black body EoS, i.e.  $p \approx \epsilon/3$  as calculated from lattice QCD [41]. The amount of rescattering observed has also led to the notion of *strongly coupled quark-gluon plasma (sQGP)*. The rescattering cross section is one to two orders of magnitude higher than what was predicted by pQCD. This means that the matter produced in heavy ion collisions at RHIC behaves more like a strongly coupled perfect fluid than a weakly interacting gas of partons.

Finally, the flow components may be investigated for identified particles. In order to be able to account for both the harmonics in eq. 1.4 and the characteristics of identified particle spectra most models discussed in [42] need a partonic stage in the evolution of heavy ion collisions.

### 1.4.3 HBT

In order to compare the experimental data to theoretical predictions it is crucial to have information on the energy density produced in the collision. In order to determine the

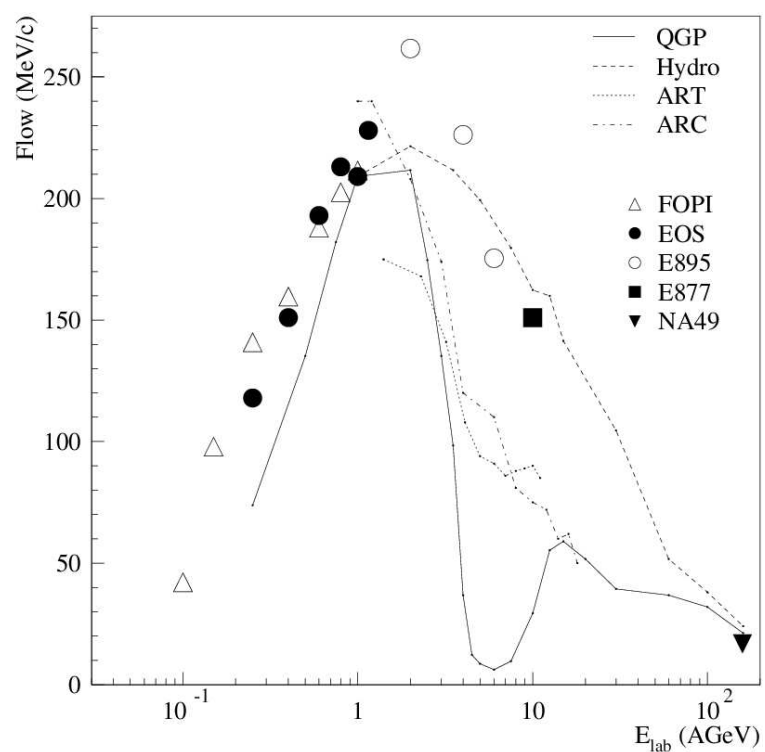


Figure 1.8: Experimental results on the transverse directed flow excitation function from BEVALAC to SPS [37].

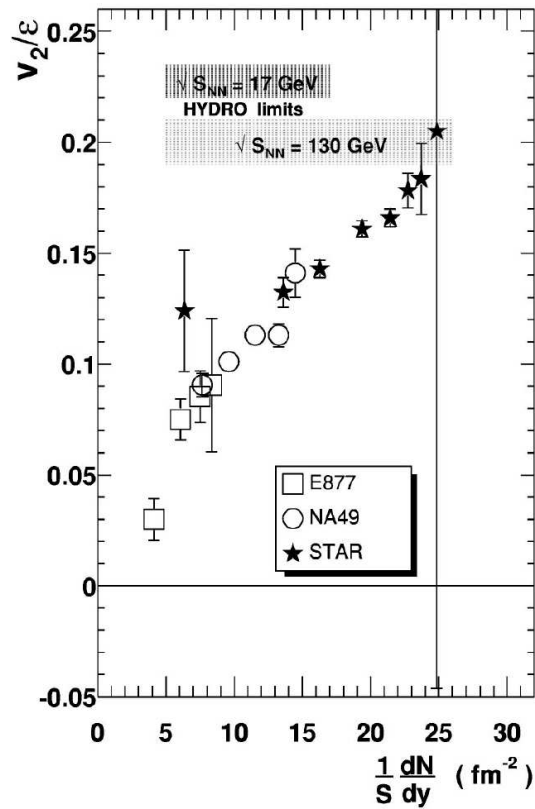


Figure 1.9: Excitation function of  $v_2/\epsilon$  versus the charged particle density at mid-rapidity. Here  $\epsilon$  is the initial eccentricity of the colliding systems defined as  $\epsilon = \frac{\langle y^2 \rangle - \langle x^2 \rangle}{\langle y^2 \rangle + \langle x^2 \rangle}$ . The shaded areas indicate the hydrodynamic predictions for flow which agree with data only at the most central collisions at RHIC.

density one has to estimate the volume of the collision system. Also, several potential QGP signatures, such as enhancement of strangeness (sec. 1.4.4), depend on the lifetime of the fireball.

In order to determine the radius of distant stars Hanbury-Brown and Twiss developed a method involving two-photon intensity interferometry [43]. They used the principle that the probability of detecting two photons in coincidence in two separate detectors is correlated with the detectors mutual separation as well as the angular diameter of the photon source. Measurements of this type, and not only for photons, are referred to as *HBT* measurements.

By performing HBT measurements on identical particles produced in heavy ion collisions, e.g.  $\pi$ ,  $K$  and  $p$ , one can deduce longitudinal and transverse radii and the lifetime of the emitting source. In addition, from using HBT one can gain information on flow patterns, as discussed in sec. 1.4.2, of the source at the freeze-out stage of the collision.

In order to deduce the space-time properties of a pion emitting source the correlation function

$$C_2(p_1, p_2) = P(p_1, p_2)/[P(p_1)P(p_2)] \quad (1.5)$$

Here  $P(p_1, \dots, p_n)$  is the probability for detecting pions with 4-momenta  $p_1, \dots, p_n$  in *one* event [44]. In other words if the emission of pions were uncorrelated  $C \equiv 1$ . It can be shown that the correlation function can be written as

$$C_2(p_1, p_2) = 1 + |\bar{\rho}(q)|^2 = C_2(q) \quad (1.6)$$

where the four-vector momentum difference  $q = p_2 - p_1$  and  $\bar{\rho}$  is the Fourier transform of the probability density  $\rho(x_1, x_2)$  of the source emitting two pions at points  $x_1$  and  $x_2$  [45].

The pion emission source is assumed to be chaotic. With incoherent emission, the emission in  $x_1$  is independent of the one in  $x_2$  and thus  $\rho(x_1, x_2) = \rho(x_1)\rho(x_2)$ . To cope with the possibility that the source is not fully chaotic a multiplicative factor  $\lambda$  is introduced in eq. 1.6 such that it reads

$$C_2(q) = 1 + \lambda|\bar{\rho}(q)|^2 \quad (1.7)$$

The normalization of  $\rho(x)$  requires that  $C_2(q=0)=2$ . The width of  $C_2$  for  $C_2 > 1$  is related via Fourier transform to the space-time size of the source. By making assumptions about the shape of  $\rho$  the expression of  $C_2$  can be simplified. For a Gaussian density  $\rho(x) = \exp(-x^2/R^2)/R^4$  the correlation becomes  $C_2(q) = 1 + \exp(-q^2/R^2)$  [46]. The spatio-temporal term  $R$  is just the inverse of the width of the region where  $C_2$  is not unity.

The particles emitted are *on-shell* with their energy, momentum and mass obeying the relation  $E = p_0 = \sqrt{\mathbf{p}^2 + m^2}$ . Therefore only three of the four components of  $q$  may be treated independently while forth component is defined from the other three.

How to express the independent components is a matter of choice. A typical parametrization was introduced by Pratt and Bertch (PB) in which the 3-vector  $\mathbf{q}$  is decomposed as  $(q_{out}, q_{side}, q_{long})$  [47, 48]. The first two components lie in the transverse plane and are respectively parallel and orthogonal to  $\mathbf{k}_T = (\mathbf{p}_{T,1} + \mathbf{p}_{T,2})/2$ .  $q_{long}$  is the difference in the longitudinal components  $q_{long} = p_{z,1} - p_{z,2}$ . The last dependent component of  $q$  is defined as  $q_0 = \beta \cdot \mathbf{q}$  where  $\beta = \mathbf{k}/k_0$ .

Measuring the correlation function experimentally as

$$C_2(q) = \frac{d^2\sigma}{dp_1 dp_2} / \left[ \frac{d\sigma}{dp_1} \frac{d\sigma}{dp_2} \right] \quad (1.8)$$

one can fit eq. 1.7 and deduce the corresponding  $R_{out}$ ,  $R_{side}$ ,  $R_{long}$  and  $R_{outlong}$ .

An equivalent parametrization of  $q$  is attributed to the work of Yano, Koonin and Podgoretskii (YKB) [49, 50]. Here a 3-vector of independent components is defined as  $\mathbf{q} = (q_{perp}, q_{para}, q_0)$ . The two first components account for the spatial information in the transverse and longitudinal directions, or in the PB language  $q_{perp} = \sqrt{q_{out}^2 + q_{side}^2}$  and  $q_{para} = q_{long}$ , respectively. The third component is defined as  $q_0 = E_1 - E_2$ .

The choice of the latter component results in measurement of  $R_0$  which directly describes the duration of emission. In the PB case the duration is convoluted with the extension in the *out* direction in the measured  $R_{out}$  and hence more difficult to extract. In addition to the other two radii  $R_{para}$  and  $R_{perp}$  the YKB parametrization provides the longitudinal expansion velocity of the source [46, 51].

Shown in fig. 1.10 are  $\pi^- \pi^-$  correlation functions at mid-rapidity for Au+Au collisions at  $\sqrt{s_{NN}} = 130$  GeV. The momentum difference was parametrized following the PB recipe. From this result it seems obvious that the production of pion pairs at low values  $q$  is correlated, as has previously been shown at lower energies.

The excitation functions of  $\lambda$  and the various PB radii are shown in fig. 1.11. Also shown are the results for  $\sqrt{R_O^2 - R_S^2}$  and  $R_O/R_S$ . When divided by the average transverse velocity  $\beta_T$  the former gives the emission time scale of pions from the fireball. The ratio  $R_O/R_S$  is believed to be sensitive to whether a QGP has been formed in context of the hydrodynamical model. For hadronic hydro the ratio is predicted to be  $\sim 1.0 - 1.2$ , while the QGP scenario gives numbers in the range of  $\sim 1.5 - 10$  [53, 54].

The chaoticity parameter  $\lambda$  is not unity throughout most of the measured energy range. This could point to coherent effects in the production of pion pairs. No big difference is seen in neither the spatial nor the temporal dimensions of the emitting source. Neither does the ratio  $R_O/R_S$  show any significant increase from AGS to RHIC.

#### 1.4.4 Strangeness enhancement

It has been observed in proton proton collisions that the production of strange mesons and baryons is suppressed relative to the ones containing only up and down quarks. This effect is attributed to the higher mass of the  $s\bar{s}$  pair. Thus the higher the strangeness content the more the particle is suppressed.

In a state of QGP strange quark pairs are produced predominantly as a result of gluon fusion, and to a lesser degree from association of  $q\bar{q}$  pairs. Calculations of the production rates of  $s\bar{s}$  from  $gg$ ,  $u\bar{u}$  and  $d\bar{d}$  indicate that the strangeness production saturates during the lifetime of the order of  $\sim 10^{-23}$  s of a plasma created in a relativistic heavy ion collision [55]. Since the QGP is believed to be abundant in gluons the production of strange particles is enhanced in a deconfined state. This is especially valid for the multi-strange baryons which in the dense medium can be formed from  $s$  quarks produced in uncorrelated reactions [56]. It is, however, possible that the collision time is too short to fully reach strangeness chemical equilibrium. The restoration of chiral symmetry discussed in sec. 1.4.6 is also likely to contribute to the strangeness enhancement.

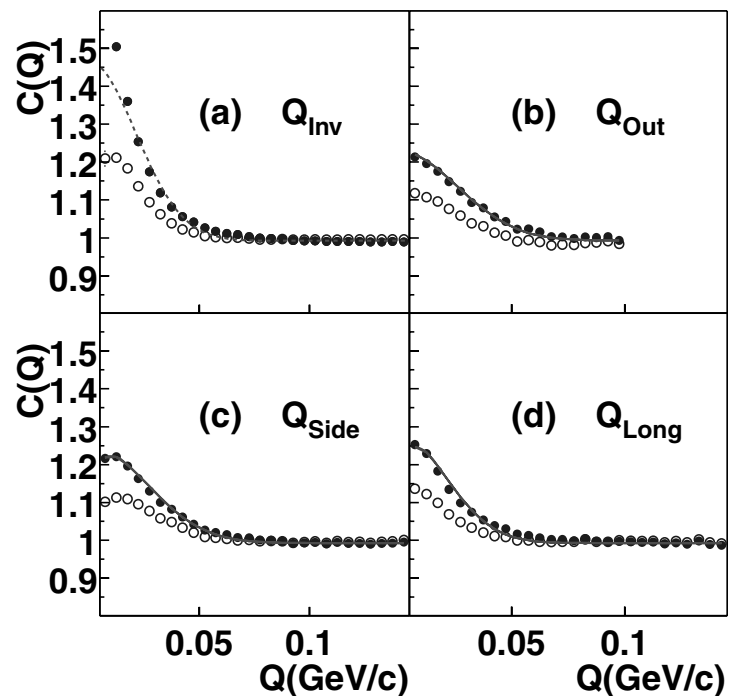


Figure 1.10:  $\pi^-\pi^-$  correlation function as measured by the STAR experiment at  $\sqrt{s_{NN}}=130\text{ GeV}$  [52]. The open and solid points are before and after Coulomb correction, respectively.

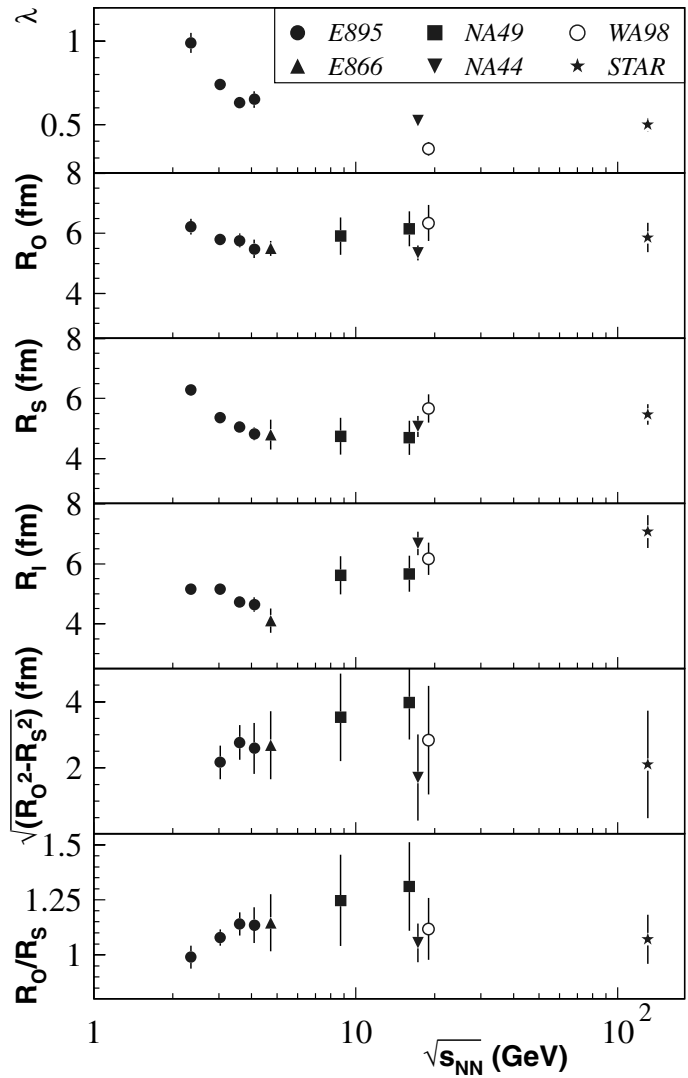


Figure 1.11: Excitation functions for various HBT parameters with the PB parametrization fitted from  $\pi^- \pi^-$  correlations at  $\sqrt{s_{NN}} = 130$  GeV [52]

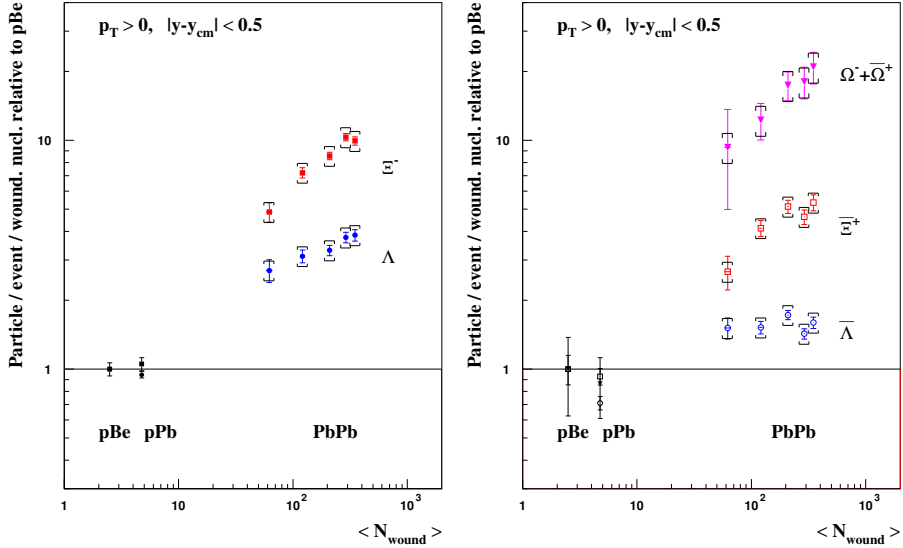


Figure 1.12: Results from the NA57 experiment showing enhancement of hyperons as a function of the number of wounded nucleons. The yields are all normalized the ones from p+Be collisions [61].

When comparing experimental data to models justified comparisons to hadron gas predictions is difficult. The reason is that most of the hadronic models, as well as partonic ones, include thermal and chemical equilibrium. Yet in the hadronic case it has been shown that strangeness equilibration time is about an order of magnitude longer than the reaction time of a heavy ion collision [56]. Also, not all models include collective flow which in particular impedes the comparison of model results to experimental results obtained in limited regions of phase space. A final limitation of models is the lack of strangeness redistribution mechanisms included which has been shown to significantly affect the abundances of (anti-)hyperons e.g. by  $n_1\pi + n_2K \leftrightarrow \bar{Y} + p$  [57]. Caution must clearly be exercised when drawing conclusions on strangeness production as signature of creation of QGP.

Experimental results on production of strange and multi-strange baryons provided E895 at AGS [58], by NA57 at the SPS (fig. 1.12) and (preliminary) STAR data at 200 GeV [59] show a significant enhancement as a function of the number of participants. For the central Pb+Pb collisions at SPS the enhancement factor reaches up about 20 for  $\Omega^- + \bar{\Omega}^+$  relative to p+Be. Also the ratio of strange to non-strange particles increases going from SPS to RHIC energies [60].

As a general characteristic the larger strangeness content of the baryons the less correspondence between enhancement predictions from hadronic models and experimental results [62]. One exception to this is at the AGS energy regime where UrQMD is able to fit the results for strangeness contents up to  $S = -2$ , i.e.  $\Xi^-$  [58]. Thermal models are well able describe the ratios of various particles at SPS and RHIC and thus indicate (close to) chemical equilibrium in the source. This fact combined with the mentioned relaxation times in the hadronic scenario being too long is a strong argument for the production of QGP.

### 1.4.5 Electromagnetic probes

Signatures which are not affected by the predominantly strongly reacting medium, i.e. photons and leptons, are referred to as *electromagnetic probes*. Since they do not interact while propagating through the medium these probes can provide signals of the very early stages of the collision undisturbed by final state effects. This is particularly interesting since the  $k_T$  spectra of direct thermal photons as well as the invariant mass spectra of di-leptons show strong dependence on the initial state [63].

Direct thermal photons from the fireball carry information on the temperature provided that thermal equilibrium has been reached. Studying the rapidity distribution of direct photons one can deduce information about the initial rapidity distribution of the source in which the photons are produced. Direct hard photons can thus provide additional information on the initial pre-equilibrium stage.

In a QGP the direct photons are produced mainly via the  $q\bar{q} \rightarrow \gamma g$  and  $gq \rightarrow \gamma q$  channels. But there is a huge background contribution from hadronic sources, whether a QGP is produced or not, dominated by  $\pi^0 \rightarrow \gamma\gamma$ ,  $\pi\pi \rightarrow \gamma\rho$  and  $\pi\rho \rightarrow \gamma\pi$ . There are also contributions from resonances, in particular  $a_1$  decaying into  $\gamma\pi$  [64]. This background dominates over the direct photons in wide dynamic ranges. Only in certain kinematic windows is expected that photons from a QGP can be seen. E.g. at RHIC and LHC energies a promising window in transverse momentum from about 2 to 5 GeV/c has been predicted [65, 66, 67].

Instead of producing  $\gamma g$  a quark anti-quark annihilation may yield a virtual photon which decays into a lepton pair. Additional di-leptons are produced from quark bremsstrahlung when scattering off gluons in the dense medium of the fireball.

The di-lepton spectrum has large background contributions from a host of sources such as pion annihilations, resonance decays,  $\pi\rho$  interactions at low mass and Drell-Yan interactions at the high mass regime. At RHIC and LHC dominant contributions from open charm decays are expected at high mass. Therefore, as with direct photons, one is likely to detect the leptons from a produced plasma only in certain kinematic windows. One such window is in the invariant mass range between the  $\phi$  and  $J/\psi$  mesons, i.e.  $1 \text{ GeV}/c^2 < M < 3 \text{ GeV}/c^2$ . This range is sometimes referred to as the *intermediate mass region (IMR)* [63].

The NA50 experiment has measured di-muons in p+A and A+A collisions at the CERN SPS. They find that the yields from p+A can be reproduced by a superposition of Drell-Yan and semi-leptonic decays of  $D$  and  $\bar{D}$  [68]. For the higher number of participants they find an excess of di-muons relative to yields scaled from p+A, especially in the IMR. Also the excess increases with the number of participants, as can be seen in fig. 1.13. Similar results from the CERES/NA45 collaboration on di-electrons [69] and from WA98 [70] direct photons show that their yields in A+A collisions can not simply be scaled from p+p or p+A.

Preliminary results from the PHENIX experiment shown in fig. 1.14 point to an enhancement of the measured  $\gamma/\pi^0$  ratio relative to an estimated  $\gamma/\pi^0$  where photonic decay products from mesons account for the bulk of the  $\gamma$  population [71]. The enhancement seen here occurs at high  $p_T$  and is more pronounced with increasing centrality. It is found to be consistent with production expectations from pQCD and subsequent suppression of strongly interacting particles in the produced dense medium (sec. 1.4.8).

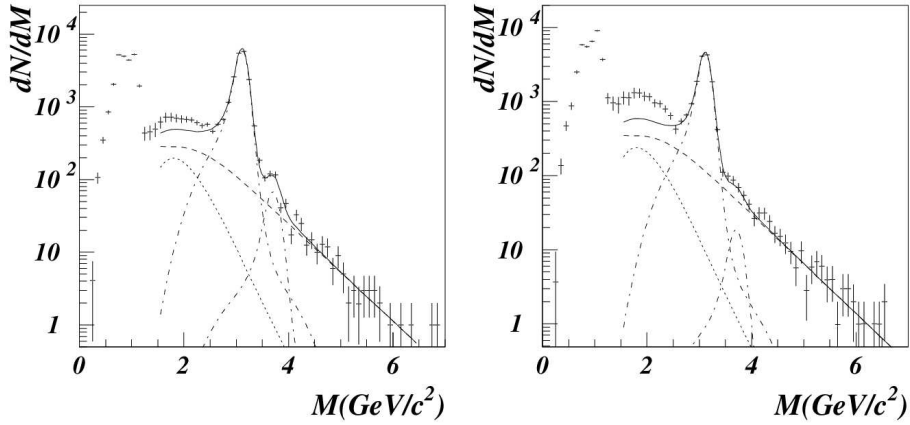


Figure 1.13: Di-muon results from Pb+Pb collisions at SPS measured by NA50. A clear excess above the expected sources (solid line) is seen below the  $J/\psi$  peak ( $m_{J/\psi} = 3.097 \text{ GeV}/c^2$ ). The excess is smaller in the peripheral bin ( $\langle N_{part} \rangle = 110$ ) in the left panel than in the central bin ( $\langle N_{part} \rangle = 381$ ) [68].

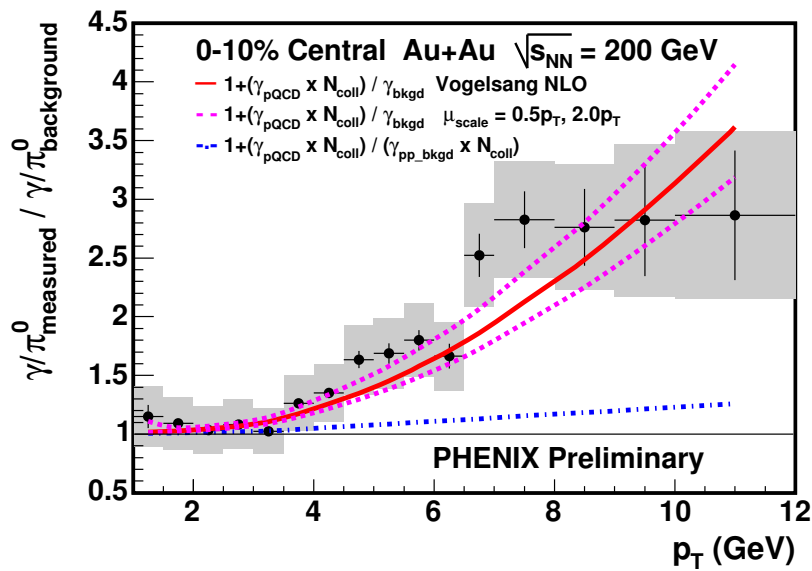


Figure 1.14: Excess of photons in central Au+Au collisions at  $\sqrt{s_{NN}} = 200 \text{ GeV}$  as determined by the PHENIX experiment. The lower dot-dashed curve indicates the expected enhancement if there was no suppression of mesons in the medium.

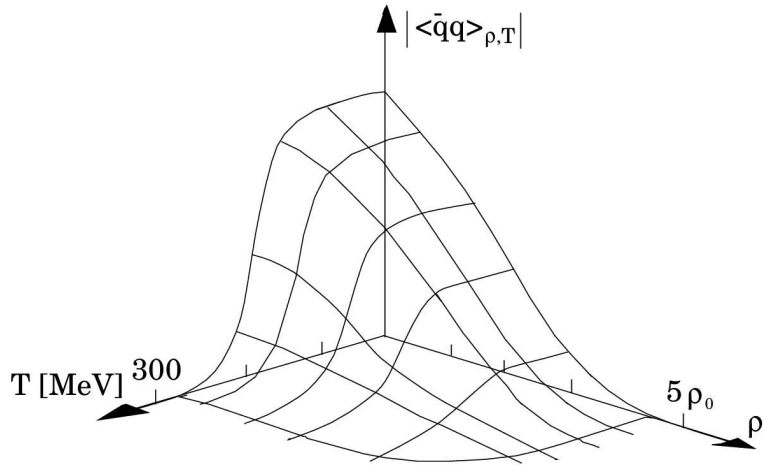


Figure 1.15: Absolute value of the quark condensate as a function of temperature and baryon density [19].

#### 1.4.6 Restoration of chiral symmetry

In the high temperature and/or baryon density limit QCD is characterized by (an approximate) chiral  $SU(3)_L \times SU(3)_R$  symmetry. This symmetry is spontaneously broken at lower energies resulting in non-zero quark condensate  $\langle q\bar{q} \rangle$  in the vacuum. From model calculations it is expected that chiral symmetry is restored in the most energetic collisions of heavy ions, where high temperature or density leads to reduced condensate as seen in fig. 1.15.

The restoration may manifest itself a.o. in altered spectral functions and masses of the  $\rho$ ,  $\omega$  and  $\phi$  mesons. In that case di-lepton mass spectra including decay of these vector mesons should be modified. E.g. the peaks of  $\rho$  and  $a_1$  may merge or simply be smeared out over a wider mass range.

The CERES/NA45 collaboration has measured di-electrons in Pb+Au collisions at 40 and 158 AGeV beam energies. In the low mass region of  $0.2 \text{ GeV}/c^2 < M < 1 \text{ GeV}/c^2$  a factor  $\sim 6$  increase is reported above the expectations from decays of neutral mesons at 40 AGeV, fig. 1.16, while a factor of  $\sim 2.5$  excess is found at 158 AGeV [72]. The access above neutral meson contributions are attributed to  $\pi^+\pi^- \rightarrow \rho \rightarrow e^+e^-$ . Its relative drop when going from 40 to 158 AGeV points to baryon density affecting the  $\rho$  modifications more than temperature. These data rule out an unmodified  $\rho$  propagator. They agree within errors both with  $\rho$  acquiring lower mass in the medium, referred to as *Brown-Rho scaling* [73] and modifications due to increased width of the  $\rho$  mass from  $\rho$ -hadron interactions [74].

Nevertheless, the modifications of the  $\rho$  does not necessarily come from QGP as reported by the STAR experiment a.o. By measuring the  $\rho \rightarrow \pi^+\pi^-$  decay channel in p+p and peripheral Au+Au at  $\sqrt{s_{NN}} = 200 \text{ GeV}$ , i.e. where no phase transition is expected, they find that the  $\rho$  mass increases with  $p_T$  and decreases with multiplicity [75].

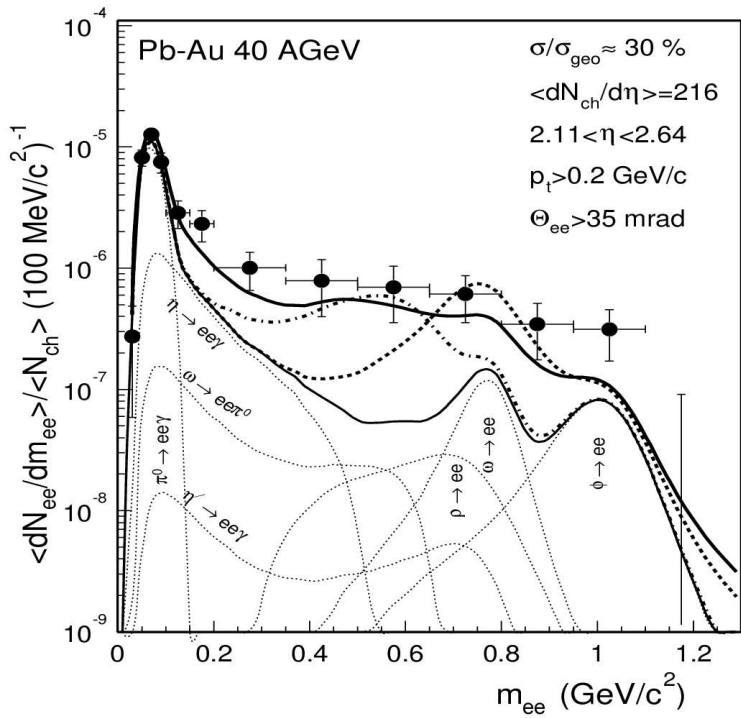


Figure 1.16: Di-electron mass spectrum from Pb+Au at 40 AGeV [72]. The thin solid line accounts for neutral meson contributions, with each meson species' contribution in thin dotted lines. Additional excess from  $\pi^+\pi^-$  annihilation via  $\rho$  propagator are included without  $\rho$  modifications (thick dashed), with in-medium reduced  $\rho$  mass (thick dash-dotted) [73] and with in-medium increased  $\rho$  width (thick solid) [74].

### 1.4.7 Production of quarkonia

The production of charmed and heavier quarks mainly occurs in the initial stages of the collision of two heavy ions. Thermal production of quarks with mass larger than the critical temperature is only a negligible contribution even at LHC energies [76]. The subsequent production mechanisms of hadrons containing charm quarks and the impact of a possible QGP on this production has been the subject of recent discussion.

Charm anti-charm quark pairs are mainly produced in  $gg \rightarrow c\bar{c}$  fusion interactions [77]. The charmed quarks may combine with abundant lighter quarks to produce open charm states, or they may combine into hidden charm mesons. Only a small fraction of the produced  $c\bar{c}$  show up as  $J/\psi$ , but its corresponding peak in the di-lepton mass spectrum is sharp and thus clearly distinguishable from the combinatorial background (fig. 1.13). The region below the  $J/\psi$  peak contains a.o. contributions from semi-leptonic decays of open charm states. Above  $M_{J/\psi}$  the dominant contribution comes from Drell-Yan.

Since leptonic probes may escape the reaction zone practically undisturbed by the dense strongly interacting medium the cross section of Drell-Yan may be calculated via perturbative QCD. The quarkonia-mesons are therefore compared to Drell-Yan to gauge whether their production is altered.

In similar manner as with the electromagnetic signatures in secs. 1.4.5 and 1.4.6 hadronic effects may lead to wrong conclusions on how a QGP affect the quarkonia. Already in p+A collisions suppression of charmonium has been observed. This is attributed to non-equilibrium interactions of the  $c\bar{c}$  with the QCD medium which decreases the probability of a  $J/\psi$  to emerge.

In the presence of a plasma of deconfined partons it has been argued that Debye screening of color charges will suppress the production of mesonic states of heavy quarks such as  $c\bar{c}$  and  $b\bar{b}$  [78]. It is expected that the onset of suppression of the larger bound states, such  $\psi'$  and  $\chi_c$ , will occur at lower temperatures than for the smaller and more tightly bound  $J/\psi$ . The same holds true for the excited bottomonium  $\Upsilon'$  state relative to  $\Upsilon$ .

It is difficult to disentangle these Debye suppression effects from the ones caused by final state dissociation reactions, such as  $\psi + \rho \rightarrow D\bar{D}$  and  $\psi + \Delta \rightarrow \Lambda_c\bar{D}$ . Non-thermal color field fluctuations and energy loss and (anti-)shadowing of the gluons prior to the fusion reaction may alter its cross section and thereby modify the production rate of the final charmonium bound state. Furthermore, any attempt to quantify the suppression of  $J/\psi$  has to take into account the feed-down from the heavier resonances, in particular  $\psi'$  and  $\chi_c$ , which, as mentioned above, have different suppression characteristics.

Another scenario of statistical recombination [79] suggests that the screening of  $J/\psi$  is overcome by recombination at the later freeze-out stage. Hence in this picture one may find an increased production of both open and hidden charm, and it therefore contradicts the scenario outlined in [78].

In the recombination scenario it is assumed that the charm quarks produced in the early stages equilibrate thermally in the QGP, i.e. there is no thermal production. Also no charmed bound states are preformed in the QGP. In that sense this model includes full screening in comparison to the partial screening in [78].

The NA50 experiment has shown results from Pb+Pb collisions which point to suppression of quarkonia at the top SPS energies (fig. 1.13). The additional *abnormal* suppres-

sion of  $J/\psi$  found in collisions of the heaviest ions suggests new suppression mechanisms. Regarding the ordinary nuclear suppression scenarios NA50 estimates that about half of its observed suppression of  $J/\psi$  in Pb+Pb comes from non-equilibrium effects. Also  $\psi'$  is found to be more suppressed than  $J/\psi$ . This occurs already in p+A but enhanced suppression is seen for the heavier systems.

Yet, the full phase-space integrated  $J/\psi$  results from NA50 [80, 81] can be explained also in the context of the statistical recombination model although only by using a higher cross section than the one estimated from NLO pQCD calculations for p+p collisions [79]. Hence, the outcome from comparison to SPS data is rather mixed.

When comparing to the first preliminary data at the top RHIC energies [82] the statistical recombination model is in agreement with the data. But here the data has very large error bars. The data suggest neither a large enhancement nor a dramatic suppression of  $J/\psi$  e.g. of the order of 20 which was predicted in [83]. At LHC the statistical recombination model predicts an enhanced production of charmonium which should be able to clearly distinguish the two reaction patterns described above.

#### 1.4.8 High $p_T$ suppression

If a QGP is produced in central heavy ion collisions it is a state of colored matter, as opposed to the hadronic state whose constituents are color neutral hadrons. Hence, the propagation of a fast parton through the QGP is expected to be affected differently depending on the phase of the matter it goes through.

High  $p_T$  particle production at the current collider energies is described by perturbative QCD (sec. 1.3.2). Partons in the initial nuclei scatter off each other and continue with high transverse momenta. The scattered partons subsequently fragment into jets of hadrons, i.e. a group of particles with high  $p_T$  whose polar angle distribution is limited within a narrow cone.

When propagating through a dense partonic matter the parton may lose energy through bremsstrahlung and its high transverse momentum is distributed over a larger number of medium partons. This would lead to a suppression of high momentum hadrons leaving the collision zone.

Alternatively the incoming partons may suffer multiple scattering before their hard collision. The result of this scattering is the creation of initial transverse degrees of freedom and hence an overall increase of momentum of the final state particles. This high  $p_T$  enhancement from incipient scattering is referred to as the *Cronin effect*.

These two pictures are expected to affect the *nuclear modification factor* in opposite directions. For a collision of nucleus A on nucleus B the factor is defined as

$$R_{AB} = \frac{d^2 N^{AB}/dp_T d\eta}{(\langle N_{coll} \rangle / \sigma_{inel}^{pp}) d^2 \sigma^{NN}/dp_T d\eta} \quad (1.9)$$

Here  $\langle N_{coll} \rangle$  is the average number of binary collisions in the A+B interaction and  $\sigma_{inel}^{pp}$  is the inelastic cross section for p+p collisions. By studying the nuclear modification factor one essentially compares the invariant spectrum values of hadrons in A+B collisions with the cross section obtained from spectra in p+p scaled by the number of binary collisions.  $R_{AB}$  is usually expressed as a function of  $p_T$  and centrality for hadrons and identified particles. If the particle production scales with the number of binary collisions, which is

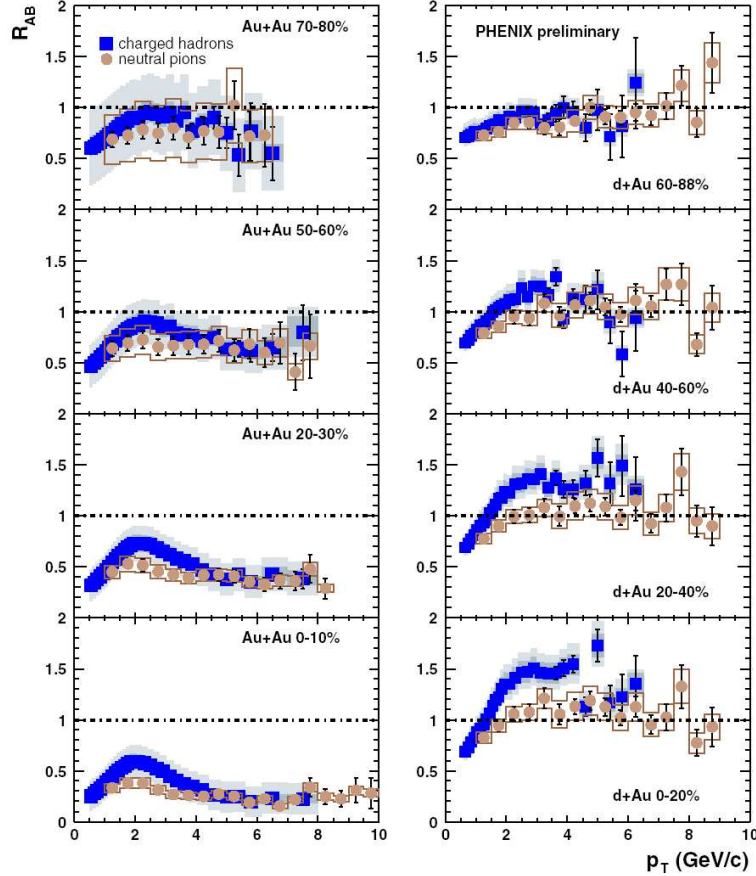


Figure 1.17: The results from PHENIX on the nuclear modification factor for charged hadrons and neutral pions in Au+Au (left panels) and preliminary results for d+Au [86]. High  $p_T$  particles in Au+Au collisions are more suppressed with increasing centrality, while the opposite trend is seen for d+Au.

typically expected in the high end of the  $p_T$  range,  $R_{AB}$  should equal unity. The low end scales with the number of participants,  $N_{part} \leq N_{coll}$ .  $R_{AB}$  should therefore be smaller than unity in this end.

At mid-rapidity in central Au+Au collisions at RHIC all the heavy ion experiments see a suppression of the high  $p_T$  hadron tail of  $R_{AuAu}$  which is attributed to partons losing energy in the dense medium [84]. In peripheral Au+Au collisions the modification factor for charged hadrons at mid-rapidity is again consistent with unity and asymmetric d+Au collisions at RHIC show stronger Cronin enhancement with increasing energy [85, 86]. Fig. 1.17 shows PHENIX' results for  $R_{AuAu}$  and (preliminary)  $R_{dAu}$  at mid-rapidity as a function of  $p_T$  and centrality. It also shows that the evolution of  $R_{AB}$  depends on particle species.

No QGP is expected in d+Au collisions. Nevertheless, more exotic suppression scenarios such as the possible gluon saturation in the incoming nuclei, i.e. nuclei in a state referred to as *color glass condensate (CGC)*, also predict high  $p_T$  suppression in d+Au collisions [87]. The comparison of nuclear modification factors in Au+Au to the one in

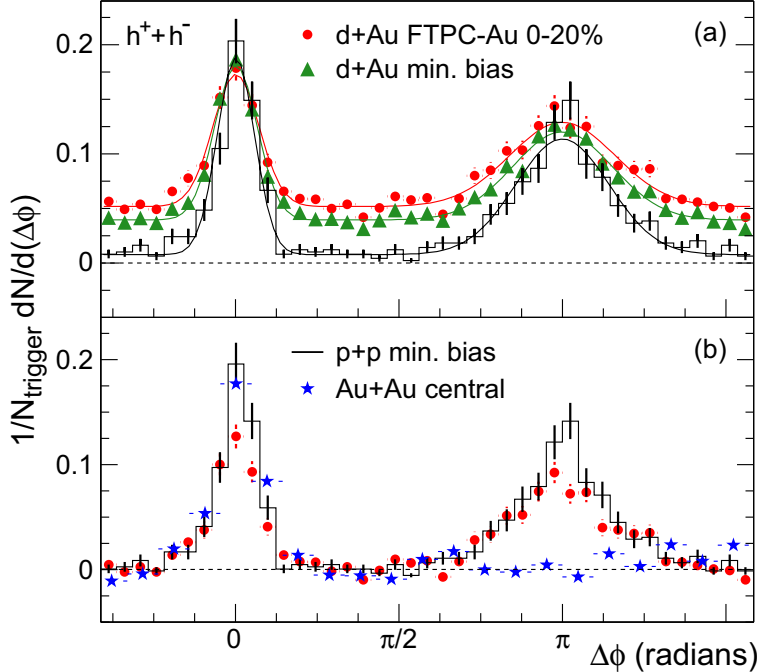


Figure 1.18: Distribution of two-particle azimuthal angle correlation measured by the STAR experiment. The upper panel shows central and min-bias d+Au distribution, while the lower one compares the central d+Au distribution to the results obtained for p+p and Au+Au. The away-side peak in Au+Au is clearly suppressed relative to p+p and d+Au [88].

d+Au was thus performed in order to rule out such possible initial state effects. The obtained different results for  $R_{AuAu}$  and  $R_{dAu}$  show that the suppression of the former is a final state effect. CGC is presented somewhat further in sec. 2.4.

Suppression of particles with high transverse momentum is also studied by the two-particle angle correlation. When triggering on a particle with high transverse momentum originating from a hard scattering and measuring the difference in azimuthal angle between this *leading particle* and other high momentum hadrons the back-to-back picture of di-jets is visible in p+p and d+Au collisions but not so in Au+Au. The upper panel in fig. 1.18 illustrates the azimuthal angle correlation in d+Au collisions at the top RHIC energy. In both central and min-bias collisions the peak around  $\Delta\phi = \pi$  (*away-side*) is comparable to the one centered at  $\Delta\phi = 0$  (*near side*). Comparing the angle correlation in central Au+Au with d+Au and p+p in the lower panel the away-side peak in Au+Au has disappeared.

The interpretation of this result relies on creation of dense partonic matter in the central Au+Au collisions. If a hard scattering occurs close to the surface of the expanding matter it is probable that the parton fragmenting radially outward ends up in the detector as a high momentum jet. The other parton going in the opposite direction due to momentum conservation is likely to suffer energy loss on its relatively longer way through the dense matter. No or very few away-side jets are therefore seen in the detector.

Results both from studies of the nuclear modification factor and of two-particle az-

imuthal correlations are difficult to explain without a dense partonic stage in the evolution of the fireball and hence points in direction of QGP.



# Chapter 2

## Collision scenarios

A collision of two heavy ions is an event of very short time span in the general language. The customary time unit is fm/c, i.e. of the order of  $10^{-24}$  s. Nevertheless, the interaction of two nuclei is described as an evolution involving several steps from the initial baryons to the final particle outcome detected in the experimental apparatus. The characterization of the collision scenario with hundreds of initial baryons and thousands of final hadrons may be a daunting task. Yet a number of theoretical descriptions exist on paper and also as computer models.

This chapter first introduces the concept of nuclear stopping. The succeeding sections present a few of the above mentioned scenario descriptions. They all involve hydrodynamic evolution (sec. 1.3.2) in different number of dimensions but they vary greatly in description of the initial state.

### 2.1 Nuclear stopping

In a collision of two high energy nuclei it is expected that excited nuclear matter is produced [89, 90]. A large fraction of the incoming longitudinal momentum is transformed into transverse degrees of freedom via multiple collisions. Alternatively one can talk about a shift of rapidity from the beam rapidity towards the more central region. This deceleration in the longitudinal direction is called *nuclear stopping power*.

To quantify the nuclear stopping it is common to look at baryon rapidity distributions, i.e. the number of net-baryons per rapidity bin as a function of rapidity. Since baryon number is a conserved quantity the integral of this distribution is known. It simply equals the number of participants which can be calculated in Monte-Carlo models. The shape of this distribution, and in particular its width, depends strongly on the nature of the successive collisions and is thereby expected to change with the oncoming of new physics [91, 92, 93].

Two extremes may be considered when it comes to the nuclear stopping in high energy collisions. One is Landau's hydrodynamical picture which describes full stopping of the incoming nuclei (sec. 2.2). In this picture a Gaussian rapidity distribution of produced particles is expected and hence the net-baryon distribution may be close to Gaussian. The other extreme is full transparency, also referred to as the Bjorken picture, in which

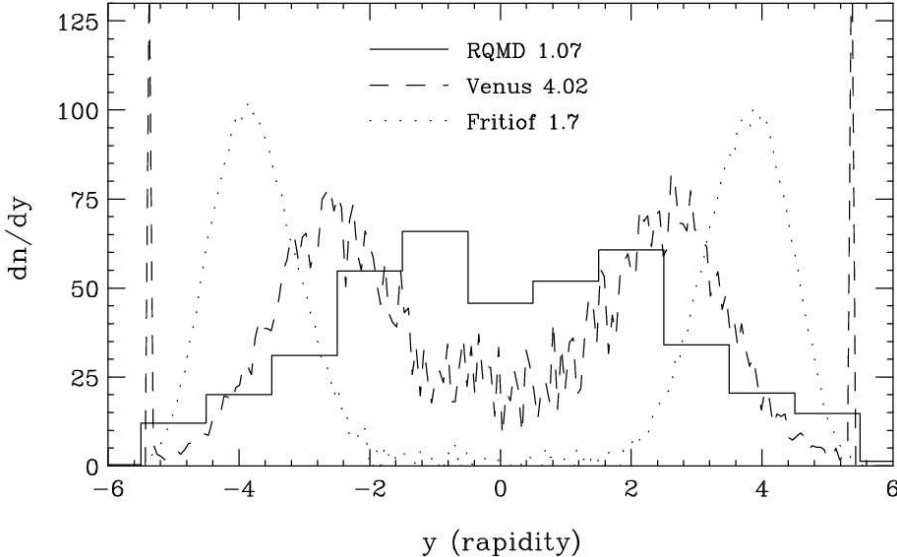


Figure 2.1: Various model simulations of nuclear stopping in Au+Au showing widely different predictions for  $dN/dy$  of net baryons at  $\sqrt{s_{NN}} = 200$  GeV [94].

the two nuclei penetrate each other without significant stopping (sec. 2.3). In this picture the net-baryon distribution around mid-rapidity is 0.

As can be seen from fig. 2.1 various models in versions prior to startup of the RHIC collider predicted greatly different stopping scenarios. With such widely differing predictions this observable has a great potential to narrow down the number of models giving reasonable descriptions of the collision outcome.

From experimental results on stopping as a function of energy it appears at first glance that stopping in the AGS regime is different from the one at the higher RHIC energies. Fig. 2.2 points to this by showing the net-proton rapidity distributions obtained at AGS, SPS and RHIC with center of mass energies of 5, 17 and 200 GeV, respectively. The rapidity distribution at AGS energies seems well described by a single Gaussian, while at the higher energies the distributions have no peak at the central rapidity.

Yet, even at the low SIS energies of  $\sqrt{s_{NN}} = 0.4 - 1.5$  GeV recent results from Zr+Ru, Ru+Ru and Zr+Zr collisions indicate a double-peak structure in the proton distribution, one from the target and one from the projectile [95]. The two peaks are separated by about one unit of rapidity and hence the convolution of the two distributions has a shape similar to the one of a single Gaussian.

Furthermore, the highest energy net-proton data from RHIC can be fairly well reproduced with the HIJING event generator [96] in the rapidity range  $0 < y < 3$  [97]. The HIJING generator is based on perturbative QCD at the partonic level. The hadronic transport model UrQMD, however, does not seem to describe the net-proton results at  $\sqrt{s_{NN}} = 200$  GeV. At the lower energies of the SPS and AGS hadronic transport models are able to reproduce the rapidity spectra if they include rescattering, string decays or multi-quark droplets [18, 98, 99].

Comparing qualitatively to the above mentioned Landau and Bjorken pictures it appears that the Landau picture is the most suitable at the lower AGS energy regime.

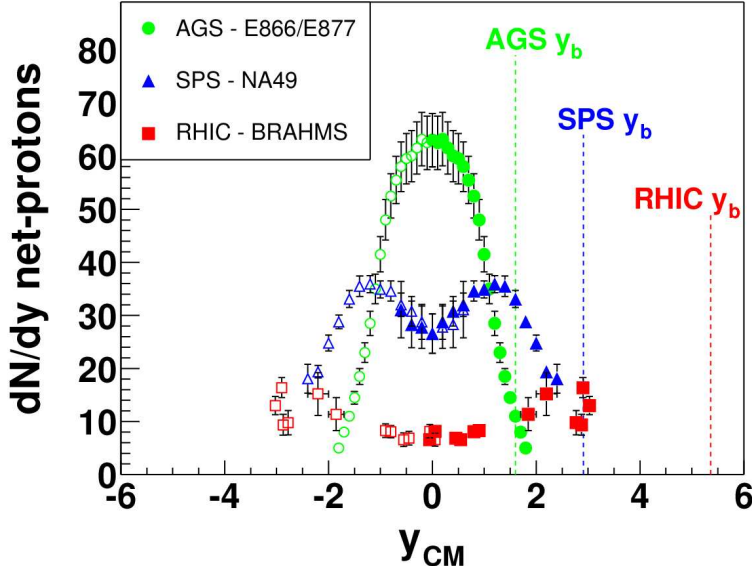


Figure 2.2: Rapidity distribution of net-protons from AGS to RHIC energies [97]. The distributions are from the 5% most central Au+Au (AGS and RHIC) and Pb+Pb (SPS) collisions.

Going to higher energies one may conclude that neither Landau nor Bjorken describe the collision. Yet, fig. 2.2 showing only net-protons does not tell the whole story since also other particles such as  $\Lambda$ ,  $\Xi$ ,  $\Omega$  and their anti-particles carry baryon number.

## 2.2 Landau picture

In the early 1950's both Fermi and Landau described the collision of two highly Lorentz contracted systems [100, 101, 102]. They assumed an initial state in which the energy of the incoming constituents is rapidly distributed in a thin slab of matter of volume  $V \propto R^3 / \sqrt{s_{NN}}$  such that the matter is thermalized. Here  $R$  is the radius of initial systems in the transverse direction. Moreover, they adopted an equation of state as expressed for a massless blackbody system whose pressure  $p$  goes with the energy density  $\epsilon$  as  $p = \epsilon / 3$ . In addition, all chemical potentials are assumed to be zero.

Landau put these initial conditions into the context of three-dimensional relativistic hydrodynamics. The evolution is assumed to be isentropic and viscosity is not considered. This description is referred to as the *Landau hydrodynamic model* as opposed to Fermi's picture where there is no hydrodynamic evolution.

Fig. 2.3 shows a simplified version of the early stages of a central heavy ion collision according to Landau. Two Lorentz contracted nuclei collide head-on and are fully stopped in a narrow volume, i.e. whose longitudinal extent is small relative to the one in the transverse direction. From there on the evolution of the system is determined by the obtained internal pressure gradients and relativistic hydrodynamics.

From the EoS one may obtain an entropy density  $\sigma \propto \epsilon^{3/4}$  and multiplied with the volume the total entropy  $S$  increases with energy density as  $S = \sigma V \propto s^{3/4} / \sqrt{s} = s^{1/4}$ .

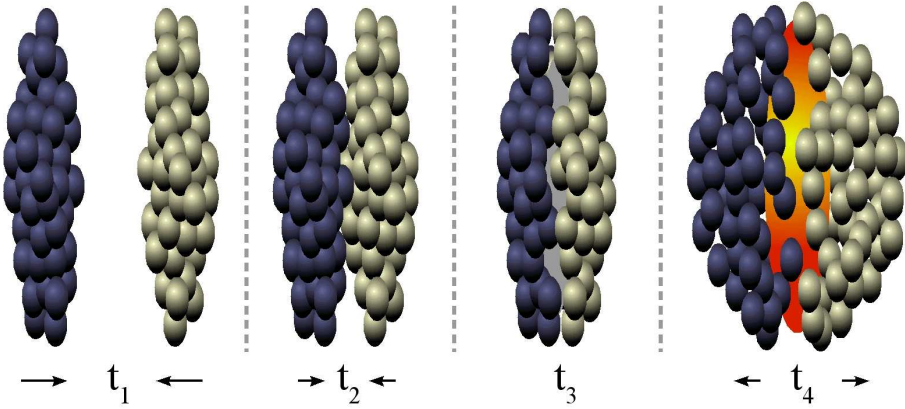


Figure 2.3: Simplified description of a central heavy ion collision in Landau’s hydrodynamic model. Two Lorentz contracted nuclei collide head-on and are fully stopped in the center-of-mass frame at  $t = t_3$ . The following evolution follows relativistic hydrodynamics.

Hence, the total multiplicity, being proportional to the total entropy, is predicted to increase as  $N_{ch} \propto s^{1/4}$  [103, 104].

The strong compression in the longitudinal direction leads to highly anisotropic distributions. From the hydrodynamic evolution one may infer Gaussian distributions for the rapidity densities of produced particles expressed as

$$\frac{dN}{dy} \sim \frac{s^{1/4}}{\sqrt{2\pi L}} \exp\left(-\frac{y^2}{2L}\right) \quad (2.1)$$

where the width of the distribution is expressed by [105]

$$L = (1/2) \ln(s/4m_p^2) = \ln(\gamma) \quad (2.2)$$

As indicated in sec. 2.1 the net-baryon distribution in the Landau picture may be close to Gaussian. The shape of the distribution depends on the longitudinal pressure gradients and the baryochemical potential. The predictions for the rapidity density of net-baryons in the Landau picture are therefore rather uncertain.

Landau did not take partons into account as his model was devised about two decades before the arrival of QCD description of strongly interacting matter. Thus, it is strictly speaking not a signature candidate for neither partonic nor hadronic evolution. The requirement is that a description involving rapid thermalization and hydrodynamic evolution is applicable. Nonetheless, hydrodynamics is only suitable in the case the mean free path of a constituent is short compared to the spatial extent of the system. This requirement as well as early thermalization does at least indicate that hydro should work even better in a partonic state than in a hadronic one.

## 2.3 Bjorken picture

Some thirty years after the advent of Landau’s description of heavy ion collisions an alternative, and to some extent opposite, scenario was outlined by Bjorken [106]. In

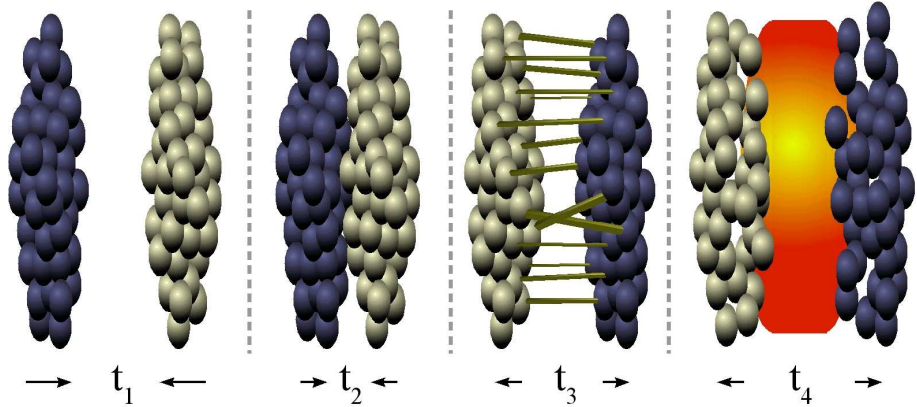


Figure 2.4: Four snapshots in the initial stages of a heavy ion collision according to Bjorken. The leading particles carrying the net-baryon number continue with rapidities close to the ones of the initial nucleons. Hence, the constituents from each nucleus are left-right-mirrored in the two right panels of this figure relative to the ones in fig. 2.3. Particle production at mid-rapidity occurs from the highly excited color field left by the nuclei.

particular the early stages of the collision differ from the Fermi/Landau description, while a Landau style hydrodynamical expansion takes place an initial time  $t_0 \sim 1 \text{ fm}/c$  after the collision of the incident nuclei.

A description of the early stages of a heavy ion collision is established by drawing analogues from results on rapidity density in  $p+p$ ,  $p+\alpha$  and  $\alpha+\alpha$  collisions at the CERN SPS and ISR. E.g. in the Bjorken model it is assumed that the constituents in each of the nuclei acquire  $\gamma \sim 2$  in their nucleus' initial rest frame when traversed by the other nucleus. Thus the baryon numbers of the incoming nuclei should be found in close proximity of the respective nuclei's fragmentation regions. I.e. the nuclei penetrate each other almost transparently, in contradiction to the Fermi/Landau full stopping scenario. Therefore the net baryon number is 0 at mid-rapidity, with correspondingly vanishing chemical potential.

Particles escaping at mid-rapidity are produced from the excited color field left by the fragmenting nuclei. This is illustrated in fig. 2.4 where the panel at  $t = t_3$  shows flux tubes which subsequently break up into quark anti-quark pairs.

Bjorken estimated an initial energy density  $\epsilon_0 = 1 - 10 \text{ GeV}/\text{fm}^3$  after the initial time  $t_0$  at SPS energies. The corresponding high entropy and particle densities ( $\rho_0 = 2 - 20 \text{ fm}^{-3}$ ) make it likely that local thermal equilibrium is rapidly obtained and thus hydrodynamics is applicable for the following evolution of the system.

From the collision of lighter systems an emerging picture of boost-invariance at mid-rapidity is applied to collisions of heavier nuclei. Boost-invariance implies that the produced particle rapidity density distribution  $dN/dy$  as a function of  $y$  is flat in a substantial rapidity range. In other words the initial energy and entropy densities,  $\epsilon_0$  and  $\sigma_0$  respectively, are the same in all center-of-mass-like frames<sup>1</sup>, i.e. constant at proper time

---

<sup>1</sup>According to Bjorken: "...i.e., in all frames where the emergent excited nuclei are, shortly after the

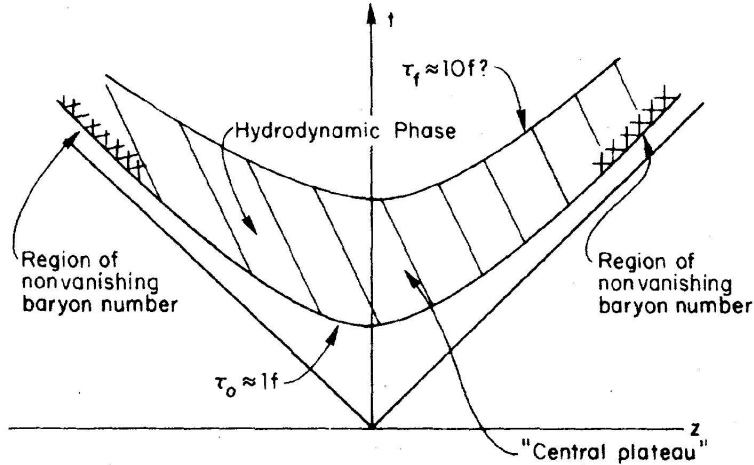


Figure 2.5: The longitudinal evolution of a heavy ion collision according to Bjorken [106]. One-dimensional hydrodynamic expansion start after an initial time  $t_0 \sim 1 \text{ fm/c}$ . The net-baryon number is found close to the asymptotic  $t = z$  line.

$$\tau_0 = (t_0^2 - z^2)^{1/2} \sim 1 \text{ fm/c} \text{ as illustrated in fig. 2.5.}$$

The hydrodynamic expansion in the first few fm/c after the collision may be described as a one-dimensional homogeneous expansion along the collision axis ( $z$  direction). The fluid a distance  $z$  away from the collision point has velocity  $z/t$ , where  $t$  is the time since the collision of the incident contracted nuclei. Later on, i.e. when the distance between the receding nuclei is greater than their nuclear diameter, three-dimensional expansion is assumed. For the expansion at all stages no viscosity or thermal conductivity is considered.

Bjorken found that in the one-dimensional expansion the entropy per unit rapidity,  $dS/dy$ , is a constant of the motion. Entropy is converted into multiplicity and hence predicting flat distribution of  $dN/dy$  for pions also after the hydrodynamic stage. In addition the yield of pions is expected to scale with the transverse extension of the nuclei, expressed in terms of the mass number  $A$  as

$$\frac{(dN_\pi/dy)_{A+A}}{(dN_\pi/dy)_{p+p}} = \left[ \frac{2 \text{ fm}}{d_0} \right]^2 A^{2/3} \quad (2.3)$$

where  $1/d_0^2$  represents the number of independent nucleon-nucleon collisions per unit area [106]. This scenario predicts an initial temperature  $T_0 \sim 200 - 300 \text{ MeV}$  in the central plateau at SPS energies, i.e. higher than typical predictions for a phase transition at  $T_c \sim 170 \text{ MeV}$ . Thus, although not requiring a transition from hadron gas to quark gluon plasma this scenario clearly supports a partonic stage in the evolution of heavy ion collisions.

---

collision, highly Lorentz-contracted pancakes receding in opposite direction from the collision point at the speed of light.”

## 2.4 CGC + hydro

Even though hydrodynamic evolution is employed in the previous two scenarios its applicability is disputed at the energies of AGS and SPS. E.g. hydrodynamics over-predicts elliptic flow  $v_2$  at SPS [107, 108]. Also the scaled elliptic flow<sup>2</sup>,  $v_2/\epsilon$ , predicted by hydrodynamics to saturate around 0.2 is not reached experimentally for energies below the RHIC regimes of 130 and 200 GeV. Thus, the pertinence of hydrodynamics is more evident at RHIC than at the lower energies.

In conjunction with theoretical work to describe heavy ion collisions at the current top beam energies as well as deep inelastic scattering the concept of color glass condensate has developed [109]. The CGC describes the state of the incident nuclei where the population of low  $x$  gluons is saturated<sup>3</sup>. This state is dense enough that it may be studied in a weak coupling classical context referred to as the McLerran-Venugopalan (MV) model [110]. Experimentally, results on deep inelastic scattering at HERA is consistent with a description involving gluon saturation [111, 112].

In [23] the collision of two slabs of CGC is used to create an initial state of matter that is subsequently allowed to expand according to relativistic three-dimensional hydrodynamics. Because of the high number of gluons in the incident CGC pancakes a rapid local thermalization and chemical equilibration within an initial time  $t_0 \sim 0.6 \text{ fm}/c$  is assumed<sup>4</sup>.

The initial conditions for hydrodynamic expansion obtained from the melting of CGC is illustrated in fig. 2.6. The gluon rapidity density is close to Gaussian, i.e. showing no indication of a boost-invariant central plateau as assumed in the Bjorken model. It is assumed that the gluon number density represents the three-flavor parton number density and that the shape of the rapidity distribution is not changed during thermalization. However, the thermalization reduces the transverse energy per parton from  $E_T/N_g \sim 1.6 \text{ GeV}$  down to about 1 GeV.

The collisions of small  $x$  partons only account for the soft part of the particle outcome. Hard parton spectra are generated from simulations with PYTHIA 6.2 [113]. The energetic partons lose energy through gluon emission while propagating at the hydrodynamic stage. The parton energy loss formula used in [23] takes into account the running strong coupling constant as well as varying parton density from the hydrodynamic simulation. Also it contains an overall normalization factor which is chosen to reproduce the nuclear modification factor of  $\pi^0$  at the 10% most central Au+Au collisions as determined by the PHENIX experiment [114].

This CGC+Hydro model gives predictions for the number and transverse energy (pseudo-)rapidity distributions in central events, seen in fig. 2.7. The rapidity distributions show no sign of boost-invariance, while the distributions in pseudo-rapidity have a dip in the central region of the abscissa.

In this model an EoS representing a baryon free fluid of massless partons is used for temperatures  $T > T_c = 170 \text{ MeV}$ . Hadronization as well as chemical freeze-out is assumed to occur at  $T = T_C$  and a partial chemical equilibrium stage is simulated by including

---

<sup>2</sup>Here  $\epsilon$  is the initial spatial eccentricity.

<sup>3</sup>Here  $x$  describes the fraction of the nucleus' momentum carried by a parton.

<sup>4</sup>The final particle multiplicities are found to be insensitive to variation of initial time in the range  $0.5 \leq t_0 \leq 1.0 \text{ fm}/c$ .

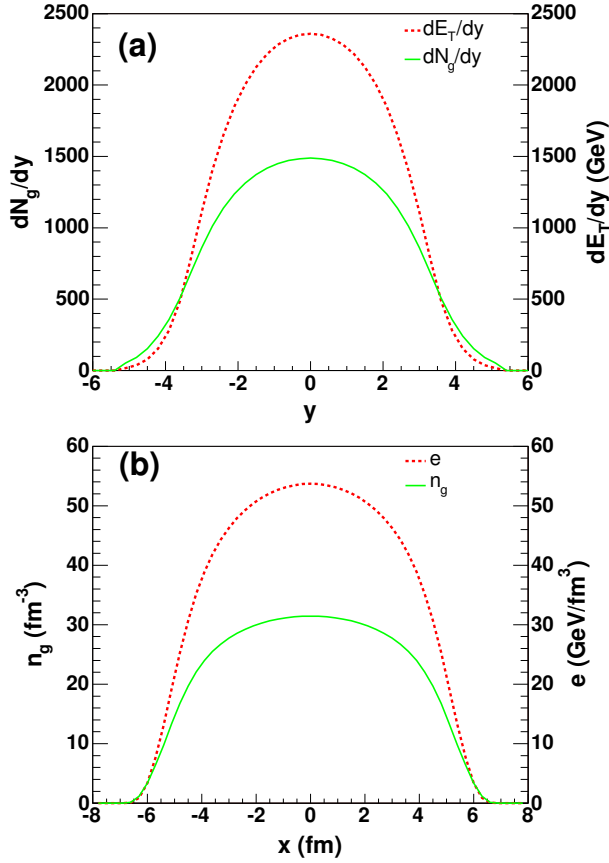


Figure 2.6: Gluon numbers (solid lines) and transverse energy (dashed lines) densities as a function of (a) rapidity and (b) transverse coordinate as obtained from collision of two slabs of CGC at  $\sqrt{s_{NN}} = 200$  GeV with an impact parameter  $b = 2.4$  fm [23]. An overall normalization factor is chosen such that the total multiplicity of hadrons is reproduced.

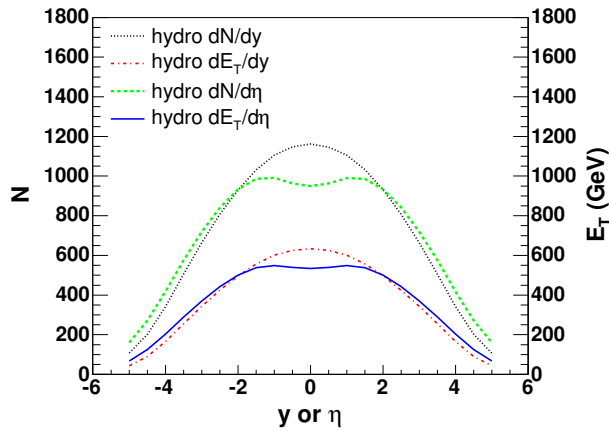


Figure 2.7: CGC+Hydro predictions for (pseudo-)rapidity distributions of all hadrons in Au+Au collisions for the same conditions as in fig. 2.6 [23]. The resulting transverse energy per particle is about 0.55 GeV after the hydrodynamic expansion.

chemical potentials for each hadron species in the EoS. This model explicitly includes a transition from partonic to hadronic degrees of freedom, in addition to the CGC description of the initial nuclei. The thermal freeze-out temperature, being a free parameter in hydrodynamic models, is here defined to be  $T_{th} = 100$  MeV.

## 2.5 Experimental tests of collision scenarios

As may be interpreted from the previous discussion one may search for signs of the different collisions scenarios in both longitudinal and transverse characteristics of the experimental data. The objective of this dissertation is therefore to examine several of these observables and search for hints pointing in the direction of any of the possible scenario descriptions.

Transverse mass spectra are obtained for identified particles at various rapidity bins from mid-rapidity around  $y=0$  to the forward region around  $y\sim 3$ . In the first unit of rapidity, i.e.  $0 \lesssim y \lesssim 1$ , the acceptance is extended to higher  $p_T$  than previously obtained by BRAHMS. By also applying corrections for weak decays contributions one may do a proper evaluation of flow effects. The size of the transverse flow has strong implications on the relevance of one-dimensional scenario descriptions.

At each rapidity bin considered the transverse spectra are fitted with the blast-wave expansion function according to the recipe in [22]. The rapidity dependence of the fit parameters is presented and discussed. By integrating the blast-wave fit functions rapidity densities are obtained in the covered rapidity range. Signs of boost invariance as well as Gaussian functional behavior are searched for both in the rapidity dependence of the fit parameters and the rapidity distributions of the identified particles. In particular the distribution of net-protons addresses nuclear stopping. For Gaussian shapes the functional widths are discussed.

In Chapter 3 the RHIC accelerator complex is described before the experimental setup of BRAHMS is presented. The analysis of the experimental data is the topic of Chapter 4 followed by obtained results in Chapter 5. In Chapter 6 these results are discussed in the context of the collision scenarios outlined in this chapter.



# Chapter 3

## The Relativistic Heavy Ion Collider and the BRAHMS experiment

### 3.1 The collider complex

The *Relativistic Heavy Ion Collider (RHIC)* is the largest component in the chain of accelerators at Brookhaven National Laboratory (BNL), NY, USA. It consists of two separate rings, each with a circumference of 3.8 km, located in a tunnel at ground level. The RHIC complex is depicted in fig. 3.1. The tunnel currently inhabited by RHIC was initially constructed for the proton-proton collider ISABEL in the late 70s. In total RHIC consists of a lattice of 1740 super-conducting magnets cooled by liquid helium at 4.5 K. At six locations the rings intersect and allow for experimental detector setups. Currently four of these intersection regions are used for experiments.

RHIC has been designed for great versatility. Its primary capability is to accelerate, store and collide beams of heavy ions, most notably Au on Au. The top energy for gold nuclei is 100 GeV/u per beam, i.e.  $\sim 100$  times the rest energy of the nucleons. With magnet systems designed for the top Au collision energy, corresponding to a magnetic rigidity<sup>1</sup> of  $B\rho = 839.5$  Tm, the design allows for acceleration of protons up to 250 GeV and typical light ions up to 125 GeV/u, i.e. solely depending on the ion charge-to-mass ratio [115].

The luminosity achieved at RHIC depends on the species being accelerated. Running with Au beam at the top energy RHIC typically achieves luminosities of about  $2 \times 10^{26} \text{ cm}^{-2} \text{ s}^{-1}$  averaged over the expected 10 h storage time. In this mode RHIC is run with  $\sim 10^9$  ions per bunch in each of the 56 bunches per ring. When running with proton beam, the luminosity may be as high as  $\sim 1 \times 10^{31} \text{ cm}^{-2} \text{ s}^{-1}$  with  $10^{11}$  protons per bunch. But even with number of particles differing by two orders of magnitude, the electric beam currents differ by less than a factor of two.

RHIC can be run in an asymmetric mode in which beams of unequal species collide. In particular the collider has been run with deuterium colliding with gold ions. Also, the collider may provide collisions in the range of energies from close to injection all the way

---

<sup>1</sup>Here  $B$  is the size of the dipole's magnetic field and  $\rho$  is the radius of the particle's circular trajectory in the dipole aperture.

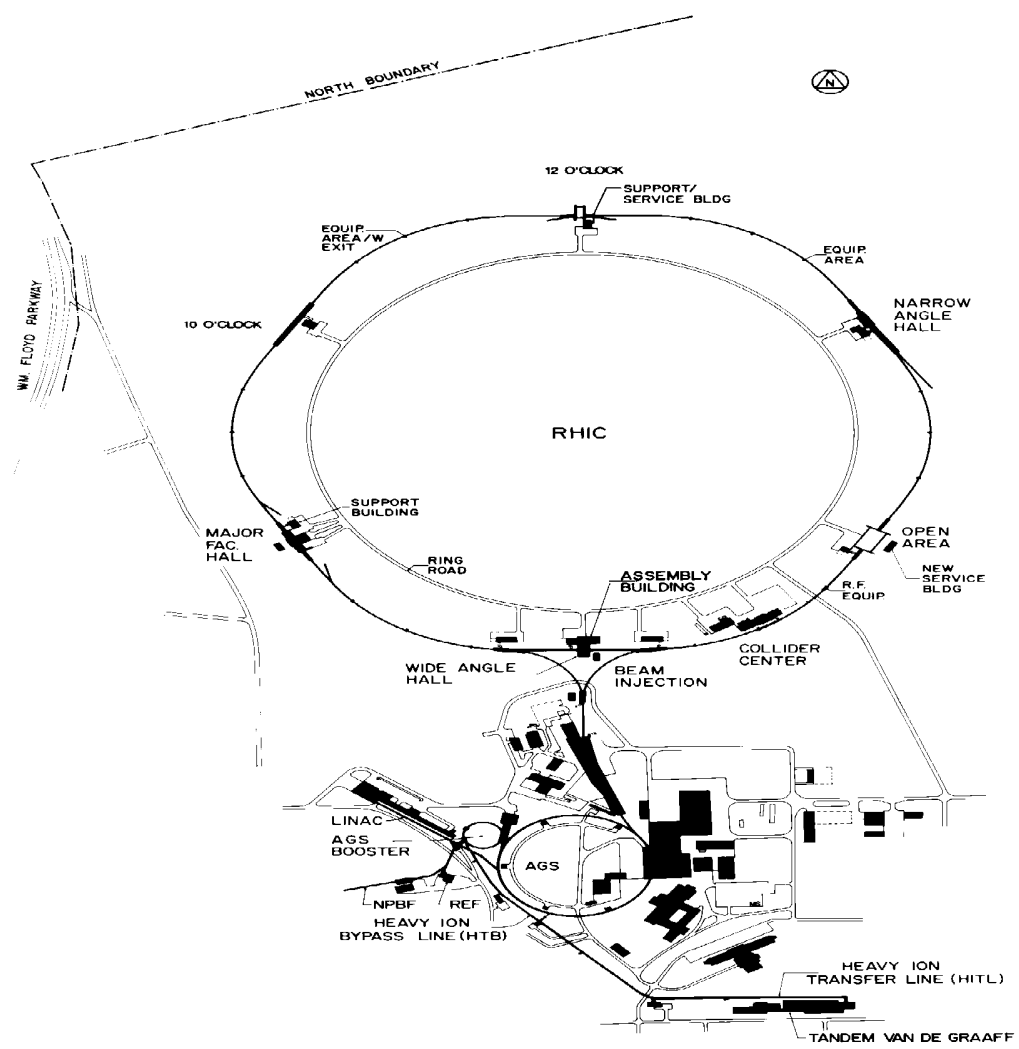


Figure 3.1: Overview of the heavy ion accelerator complex at BNL.

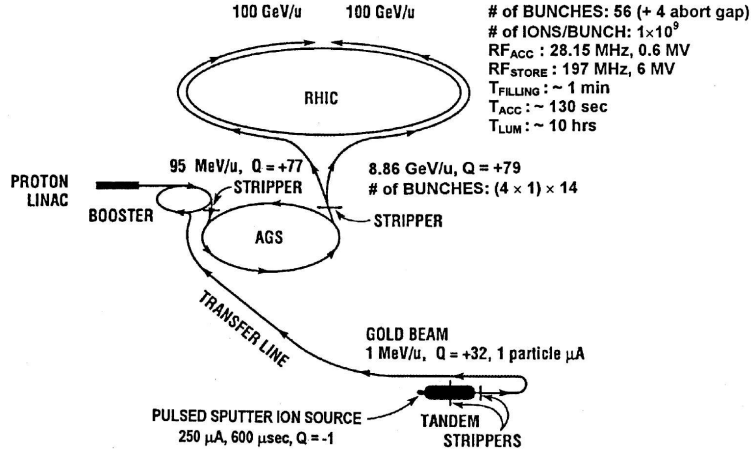


Figure 3.2: Stepwise acceleration in the RHIC complex.

up to the defined top energies, although with a smaller luminosity at the lowest energies<sup>2</sup>. Au ions have an injection energy of 8.86 GeV/u while the one for protons is 23.4 GeV. RHIC provides full luminosity and the expected lifetime of 10 h for beam energies above 30 GeV/u.

The stepwise acceleration in the RHIC complex is illustrated in fig. 3.2. Ions are extracted from a pulsed sputter ion source and gain an initial boost in the Tandem Van de Graaff, where ions with electric charge  $Q = -1$  are accelerated from ground potential to +14 MV. Upon arrival at the anode plane the negative charged ions penetrate a stripping foil ridding them of a number of electrons. This number is a function of the species being accelerated, where e.g. gold after stripping have a charge of  $Q = +12$ . The now positively charged ions are accelerated back to ground potential, stripped further and transferred to the Booster 850 m away through the heavy ion transfer line.

The 600  $\mu\text{s}$  Tandem pulse is filled in 45 turns of the Booster synchrotron. After the subsequent capture into six bunches the ions are accelerated (up to 95 MeV/u for gold ions) and led through another stripping foil into the AGS. Four Booster cycles are required to fill the AGS with 24 bunches. In the AGS the beam is debunched and rebunched into four bunches followed by acceleration (up to 8.86 GeV/u for Au). The two last electrons are stripped upon exiting the AGS and the beam is led through the AGS-to-RHIC (AtR) transfer line and finally fed into RHIC. 14 AGS cycles are necessary to fill each ring in RHIC corresponding to a filling time of about one minute per ring.

When RHIC is filled the acceleration radio frequency (RF) system take the ions up to the desired energy and shorten the bunches before transfer to the storage RF system. The higher frequency of 197 MHz in the storage RF system limits the bunch length in comparison to the 28.15 MHz acceleration RF. In order to avoid eddy currents and dynamic magnetization the acceleration in RHIC is only allowed to take about two minutes.

---

<sup>2</sup>In the first approximation the luminosity is proportional to the beam energy [115].

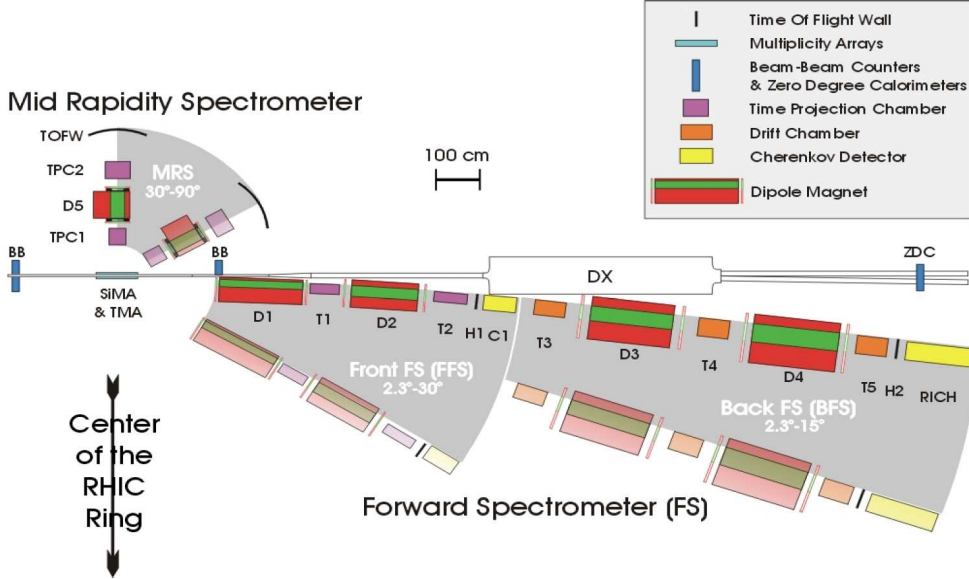


Figure 3.3: Birds-eye view of the BRAHMS experimental setup consisting of two rotatable spectrometer arms and global detectors.

## 3.2 BRAHMS in general

BRAHMS is one of the 2 small heavy ion experiments at RHIC. It was constructed to scan the charged hadron production in the widest possible kinematic range in  $y, p_T$  space, and in particular extend beyond the mid-rapidity region covered by the other RHIC experiments. The layout of BRAHMS, depicted in fig. 3.3, shows the two-spectrometer solution to the task given. Each spectrometer arm consists of tracking detectors and dipole magnets for momentum determination, and time-of-flight and Cherenkov detectors for particle identification (PID). In addition several global detectors for event characterization are installed close to the beam pipe but not on the spectrometer platforms. The conceptual design is largely inspired the ones of AGS experiments E802 [116] and E866 [117].

Each spectrometer arm covers only a small solid angle but can be rotated in the horizontal plane with pivot at the nominal interaction point. A pseudo-rapidity range of  $0 < \eta < 3.9$  is thus covered at several consecutive angular settings. Momentum space is scanned by varying the field strength of the dipole magnets in the spectrometers. By combining data sets at various angle and magnetic field settings BRAHMS can measure pions, kaons and protons in its design acceptance shown in fig. 3.4 and further described in [94].

In this dissertation certain spectrometer settings are presented as examples. The notation used to describe a given combination of spectrometer angle ( $\theta$ ), magnet polarity ( $P$ ) and magnet current ( $I$ ) is  $\theta\_PI$ . Hence, a setting ad  $90^\circ$ , B polarity and a magnetic current of 1000 A is presented as “90\_B1000”. Some settings in the MRS also have a trailing  $b$  in their setting descriptor. This indicates that the setting had the magnet and detectors moved 50 cm further away from the interaction point relative to their nominal position. By convention the polarities are named such that A polarity bend negative

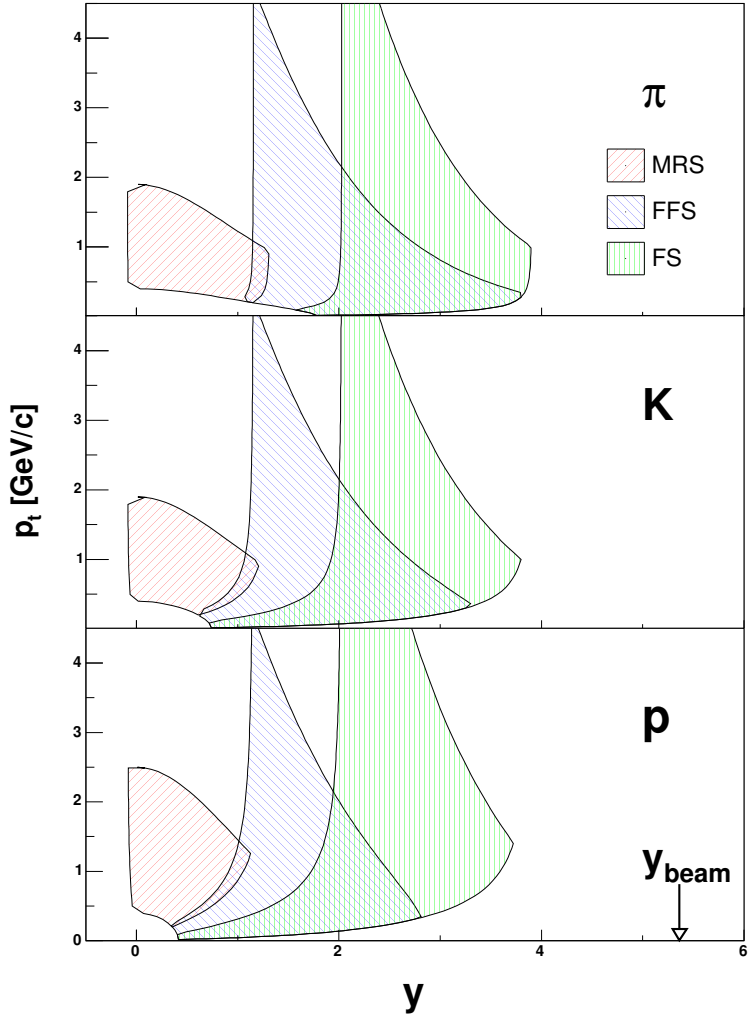


Figure 3.4: The designed acceptance for pions, kaons and protons in  $y, p_T$  space. The plot represents the integrated acceptance from numerous angle and magnetic field combinations.

particles to the right when seen from above.

### 3.2.1 Forward Spectrometer

The forward spectrometer (FS) detects particles escaping the interaction point with small polar angles relative to the beam pipe. In its full extent the spectrometer is operated in the angular range of  $2.3^\circ < \theta < 15^\circ$ . The lower limit is a constraint set by the location of the DX magnet on the accelerator. At a given angular setting it covers a solid angle of 0.8 msr.

The FS can also be operated in a low-momentum mode using only its front half, referred to in the following as the front-forward spectrometer (FFS). In this mode the upper limit of the polar angle is increased to  $30^\circ$ . The FFS and the back-forward spectrometer

(BFS) correspond to separate platforms that can be rotated independently around the nominal interaction point.

Tracking in the FS is performed by the two time-projection chambers (TPCs) T1 and T2 and three drift chambers (DCs) T3, T4 and T5. Together with information on bending in dipole magnets D2 through D4 the momentum and charge of the particles are determined. T1, T2 and D2 are located on the FFS, while the DCs, D3 and D4 are mounted on the BFS.

In addition to the dipole magnets used for momentum determination there is dipole magnet D1 placed in front of T1. D1 has a maximum field of about 1.3 T which allows it to sweep 25 GeV/c charged particles into the spectrometer arm. It also removes much background which is of crucial importance in the high multiplicity fragmentation region at small polar angles.

PID in the FS is performed in manners depending on the mode in which it is run. In the low momentum mode hodoscope H1 and threshold Cherenkov detector C1 are used (sec. 3.5.2). H1 can with a  $2\sigma$  cut separate  $\pi$  and  $K$  up to  $p < 2.8 - 3.5$  GeV/c, while protons can be identified up to  $p < 3.5 - 5.5$  GeV/c. These limits depend primarily on the size of the magnetic fields which dictates the momentum resolution. Above  $p \sim 2.6$  GeV/c pions can be vetoed using C1 and thus extend the particle identification (PID) capabilities for  $\pi$  and  $K$  up to the proton limit.

Using the FS in its full length low momentum PID is performed using hodoscope H2 in conjunction with H1, while the ring imaging Cherenkov detector (RICH) identifies particles in the highest momentum range. Information on particle identity can be extracted from the RICH in terms of the recorded radius of the ring. Also, the RICH can be used to veto light particles as described for C1. Using the RICH pions can be separated from kaons up to  $p \sim 25$  GeV/c while protons can be identified up to  $p \sim 35$  GeV/c.

In one magnetic field setting only particles with the same charge sign can be tracked and identified in the FS. The polarity of the magnetic field is inverted in order to track particles of both charge signs. In this way the spectrometer's acceptance for charge conjugate particles is the same.

### 3.2.2 Mid-rapidity Spectrometer

Particles emanating from the collision vertex with polar angles in the range  $30^\circ < \theta < 95^\circ$  are detected by the mid-rapidity spectrometer (MRS). It contains two TPCs called TPM1 and TPM2, dipole magnet D5 and time-of-flight wall TOFW. The spectrometer covers a solid angle of 6.5 msr in each angular setting.

As in the forward spectrometer the momentum of charged particles is determined from their bending in the field of a dipole magnet. But in contrast to the FS the MRS may track particles of both charge signs at any magnetic field configuration.

PID at mid-rapidity is deduced using time-of-flight information from TOFW. The average particle momenta in the rapidity window covered by the MRS is significantly lower than at more forward rapidities. Pions and kaons are separated on a track-by-track basis up to  $p \sim 2$  GeV/c, while proton identification is extended up to  $p \sim 3.5$  GeV/c<sup>3</sup>.

---

<sup>3</sup>Since the data run whose analysis is presented in this dissertation the mid-rapidity spectrometer has been upgraded with a Cherenkov detector of similar types as C1. With the use of this new detector, C4,

### 3.3 Global detectors

The characterization of events in terms of centrality and location of the primary vertex is performed using detectors that are not placed on the spectrometer arms. Their location was thus fixed during collection of the data used in this analysis. Signals from these global detectors are also used in constructing the level 0 and 1 triggers.

#### 3.3.1 Multiplicity array

Surrounding the nominal interaction point there is a hexagonal two-layer multiplicity array (MA). The inner layer consists of silicon strip wafers located 5.3 cm from the beam axis. Outside the Si, at 13.9 cm from the beam axis, plastic scintillator tiles are mounted. Both Si and tile multiplicity barrels detect the loss of energy of penetrating charged particles. The multiplicity of the event is then determined by dividing the deposited energy by the predicted average energy loss of a single particle as derived from calibrations with minimum ionizing particles and simulations using GEANT [118]. The centrality is further deduced from multiplicity using model calculations and the arrays' response in realistic simulations. The MA spans a range in pseudo-rapidity of  $|\eta| < 2.2$ .

The silicon barrel contains a total of 25 wafers with dimensions  $4\text{ cm} \times 6\text{ cm} \times 300\text{ }\mu\text{m}$ . Each wafer is divided into seven segments for which energy loss is recorded. During the first three runs of RHIC the wafers were segmented along the beam direction<sup>4</sup>. In order not to interfere with particles escaping in the directions of the spectrometer arms only three rows have been fully instrumented, each with six wafers, adding up to a total of 42 bins in  $\eta$ . One row has five wafers and two rows have one wafer so that one hexagon is populated in full. Each wafer is mounted onto its front-end electronics which in turn is attached to the barrel support structure.

Each row in the tile barrel has room for eight tiles, but only four rows contain this number of tiles. In addition one row has four tiles and the last one has two tiles. In sum there are 38 tiles. The dimension of the tiles is  $12\text{ cm} \times 12\text{ cm} \times 0.5\text{ cm}$ . Light created in the tiles is collected by an optical fiber inlaid into a groove 2 mm deep and 1.2 mm wide running along the edge of each tile and sent to photo-multiplier tubes (PMTs) located above and below the barrels.

Since both Si and tiles provide information on multiplicity the calculated multiplicity in the further analysis is the average of these two measurements. Their distributions of charged particles are highly correlated as can be seen in fig. 3.5. The signal from the tiles is fast and is therefore a component in the level 1 trigger.

#### 3.3.2 Beam-beam counters

At 220 cm on either side of the nominal interaction point there is an array of Cherenkov radiators surrounding the beam pipe. These arrays are referred to as beam-beam counters (BB). The counter on the right hand side of the interaction point (fig. 3.3) only partially

---

pion and kaons may be separated up to momenta of  $p \lesssim 9.5\text{ GeV}/c$ , while protons may be identified up to  $p \lesssim 18\text{ GeV}/c$ .

<sup>4</sup>Before the 2004 data run the silicon wafers were rotated  $90^\circ$  relative to their normal axis of entrance to be able to measure elliptic flow.

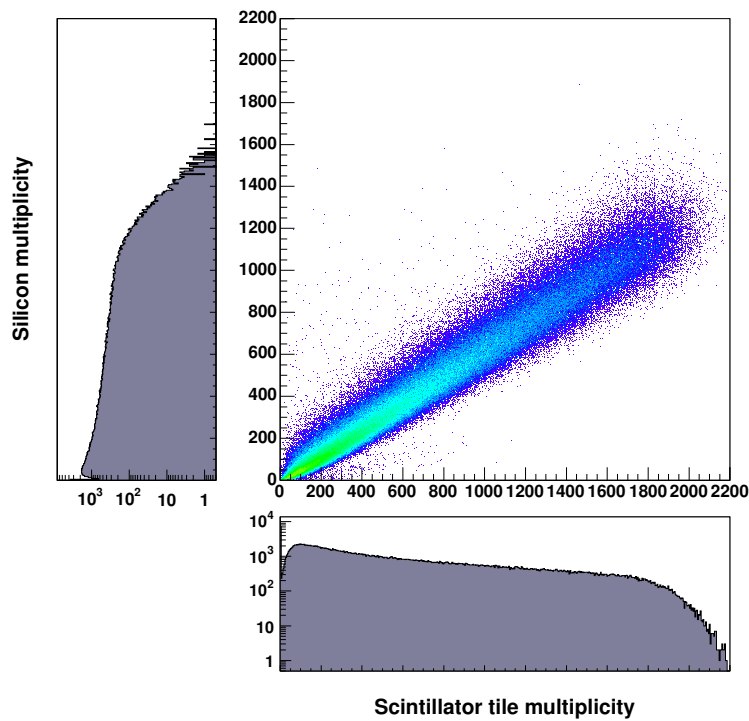


Figure 3.5: The correlation of the multiplicity as determined by the silicon and tiles in the multiplicity array (big panel). The individual distribution of Si (left) has a somewhat lower upper limit than the one for the tiles (bottom). The reason for this difference is attributed to different Landau distributions of energy depositions in the two barrels and a slightly higher probability for saturation in the readout electronics of the scintillators.

encircles the beam pipe in order to let the forward spectrometer move as close to the pipe as possible. Their acceptances in polar angle is limited to  $1.6^\circ < \theta < 5.8^\circ$ .

Each array is composed of lucite radiators of two different sizes glued to PMTs. The smaller ones have a diameter 0.95 cm and a length of 4 cm, while the bigger ones measure 2.54 cm and 3 cm in diameter and length, respectively. The main function of the BB counters is to provide a good timing signal for the level 0 trigger and as start time for the time-of-flight detectors. The timing signal is also used to determine the primary interaction vertex.

In the forward region timing signals may be impeded by multiple particles going through the radiators in central events. Yet, in peripheral events the radiators have to cover a big enough solid angle to have at least one hit. In order to cope with these requirements a design with both small and big radiators was chosen. The left array has 36 small and 8 big radiator/PMT modules, while the one on the right hand side has 30 small and 5 big modules.

A prototype test of the radiator/PMT modules was performed with pions from the AGS. The resolution of the big modules after slewing correction<sup>5</sup> was found to be  $\sim 60$  ps.

The start time is constructed from the timing information of both left and right BB arrays. It can be expressed as

$$T_0 = \frac{T_L + T_R}{2} + T_{const} \quad (3.1)$$

Here  $T_L$  and  $T_R$  correspond to the time as recorded by the BB left and right, respectively.  $T_{const}$  represents the delay caused by cables and electronics. This expression assumes that particles move with the same velocity towards both left and right BB counters.

The location of the primary vertex is determined from the timing difference between the left and right array, i.e.

$$z_{BB} = c (T_L - T_R)/2 \quad (3.2)$$

where  $c$  denotes the speed of light in vacuum. As discussed in sec. 3.4.1 the vertex can also be determined with higher accuracy from tracks in TPM1 projected back to the beam line. The correlation of vertices determined from BB timing difference and TPM1 tracks is shown in fig. 3.6. Its main contribution comes from the timing resolution. In general the BB vertex resolution is better than 1.6 cm.

### 3.3.3 Zero-degree calorimeters

One zero-degree calorimeter (ZDC) is placed on either side at 18 m from the nominal interaction point. Only the right ZDC can be seen in fig. 3.3. Being placed behind the DX magnets they record neutrons emitted from the collision in a very narrow cone around the beam axis.

In heavy ion collisions spectator neutrons from both nuclei are usually emitted with small transverse momentum. Typically at RHIC these evaporation neutrons emerge with polar angles less than 2 mr. Incoming neutrons go through a sandwich structure of dense

---

<sup>5</sup> Slewing, also referred to as *time walk*, is caused by time-to-digital converters' (TDCs) raw timing signal depending on the amplitude. By plotting time as a function of amplitude this effect may be parametrized and thus corrected for.

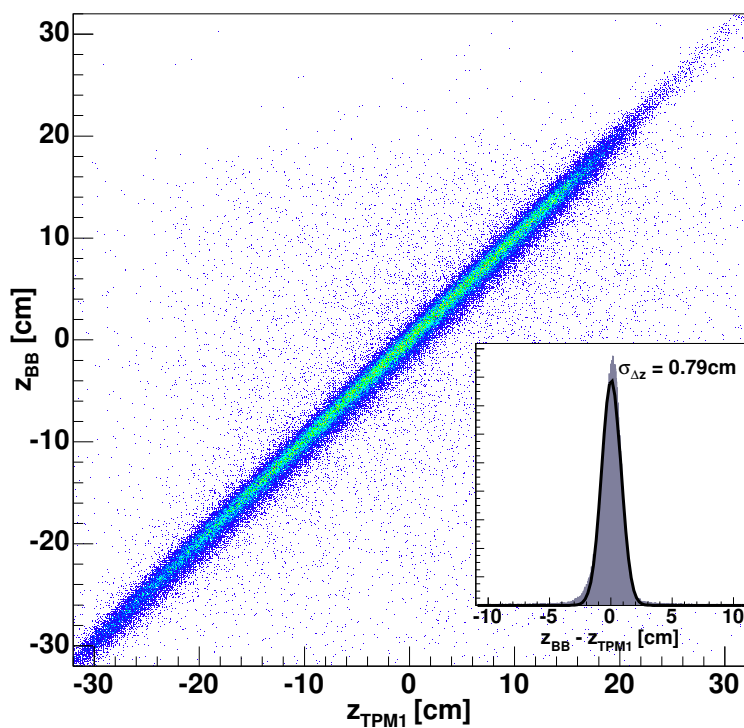


Figure 3.6: Correlation of the location of the primary vertex determined from BB timing difference and from reconstructed particle tracks in TPM1 projected back to the beam line. The main component in the width of the distribution is the timing uncertainty.

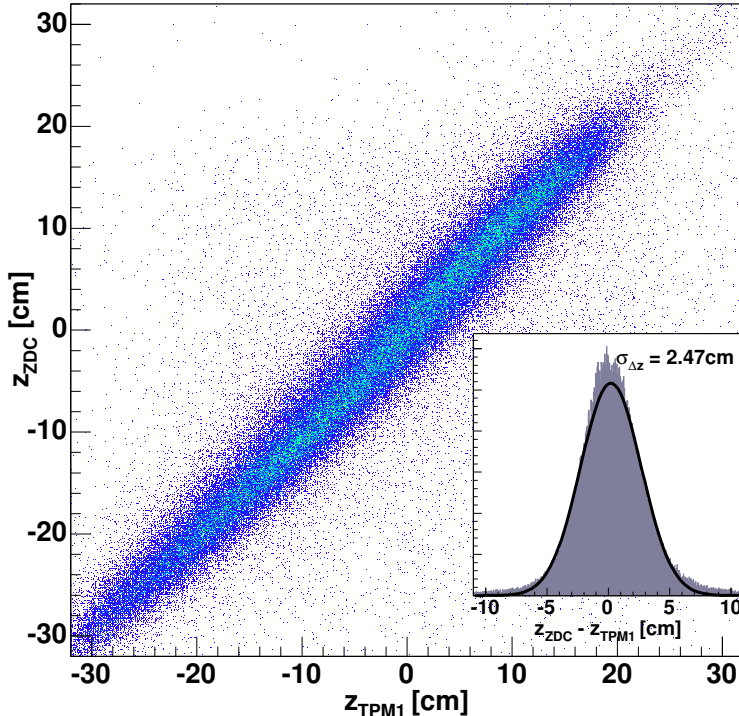


Figure 3.7: Correlation of vertex determined using ZDC and from projecting tracks in TPM1 to the beam axis. Due to worse timing resolution in the ZDCs relative to the BB counters the vertex resolution is not as good as in fig. 3.6.

tungsten absorber and quartz fiber sampling Cherenkov light from the high-energy end of the particle spectrum. Each ZDC has three modules with alternating absorber and radiator.

As with the BB counters the ZDC timing signal is corrected for slewing. The corrected time gives information on the primary collision vertex and may supply timing detectors such as TOFs and DCs with a starting signal. The ZDCs also provide a component in the minimum bias trigger. Typical timing resolution for the ZDCs is around 170 ps. This leads to a higher uncertainty in the vertex determined with ZDCs than the one determined from BB timing difference, as can be seen from fig. 3.7. In general the ZDC vertex resolution is better than 3.6 cm.

The signal amplitude (ADC signal) from the calorimeters is translated into number of spectator neutrons. This number is correlated with collision geometry. The ZDCs are common to all RHIC experiments, and collision centrality as determined by the ZDC could therefore be used when comparing experimental results from the different RHIC experiments. When tuning the RHIC beams the beam operators also uses the ZDCs to gain information on luminosity.

When ions in the beam hit nuclei in gas molecules in the beam pipe in the vicinity of the interaction region (IR) it may cause a shower of background particles depositing energy in the ZDCs and other detectors. The ZDC modules are lined up along the beam direction, and there is thus a time difference, typically about 1.5 ns between the first and

Trigger ID	Requirement
1	Coincidence in BBs with $N_L \geq 2$ and $N_R \geq 2$ .
2	Coincidence in BBs with $N_L \geq 1$ and $N_R \geq 1$ .
3	Multiplicity in tiles corresponding to the top $\sim 20\%$ most central events.
4	Coincidence within $\sim 5$ ns in ZDCs and RHIC RF clock. The energy from each ZDC module must be $> 25$ GeV, and the number of hits in the tiles array must be $> 4$ .
5	Vertex as determined from narrow coincidence in BBs, effectively selecting events with $ z_{BB}  \lesssim 25$ cm.
6	Vertex and multiplicity, i.e. triggers 3 & 5.
7	Calibration pulser.
8	Synchronization trigger at 1 Hz.

Table 3.1: List of trigger IDs and the corresponding requirements.  $N_L$  and  $N_R$  in triggers 1 and 2 represent the number of PMTs with hits in the left and right BB arrays, respectively.

the last module. By determining which module was hit first one can reject upstream beam-gas events from the data sample.

### 3.3.4 Trigger system

The task of the trigger system applied in BRAHMS is twofold. First it selects events of interest, i.e. collisions of nuclei fulfilling requirements such as centrality or the vertex' offset from the nominal location. Secondly, it reduces the number of collisions per second to be read out from about 1.2 kHz, which is the collision frequency when RHIC is running with gold on gold, down to a manageable rate of  $\sim 100$  Hz that can be stored on tape [119].

BRAHMS has two levels of triggers, named level 0 and 1. The level 0 trigger is defined to start ADCs and TDCs. It also opens the TPC gating grids and start the readout of the TPCs. The level 1 trigger then interrupts the readout VME processors.

Level 0 is composed of signals from the various global detectors. BB and ZDC assures that the primary vertex is located within the spectrometers' acceptance, and the MA select events of high centrality. In total the trigger bit mask created for each event contains eight bits including pulser signal for calibration and synchronization bit for background studies. Table 3.1 lists the various trigger bits and the corresponding conditions that must be satisfied.

## 3.4 Tracking detectors

In order to deduce the momentum of charged particles going through the spectrometer arms their bending angle in one or several dipole magnets is determined. Straight line segments of a charged particle's trajectory are reconstructed in three dimensions in the TPCs and DCs. When segments are matched in a magnet the bending angle is calculated and thus the momentum is found. The charge is determined from the direction of the

bending in the horizontal plane, i.e. whether the particle's direction after the magnet has been shifted to the left or right relative to the direction before entering the magnet. Good track matching and momentum resolution thus depends on the resolution of the tracking detectors.

### 3.4.1 Time projection chambers

In BRAHMS' experimental setup there are four TPCs, i.e. T1 and T2 in the forward spectrometer and TPM1 and TPM2 in the mid-rapidity spectrometer. Between each pair of TPCs there is a dipole magnet. The TPCs in BRAHMS were designed to provide an intrinsic track resolution less than  $400\text{ }\mu\text{m}$  and a two-track resolution smaller than 15 mm.

The four TPCs share a set of common features. They are made of lucite with a  $25\text{ }\mu\text{m}$  mylar foil at the particle entrance and exit. Thin aluminized mylar strips create a close to linear vertical drift field from a potential of  $\sim -5\text{ kV}$  on the bottom to ground potential close to the readout plane on top. Non-linearities occur particularly along the edges of the cage defined by the mylar strips. These effects are minute and are corrected for off-line as described in [97].

A mixture of 90% Ar and 10% CO<sub>2</sub> is used for drift gas. This mixture has a slow drift velocity, which is suitable for the small drift lengths of 21 – 22 cm. With a drift field of about 230 V/cm the gas yields a drift velocity  $v_{drift} \sim 1.6\text{ cm}/\mu\text{s}$ . The chosen gas mixture also has small diffusion constants. I.e. in the transverse direction it has a constant of  $D_T = 190\text{ }\mu\text{m}/\sqrt{\text{cm}}$ , while the longitudinal diffusion constant  $D_L = 240\text{ }\mu\text{m}/\sqrt{\text{cm}}$  [120].

Each TPC has from 12 to 20 pad rows but with the exception of TPM1 there are rows in each TPC that are not instrumented. The pad width ranges from 3 to 4.2 mm. The pulse height distribution along the pad rows is given by the pad response function

$$P_i = A \exp(-(x - x_i)^2 / 2\sigma_x^2) \quad (3.3)$$

in which the index  $i$  refers to distinct pads. The width of the pad response function depends on the diffusion constants, drift length and track angle. As was found in [121] the dependence of  $\sigma_x$  on drift length in the TPCs of BRAHMS limited and typical values are in the range  $3.0\text{ mm} < \sigma_x < 3.5\text{ mm}$ .

The drift time of ionization electrons yields the vertical components of track position and slope. The pulse height of each pad is sampled with switched capacitor arrays in the front-end electronic (FEE) read out cards on top of the TPCs. With arrays clocked at 10 MHz this corresponds to 100 ns time bins. Before sampling in the FEE cards the signal from each pad is passed through a preamplifier followed by a shaping amplifier. Each FEE card amplifies and samples the signal of 32 pads.

The proportional readout region is separated from the drift region by a gating grid which is connected to a pulser. The gating grid is the lower wire plane in fig. 3.8. In the case of a collision the gating grid pulser provides the grid with a potential of  $-180\text{ V}$  for a duration of  $20\text{ }\mu\text{s}$  thus rendering it transparent for electrons drifting into the proportional region. The rest of the time adjacent wires have alternating potentials of  $-100\text{ V}$  and  $-260\text{ V}$ . The resulting gating field prevents ions from the readout region to migrate into the drift region and create non-uniformities in the drift field.

8 mm above the gating grid there is a cathode grid, also referred to as Frisch grid. An additional 4.5 mm further up are located a grid of alternating sense (anode) and field wires.

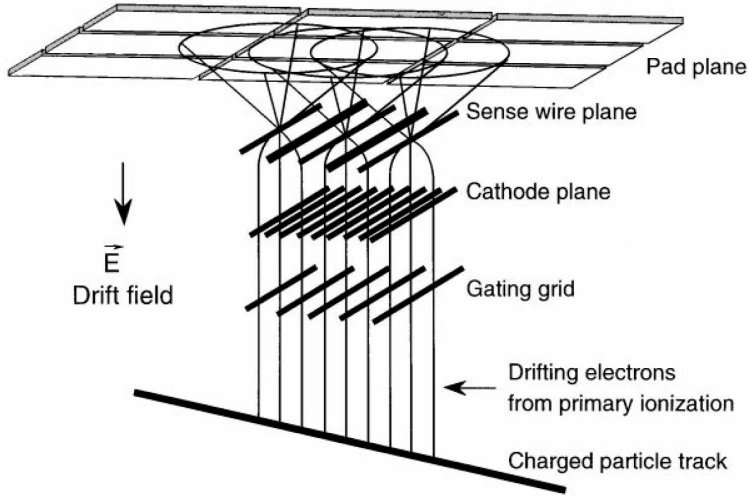


Figure 3.8: The layout of the proportional chamber region of a TPC. The BRAHMS TPCs are located outside magnetic fields and the tracks are therefore straight lines. The drawing was taken from [122].

Electrons from the ionization by tracks that have drifted up to this level are multiplied by a factor of  $\sim 10^4$  when avalanching towards the sense wires. The image charges from positive ion clouds around the wires are induced on the pads located 4.5 mm above the sense/field grid. Typical primary clusters give image charge on 3-5 pads.

Using cosmic radiation the TPCs were tested and resolution measured. The resolution found is well within the design criteria. In the horizontal direction resolutions of  $250 - 300 \mu\text{m}$  were found, while in the vertical direction the measured resolutions was found to be  $300 - 350 \mu\text{m}$ .

### 3.4.2 Drift chambers

Further away from the nominal interaction vertex, at distances of 10.5, 14.5 and 18.4 m in the FS, the drift chambers T3, T4 and T5 are located, respectively. The design of T4 and T5 is identical, while T3 has some slight modifications due to the higher occupancy closer to the vertex.

Each DC has three modules. In each module there are wire planes at different rotations, or *views*, defined as  $x$ ,  $y$ ,  $u$  and  $v$ . Here  $x$  and  $y$  views correspond to wire planes giving hit information along the local  $x$  (horizontal) and  $y$  (vertical) directions, respectively. The wire direction is orthogonal to the view direction. The  $u$  and  $v$  planes have wires rotated  $+$  and  $- 18^\circ$  relative to the  $x$  views. One plane has three frames. The central frame has alternating sense and cathode wires, where in T3 the sense wire spacing the 1 cm and in T4 and T5 it is 2.2 cm. On either side of the sense frame there is a frame with field shaping wires. The active area seen by the incomming particles along the spectrometer axis is  $30 \times 40 \text{ cm}^2$  in T3 and  $35 \times 50 \text{ cm}^2$  in T4 and T5.

T3 has 10 detection planes in each module, while T4 and T5 has 8. After each  $x$  and  $y$  plane follows an  $x'$  and a  $y'$  plane. This holds true in similar manner for the  $u$  and  $v$

planes. These primed planes have the same direction as their respective unprimed ones, but are shifted by a quarter of the sense wire spacing. In this way left-right ambiguities are removed. Finally, each module in T3, where the occupancy is highest, has an additional  $x$  and  $y$  plane.

The drift chambers are filled with a gas mixture of  $\sim 67\%$  Ar and  $33\%$  C<sub>4</sub>H<sub>10</sub>, with an addition of minute quantities of ethanol vapor to remove molecular residues depositing on the sense wires.

As it has turned out the drift chambers perform with better resolution than the original design required. A positional resolution of  $82\mu\text{m}$  has been achieved, while the original resolution suggested  $300\mu\text{m}$  FWHM.

## 3.5 Particle identification detectors

After tracking a particle through the spectrometer its momentum and charge is known. To fully know the identity of a low momentum particle its time of flight is determined. For a high momentum particle in the FS the ring of its Cherenkov shock wave is also measured.

### 3.5.1 Time-of-flight detectors

BRAHMS utilizes time-of-flight measurements for particle identification both in the MRS and twofold in the FS. The detectors consist of vertical plastic scintillator slats with PMTs mounted at either end of each slat. Both signal amplitude and timing are recorded for each slat. The ADC signal is used here to determine if the hit has signal above pedestal in which case the hit may be associated with a reconstructed track. Also the amplitude is necessary to correct the timing signal for slewing (footnote on page 47).

In the MRS the TOFW has 125 slats divided over six planes and placed side by side. The planes are located on an arc with a curvature radius of 240 cm centered in the center of D5. With this geometry tracks leaving D5 will hit the panels at close to  $90^\circ$  relative to the panel plane. Each in TOFW has dimensions  $1.27 \times 22 \times 1.25\text{ cm}^3$  and is wrapped in aluminum foil and black tape giving some small fraction of dead space between the scintillators. This is corrected for in the further analysis.

The slats in H1 and H2 each measure 1 cm in the  $x$  direction. Their  $y$  and  $z$  dimensions are  $20 \times 1\text{ cm}^2$  in H1 and  $40 \times 1.5\text{ cm}^2$  in H2. H1 has a total of 40 slats, while H2 has 32. In these two hodoscopes the slats are alternately placed in two staggered planes with a separation of 1 cm between each plane, seen in fig. 4.5. By choosing this geometry the wrapping of slats does not cause any dead area for particles impinging at  $90^\circ$  upon the slat planes.

In a test setup the intrinsic timing resolutions of the slats were found to be  $\sim 65\text{ ps}$ . This does, however, not account for the full resolution of time-of-flight since there is also a contribution from uncertainty in the start time. The total time-of-flight resolution was found to be of the order of 90 ps. A small error in the particle identification capabilities of the hodoscopes also comes from the uncertainty in location of the primary vertex.

### 3.5.2 Threshold Cherenkov detector

At the end of the FFS threshold Cherenkov detector C1 is mounted. It is filled with a gas mixture of  $\text{C}_4\text{F}_{10}$  at atmospheric pressure giving an index of refraction of 1.001380. This corresponds to a radiation threshold for pions and kaons of  $p_\pi \sim 2.6 \text{ GeV}/c$  and  $p_K \sim 9.3 \text{ GeV}/c$ , respectively. C1's main function using only the FFS is to veto pions and thereby extend the upper momentum limit for pion and kaon identification to the one of protons (sec. 3.2.1).

The radiator of C1 has dimensions of  $50 \times 40 \times 75 \text{ cm}^3$ . The light cone from a particle above threshold is reflected by mirrors at the radiator end cap to PMTs located on top and below the radiator volume. On either side of the volume there are 16 phototubes packed along two rows. The detection segmentation in x and y is thus  $16 \times 4$  bins, where each bin has a PMT of  $2''$  diameter. The entrance and exit windows are made of  $25.4 \mu\text{m}$  aluminum foils.

C1 did not work optimally during the 2001 data run. The reason for this seems to be significant amount of background particles contaminating the signal and preventing reliable vetoing above threshold. Hence, in the further analysis PID information from C1 is discarded.

### 3.5.3 Ring imaging Cherenkov detector

The highest momentum particles in the FS are identified in part using the radius of the ring of Cherenkov light they create when propagating through the detector volume of the RICH. It has momentum thresholds for pions, kaons and protons of the order of 2.5, 7.8 and  $14.5 \text{ GeV}/c$ , respectively. These thresholds come from the mixture of  $\text{C}_4\text{F}_{10}$  and  $\text{C}_5\text{F}_{12}$  maintained with a pressure around 1.25 atm. Since the RICH was found to leak somewhat, the refractive index is calibrated accordingly (sec. 4.4.3).

Particles traversing the radiator volume with a  $\beta$  above threshold creates a light wave front that is reflected in a spherical mirror close to the end cap of the radiator volume. The mirror having a radius of curvature of 3 m and an axis of  $8^\circ$  relative to the detector z axis focuses the light cone onto an array of 80 photomultipliers located on top of the RICH. Each PMT has four pixels giving a total RICH segmentation of 320. The active area of each pixel is  $1.2 \times 1.2 \text{ cm}^2$  and there is a dead space of  $\sim 2 \text{ mm}$  between each PMT. With this setup  $\pi$  and  $K$  can be separated up to momenta of  $\sim 20 \text{ GeV}/c$  while protons can be tagged all the way to  $\sim 35 \text{ GeV}/c$ .

# Chapter 4

## Data analysis

The BRAHMS experiment consist of numerous detector components each providing small pieces of information to characterize events and tracks. Timing information from BB counters and ZDCs is translated into position coordinates of the primary interaction vertex. Arrays of ADC values from the tracking detectors are combined to form clusters of charge and subsequently detector hits. Furthermore, the hits in the TPCs and DCs have to be linked into track segments, before the segments are matched in the magnets to form spectrometer tracks. Adding information from Hodoscopes and Cherenkovs the ID of the particles may be determined. Various cuts and corrections are applied to the data.

This chapter describes the process of data analysis before the main results are presented in ch. 5. Software for large parts of this analysis was developed in joint effort by the BRAHMS collaboration. This part of the analysis includes the readout and detector hit generation of data from the detectors, centrality and vertex determination, local and global tracking, matching of hodoscope and Cherenkov hits to the global tracks and finally generation of data summary trees (sec. 4.2.3).

The main effort in analysis performed in this work involves particle identification by two statistical approaches. One of these methods extends the PID capabilities in the MRS to momentum limits of the order of 1 GeV/c higher than what was previously performed in other analyses, e.g. [97, 123]. In the second method presented here the PID information provided by the particle identification detectors in the forward arm, i.e. H1, H2 and RICH, are combined in a seamless manner.

### 4.1 Event selection

The global detectors presented in sec. 3.3 provide information to characterize the events. As described in sec. 3.3.4 they provide a low level selection of events during data recording when events are accepted or rejected based on trigger requirements.

The multiplicity array surrounding the nominal interaction point provide centrality information. In this study only the 10% most central events are considered, and the results presented in ch. 5 are in effect averaged over this centrality range.

Moreover, only primary vertices in the range  $|z_{BB}| < 20$  cm (relative to the nominal interaction point at  $z = 0$ ) are accepted for the forward spectrometer. In the mid-rapidity

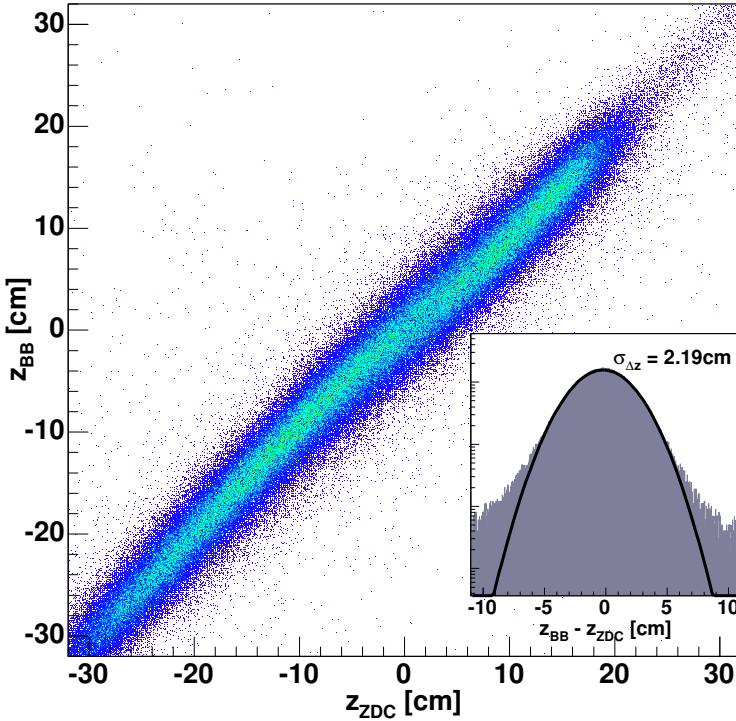


Figure 4.1: Correlation of the location of the primary vertex determined from BB and ZDC timing differences before event selection. The one-dimensional distribution is fitted with a Gaussian and its width is used for event selection. A  $3\sigma$  cut removes 1–3% of the events.

spectrometer events in the range  $|z_{BB}| < 15$  cm are accepted. These limits were chosen from the acceptance obtained in simulated tracking through the spectrometers. The acceptance of tracks decreases significantly beyond these bounds. Also the acceptance of the MA decreases as a function of increasing  $|z|$ .

In addition the timing signal from the ZDCs can be used to determine the location of the primary interaction vertex. Fig. 4.1 shows the correlation in one data run between the vertex determined from BB timing and the one determined from ZDCs. Therefore the difference in vertex as determined by BB counters and ZDC,  $\Delta(z) = z_{BB} - z_{ZDC}$ , is first fitted with a Gaussian and a  $3\sigma$  cut is applied.

As described in [97, 123] the location of the primary interaction vertex can be determined from the BB counters in three ways, using only large tubes, only small tubes or using the fastest tubes. It was found that the latter method is more likely to introduce background events than the two former methods. Therefore, in case the BB vertex can only be determined using the fastest signal the event is discarded. Yet, this occurs only in about 0.01% of the events and thus does not correspond to significant loss in statistics.

## 4.2 Stepwise data reduction

### 4.2.1 Local tracking

Local tracking describes the process in which electric charge liberated by a charged particle traversing a detector is combined first into detector hits. Subsequently the hits are linked into track segments. BRAHMS has five tracking detectors in the forward spectrometer and two in the mid-rapidity spectrometer. In the experimental setup of BRAHMS these detectors are all located outside the magnetic fields of the spectrometer bending magnets. Therefore local tracking consist of fitting straight lines to the detector hits.

A local coordinate system is defined for each spectrometer detector. The longitudinal direction of the mother spectrometer defines the z axis of each detector. The horizontal and vertical directions normal to the z direction are called x and y, respectively.

#### TPC tracking

A hit in one of the time projection chambers corresponds to liberated electric charge drifting to the read-out pads at the top of the chamber (fig. 3.8). Each TPC has a number of pads ordered into 8-12 rows that are instrumented with read-out electronics. The rows extend in the x direction, and thus the spatial location of the detected charge along the pad row defines the local x component of the hit. From the drift time of the liberated electrons the y component of the hit is deduced. And finally, the z component is determined from the z coordinate of the pad row.

Track fitting is performed starting at the last pad row of each TPC where the occupancy is lowest. A track is defined for each hit in the rear row. Then the closest pad row is scanned for hits that are within a pyramid shaped search window. The peak of this pyramid is located at the coordinate of the hit in the last row and the bottom plane is spanned in the detector x,y space. If one hit is found within the search window it is added to the track. If more than one matching hit is found new tracks are defined with end points at these hits. This algorithm propagates towards the front of the TPC until either reaching the front of the chamber or reaching a predefined limit of number of rows without hits. At each step the search window is recalculated and in effect becoming narrower and narrower. See [97, 123] for more detailed descriptions on local tracking in the TPCs.

Fig. 4.2 shows the result of combining hits in T1 into straight lines. In this event the path of three tracks passing through T1 were fitted. Numerous hits do not correspond to reconstructed tracks. They stem from various sources such as background tracks and noise in the read-out electronics. Also, since the efficiency of the detector including the read-out electronics is not 100% (although very close) a small number of particles do not leave enough hits in the detector for the reconstruction of a detector track. These missing good tracks are taken into account in terms off tracking efficiency correction (sec. 4.5.2).

#### DC tracking

In a similar manner hits in the drift chambers are deduced from the spatial charge liberated by traversing charged particles. The local z component of each hit is the one of each DC module (sec. 3.4.2). Components along x and y are deduced from the combined

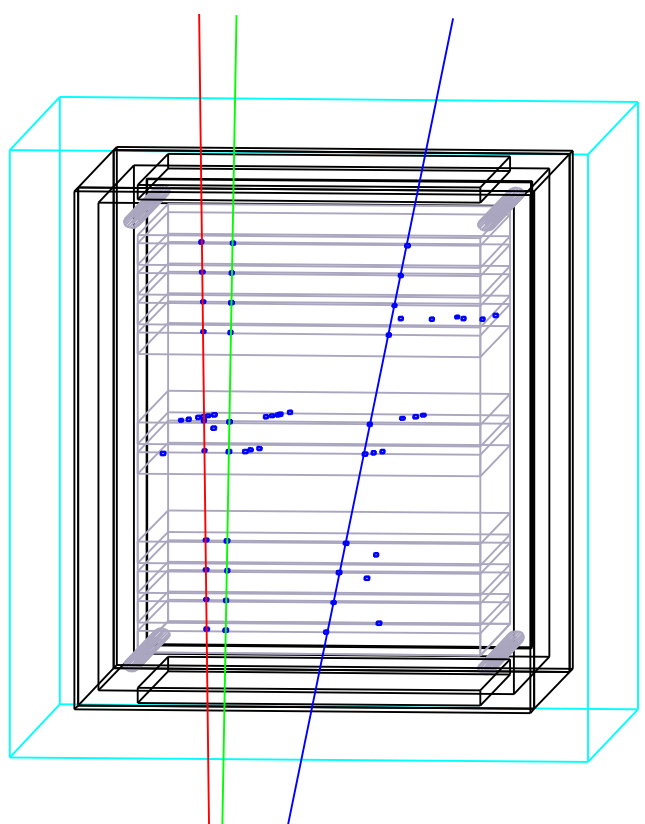
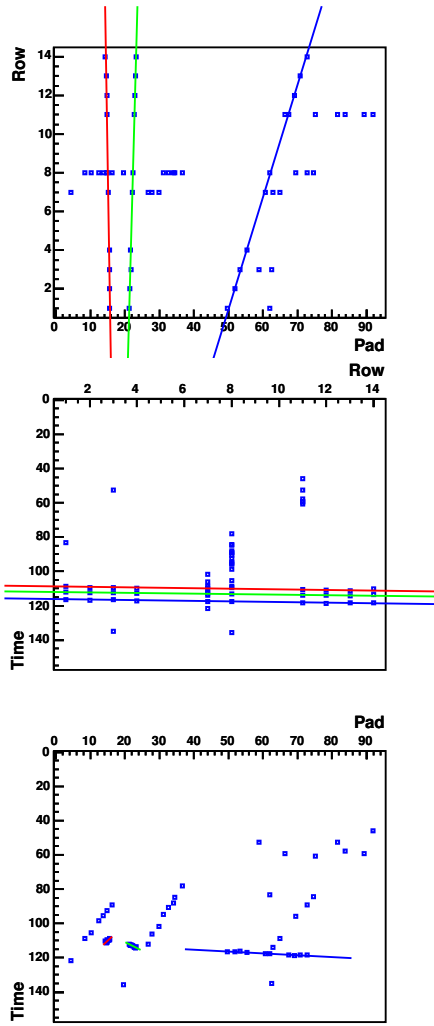


Figure 4.2: Three track segments are reconstructed from hits in T1. The left panels show two-dimensional projections on the axes of the TPC.

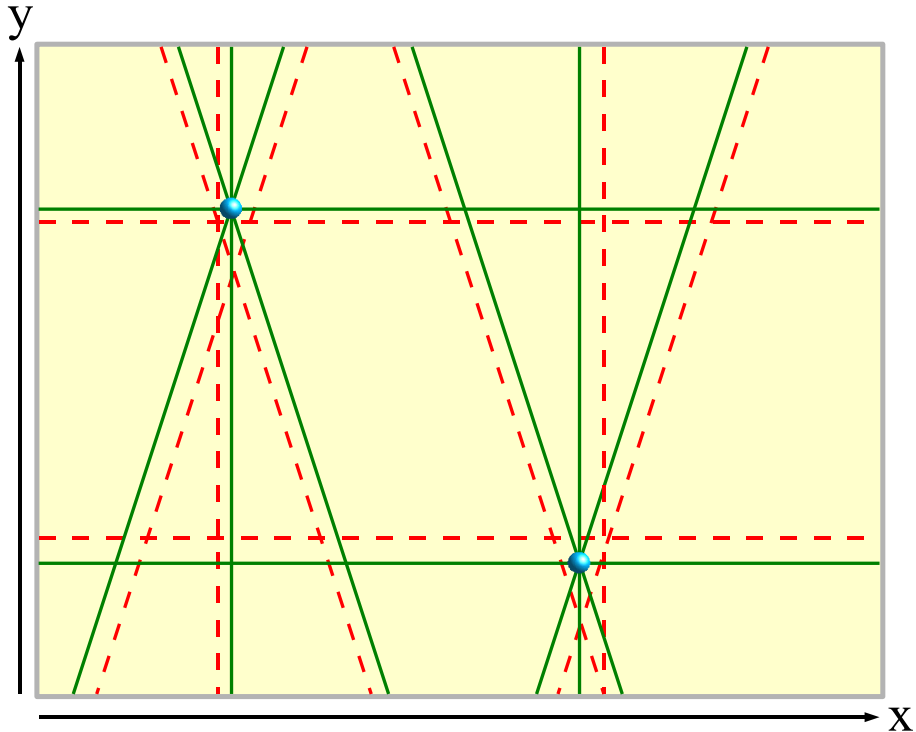


Figure 4.3: Projection image of two particles traversing a DC modules and generating hits in the anode wires. The location of a track's hit in a module corresponds to the intersection of four solid lines. The dashed lines indicate false position components before the left-right ambiguity is solved.

transversal information as determined in the various view planes of each module. Fig. 4.3 illustrates how the location of hits is determined in a DC module. The drift time of the charge from ionization until it avalanches onto an anode wire multiplied by the drift velocity gives the drift distance.

Only one wire plane can not provide information about which side of the wire the space charge drifted from. There is therefore a left-right ambiguity illustrated in fig. 4.3 which is solved with the staggered redundant planes in each view direction. The solid lines in the figure are thus deemed the true hits, while the dashed ones are deemed false. In this way every module yield position information in all three spatial directions.

Since each DC has three modules a track traversing it can generate at most three DC hits on its way. The hits are subsequently fitted with straight lines in a similar manner as for the TPCs.

Also in the drift chambers some hits are lost due to detector inefficiencies. Especially T3 is prone to suffer from background from the RHIC DX magnet [124]. T5 suffers some background from upstream collisions, in particular with the forward spectrometers positioned at small polar angles, while T4 has the cleanest operation conditions being partly sheltered by the dipole magnets on either side along the forward spectrometer.

An alternative DC tracking procedure had to be applied to T5 due to technical problems at the end of the data run used for this analysis. Due to a broken wire in the central

module of T5 the module could not be used. Therefore only the two end modules of the chamber could provide hit information, which generates too much combinatorial background in the track fitting stage. The alternative approach applied uses tracks found in T3 and T4, which are also matched in the D3 magnet (sec. 4.2.2). After matching in D3 the momentum of the particle is known, and the matched track may be traced through D4 and into T5. In this way hits found in T5 in the vicinity of the projected track are attributed to real spectrometer tracks and fitted. See [124] for a closer description of this tracking approach.

### 4.2.2 Global tracking

After linear track segments have been reconstructed in the tracking detectors the next step called global tracking involves matching of track segments to reconstruct the full trajectory of a particle through the mid-rapidity or the forward spectrometer. Matched tracks are finally projected back to the primary interaction vertex.

#### Magnet matching

From the track segments recorded in the TPCs and DCs tracklets on either side of the dipole magnets are matched as a first step on the way to forming spectrometer tracks. The magnetic field components in directions other than the vertical one are negligible. Thus the bending of the trajectory of a charged particle caused by the Lorentz force according to

$$\vec{F} = q \cdot \vec{v} \times \vec{B} \quad (4.1)$$

solely affects the horizontal component of the particle's motion. Here  $q$  and  $\vec{v}$  are the charge and velocity of the particle, respectively, and  $\vec{B}$  is the magnetic field. The particle's momentum can be calculated from

$$\vec{p} = q \cdot \int \vec{B} \times d\vec{\rho} \quad (4.2)$$

where  $\rho$  is the trajectory curvature. Since  $B = B_y$  eq. 4.2 translates into

$$p_{xz} = q \int B dr \quad (4.3)$$

in which  $r$  describes the circular radius of curvature of the trajectory in the magnet's x,z plane<sup>1</sup>. In terms of the polar angles of the particle at entry and exit of the magnet,  $\theta_{in}$  and  $\theta_{out}$  respectively, the momentum in the x,z plane may be expressed as

$$p_{xz} = \frac{q \int B dl}{\sin \theta_{in} - \sin \theta_{out}} \quad (4.4)$$

The description of the magnetic fields is simplified by applying an *effective edge* approximation. This simplification implies that in eq. 4.4 the line integral of the magnetic

---

<sup>1</sup>The local coordinate systems of the dipole magnets follow the same convention as for the tracking detectors.

field over the length of the magnet is replaced by a term that in effect describes a rectangular box-shaped magnetic field. The momentum in the horizontal plane thus reads

$$p_{xz} = \frac{qB\Delta l}{\sin \theta_{in} - \sin \theta_{out}} \quad (4.5)$$

Here  $\Delta l$  describes the length of the effective magnetic field, i.e. between the effective edge entrance and exit planes.

For each detector track candidate pair, i.e. one linear track segment in the front and one at the back of the magnet, a straight line is drawn between the segments' intersections with the effective edge entrance and exit planes. At equi-distance from the enter and exit points and orthogonal to their joining line segment a matching plane is constructed. At the matching plane front and back segments are combined based on their bending angle ( $\Delta(\theta)$ ) and y components of position ( $\Delta(y)$ ) and track gradients ( $\Delta(\alpha_y)$ )<sup>2</sup>. The three matching components are divided by their respective standard deviations obtained from fits to the single  $\Delta$ -distributions. The resulting relative errors are subsequently added in quadrature, defining an elipsoide in the matching space. A  $3\sigma$  cut is applied on the combined sum of relative errors.

When tracking through the FS one has a choice for the front detector for matching in D3. Detector tracks from either T2 (TPC) or T3 (DC) may be used. In most cases matching in D3 is performed combining T4 segments with the ones from both T2 and T3.

Fig. 4.4 illustrates the effect of these matching cuts on  $\Delta(y)$  and  $\Delta(\alpha_y)$  for track segments from TPM1 and TPM2. Only the small shaded area around the centroid in the distribution is left and attributed to full spectrometer tracks traversing TPM1, D5 and TPM2.

When two detector tracks have been matched the momentum of the spectrometer track is calculated from eq. 4.5 and

$$p = p_{xz}/\sqrt{1 - \alpha_y^2} \quad (4.6)$$

Even with quite stringent cuts on the matching parameters it is possible that one rear track is matched with two or more front tracks. In order to remove such ambiguities the best match is selected based on  $\chi^2$  calculated from the matching parameters as

$$\chi^2 = \left[ \left( \frac{\Delta(\theta) - \Delta_o(\theta)}{\sigma_{\Delta(\theta)}} \right)^2 + \left( \frac{\Delta(y) - \Delta_o(y)}{\sigma_{\Delta(y)}} \right)^2 + \left( \frac{\Delta(\alpha_y) - \Delta_o(\alpha_y)}{\sigma_{\Delta(\alpha_y)}} \right)^2 \right] / 3 \quad (4.7)$$

in which the terms with subscript  $o$  are the offsets from 0 as determined from the fit to the single distribution in each matching parameter.

### Additional matching in the FS

In the MRS and using the FFS only creation of spectrometer tracks is completed after the previous step of in-magnet matching. For the full FS the results of matching in each magnet have to be combined in order to create full FS spectrometer tracks.

---

<sup>2</sup>Since the track segments are linear in the tracking detectors they are parametrized in local coordinates as  $x = x_0 + \alpha_x \cdot z$  and  $y = y_0 + \alpha_y \cdot z$ .

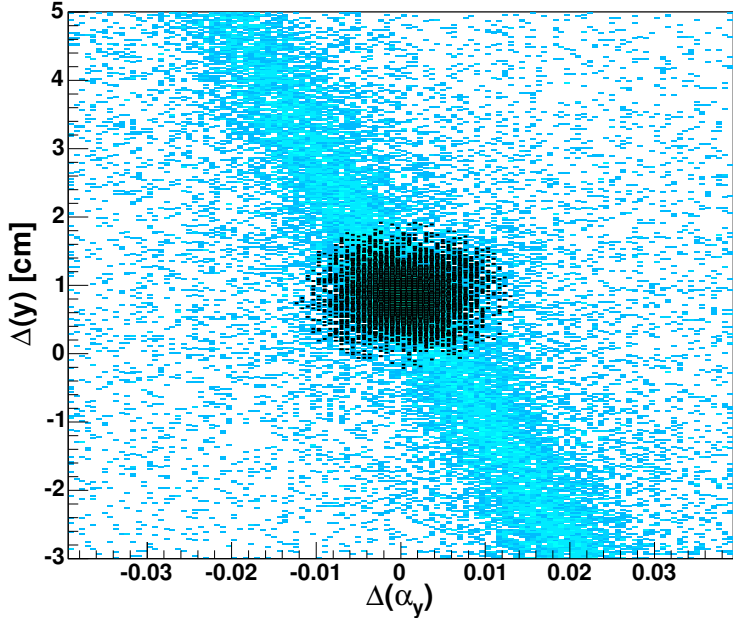


Figure 4.4: Track matching in MRS strictly limits the distribution in  $\Delta(y)$  and  $\Delta(\alpha_y)$ . Only the shaded central area corresponds to tracks surviving the matching cuts.

First the segments of spectrometer tracks obtained from matching in D3 and D4 are combined into BFS tracks. This step is straight forward as tracks in T4 are used for combinations in both D3 and D4. Thus the creation of a BFS track is achieved by combining D3 and D4 segments that have the same detector track in T4.

Finally, the output from matching in FFS and BFS separately is combined and full FS spectrometer tracks created. In the event that T2 is used as front detector for matching in the D3 magnet, full FS tracks are generated from FFS and BFS segments that share detector track in T2.

If T3 is used as front detector for D3 matching is done similarly to the matching in magnets using the difference in track position in x and y directions ( $\Delta(x)$  and  $\Delta(y)$ ) as well as the x and y components of the track slope ( $\Delta(\alpha_x)$  and  $\Delta(\alpha_y)$ ). Also, if two or more FFS tracks share one track in the BFS a  $\chi^2$  selection in the matching parameters is applied analogously to the selection in the magnets.

## Vertex projection

The tracks have to be traced back to the primary interaction vertex. There are two reasons for this. First, the hodoscopes provide PID information in terms of the calculated speed of the particles. For this the track length is needed. Secondly, by applying cuts on the projection back to the primary vertex it is possible to remove a host of decay products and other background particles from the data sample.

Vertex projection is performed in different manners in the two spectrometers. In the

MRS the x position of the tracks in the global coordinate system<sup>3</sup> is fixed at 0. Thus the mid-rapidity spectrometer tracks are in effect projected to a plane centered at the axis of the beam pipe. In this way the z component of the MRS track at global  $x=0$  can be compared to the vertices as determined by the BB and ZDC, as was shown in figs. 3.6 and 3.7.

In the FS a different approach is used. It was early found that it was futile to project FFS tracks to the beam axis for settings with the smallest spectrometer angles. A projection from T1 involves a distance more than five times the distance from TPM1. Also, along the flight path from the vertex to T1 there is D1 through which the particles have to be back-traced. Therefore a projection plane centered at  $z=z_{BB}$  is defined whose normal is parallel to the beam line. The momentum of the particle as calculated in dipole magnets D2 through D4 is used to swim the particle back through D1 to the projection plane.

#### 4.2.3 ID information

When the trajectory of a particle has been reconstructed through a spectrometer it is matched with hits in hodoscopes and Cherenkovs. Using the information of these latter detectors the ID of the particle can be determined.

##### Matching hodoscope hits

A scintillator slat in a hodoscope produces a hit when it is penetrated by a charged particle. The timing information from the hodoscope together with the length of the corresponding particle track determine the particle's speed according to

$$\beta = \frac{l}{ct} \quad (4.8)$$

Here  $l$  is the length of the track from the primary vertex to the slat,  $t$  the corresponding time of flight and  $c$  the speed of light.

In order to determine the correspondence between a spectrometer track and a TOF hit the track is projected onto the TOF plane. This matching removes a lot of background hits in the hodoscopes. Only about 5 – 20% of the hodoscope hits above pedestals correspond to spectrometer tracks [123].

Because of limited resolution in particle tracking valid TOF hits may not be found in the slat to which the track is projected. If there is no hit in the slat pointed to by an MRS track the slats on either side of the one pointed to are searched. This corresponds to a matching window of  $\pm 1.2$  cm along the local x direction.

In the FS the picture is slightly different as the slats are staggered as shown in fig. 4.5. In case of there being only one slat with hit in the area pointed to by the track the same matching algorithm as applied in the mid-rapidity spectrometer is used here. Yet, the projection of one of the tracks in fig. 4.5 traverses two slats. If both have hits that are deemed valid they are also both associated with the track. And in the event that only one of the hits is good, this is the one attributed to the spectrometer track. Finally, if

---

<sup>3</sup>The global coordinate system is defined with z along the axis of the beam pipe, y in the vertical direction and x horizontal and orthogonal to z; fig. A.1.

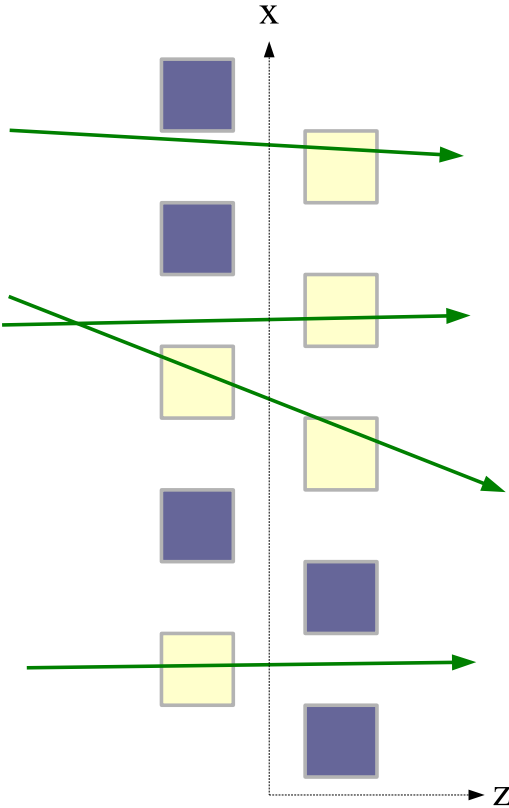


Figure 4.5: Several tracks intersecting a number of scintillator slats H1. The dark shaded slats have no hits.

both slats pointed to by the track do not have valid hits neighboring slats are searched for hits as in the MRS.

### Matching Cherenkov hits

Only the forward spectrometer contains Cherenkov detectors<sup>4</sup> and thus the following procedure applies only here. Since it turned out quite early that C1 was not working optimally (sec. 3.5.2) the description of matching C1 hits to trajectories is omitted here. It is, however, in principle closely related to the procedure applied for hits in the RICH.

In a Cherenkov detector, in which the gas mixture has refractive index  $n$ , particles with velocity

$$v > c/n \quad (4.9)$$

create shock waves of visible light. Here  $c$  is the ordinary speed of light in vacuum. The angle of this wave's direction,  $\theta_r$ , relative to the direction of the incoming particle is calculated from

$$\cos \theta_r = \frac{1}{\beta n} \quad (4.10)$$

---

<sup>4</sup>Since the run from which data is analyzed in this thesis a Cherenkov detector has also been added to the MRS.

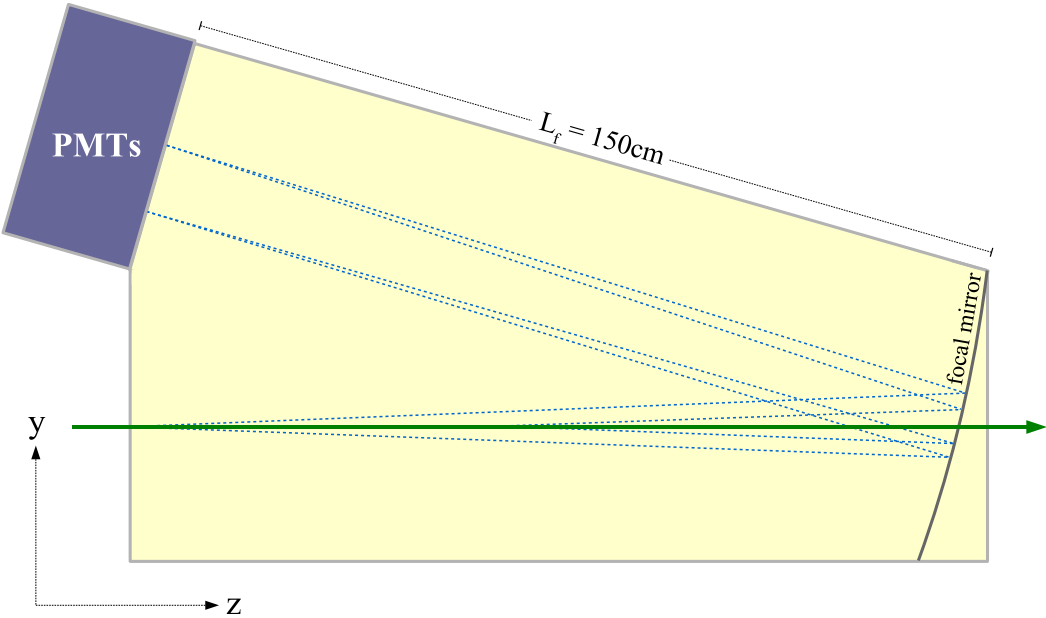


Figure 4.6: Ring generation from a particle traversing the RICH. The dashed lines indicate the direction of photons in the induced shock wave.

Fig. 4.6 illustrates the geometry of the RICH and the principles for reconstructing a ring in the PMT detection plane. The spherical mirror at the rear end of the detector cage has a defined focal length  $L_f = 150\text{ cm}$ . PMTs for readout are located at distance  $L_f$  from the mirror and Cherenkov light reflected from the mirror thus generates rings on the PMT plane as shown in fig. 4.7. Each dark square corresponds to the hit in one of the 80 PMTs, and size of the square is proportional to the signal size.

The ring generated has radius  $r$  related to  $\theta_r$  and the focal length according to

$$\tan \theta_r = \frac{r}{L_f} \quad (4.11)$$

Hence combining eqs. 4.10 and 4.11 one may for a given particle mass correlate the measured radius with the corresponding particle momentum following

$$r = L_f \sqrt{\frac{n^2}{1 + m^2/p^2} - 1} \quad (4.12)$$

### Data summary trees

The previous analysis steps, as well as most of the ones to be discussed in the remainder of this chapter, are all done using analysis software based on the ROOT framework [125]. In order to allow for fast analysis and small data storage size the various bits and pieces of event and track information obtained up to this level are put into one homogeneous data structure. This format is referred to as *data summary tree (DST)*, illustrated in fig. 4.8.

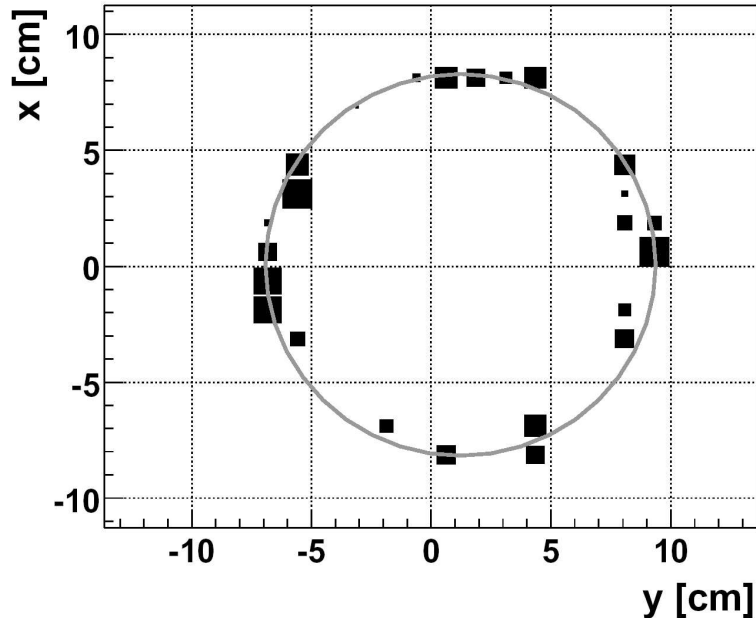


Figure 4.7: The hits generated in the PMTs of the RICH are lying on circular circumference. A ring is fitted to the PMT hits and its radius calculated.

In DSTs defined for the BRAHMS experiment there are three main branches. One contains the global information as determined by BB, MA and ZDC as well as trigger data as determined online by the DAQ system. The two other branches contain track data as reconstructed in the MRS and FS. The remaining part of the data analysis is done using DSTs as input.

### 4.3 Track selection

In high energy heavy ion collisions a host of short lived particles and resonances are produced. The detection of these particles is interesting as such but they are considered unwanted background for this analysis of the primary production of  $\pi$ ,  $K$  and  $p$ . Also, especially protons may be knocked out from the beam pipe, magnets, detector components etc. These secondary protons are likely to pollute the primary spectra as their ID will be wrongly determined e.g. from wrong correlation of time of flight and track length. Hence they should be removed from the sample.

As means to get rid of particles not originating at the projected vertex a  $3\sigma$  cut at the spectrometers' projection planes described in sec. 4.2.2 is applied. This means cutting in global y and z vertex coordinates for tracks in the MRS and in x and y coordinates for particles going through the FS.

Another selection is based on the tracks' proximity to the inner walls of the magnet gaps. As described in sec. 3.4.1 some inhomogeneities in the drift velocity of the TPCs were found. Therefore particles in the MRS whose tracks are propagated closer than 1 cm from the magnet walls are rejected. This fiducial cut effectively removes about 20% of the data recorded by the mid-rapidity spectrometer since D5 only has a vertical opening

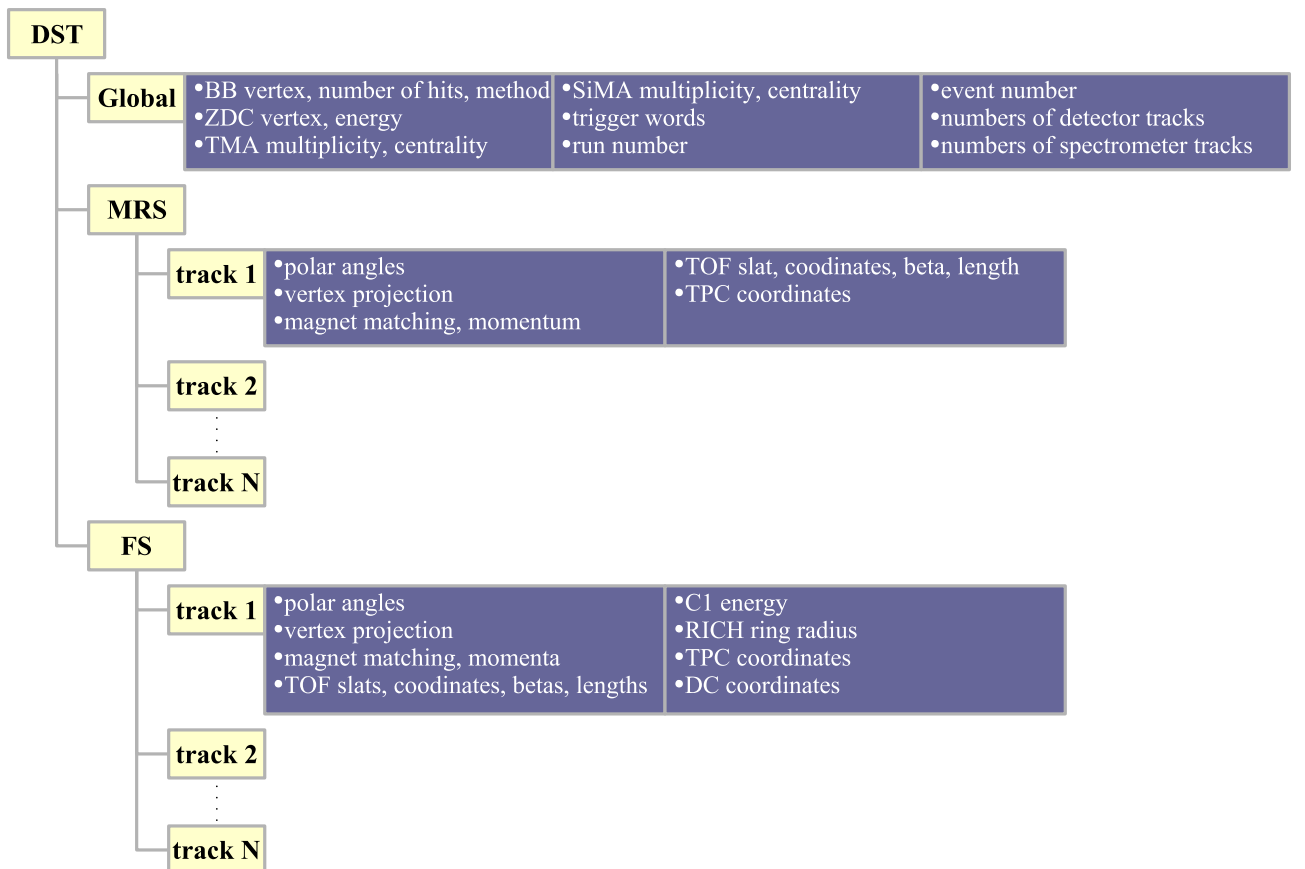


Figure 4.8: After global tracking and ID detector matching the data is organized into DST structure for easy and fast analysis.

of  $\sim 10$  cm. The horizontal dimension of the gap in D5 is  $\sim 36$  cm and thus a 1 cm cut on either side has less impact on statistics.

In the forward arm particles are projected to the entrance plane of D1 using the known magnetic field in D1 and the momentum reconstructed from bending further back. Particles are discarded if they hit the edges of the aperture of D1. Fiducial cuts analogous to the one applied for D5 are used also for the other FS magnets. But D1 is the device primarily limiting the FS acceptance and in comparison the fiducial cuts for D2 through D4 have little effect on available statistics.

When acceptance maps (sec. 4.5.1) are created the cuts from proximity to magnet walls are accounted for.

## 4.4 Particle identification

The BRAHMS experiment was constructed for particle identification (PID) in a wide kinematic window in rapidity and transverse momentum as shown in fig. 3.4. In the mid-rapidity spectrometer PID is performed by measuring the particles' time of flight. In the FS different approaches for identification are used depending on the particles' momenta. The kinematic limits for PID are determined by the resolution of the identification detectors as well as the uncertainty in momentum determination. In the following these limits and the PID methods are described.

### 4.4.1 Momentum resolution

The methods for particle identification applied in this analysis all rely on the resolution of momentum as determined by the dipole magnets and the spatial resolution of the tracking devices. This resolution,  $\sigma_p$ , may be parametrized in terms of particle momentum and mass as.

$$\frac{\sigma_p^2}{p^2} = p^2 \sigma_\alpha^2 + \left(1 + \frac{m^2}{p^2}\right) \sigma_{ms}^2 \quad (4.13)$$

Here  $\sigma_\alpha$  is a term proportional to the angular resolution in tracking and inversely proportional to the magnetic field size.  $\sigma_{ms}$  is the resolution component resulting from multiple scattering when propagating through the spectrometer.

### 4.4.2 Time of flight

TOFW in the MRS and H1 and H2 in the FS provide information for the particle' identification by measuring their time of flight from the primary interaction vertex to the detectors' respective scintillator slats. In this section the procedure for PID in the MRS is described. The method applied using the hodoscopes in the FS follows analogously.

Using the measured time  $t$  and corresponding track length  $l$  from the primary vertex to the slat with valid hit the velocity of the particle is calculated as<sup>5</sup>

$$\beta_t = \frac{l}{t} \quad (4.14)$$

---

<sup>5</sup>Natural units are used and thus  $c=1$ .

From error propagation it follows that the uncertainty in  $\beta_t$  is related to the ones of the  $l$  and  $t$  according to

$$\frac{\sigma_{\beta_t}^2}{\beta_t^2} = \frac{\sigma_t^2}{t^2} + \frac{\sigma_l^2}{l^2} \quad (4.15)$$

The former term in the expression above is significantly larger than the latter. Therefore in the following the uncertainty in velocity as determined from the time of flight is approximated by

$$\frac{\sigma_{\beta_t}^2}{\beta_t^2} \approx \frac{\sigma_t^2}{t^2} \quad (4.16)$$

The velocity of a particle may also be inferred from its momentum  $p$  and mass  $m$  according to

$$\beta_p = \frac{1}{\sqrt{1 + m^2/p^2}} \quad (4.17)$$

and the corresponding  $\sigma_{\beta_p}$  is a function of  $\sigma_p$ .

Two methods for particle identification using time-of-flight measurements are applied in this analysis. The one applied at low momentum is analogous to PID based on invariant mass used in [97, 123]. At high momentum in the MRS an alternative inclusive identification method is used, pushing PID to a limit in  $p_T$  typically 1 GeV/c higher than what may be achieved with the low momentum method.

### Low momentum exclusive identification

This algorithm compares  $1/\beta_t$  with  $1/\beta_p = \sqrt{1 + m^2/p^2}$  calculated with the masses of  $\pi$ ,  $K$  and  $p$ . By correlating the measurements of velocity from the hodoscopes with the momenta found from the bending radius in the dipole magnets it can be seen qualitatively in fig. 4.9 that different particle species correspond to separate bands for low  $|p|$ . Here positively and negatively charged particles are plotted with positive and negative momenta, respectively.

Fig. 4.10 shows the distribution of  $\Delta(1/\beta) = 1/\beta_p - 1/\beta_t$  for negative particles from one MRS setting. The momentum range chosen for the distribution shown, i.e.  $p \in [1, 2]$  GeV/c, is low enough that  $K^-$  and  $\bar{p}$  are excluded. Thus it is primarily populated by pions. The distribution is well fitted with a single Gaussian. It is assumed that the distribution of  $\Delta(1/\beta)$  is Gaussian for each particle species, an assumption that was verified when plotting each species'  $\Delta(1/\beta)$  after identification.

This Gaussian distribution has a width that can be inferred from the uncertainties of  $p$  and  $t$ . By combining eqs. 4.13 and 4.16 one may express the uncertainty in  $\Delta(1/\beta)$  as

$$\sigma_{\Delta(1/\beta)}^2 = \frac{\sigma_t^2}{l^2} + m^4 \left( \frac{\sigma_\alpha^2}{p^2 + m^2} + \frac{\sigma_{ms}^2}{p^4} \right) \quad (4.18)$$

Eq. 4.18 has three unknown  $\sigma$  parameters. In order to obtain these parameters a crude particle identification is performed and distributions of  $\Delta(1/\beta)$  filled for the various particle species.

The crude PID method uses the former term in eq. 4.13 as momentum uncertainty in the high momentum region. This is a simplification that is valid since the uncertainty from multiple scattering only contributes at low momentum, shown in fig. 4.11.  $\sigma_t$  for

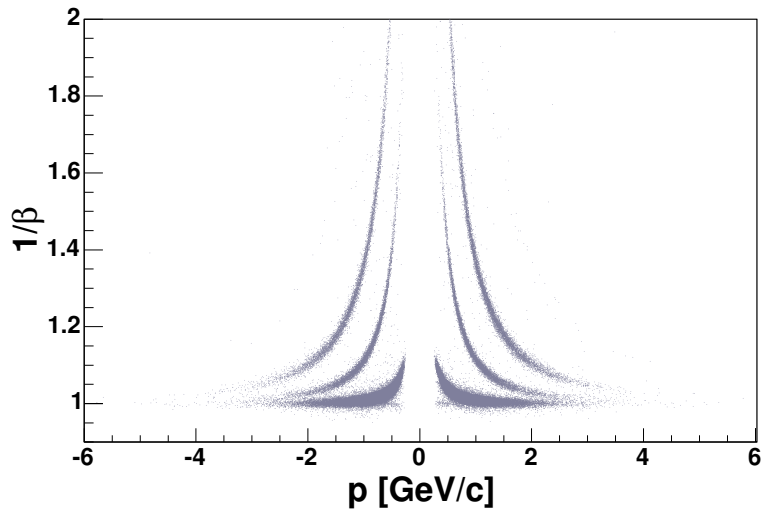


Figure 4.9: The different particle species correspond to separable bands in the correlation of  $1/\beta_t$  with  $p$  in the MRS.

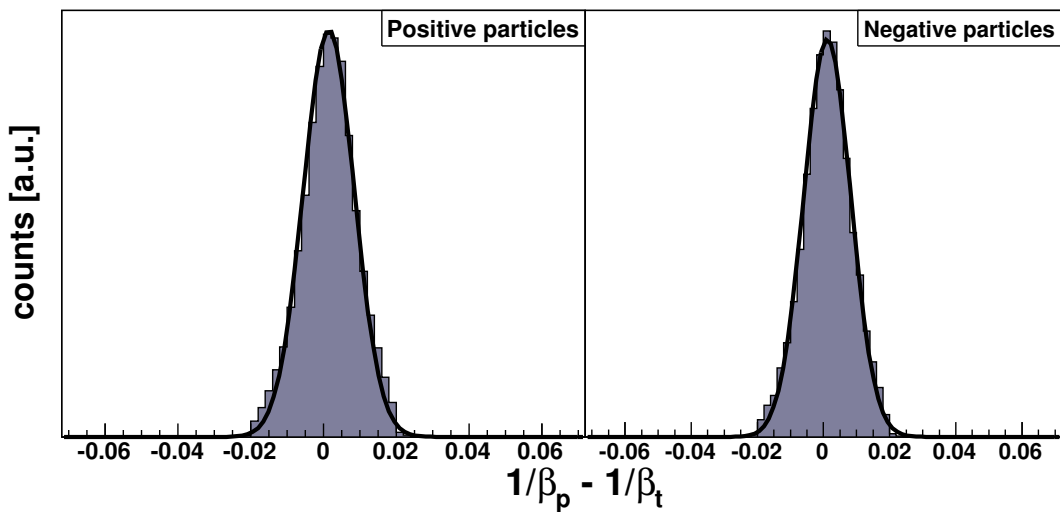


Figure 4.10: Distributions of  $\Delta(1/\beta)$  for charged particles with  $|p| \in [1, 2]$  GeV/c in one mid-rapidity spectrometer setting. The distributions are fitted with a single Gaussians.

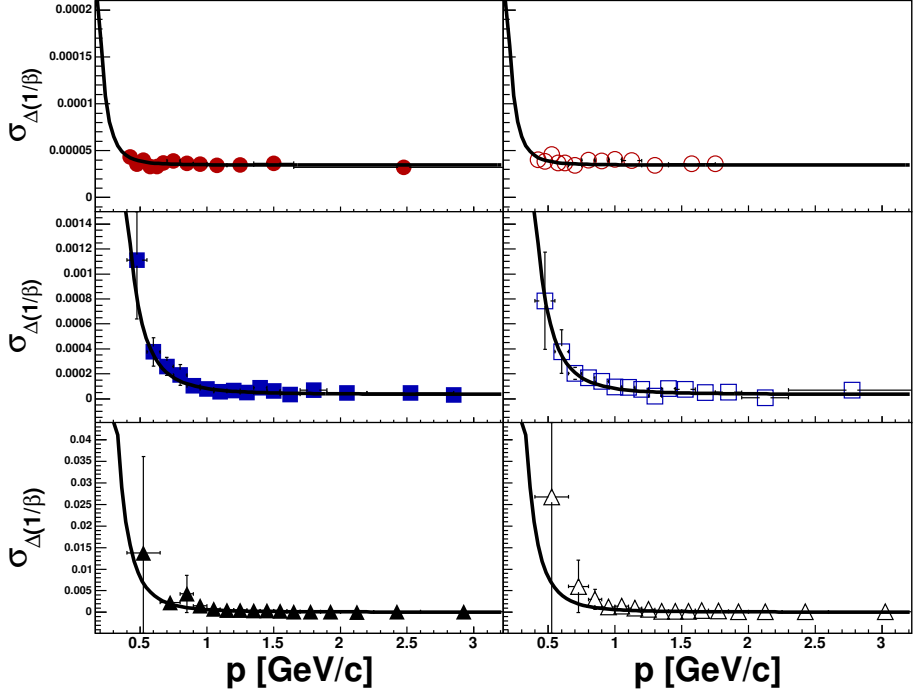


Figure 4.11: Time-of-flight resolution fits for TOFW. Pions (upper panels), kaons (middle) and protons are well fitted with eq. 4.18. The left (right) panels show positively (negatively) charged particles.

this preliminary PID is obtained from  $\Delta(1/\beta)$  as shown in fig. 4.10 and eq. 4.16. Below the momentum limits where the different species are easily distinguishable in fig. 4.9 the rough PID includes all particles within  $\sim 3 \sigma_{\Delta(1/\beta)}$ .

Each species' distribution of  $\Delta(1/\beta)$  vs  $p$  is divided into slices in  $p$  and each slice is fitted with a single Gaussian<sup>6</sup>. The resulting widths are then fitted simultaneously for  $\pi^\pm$ ,  $K^\pm$ ,  $p$  and  $\bar{p}$  with eq. 4.18. The result of this latter step is shown in fig. 4.11.

After the  $\sigma$  parameters in eq. 4.18 have been found the final particle identification may be performed. The particle' measured momenta and inverse  $\beta$  are compared with the corresponding values of  $\pi$ ,  $K$  and  $p$ . This is illustrated in fig. 4.12 in which a particle is detected with  $p = 0.65 \text{ GeV}/c$  and  $1/\beta = 1.27$ .

The distances of closest approach from the measured  $(p, 1/\beta)$  to the  $1/\beta$  curve of each particle species are found. The calculated distances are shown as dotted lines in fig. 4.12. At the closest approach for each species the corresponding uncertainty in momentum is calculated. This uncertainty in combination with the uncertainty in  $1/\beta$  are shown as normalized two-dimensional Gaussians on the  $1/\beta$  curves.

For each species whose distance of closest approach and uncertainty Gaussian are such that the measured  $(p, 1/\beta)$  falls within the  $2\sigma$  contour the normalized Gaussian is evaluated at  $(p, 1/\beta)$ . I.e. for the case shown in fig. 4.12 the obtained ( $p = 0.65, 1/\beta = 1.27$ ) falls outside the  $2\sigma$  contour of both pions and protons, but it is within the  $2\sigma$

---

<sup>6</sup>This method for obtaining the three  $\sigma$  parameters is analogous to the one used in [97, 123] where the widths in  $m^2$  were fitted.

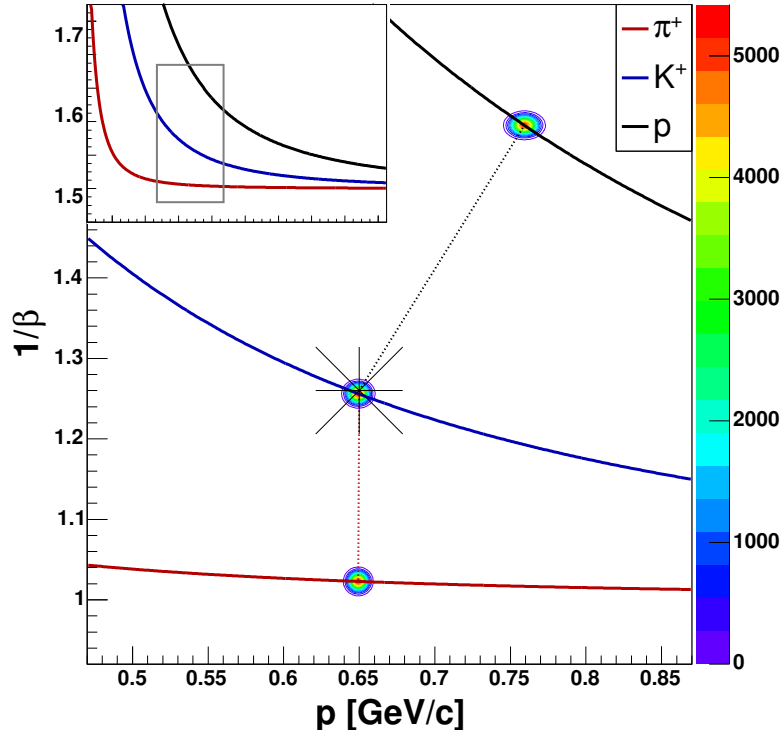


Figure 4.12: Illustration of particle identification of a low momentum positively charged particle measured with  $p = 0.65 \text{ GeV}/c$  and  $1/\beta = 1.27$ . The solid lines correspond to the expected relation between the momentum and the inverse  $\beta$  according to eq. 4.17. The inlaid panel shows the area which is zoomed into in the big panel. Dotted lines represent the distance of closest approach from the measured  $(p, 1/\beta)$  point to the various  $1/\beta(p)$  relation curves. Uncertainties in  $p$  and  $1/\beta$  are depicted by two-dimensional Gaussian distributions shown as contours.

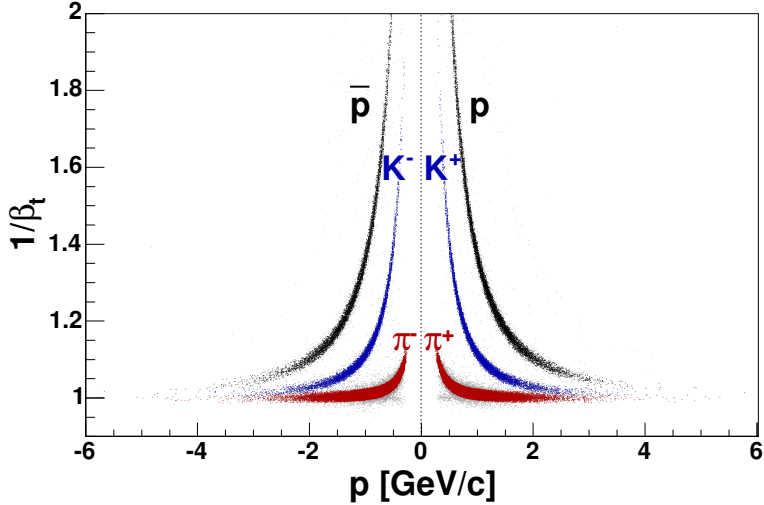


Figure 4.13: The identity of the particles becomes apparent when correlating the  $1/\beta_t$  from TOFW with  $p$  determined from bending of the particles' trajectories in the magnetic field of D5.

Limit	TOFW	H1	H2
$p_{\pi-K}$	$1.5 - 2 \text{ GeV}/c$	$2.75 - 3.25 \text{ GeV}/c$	$4.25 - 5 \text{ GeV}/c$
$p_{K-p}$	$2.5 - 3.254 \text{ GeV}/c$	$3.5 - 5.754 \text{ GeV}/c$	$6.75 - 7.75 \text{ GeV}/c$

Table 4.1: Typical upper momentum limits for particle identification using the low momentum exclusive method.

contour of kaons. The identity here is therefore  $K^+$ . When approaching the higher momenta where the Gaussians start to overlap one may e.g. have  $(p, 1/\beta)$  coordinates within the  $2\sigma$  contour of both pions and kaons. The identity is hence determined from the values of the respective Gaussians.

Fig. 4.13 shows the correlation of  $1/\beta_t$  and  $p$  for the mid-rapidity spectrometer as in fig. 4.9 overlaid with bands corresponding to identified pions, kaons and protons. The setting shown corresponds to the highest magnetic field setting of 6 kG applied in the run of 2001.

As seen from fig. 4.9 in this magnetic setting it is possible to distinguish pions and kaons with a  $2\sigma$  cut up to  $p_{\pi-K} \sim 2 \text{ GeV}/c$ . Protons may be separated from kaons up to  $p_{K-p} \sim 3.25 \text{ GeV}/c$ . Table 4.1 lists each hodoscopes typical limits  $p_{\pi-K}$  and  $p_{K-p}$  below which the low momentum PID based on time of flight is applicable.

### High momentum inclusive identification

Above the magnetic field dependent limits in table 4.1 particles may no longer be identified track by track using cuts in  $\Delta(1/\beta)$ . It is, however, possible to assign ID to particles in an inclusive manner. This method is applied in the MRS only since the FS provided too

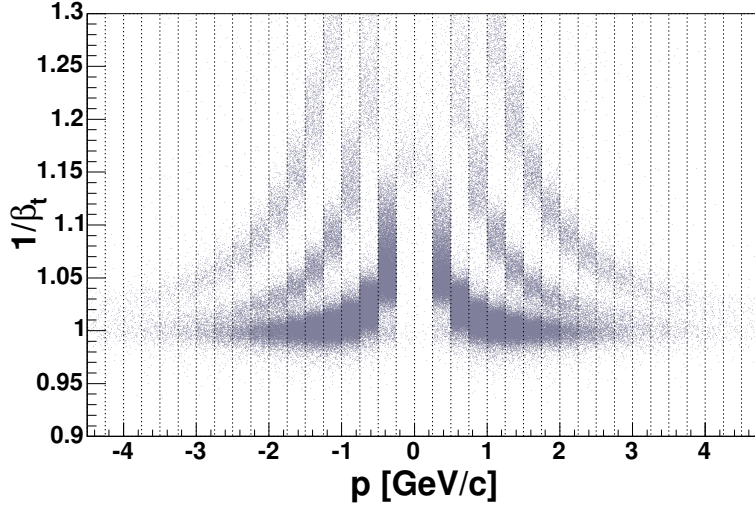


Figure 4.14:  $1/\beta_t$  plotted vs  $p$  for particles with  $\eta \in [0.9, 1.1]$  detected by the MRS. The binning along the momentum axis was chosen wide enough to have enough statistics for fitting functions to each momentum bin's distribution in  $1/\beta_t$  and narrow enough so that this distribution is approximately described by a triple Gaussian.

little data to extract PID probabilities, explained below. But with more statistics this method may also be used in the FS.

ID is assigned to each track based on the relative abundance of each particle species. I.e. probabilities for a track with given kinematic characteristics being a pion, kaon or proton are calculated prior to this assignment.

PID probabilities are calculated from the correlation of  $1/\beta_t$  vs.  $p$  measured for various windows in pseudo-rapidity  $\eta$ . First the phase space covered by the MRS is segmented in pseudo-rapidity. Here the range in  $\eta$  was divided into slices of width  $\Delta(\eta) = 0.2$ . For each range in  $\eta$  a correlation histogram of  $1/\beta_t$  vs.  $p$  is filled, as shown in fig. 4.14 for  $\eta \in [0.9, 1.1]$ . As illustrated in the figure the  $p$  axis is segmented in bins of width  $\Delta(p) = 0.25$  GeV/c.

Every  $1/\beta_t$  distribution is obtained from several spectrometer settings, i.e. different magnetic field values and thus correspondingly different momentum uncertainties. They are, however, found to be sufficiently well described by triple Gaussian distributions, in which each single Gaussian component is attributed to the population from pions, kaons and protons, respectively. Fig. 4.15 shows several momentum slices for negative particles that are fitted with triple Gaussians. The slices were obtained from the distribution in fig. 4.14. Single Gaussians are deduced from the fitted parameters of the triple Gaussians.

After fitting the distributions the PID probability for each particle species is obtained by integrating the corresponding fit function and dividing the integral by the sum of integrals. In other words, the probability  $P_i$  for a particle having identity  $i$  is calculated as

$$P_i = \frac{\int_{\mu_i-3\sigma_i}^{\mu_i+3\sigma_i} f_i(1/\beta_t) d(1/\beta_t)}{\sum_j \int_{\mu_j-3\sigma_j}^{\mu_j+3\sigma_j} f_j(1/\beta_t) d(1/\beta_t)} \quad (4.19)$$

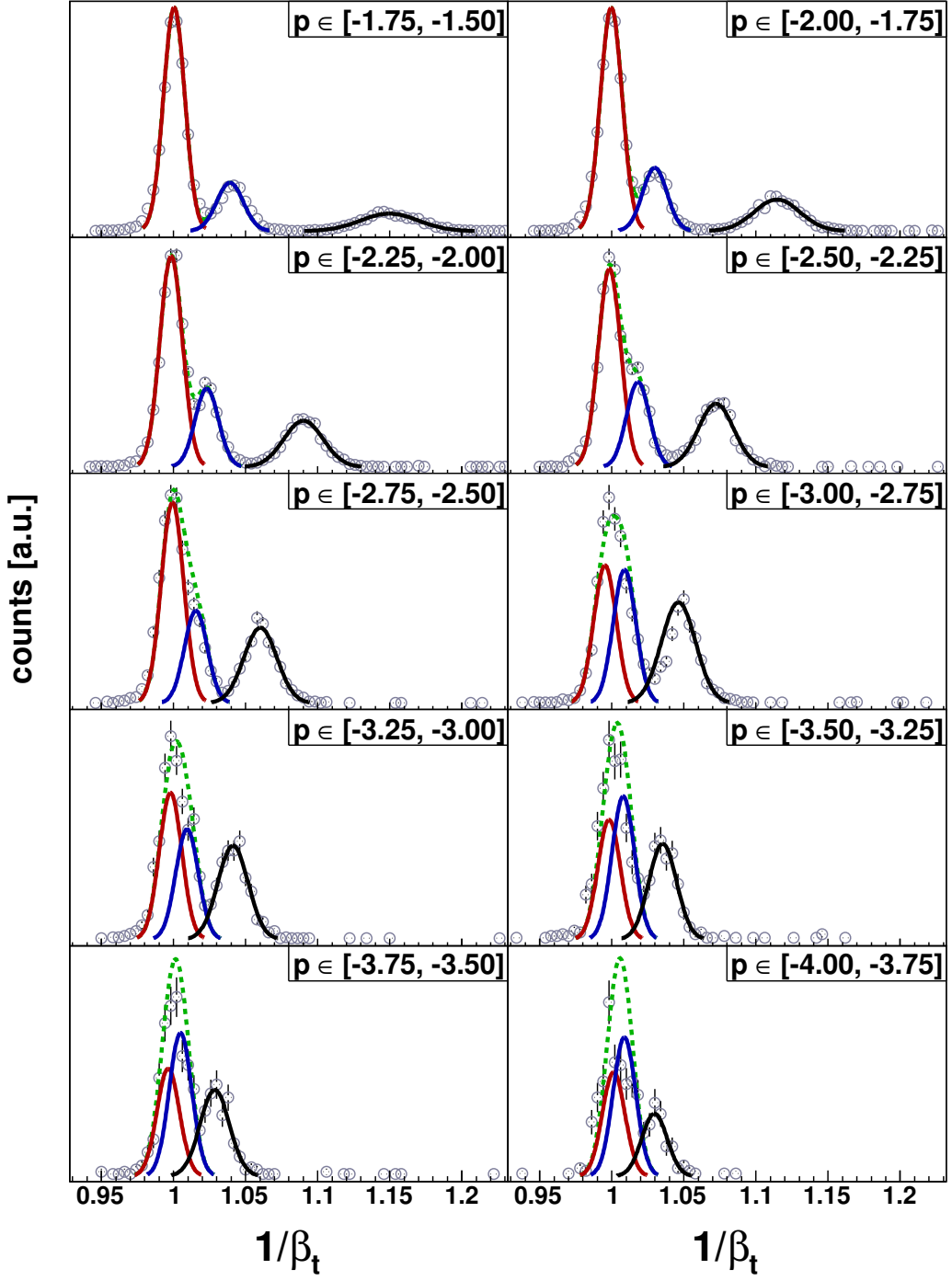


Figure 4.15: The distributions of  $1/\beta_t$  for negative particles in various slices in momenta. The data includes many spectrometer settings covering the pseudo-rapidity range  $\eta \in [0.9, 1.1]$ . Each distribution is fitted with a triple Gaussian extracting the relative population of each particle species. In each panel the solid lines indicate the fit result for  $\pi^-$  (left),  $K^-$  (center) and  $\bar{p}$ . The dashed lines represent negative mesons, i.e. the sum of  $\pi^-$  and  $K^-$ . Qualitative upper momentum limits for inclusive PID are imposed. Here it seems futile to extend separation of  $\pi^-$  and  $K^-$  beyond  $|p| = 3.25 \text{ GeV}/c$  while  $\bar{p}$  may be identified at least up to  $|p| = 3.75 \text{ GeV}/c$ .

Particle species	$\pi$	$K$	$p$
Momentum threshold [GeV/c]	2.19	7.76	14.75

Table 4.2: Nominal threshold in momentum above which each particle species induce Cherenkov radiation in a medium with refractive index  $n_0 = 1.00202$ .

in which index  $j$  runs over  $\pi$ ,  $K$  and  $p$ , i.e. *either* positive or negative particles.  $f_i$  is the single Gaussian obtained for particle  $i$  using the corresponding parameters from the triple Gaussian fit to the inverse  $\beta_t$  distribution.

The applicability of this method depends strongly on the amount of statistics covering the given regions in  $\eta$  and  $p$ . The solid angle covered by the mid-rapidity spectrometer at each spectrometer setting is wider than the one of the forward arm. Also the MRS covered a smaller range in  $\eta$  than the FS during the experimental run of 2001 resulting in higher statistics at each pseudo-rapidity window close to mid-rapidity. Thus the data recorded by the forward spectrometer was early found to be insufficient for using this PID method.

The momentum limits for the inclusive particle identification are gauged from the slices as shown in fig. 4.15. Typical upper momentum limits for separation of  $\pi$  and  $K$  are  $3 - 3.5$  GeV/c. Protons may be separated from mesons up to momenta of  $3.5 - 4.5$  GeV/c. These are all qualitative limits and systematic errors increase with increasing momenta to reflect the relative uncertainty in determining the identity of particles.

#### 4.4.3 Cherenkov rings

In the forward arm particles with high momentum are identified primarily using information from the RICH. The  $C_4F_{10} / C_5F_{12}$  gas mixture has a nominal refractive index  $n_0 = 1.00202$ . Corresponding nominal momentum limits above which the different particles yield Cherenkov radiation may be inferred from eq. 4.9 as

$$p_0 = \sqrt{\frac{m^2}{n_0^2 - 1}} \quad (4.20)$$

Table 4.2 lists momentum thresholds for the RICH calculated using the refractive index  $n = n_0$ .

As mentioned in sec. 3.5.3 it turned out that the gas in the RICH was continuously leaking resulting in lower refractive index and higher momentum thresholds for generation of Cherenkov light. In order to remedy the effect of slow outflow on the PID capabilities of the RICH the index of refraction was calibrated before final particle identification.

Solving eq. 4.12 with respect to the refractive index  $n$  it may be expressed as

$$n = \sqrt{(r^2/L_f^2 + 1)(1 + m^2/p^2)} \quad (4.21)$$

By performing a preliminary particle identification using  $n = n_0$  and calculating  $n$  for pions refractive indices in the range  $1.00190 - 1.00201$  were found and ultimately applied in the PID. The calibration procedure is explained more thoroughly in [85].

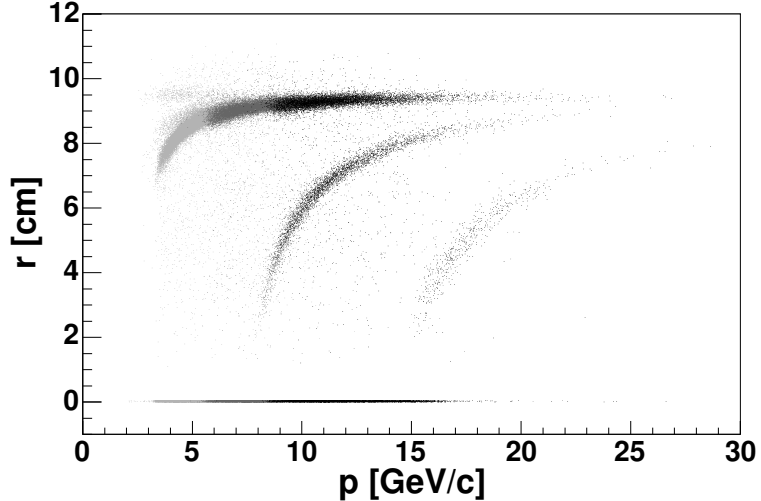


Figure 4.16: Radii of detected Cherenkov light rings plotted against the corresponding momenta for positive particles. The different shades correspond to three different magnetic field strengths with the forward arm located at  $4^\circ$ .

Particles are identified in the RICH by correlating their momentum and the radius of the Cherenkov light cone they produce in the radiator gas, shown in fig. 4.16. Several bands corresponding to different particle species may be identified qualitatively. The data points with  $r = 0$  indicate particles with momenta below threshold for light emission.

The width of the bands stem from uncertainties in determining momentum and ring radius. At the momentum ranges where the RICH provides PID information the  $\sigma_{ms}$  component of eq. 4.13 is negligible. This may be inferred a.o. from fig. 4.11 in which  $\sigma_{ms}$  is the component to induce a rise in  $\sigma_{\Delta(1/\beta)}$  for the lowest momenta. The momentum resolution used to determine the identification characteristics of the RICH is therefore simplified by the approximation

$$\frac{\sigma_p}{p} \approx p \sigma_\alpha \quad (4.22)$$

The quantitative determination of particle ID using the RICH is performed analogously to identity determination with  $p$  and  $1/\beta$  using the hodoscopes. The measured light cone radius  $r$  is compared to  $r_p$  calculated with eq. 4.12. This identification procedure, as in the case with the hodoscopes, relies on the precise knowledge of the involved measurement resolutions.

The distribution of  $\Delta(r) = r - r_p$  is Gaussian when  $r_p$  is calculated assuming the right particle mass. Fig. 4.17 shows this difference for positive particles in the momentum region between the pion and kaon thresholds, i.e. where the bulk of the sample consists of  $\pi^+$ .

When plotting the  $\Delta(r)$  distribution with logarithmic ordinate one sees the long tails that are mainly populated by decay products and leptons. By introducing PID cuts in similar manner as was done for the hodoscopes one may effectively remove most of the population in the tails. Also, since identification information from the various PID

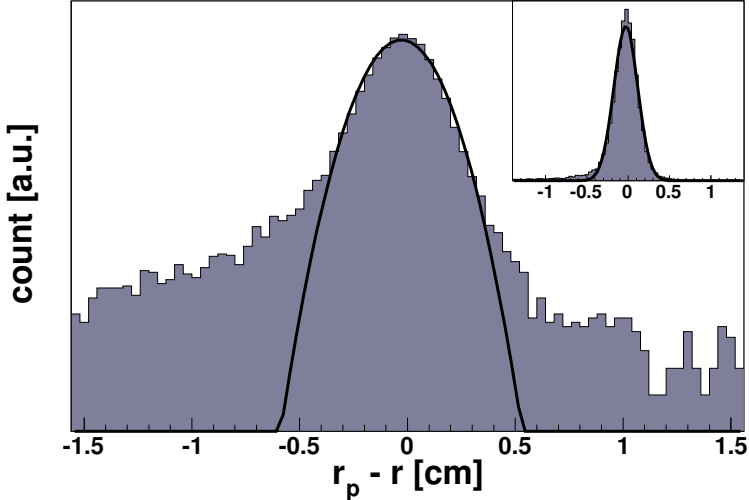


Figure 4.17: Distribution of  $\Delta(r) = r - r_p$  for particles inducing Cherenkov light and having momenta between the pion and kaon thresholds. The distribution is fitted with a single Gaussian. Long tails become apparent when plotting the distribution with logarithmic ordinate axis as shown in the large panel.

detectors in the FS are combined as described in sec. 4.4.4 the contribution e.g. from leptons in the pion sample is deemed insignificant.

The width of the  $\Delta(r)$  distribution comes from the uncertainty in ring measurement,  $\sigma_r$ , and from momentum determination calculated with eq. 4.22. Hence, from error propagation the uncertainty in  $\Delta(r)$  is expressed as

$$\sigma_{\Delta(r)} = \sqrt{\frac{L_f^2 n^4 m^4 \sigma_\alpha^2 p^4}{(n^2 - 1 - m^2/p^2)(p^2 + m^2)^3} + \sigma_r^2} \quad (4.23)$$

Using particles selected in a wide region around the pion band of fig. 4.16 and with momenta in the range  $p \in [10, 20]$  GeV/c various values for  $\sigma_{\Delta(r)}$  are obtained. Eq. 4.23 is then solved with respect to  $\sigma_r$ . From the previously calculated  $\sigma_\alpha$  and measured  $\sigma_{\Delta(r)}$  the uncertainty in radius determination was found to be in the range of 0.10 to 0.17 cm.

The final step to deduce identity information from the RICH depends on the momentum of the track and the thresholds for the various particle species. If a light cone was generated particles of species  $i$  are considered whose momentum threshold  $p_0^i$  is below the measured track momentum. The distance of closest approach from the track's  $(p, r)$  coordinate to the considered species'  $r_p^i$  curve is found. At the determined closest point  $(p^i, r_p^i)$  the uncertainty in  $p$  is deduced with the first term in eq. 4.23 and a normalized two-dimensional Gaussian created whose width parameters are  $\sigma_p^i$  and  $\sigma_r$ .

If the measured  $(p, r)$  is within the  $2\sigma$  contour of only one of the considered species the identity component from the RICH is set to that particular species. If, however, the particle's  $(p, r)$  is within the  $2\sigma$  limit of more than one species the identity is determined from the highest value of the two-dimensional Gaussians evaluated at the given momentum and radius.

On the other hand, if there was no ring radius recorded for a given track the possible IDs corresponding to momentum thresholds that are lower than the tracks momentum are discarded. E.g if a track has momentum  $p = 5 \text{ GeV}/c$  and no light was generated one may conclude it is not generated by a pion whose threshold is of the order of  $2 \text{ GeV}/c$ . This means that in this case one may only deduce that the particle is a kaon or a heavier particle. This is, nevertheless, useful information as described in sec. 4.4.4.

#### 4.4.4 Combination of ID in the forward arm

In the FS three detectors were used for particle identification. The two hodoscopes H1 and H2 provide PID information in the the low momentum ranges listed in table 4.1 while the ring imaging Cherenkov detector has its strength in the high momentum region above the thresholds tabulated in table 4.2. In order to provide particle identification in the full range of the spectrometer one may split the covered momentum window into regions and let one detector only be responsible for identification in each sub-window. This was done in [97, 123, 85] in which H2 was used for low momentum and RICH for high momentum particles.

In this analysis the various pieces of identity information provided by each PID detector is combined. This still means that the hodoscopes are mainly responsible for PID of low momentum particles and the RICH for the ones with higher momenta. But the transition between these ranges is smooth.

The hodoscopes and the RICH each provide a probability that the a given particle is a pion, kaon or a proton. I.e. as mentioned in sec. 3.2.1, only particles of the same charge sign are detected in one spectrometer setting of the forward arm. For each particle species the probability obtained from each detector is multiplied to yield the final probability. That means that the combined probability for species  $i$ ,  $P_i$ , is a result of the detector specific probabilities  $P_i(j)$  according to

$$P_i = \frac{\prod_j P_i(j)}{\sum_k \prod_j P_k(j)} \quad (4.24)$$

in which  $k$  runs over  $\pi$ ,  $K$  and  $p$  and the detector index  $j$  runs over H1, H2 and RICH.

The identification detectors have intrinsic inefficiencies that lowers their performance. Corrections for this are discussed more in depth in sec. 4.5.2. When combining PID information from various detectors the efficiency of the procedure outlined above decreases as the product of the efficiencies of each PID detector. Assuming e.g. detector efficiencies  $\epsilon_j \approx 95\%$  for each detector, the overall efficiency for PID has an upper limit of  $\epsilon_{PID} = \prod_j \epsilon_j \approx 86\%$ .

As an attempt to remedy the effect of detector inefficiency the algorithm includes a uniqueness test. If one of the PID detectors gives  $P_i(j) = 1$ , i.e. 100% probability for a particle having identity  $i$ , then the combined PID is also 100% for identity  $i$  and 0 for the other species.

For each PID detector the identification algorithm implies cuts along the  $2\sigma$  contours as described in secs. 4.4.2 and 4.4.3. This correction is also addressed in sec. 4.5.2.

## 4.5 Corrections

Before spectra and yields can be deduced from the data a number of corrections have to be applied. The spectrometers' limited coverage in solid angle is taken into account through acceptance correction. The various detector components have high yet limited efficiency. Particles experience multiple scattering when traversing the spectrometer arms causing deflection from the original path and loss in momentum. A fraction of the pions and kaons decay in flight. This loss has to be compensated. Also, other unstable particles, like  $\Lambda$  and  $K^0$  feed into the sample, primarily polluting  $p$  and  $\pi$ , respectively. The amount is estimated and corrected for. Protons and anti-protons have a significantly high cross section for being absorbed on their way through the spectrometer arms and thus it is necessary to correct for this. Finally, certain cuts applied in the earlier steps of the analysis cause corrections at later times.

Most of the corrections are deduced using BRAG, a simulation software package based on GEANT 3.21 [118]. Using BRAG the experimental setup is simulated when generated particles penetrate the detector components. Realistic energy depositions by the particles are translated into hits which can be used in further analysis in the same way as hits from real particles.

This section describes the various corrections applied to the data.

### 4.5.1 Acceptance correction

The spectrometer arms only cover a small portion of the full  $4\pi$  range of solid angle, with the MRS covering an order of magnitude more than the FS, as mentioned in sec. 3.2. The limited acceptance is thus corrected for using Monte-Carlo simulations with BRAG.

Pions with flat distributions in global coordinate  $z$ , momentum  $p$  and polar angles  $\theta$  and  $\phi$  are thrown in direction of the spectrometer arms. The particles are thrown from global  $(x, y) = (0, 0)$ , i.e. from the beam line axis. In order to match the selected BB vertex ranges of sec. 4.1 it is required that the origin for pions thrown into the FS has  $|z| < 20$  cm and  $|z| < 15$  cm for the MRS. The ranges in  $p$ ,  $\theta$  and  $\phi$  are so that they extend beyond the respective ranges for particles that can be traced through each spectrometer. Since the acceptance depends on the location of the origin along the beam axis correction values are deduced separately for vertex bins of width  $\Delta(z) = 5$  cm.

A high number of pions are thrown into each spectrometer, the number being high enough that the final systematic errors of the spectra are not perceptibly affected by the error introduced in acceptance correction. An acceptance map is generated for every particle species at each spectrometer setting and vertex bin. Yet, the Monte-Carlo simulation is simplified since positive particles in one spectrometer setting have the same acceptance as negative particles where the polarity of the magnetic field is reversed. Thus not all spectrometer settings have to be simulated.

In these simulations only continuous energy loss is considered. I.e. there is no dependence on particle species for given  $p$ ,  $\theta$  and  $\phi$ . Yet, the final correction values are presented in terms of rapidity  $y$  and transverse momentum  $p_T$  or transverse mass  $m_T$ . For the transformation from  $(\theta, p)$  to  $(y, p_T)$  for  $K$  and  $p$  the pion mass is replaced by the  $m_K$  and  $m_p$ , respectively.

The acceptance maps in fig. 4.18 show the  $(y, p_T)$  distribution of correction values

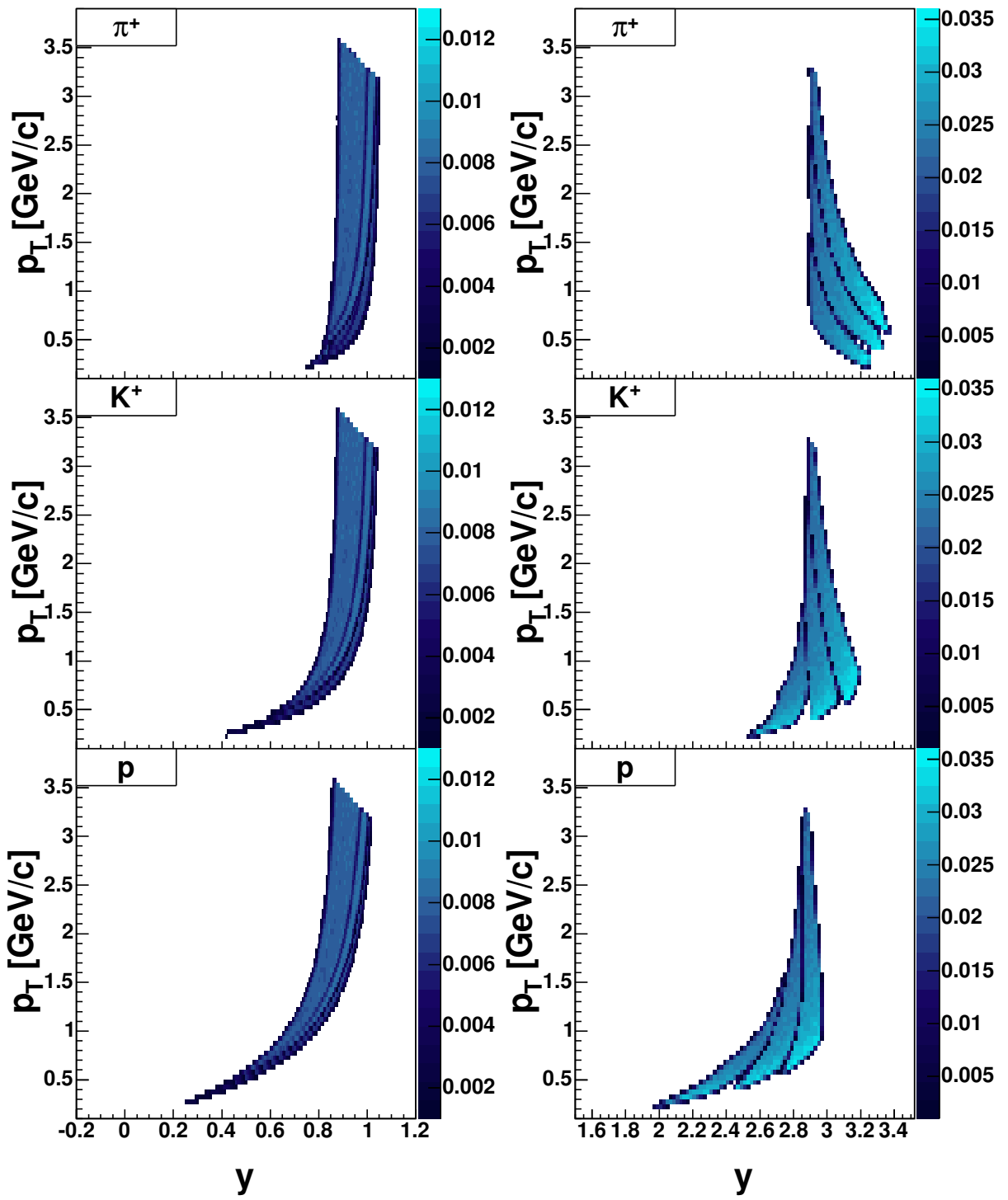


Figure 4.18: Several acceptance maps generated with  $z \in [0, 5]$  cm for the MRS at  $40^\circ$  (left panels) and the FS at  $4^\circ$ . The different maps for every particle species correspond to three different magnetic field settings in each spectrometer. All the maps are obtained with the spectrometers at B polarity, which for the FS exclude negative particles. The darker central bands in the MRS maps indicate lower acceptance where particles hit bad slats in TOFW.

obtained with  $z \in [0, 5]$  cm for three settings in each spectrometer, all with B polarity. The mid-rapidity spectrometer is placed at  $40^\circ$  and the forward spectrometer at  $4^\circ$ . Each cell contains a number deduced as

$$\epsilon_a(y, p_T) = \frac{N_r(y, p_T)}{N_t(y, p_T)} \cdot \frac{\Delta(\phi)}{2\pi} \quad (4.25)$$

Here  $N_t(y, p_T)$  is the number of particles thrown with rapidity  $y$  and transverse momentum  $p_T$ ,  $N_r(y, p_T)$  is the number of particles reconstructed with the same kinematic characteristics and  $\Delta(\phi)/2\pi$  normalizes the value to the azimuthal range covered by the spectrometer. Similar maps are obtained in coordinates  $(y, m_T - m)$ , in which  $m$  is the mass of the particle.

$\epsilon_a(y, p_T)$  expresses the probability that a particle with rapidity  $y$  and transverse momentum  $p_T$  is accepted in a spectrometer. Hence, to correct for the limited acceptance the data is multiplied by the correction factor  $c_a(y, p_T) = 1/\epsilon_a(y, p_T)$ .

#### 4.5.2 Detector efficiency correction

BRAHMS' detector setup consists of numerous sub-detector components that perform with high levels of efficiency. Nevertheless, when measurements from several of these sub-detectors are combined to form spectrometer tracks the detection efficiencies of the full spectrometers are convolutions of the efficiencies of their respective sub-detectors. A proper treatment of detector efficiency is particularly important when using the full forward arm for which tracks are reconstructed using five tracking devices and PID information is extracted from one Cherenkov detector and two hodoscopes.

##### TPC tracking efficiency

Tracking efficiency for the time projection chambers is estimated using BRAG by simulating the passing of charged particles through the detector. The detector hits thus obtained are transformed into realistic arrays of ADC values like the ones obtained as raw data from real events. The data structure including the array of ADC values is referred to as a TPC *sequence*. Simulated sequences are embedded into sets of sequences obtained in real Au+Au collisions.

From there on local tracking proceeds as described in sec. 4.2.1 not differing between simulated and real data. After local tracks are reconstructed tracking efficiency is extracted as the number of reconstructed embedded tracks  $N_{re}$  relative to the number of embedded tracks  $N_e$ , i.e.

$$\epsilon_{tr}^{emb} = \frac{N_{re}}{N_e} \quad (4.26)$$

A reconstructed track is said to come from a simulated track if the volumes of their respective associated cylinders with radius  $r = 4$  mm overlap by more than 60% [126].

By embedding into real data the tracking efficiency is studied as a function of occupancy in the detectors. It was found in [126] that the efficiency in the MRS tracking detectors decreases linearly with the number of hits in each TPC. Fig. 4.19 shows the resulting combined tracking efficiency  $\epsilon_{tr}^{emb}$  for the mid-rapidity chambers plotted as a function of number of TPC hits.

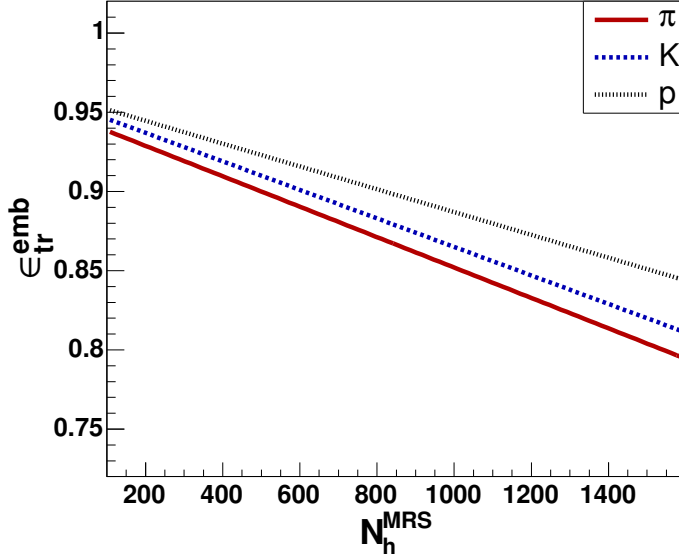


Figure 4.19: Results of tracking efficiency in the MRS as determined by embedding simulated TPC hits into real data. The unit along the abscissae is the number of real TPC hits per event in the spectrometer, i.e. the sum of hits in TPM1 and TPM2.

The efficiency for the MRS is the average result obtained for the various settings covered. The difference between settings was deemed smaller than the statistical uncertainty. There are also some small variations between the various particles species. This is attributed to increasing energy deposition with increasing particle mass in the low momentum region covered by the mid-rapidity spectrometer.

In [126] the efficiency of T1 and T2 in the forward arm were studied in the same framework as for the mid-rapidity TPCs. But the results obtained for the FFS were ambiguous. There were large variations between the various spectrometer settings. Also the efficiency showed different dependence whether they are correlated with the number of hits and the number of tracks. This behavior is particularly peculiar since the number of tracks is a priori assumed to increase steadily with the number of hits.

Since the tracking efficiency determined by embedding simulated T1 and T2 tracks in the data is disputed the FFS tracking efficiency used in this analysis are determined from the data. This estimation relies on comparison of the number of track segments in the detector being studied to the number of reference tracks reconstructed using other tracking devices. Tracks from other devices are projected to the detector whose efficiency is to be estimated [127].

This is especially suitable in the forward arm where a redundant number of tracking detectors may reconstruct trajectories and calculate the corresponding momenta. In this way tracks reconstructed e.g. using T2 through T5 may be propagated through D2 and compared with tracks reconstructed in T1. The method may in principle also be used in the mid-rapidity spectrometer but only in runs with magnet D5 turned off and hence not studied as a function of momentum. This was done only as a consistency check for the efficiencies estimated by track embedding [97]. Matching of detector tracks and reference tracks is done analogously to track matching in the magnets described in sec. 4.2.2.

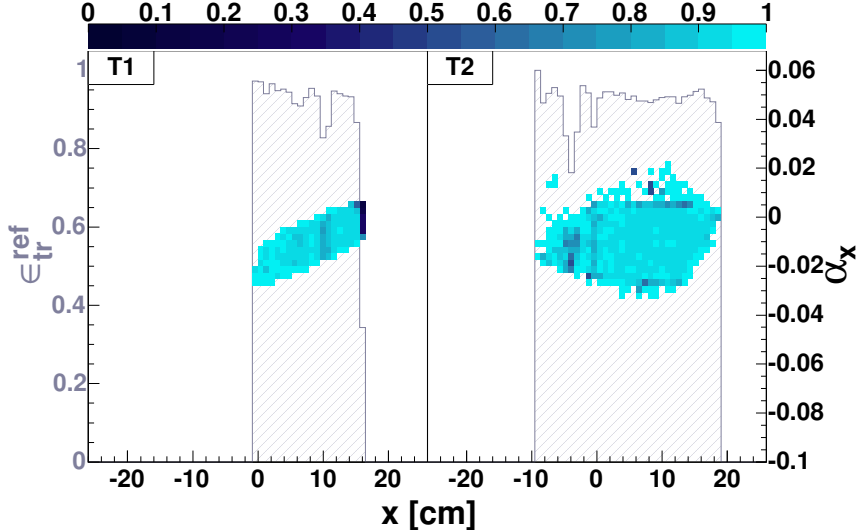


Figure 4.20: Results for tracking efficiency in T1 and T2 obtained with projecting reference tracks. The efficiencies shown are deduced with FS operated at  $3^\circ$  and with magnets at A polarity with magnet current of 1692 A. The axis on the right hand side shows the x component of the detector track slope corresponding to the front histograms, while the left axis is the scale of the rear plot.

The resulting efficiency is calculated as the number of detector tracks matching projected ones,  $N_m$ , relative to the number of projected tracks,  $N_p$ , i.e. expressed as the fraction

$$\epsilon_{tr}^{ref} = \frac{N_m}{N_p} \quad (4.27)$$

Using this reference method the efficiency is deduced as a function of event centrality and the detector tracks' position and slope in the horizontal plane. The latter two variables effectively incorporates momentum dependence for detectors located behind dipole magnets since the bending of charged particles and hence their x components of position and slope depend on momentum.

Fig. 4.20 shows efficiency results obtained for T1 and T2 for a high field setting with the FS at  $3^\circ$ . The foreground two-dimensional plots show tracking efficiency as a function of horizontal position  $x$  and slope  $\alpha_x$ , while the rear plots show the projection of  $\epsilon_{tr}^{ref}$  along the abscissa.

### DC tracking efficiency

Tracking efficiency for the drift chambers T3 through T5 is obtained as for T1 and T2 by projecting reference tracks. The FS tracking efficiencies are averaged over runs for the various spectrometer settings. This was particularly necessary for the DCs due to variations in the amount of background radiation affecting the performance of T3 and T5.

Fig. 4.21 shows the DC tracking efficiencies obtained for the same setting as for fig. 4.20. This setting shows low tracking efficiency for T3 compared to the other two

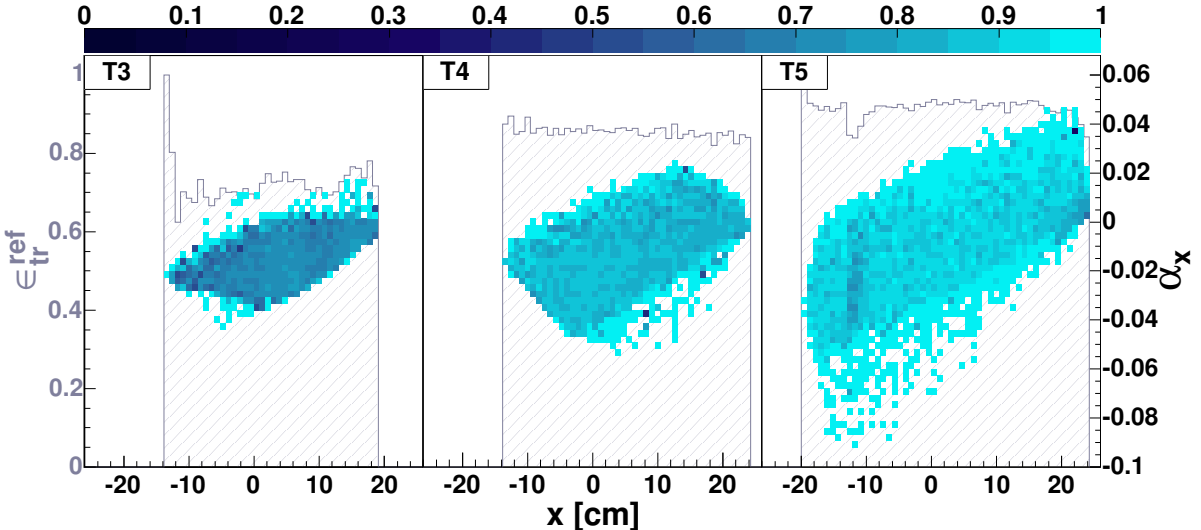


Figure 4.21: Results for tracking efficiency in T3, T4 and T5 obtained with projecting reference tracks. The correspondence of axes to histograms is as in fig. 4.20, as is the spectrometer setting.

drift chambers. Nevertheless, since T2 which has higher efficiency it may be used as front detector for matching in D3. This way the low efficiency for T3 does not cause loss in efficiency in the forward arm.

### Hodoscope efficiency

The efficiency of the hodoscopes is investigated in similar manner as when projecting reference tracks to estimate TPC and DC efficiencies. Detector tracks reconstructed in the closest tracking device are projected to the plane spanned by the scintillating slats of each hodoscope. Thus the efficiency may be gauged for each slat by dividing the number of hits corresponding to traversing tracks by the number of tracks.

The inefficiency of TOFW is mainly caused by particles going through the aluminum and tape wrapping and hence not scintillating in the plastic. The panels of TOFW are placed along a circular arc. Thus the angle of their normal relative to the spectrometer axis increases with increasing distance from the axis. This means that both low and high momentum particles impinge on slat panels with similar angle relative to the panel's normal. For this reason no momentum dependence on the efficiency of TOFW was found. A constant efficiency of 93% was deduced for TOFW [97].

In the forward arm the picture is slightly different. Since the slats are staggered as depicted in fig. 4.5 it is possible to go through the hodoscope plane without generating light, i.e. if particles intersect the plane with large angles relative to the plane's normal. This possible dependence on the hodoscope's local x coordinate reflects the dependence on momentum. Because of the staggered setup there should be no loss of efficiency due to the slat wrapping as for TOFW.

As described in [97, 123] a dependence on slat number, and thus on the local x coordinate was found for H1. In this hodoscope the efficiency varies from 93% to close

to 100%. No such dependence was found for H2 illustrating that all tracks cross its slat plane with very similar angles. An efficiency of 98% was estimated for H2.

The efficiencies of the hodoscopes are also affected from multiple tracks corresponding to one hit. These hits are removed from the sample. In [123] it was found that 5% of the hits in H1, <1% in H2 and <2% of the hits in TOFW associated with projected tracks are multiple hits. These percentages correspond to hodoscope inefficiencies from multiple hits. Efficiencies from multiple hits are hence added in quadrature with the respective efficiencies mentioned above.

### RICH efficiency

In [85] the efficiency of RICH was studied by embedding digitized hits of simulated pions into real RICH hits, i.e. analogously to tracking efficiency by track embedding described in sec. 4.5.2. In this simulation weak decay of pions was turned off. The efficiency deduced for RICH by this method is  $\sim 3\%$  for pions with momenta above  $3 \text{ GeV}/c$ . The generation of Cherenkov light does not depend on particle species but on the particle's momentum. Efficiency determined using simulated pions is therefore used also for kaons and protons.

It was found that the efficiency is not constant around the threshold but experiences a rise over a momentum range of about  $0.5 \text{ GeV}/c$ . When identifying particles corresponding ranges in momentum above the calculated momentum thresholds are considered highly inefficient and no ring in the RICH is expected.

The inefficiency of the RICH leads to mis-identification of particles. If no light ring is reconstructed for a pion going through the RICH with momentum between the pion and kaon thresholds the RICH identification algorithm concludes that the particle is either a kaon or a proton. The kaon and proton samples are therefore polluted by wrongly identified pions. In similar manner it is possible for kaons below the proton threshold to pollute the proton sample.

This feeding of mis-identified particles of certain species into the samples of other species is corrected for. Correction factors are calculated for various intervals in momentum for the different particles. The calculation of the RICH efficiency correction factors is outlined in App. B.

### PID efficiency in the forward arm

As described in sec. 4.4.4 the identity of particles that go through the full forward spectrometer is determined using information from possibly as many as three PID detectors. Therefore the effects of hodoscope and RICH efficiencies on the identified spectra obtained for the full FS have to be conjointly considered. In fact, since the identity is determined using at least one identifying detector the combined PID efficiency is as good as the best PID detector when using the full forward arm.

### 4.5.3 Multiple scattering correction

When an electrically charged particle is traversing any atomic medium it is subject to multiple elastic Coulomb scattering (MS) which deflects it from its original path and lowers its momentum. It is thus possible that particles that would have ended up within

the acceptance if there was no MS are deflected out of the acceptance window. Following the same argument some particles outside the spectrometers' acceptance may have their trajectories bent into the region of phase space covered by the spectrometers.

The effect of MS has to be corrected for. This is done in Monte-Carlo simulations by throwing pions, kaons and protons in wide angular and kinematic windows for each spectrometer setting. The angular distributions are wider than the solid angles delimited by the spectrometers.

Momenta are distributed according to a convolution of semi-realistic rapidity and  $m_T$  distributions. The rapidity distributions,  $\frac{dN}{dy}(y)$ , are taken from simulated Au+Au collisions with the HIJING model [96], while exponentials  $m_T = a \cdot \exp(-m_T/T)$  are used for the transverse kinematic components in which the effective temperature  $T$  is a linear function of  $y$ .

The trajectories of particles are fully digitized in the various sub-detectors, and simulated tracks go through the same analysis chain as the data, with matching, momentum determination and particle identification. One half of the simulations were done with MS on, and the other half with MS off. The correction factor  $\epsilon_{MS}$  is thus calculated as

$$\epsilon_{MS} = \frac{N_{MS}}{N_{\text{MS}}} \quad (4.28)$$

in which  $N_{MS}$  and  $N_{\text{MS}}$  respectively correspond to the number of tracks going through the spectrometer with and without multiple scattering. The correction is parametrized for each particle species as a function of momentum. I.e.  $N_{MS}(p)/N_{\text{MS}}(p)$  from the data is fitted with

$$\epsilon_{MS}(p) = a - b \cdot \exp(-cp) \quad (4.29)$$

Fig. 4.22 shows the obtained correction parameters at selected spectrometer settings for the MRS and the forward arm in its two modes of operation. The Coulomb scattering described by the Rutherford cross section goes as the square of the inverse energy of the particle. It is therefore the lower regions in the momentum ranges covered by BRAHMS' spectrometers that are affected by MS.

#### 4.5.4 Weak decay correction

Pions and kaons are subject to weak decay in flight through the spectrometers. Since kaons have a smaller mean lifetime than pions<sup>7</sup> a correspondingly higher correction is applied to  $K^\pm$  than to  $\pi^\pm$ . Simulations analogous to the ones used for MS corrections are performed also for the correction for weak decays. Simple estimates of correction factors in terms of the particles' mean lifetime  $\tau$  and their time of flight through the spectrometers do not take into account the possibility of decay products being identified as their mother particle.

The selected mesons are propagated through the spectrometer, with two simulation runs for each species and spectrometer setting. One run has weak decay turned off while in the other run the mesons are allowed to decay. Some selected corrections values are shown in fig. 4.23. The correction,  $\epsilon_{WD}(p) = N_{WD}(p)/N_{\text{WD}}(p)$ , being the ratio of the

---

<sup>7</sup>The mean life time for kaons is  $\tau_K = 1.2385 \cdot 10^{-8}$  s while the one for pions is  $\tau_\pi = 2.6033 \cdot 10^{-8}$  s [128].

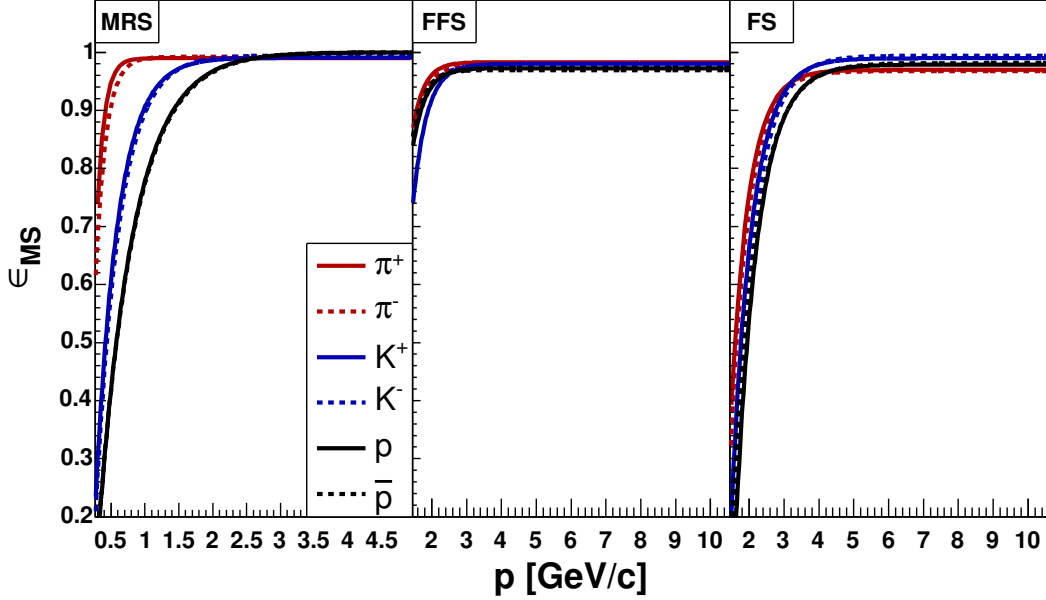


Figure 4.22: Fitted correction functions for multiple scattering. The mid-rapidity panel shows results obtained for  $90^\circ$  with D5 set at a current of 350 A and B polarity. The results for the forward arm are obtained with D1 set at 676 A, and with the FFS positioned at  $8^\circ$  and FS at  $4^\circ$ .

number of identified particles with weak decay on relative to the number with decay off is fitted with a function of the same form as eq. 4.29.

#### 4.5.5 Absorption correction

Correction simulations similar to the ones described in secs. 4.5.3 and 4.5.4 are performed to estimate the effect of absorption of  $p$  and  $\bar{p}$ . This correction is necessary due to inelastic interactions of (anti-)protons with the matter they traverse, whether it be air and other gases in the spectrometers or the beryllium beam pipe. Fig. 4.24 illustrates the absorption corrections for the settings shown in figs. 4.22 and 4.23. Once again the correction is mainly pronounced at low momentum and the fitted functional form for this correction,  $\epsilon_{ABS}(p) = N_{ABS}(p)/N_{ABS}(p)$ , is the one expressed in eq. 4.29.

#### 4.5.6 Feed-down correction

The final correction to be simulated is the contribution in the samples of pions and protons from decaying hyperons and mesons. A host of weakly decaying particles are produced in a heavy ion collision. The abundances and primary decay channels of some of them are such that they are likely to pollute the sample of primary hadrons. Their apparent temperature is not likely to coincide with the one of the primary hadrons. Without correcting for feed-down the fitted temperature and yields may be wrong.

The weakly decaying particles and corresponding channels mainly responsible for the

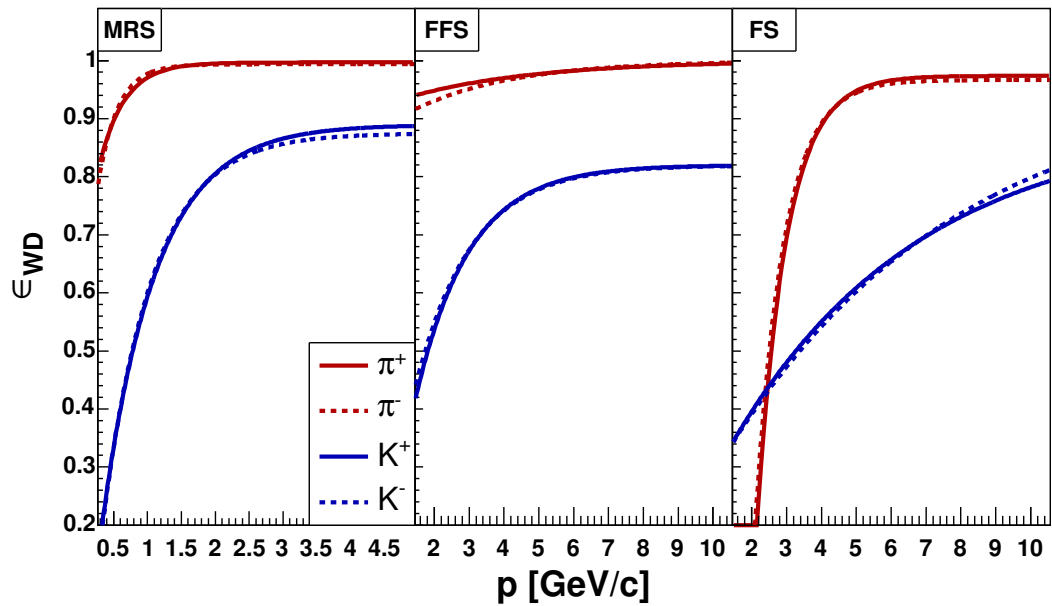


Figure 4.23: Fitted correction functions for weak decay of pions and kaons. The settings are the same as in fig. 4.22.

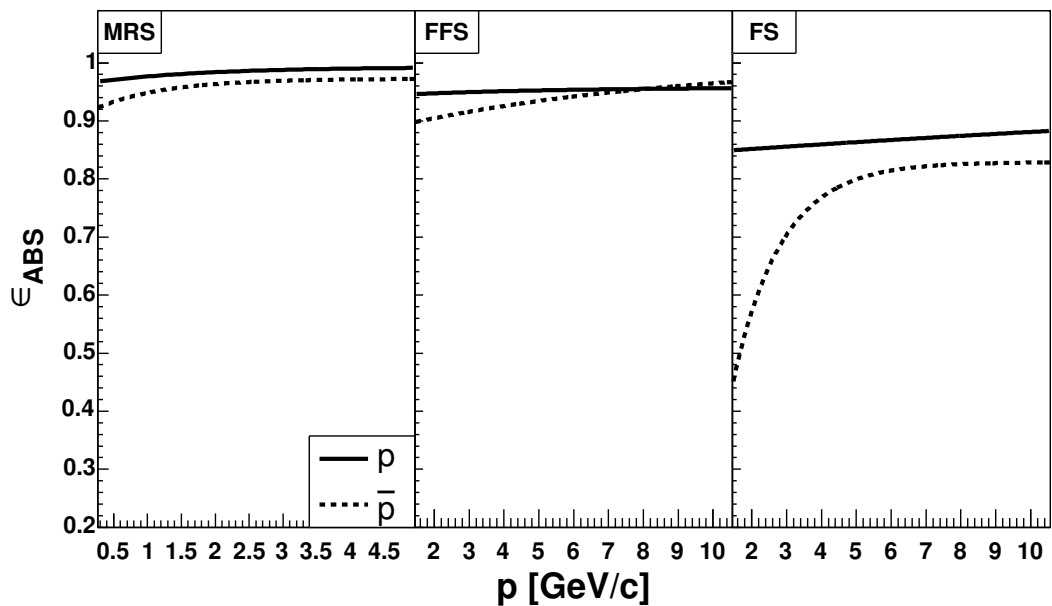


Figure 4.24: Fitted correction functions for absorption of (anti-)protons. The settings are the same as in fig. 4.24.

feed-down pollution are



with respective mean life times in terms of  $c\tau$  of 7.89 cm for  $\Lambda$  and  $\bar{\Lambda}$  and 2.68 cm for  $K_s^0$  [128]. The branching ratio for the listed  $\Lambda$  and  $\bar{\Lambda}$  decay channel is 63.9%, while the stated  $K_s^0$  has a branching ratio of 68.6%.

Other strangeness carriers, such as  $\Sigma$ ,  $\Xi$  and  $\Omega$  are not considered explicitly here. Nevertheless, the applied experimental ratios of  $\Lambda/p$  and  $\bar{\Lambda}/\Lambda$  also include feed-down from heavier hyperons, mainly  $\Sigma^0$  and  $\Xi$ . Hence the included corrections account for feed-down from primary and secondary  $\Lambda$ s. Contribution from  $\Sigma^+ \rightarrow p + \pi^0$  is not addressed in this analysis.

Monte-Carlo simulations for feed-down correction are carried out in similar manner as for the acceptance correction described in sec. 4.5.1. In this study semi-realistic distributions of  $\Lambda$  and  $K_s^0$  are thrown in a general direction of the spectrometer arms for various spectrometer settings. I.e. distribution in solid angle has to be wide enough to account for the possible opening angles of weak decays. Similar semi-realistic distributions of the corresponding primary charged hadrons ( $p$  and  $\pi^\pm$ ) are thrown in exactly the same region of phase space, for comparison.

The longitudinal kinematics follow a double Gaussian parametrization of  $dN/dy$  obtained from HIJING. In the transverse direction the thrown particles follow a thermal  $p_T$  distribution with an  $y$ -dependent inverse slope  $T$ . The functional behavior of  $T(y)$  for charged pions and kaons is taken from [123] and [97] for protons. It is assumed that the effective temperatures of  $K_s^0$ ,  $\Lambda$  and  $\bar{\Lambda}$  follow the ones of  $K^\pm$ ,  $p$  and  $\bar{p}$ , respectively.

The thrown particles are digitized in BRAG and reconstructed in the usual framework described earlier in this chapter. A significant fraction of decay products are discarded in the applied cuts. Especially cutting on the origin of the track, i.e. around the primary vertex, removes a large fraction of decay pions whose angle relative to their mother particle is larger than the angle of protons from the decay of  $\Lambda$ s.

Correction factors are determined as the number of secondary particles relative to the sum of primaries and secondaries and investigated as a function of transverse momentum. E.g. the ratio  $\pi^-$  from the decay of  $K_s^0$  relative to the total number of negative pions is determined as

$$r_{FD}^{K_s^0 \rightarrow \pi^-}(p_T) = \frac{CN_{r,2}^{\pi^-}(p_T)}{N_{r,1}^{\pi^-}(p_T) + CN_{r,2}^{\pi^-}(p_T)} \quad (4.33)$$

Here  $N_{r,1}^{\pi^-}(p_T)$  and  $N_{r,2}^{\pi^-}(p_T)$  correspond to the numbers of reconstructed primary and secondary negative pions in the given bin of transverse momentum. The factor  $C$  takes care of normalization with respect to the number of thrown  $K_s^0$  and primary  $\pi^-$ , i.e.  $N_t^{K_s^0}$  and  $N_t^{\pi^-}$  respectively.  $C$  also takes care of the empirical or modelled relative abundance of  $K_s^0$  and  $\pi^-$  in terms of their respective rapidity densities  $dN_{K_s^0}/dy$  and  $dN_{\pi^-}/dy$  integrated over the rapidity range corresponding to a given spectrometer setting. Thus,  $C$  is

calculated for each spectrometer setting as

$$C = \frac{N_t^{\pi^-}}{N_t^{K_s^0}} \cdot \frac{\int \frac{dN_{K_s^0}}{dy} dy}{\int \frac{dN_{\pi^-}}{dy} dy} \quad (4.34)$$

The ratio  $r_{FD}^{K_s^0 \rightarrow \pi^-}(p_T)$  accounts for the relative number of  $K_s^0$  decay products ending up in the spectrum of all negative pions. The relative number of primary  $\pi^-$ ,  $n_{r,1}^{\pi^-}$ , is obtained from the sum of primary and secondary ( $n_{r,2}^{\pi^-}$ ) pions and  $r_{FD}^{K_s^0 \rightarrow \pi^-}$  according to

$$\frac{n_{r,1}^{\pi^-}}{n_{r,1}^{\pi^-} + n_{r,2}^{\pi^-}} = \frac{n_{r,1}^{\pi^-} + n_{r,2}^{\pi^-} - n_{r,2}^{\pi^-}}{n_{r,1}^{\pi^-} + n_{r,2}^{\pi^-}} = 1 - r_{FD}^{K_s^0 \rightarrow \pi^-} \quad (4.35)$$

Here the lower case  $n_{r,i}^{\pi^-}$  includes the normalization of the  $N_{r,i}^{\pi^-}$  in eq. 4.33 so that  $n_{r,1}^{\pi^-} = N_{r,1}^{\pi^-}$  and  $n_{r,2}^{\pi^-} = CN_{r,2}^{\pi^-}$ . In terms of the correction factor  $\epsilon_{FD}^{K_s^0 \rightarrow \pi^-}$  to be applied to the negative pions we get

$$n_{r,1}^{\pi^-} = (n_{r,1}^{\pi^-} + n_{r,2}^{\pi^-}) (1 - r_{FD}^{K_s^0 \rightarrow \pi^-}) = \frac{n_{r,1}^{\pi^-} + n_{r,2}^{\pi^-}}{\epsilon_{FD}^{K_s^0 \rightarrow \pi^-}} \quad (4.36)$$

$$\Downarrow \quad \epsilon_{FD}^{K_s^0 \rightarrow \pi^-} = \frac{1}{1 - r_{FD}^{K_s^0 \rightarrow \pi^-}} \quad (4.37)$$

The calculations of contribution from  $\Lambda$  and  $\bar{\Lambda}$  to the samples of  $\pi^\pm$ ,  $p$  and  $\bar{p}$  follow analogously. At RHIC energies inclusive measurements of  $\Lambda/p \sim 40.9$  is obtained at mid-rapidity [129] and the HIJING parametrization mentioned above is used for the ratio at higher rapidity. Using the thermal model ansatz  $\bar{\Lambda}/\Lambda \approx \bar{p}/p \cdot K^+/K^-$  [130] the ratio of  $\bar{\Lambda}$  to  $\bar{p}$  is calculated as  $\bar{\Lambda}/\bar{p} = \Lambda/p \cdot \bar{\Lambda}/\Lambda \cdot p/\bar{p} = \Lambda/p \cdot K^+/K^-$  with kaon ratio determined from [123]. It is further assumed that the rapidity dependence of neutral kaons relative to pions go as  $K_s^0/\pi \approx 0.5 \cdot (K^+ + K^-)/\pi \approx 0.14 - 0.15$  according to [123]. More in-depth description of the procedure to calculate feed-down corrections may be found in [131].

It was found that (anti-)lambda contribute  $r_{FD}^{\Lambda \rightarrow \pi} \lesssim 1 - 2\%$  in the pion spectra. This contribution is deemed insignificant in comparison to the overall error and hence not corrected for in the final results.

Various calculated corrections are shown in fig. 4.25. The corrections used in the subsequent analysis are averaged values. I.e. one correction function is fitted for each spectrometer and each of the decay channels  $\Lambda \rightarrow p + \pi^-$ ,  $\bar{\Lambda} \rightarrow \bar{p} + \pi^+$  and  $K_s^0 \rightarrow \pi^+ + \pi^-$ .

The general picture indicate the correction factors for  $\Lambda$  and  $\bar{\Lambda}$  contributions in the (anti-)proton data around  $r_{FD}^{\Lambda \rightarrow p} \sim 35 - 45\%$ , i.e. decreasing with increasing transverse momentum. The obtained correction for  $K_s^0$  feeding the spectra of  $\pi^\pm$  are constants around  $r_{FD}^{K_s^0 \rightarrow \pi^\pm} \sim 4 - 5\%$ .

## 4.6 Spectrum projection

The previous steps of analysis generate two-dimensional corrected differential yields in  $(y, p_T)$  for each vertex bin in every spectrometer setting considered. There are eight

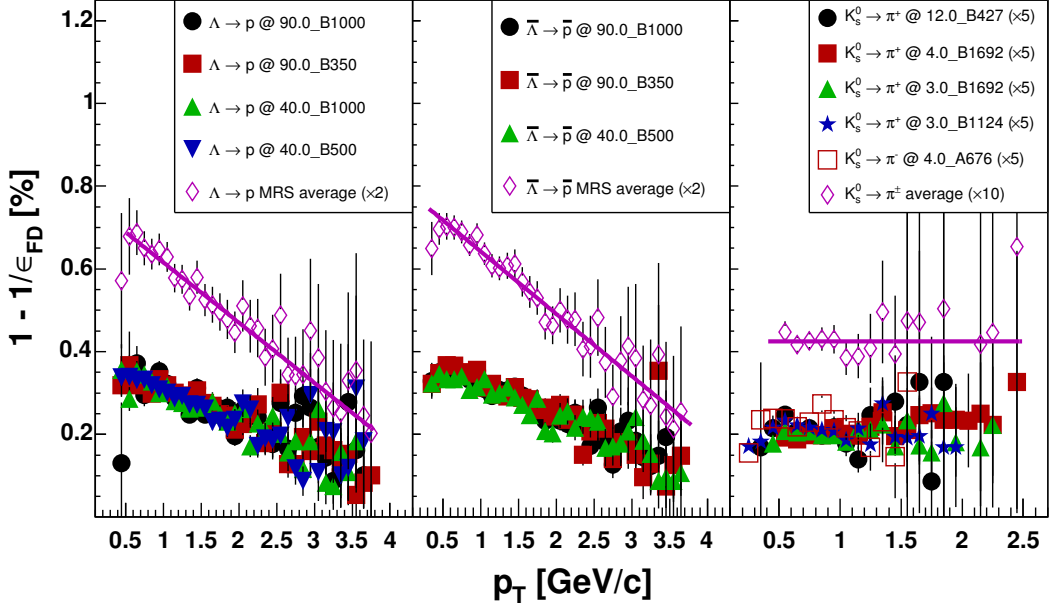


Figure 4.25: Calculated feed-down correction factors as a function of transverse momentum for MRS  $p$  and  $\bar{p}$  contributions from  $\Lambda$  (left) and  $\bar{\Lambda}$  (middle) respectively, and  $\pi^\pm$  contributions from  $K_s^0$  in the FS. Results for various spectrometer settings are averaged as indicated. The corrections to  $p$  and  $\bar{p}$  are fitted with a first order polynomial while the  $\pi^\pm$  corrections are fitted with a constant value since no  $p_T$  dependence was observed.

vertex bins for each spectrometer setting in the forward arm and six vertex bins for the mid-rapidity spectrometer settings. The width of the vertex bins are  $\Delta(z) = 5$  cm. Results obtained for each vertex bin and spectrometer setting covering the same region of phase space are combined. The individual differences between measurements in the same kinematic window provide an estimate for the systematic error of the results shown in ch. 5 and are discussed further in sec. 4.7.

#### 4.6.1 Correction and normalization

The goal of the analysis presented in this chapter is to obtain identified particle normalized invariant spectra of the form

$$f(p_T) = \frac{1}{2\pi N_{ev}} \frac{1}{p_T} \frac{d^2N}{dy dp_T} \quad (4.38)$$

where  $N_{ev}$  is the number of events and all corrections described in sec. 4.5 are taken into account.

The correction factors may be applied to the data at different stages in the analysis. Corrections depending on track parameters such as momentum and the horizontal position and slope in the tracking detectors are applied when filling the  $(y, p_T)$  histograms. Applying the momentum dependent corrections at this level limits the systematical errors introduced by discrete binning of the data in  $(y, p_T)$  space. For the same reason

division by  $p_T$  is done at the same stage, and so is PID efficiency corrections. Only acceptance correction together with normalization to the number of events are applied after the two-dimensional differential yields are obtained.

The value for each bin in the two-dimensional histogram for setting  $s$  and vertex bin  $v$  corresponds to the number of particles in the bin with rapidity  $y$  and transverse momentum  $p_T$  divided by  $p_T$ . All corrections but acceptance are applied. Hence every histogram contains values of

$$\mathbf{n}^{s,v}(y, p_T) = \frac{n_{\epsilon}^{s,v}(y, p_T)}{p_T \prod_i \epsilon_i(y, p_T)} = \frac{n^{s,v}(y, p_T)}{p_T} \quad (4.39)$$

Here  $n_{\epsilon}(y, p_T)$  is the uncorrected (raw) number of particles with rapidity  $y$  and transverse momentum  $p_T$  and  $\epsilon_i$  represent the various corrections applicable for each particle species excluding the acceptance correction  $\epsilon_a$ . The bold notation is used to indicate that the effective number of tracks before acceptance correction,  $n^{s,v}$ , is divided by  $p_T$ . In order to obtain normalized invariant spectra of the form described by eq. 4.38 correction histograms for each vertex bin and setting,  $c^{s,v}(y, p_T)$ , are defined as

$$c^{s,v}(y, p_T) = \frac{1}{2\pi N_{ev}^{s,v} \epsilon_a^{s,v}(y, p_T) \Delta(y) \Delta(p_T)} \quad (4.40)$$

Here  $\Delta(y)$  and  $\Delta(p_T)$  describe the width of the rapidity and transverse momentum bins, respectively. Thus, the fully corrected and normalized differential yields from which invariant spectrum for setting  $s$  and vertex bin  $v$  may be projected come out as

$$\mathbf{N}^{s,v}(y, p_T) = \mathbf{n}^{s,v}(y, p_T) \cdot c^{s,v}(y, p_T) \quad (4.41)$$

#### 4.6.2 Combination of vertex bins

The results obtained for each vertex bin in a spectrometer setting cover similar windows in  $(y, p_T)$  space and are therefore combined by weighted average. I.e. the result obtained for a given setting may be calculated as

$$\mathbf{N}^s(y, p_T) = \frac{\sum_v \mathbf{N}^{s,v}(y, p_T) \cdot w^{s,v}(y, p_T)}{\sum_v w^{s,v}(y, p_T)} \quad (4.42)$$

where  $w^{s,v}(y, p_T)$  describes the weight for vertex bin  $v$ . The choice for this weight is

$$w^{s,v}(y, p_T) = \frac{1}{c^{s,v}(y, p_T)} \quad (4.43)$$

Hence, the vertex and  $(y, p_T)$  bins with the largest correction component from acceptance and normalization to number of events, eq. 4.40, bear the least weight. Choosing the weight as the inverse of the correction has the benefit of simplifying the weighted average. By using eqs. 4.41 and 4.43 in eq. 4.42 the differential yield for a given setting is expressed as

$$\mathbf{N}^s(y, p_T) = \left( \sum_v \mathbf{n}^{s,v}(y, p_T) \right) \cdot \left( \sum_v \frac{1}{c^{s,v}(y, p_T)} \right)^{-1} \quad (4.44)$$

### 4.6.3 Combination of spectrometer settings

As for the various vertex bins for a given setting several settings typically cover the same range in  $(y, p_T)$  space and are combined by weighted average once more. That is

$$\mathbf{N}(y, p_T) = \frac{\sum_s \mathbf{N}^s(y, p_T) \cdot w^s(y, p_T)}{\sum_s w^s(y, p_T)} \quad (4.45)$$

The choice of weight  $w^s(y, p_T)$  comes from the last term in eq. 4.44, which may be interpreted as an effective correction for setting  $s$ . Therefore

$$w^s(y, p_T) = \frac{1}{c^s(y, p_T)} = \sum_v \frac{1}{c^{s,v}(y, p_T)} \quad (4.46)$$

Using eqs. 4.44 and 4.46 in eq. 4.45 the differential yields in  $(y, p_T)$  from the combination of settings and their vertex bins is expressed as

$$\mathbf{N}(y, p_T) = \left( \sum_s \sum_v \mathbf{n}^{s,v}(y, p_T) \right) \cdot \left( \sum_s \sum_v \frac{1}{c^{s,v}(y, p_T)} \right)^{-1} \quad (4.47)$$

### 4.6.4 Average over rapidity bins

At this stage the content of each bin in  $N(y, p_T)$  contains the value of

$$\mathbf{N}(y, p_T) = \frac{1}{2\pi N_{ev}} \frac{1}{p_T} \frac{n(y, p_T)}{\Delta(y)\Delta(p_T)} \quad (4.48)$$

averaged over spectrometer settings and their vertex bins. It is desirable to obtain invariant spectra with good statistics for several selected values of rapidity, as shown in ch. 5. Thus multiple bins in rapidity around the selected  $y$  values are combined by weighted average. Following the arguments of secs. 4.6.2 and 4.6.3 the spectrum values  $\mathbf{N}(p_T)$  are obtained as

$$\mathbf{N}(p_T) = \frac{\sum_y \mathbf{N}(y, p_T) \cdot w(y, p_T)}{\sum_y w(y, p_T)} \quad (4.49)$$

$$= \left( \sum_y \sum_s \sum_v \mathbf{n}^{s,v}(y, p_T) \right) \cdot \left( \sum_y \sum_s \sum_v \frac{1}{c^{s,v}(y, p_T)} \right)^{-1} \quad (4.50)$$

## 4.7 Systematic errors

In this analysis systematic errors have been estimated from the data. Two main sources of systematic errors are considered. One component is attributed to the errors introduced by wrong normalization and the various corrections described in sec. 4.5. The other contribution is a result of the chosen fit function.

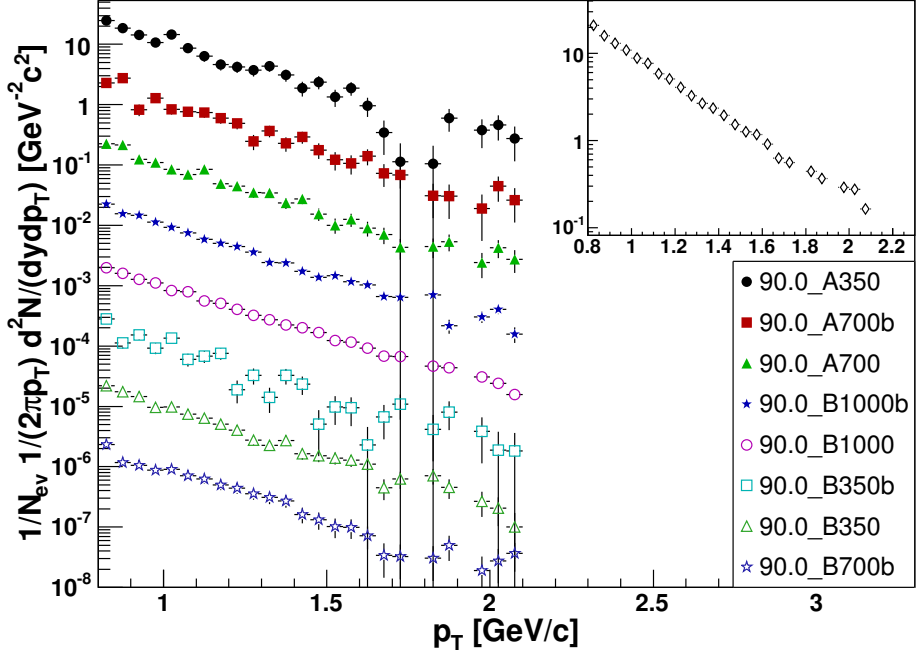


Figure 4.26: Invariant  $p_T$  spectrum values obtained for negative pions around  $y = 0$  all scaled by 0.1 relative to the spectrum above. The small panel is the weighted average of the spectra at each setting, for which the weight of each bin is the inverse statistical error. Only  $p_T$  bins where all settings have non-zero values are shown.

#### 4.7.1 Setting dependent errors

At various regions of phase space BRAHMS has redundant measurements. The variation in results obtained for the individual settings provides an estimate for errors occurring due to normalization to number of events as well as corrections for decay, absorption, feed-down, multiple scattering, geometric acceptance and detector efficiency.

It is assumed that the systematic error is of the same relative order of magnitude for the different species. For this reason pions are used for the error estimation since their relative statistical error is much smaller than for kaons and protons. At a given setting pions typically outnumber kaons and protons by an order of magnitude and the estimation of systematic error is less affected by the sometimes high statistical errors.

Consider the region around  $y = 0$ . The results presented in ch. 5 are obtained from 8 different settings. Some settings correspond to low magnetic fields and thus populate the low end of the spectra in sec. 5.1. Other settings with higher magnetic fields provide most of the population at high transverse momenta. There is, however, a certain range in  $p_T$  in which a high number of settings, possibly all, contribute. By comparing the spectrum values for bins in this intermediate  $p_T$  range the setting dependent errors are estimated.

First invariant spectra are obtained for the different settings. Following this step a weighted average spectrum is constructed analogously to the procedure outlined in sec. 4.6.3. Fig. 4.26 shows the invariant  $p_T$  spectra obtained for negative pions in the rapidity range  $y \in [-0.05, 0.05]$ .

By excluding one setting from the calculation of the weighted average and thereafter

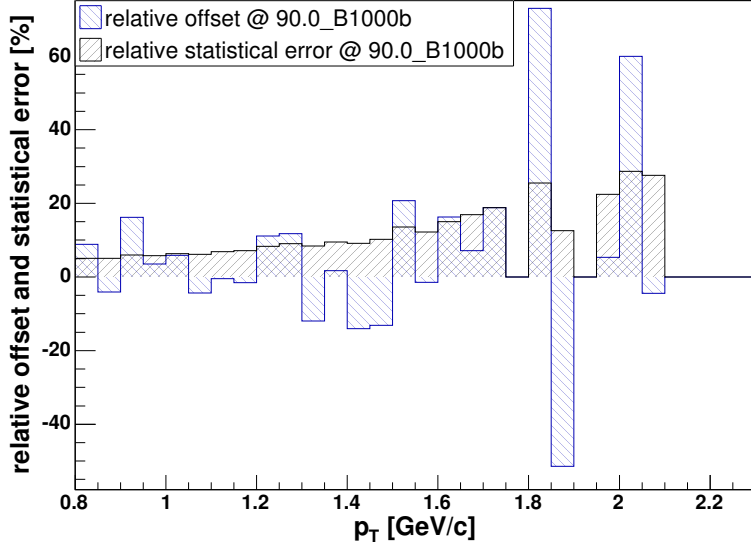


Figure 4.27: The relative offset of negative pion  $p_T$  spectrum calculated for setting 90.0\_B1000b relative to the weighted average calculated without using this setting. Also shown is the relative statistical error of this setting. For this particular setting the systematic error in the high end, the region where inclusive PID is performed, is large compared to the low end. Yet the average systematic uncertainties as calculated with eq. 4.51 in the high  $p_T$  region is (only)  $\lesssim 20\%$ .

plotting the difference between this average spectrum and the one for the excluded setting one may get an idea of the systematic error. Fig. 4.27 shows the relative difference between the spectrum for positive pions in setting 90.0\_B1000b and the average calculated without data from this setting. For comparison the distribution of relative difference is overlaid with the setting's distribution of statistical errors.

Fig. 4.27 and similar plots for other settings around  $y=1$  and  $y=3$  shows that the relative offset scales rather well with the content in each  $p_T$  bin. The increase for the higher  $p_T$  range is typically attributed to an increase in the statistical error. The systematic error is therefore based on calculations according to

$$\epsilon_{sys} = \frac{\sum_i \sqrt{\delta_i^2 - \epsilon_{stat,i}^2}}{n} \quad (4.51)$$

Here the index  $i$  corresponds to each of the  $n$  bins in the  $p_T$  range with overlap between the various settings.  $\epsilon_{sys}$  and  $\epsilon_{stat}$  refer to systematic and statistical errors, respectively.  $\delta$  is the difference between the setting under consideration and the weighted average spectrum, as shown in the rear plot of fig. 4.27. For this estimation to work the settings with the fewest number of counts are not used since for those data sets the statistical error is often too large.

In the MRS this systematical error contribution is estimated to 15%. An additional 5% is estimated for the high  $p_T$  region in which inclusive identification (sec. 4.4.2) is applied. The error estimated for FS is somewhat higher, i.e. consistent with 20%. This value is also used at  $y=2$  since very few overlapping bins in the invariant spectra exist

at this rapidity. These estimated systematic errors are added in quadrature with the statistical errors for each bin in  $p_T$  or  $m_T$  spectra before they are fitted as described in sec. 5.2.

#### 4.7.2 Errors from fits

In order to deduce rapidity densities it is necessary to fit chosen functions to the invariant spectra of identified particles as described in sec. 5.2. Following the fit procedure the rapidity densities are in most cases obtained by integrating the fitted functions<sup>8</sup>. The choice of fit function, and especially the degree to which it describes a spectrum at the low end, has some impact on the obtained extrapolated yield.

By comparing the integral values for the chosen fit function to the result obtained with other functions used in the field, additional systematic errors are included in the obtained  $dN/dy$ . All species are compared to exponentials in  $p_T$  and  $m_T$ . In addition pions are fitted with a power law function in  $p_T$  and protons are fitted with a Boltzmann function in  $m_T$  as well as Gaussian in  $p_T$ . The systematic errors from choice of fit function are added in quadrature to the errors already present from statistical uncertainties and differences among settings. Added fit errors range from 1 to 8% depending on the particle species and rapidity.

---

<sup>8</sup>Some fit functions like Gaussians and exponentials in  $m_T$  provide the rapidity density without integration since it may be chosen to be a fit parameter.



# Chapter 5

## Results

Using the hardware components described in ch. 3 and analysis software whose principles are outlined in ch. 4 invariant spectra of identified particles are obtained and further results are derived from these data. In this chapter are presented the invariant spectra of  $\pi^\pm$ ,  $K^\pm$ ,  $p$  and  $\bar{p}$  in the 10% most central Au+Au collisions at  $\sqrt{s_{NN}} = 200 \text{ GeV}$ . This event centrality corresponds to an average number of participants  $N_{part} = 328 \pm 6$  as estimated by HIJING [132]. Functional fits to the spectra are described and extrapolated yields, temperature as well as derived results for the transverse kinematics are shown. Unless otherwise noted the plots show statistic and systematic errors. In ch. 6 these results are discussed in terms of various results from BRAHMS and other experiments as well as to model pre- and postdictions.

### 5.1 Invariant spectra

Invariant spectra are projected as described in sec. 4.6 from differential yields in  $(y, p_T)$  or  $(y, m_T - m)$ . In fig. 5.1 the obtained differential yields in  $(y, m_T - m)$  divided by  $m_T$  for the combination of all spectrometer settings are shown. I.e. the result after the step depicted in sec. 4.6.3.

From two-dimensional histograms invariant spectra are projected according to the recipe of sec. 4.6.4. The spectra in fig. 5.2 are obtained from rapidity windows of width  $\Delta(y) = 0.1$  for all particle species in the MRS. Spectra of pions and kaons presented for  $y = 3$  are generated from bins in a rapidity window  $\Delta(y) = 0.1$  around the central rapidity while for (anti-)protons a rapidity window  $\Delta(y) = 0.2$  was deemed necessary to have sufficient statistics.

The results around  $y = 2$  are treated in a distinct manner. No pion data exist exactly at this intermediate  $y$  value. Therefore spectra for  $\pi^\pm$  are generated using data in the range  $y \in [2.1, 2.2]$ . Similarly for kaons there is little data just below  $y = 2$ . The spectra presented here are hence combined from data at rapidities  $y \in [2.0, 2.2]$ . Spectra for  $p$  and  $\bar{p}$  around  $y = 2$  are obtained in the range  $y \in [1.9, 2.1]$ .

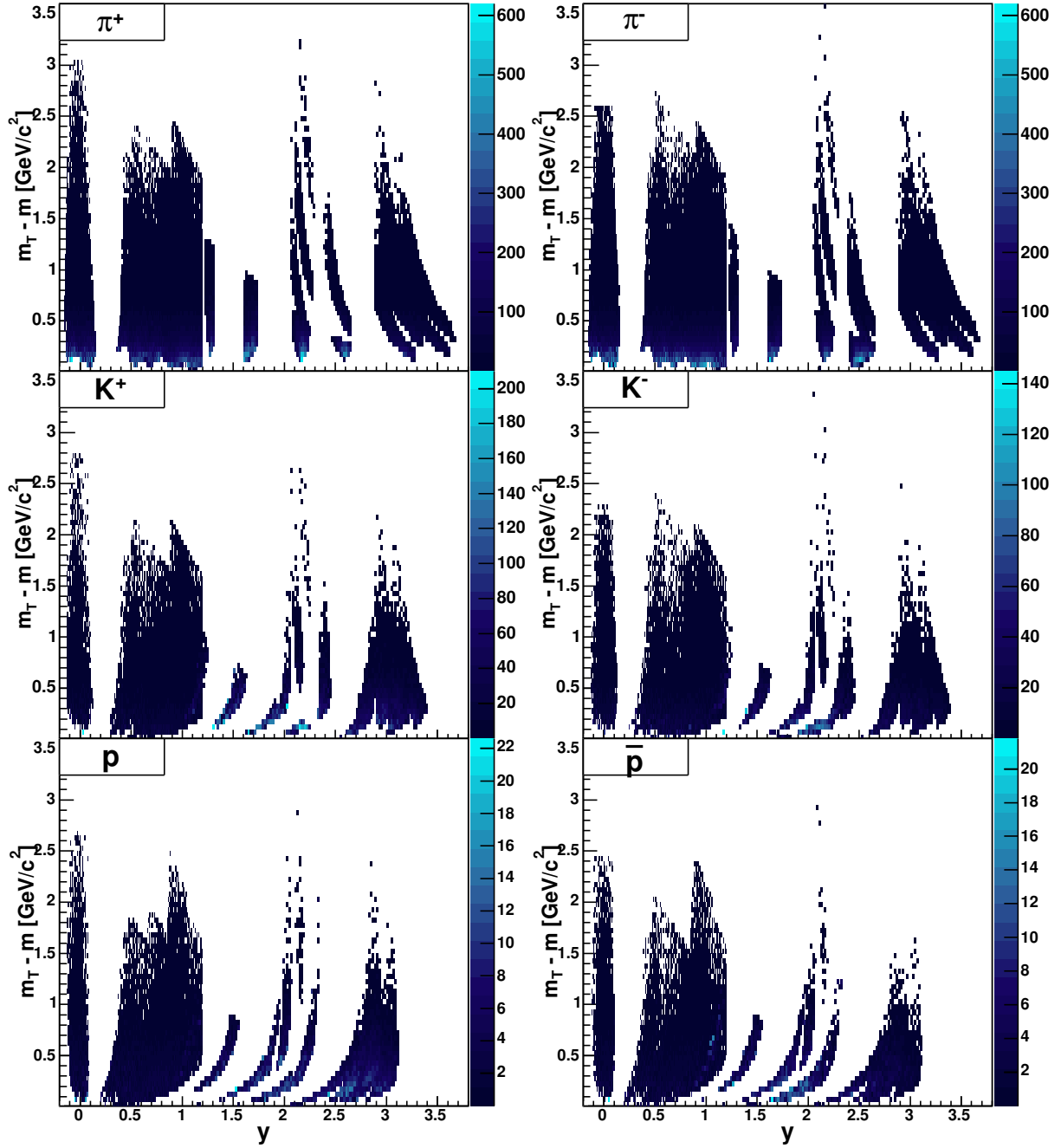


Figure 5.1: Two-dimensional differential yields as obtained with BRAHMS' spectrometers for  $\pi^\pm$ ,  $K^\pm$ ,  $p$  and  $\bar{p}$  in the 10% most central Au+Au collisions at  $\sqrt{s_{NN}} = 200 \text{ GeV}$ . The segmentation for the MRS data, i.e. roughly the first unit in rapidity, is higher than for the FS data due to higher statistics collected with the mid-rapidity spectrometer.

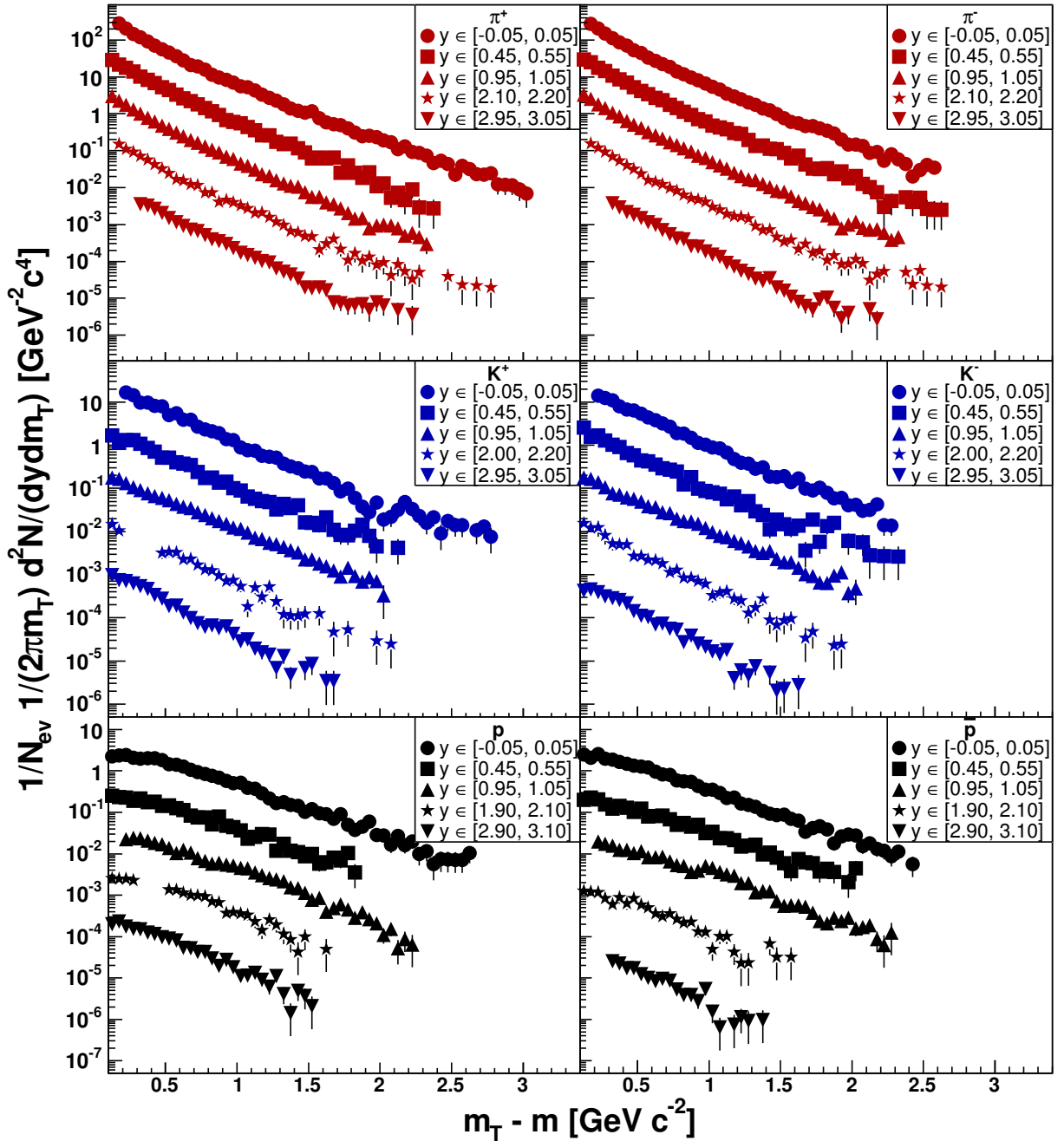


Figure 5.2: Invariant  $m_T$  spectra obtained for the 10% most central Au+Au collisions at  $\sqrt{s_{NN}} = 200$  GeV around rapidities  $y = 0, 0.5, 1, 2$  and  $3$ . For clarity the spectra are scaled by  $10^0, 10^{-1}, 10^{-2}, 10^{-3}$  and  $10^{-4}$ , respectively.

## 5.2 Fits to spectra

The ranges of the spectra shown in fig. 5.2 are limited by the acceptance of the spectrometers. The regions outside of the covered acceptance may be extrapolated by assuming some parametrization which also describes the spectra within the acceptance. By introducing fit functions to describe the low and high ends of the spectra one effectively introduces some model dependence in the results obtained from function integration. This dependence and enclosed systematic uncertainty is taken into account in the overall systematics (sec. 4.7).

A host of fit functions exist in the literature. Exponentials in  $p_T$  or  $m_T$  stem from the assumed thermal distribution for the transverse degrees of freedom and are typically able to describe the soft parts of the spectra. The high end of the spectra, in particular the pion spectra, are well described by power law in  $p_T$  since this range has contributions from hard scattering described by pQCD. The Boltzmann distribution describing emission from a classical thermalized source is sometimes preferred typically for protons.

Yet, one of the earliest results from Au+Au collisions at  $\sqrt{s_{NN}} = 130$  GeV at RHIC showed the existence of strong transverse flow in central collisions [133]. In the presence of transverse flow the invariant  $p_T$  and  $m_T$  spectra are flattened, in reality enhancing the effective temperature as determined with exponential fit functions.

Also, transverse flow affects the exponential fit effective temperatures for the heavier particles more than it does for the lighter ones [30]. Results obtained at the AGS confirm this tendency for  $\pi$ ,  $K$  and  $p$  [134]. One may approximate the mass dependence by the relation  $\langle E \rangle \approx \langle E_{th} \rangle + \frac{1}{2}mv_{flow}^2$ . I.e. the energy  $\langle E \rangle$  is roughly a linear function of the particle mass with gradient equal to the squared flow velocity. The thermal energy,  $\langle E_{th} \rangle$ , is determined from the intercept with the ordinate axis.

In order to incorporate flow effects the spectra are fitted according to the directions in [22]. This hydro-inspired parametrization, often referred to as a blast-wave parametrization, takes into account possible flow contributions both in the longitudinal and transverse direction. The expansion velocity in the transverse direction is assumed to have a profile parametrized as a function of transverse radius  $r$  according to

$$\beta_r(r) = \beta_s \left( \frac{r}{R} \right)^n \quad (5.1)$$

in which  $\beta_s$  is the velocity of the surface of the expanding medium and  $R$  is its transverse geometric radius at freeze-out. A transverse boost angle is defined as  $\rho = \tanh^{-1} \beta_r$ . The resulting invariant  $m_T$  spectrum for particle species  $i$  is expressed as

$$\frac{dN_i}{m_T dm_T} = C_i \int_0^R r dr m_T I_0 \left( \frac{p_T \sinh \rho}{T} \right) K_1 \left( \frac{m_T \cosh \rho}{T} \right) \quad (5.2)$$

In this expression  $T$  is the thermal freeze-out temperature and  $I_0$  and  $K_1$  are modified Bessel functions<sup>1</sup>.  $C_i$  is a normalization constant.

The blast-wave parametrization implies that the invariant spectra of various particle species may be fitted simultaneously since their transverse expansion is described by a

---

<sup>1</sup>The modified Bessel functions are expressed as  $I_0(z) = (2\pi)^{-1} \int_0^{2\pi} e^{z \cos \phi} d\phi$  and  $K_1(z) = \int_0^\infty \cosh y e^{-z \cosh y} dy$ .

y	0	0.5	1	2	3
$T$ [MeV]	$111.1 \pm 1.6$	$104.4 \pm 1.8$	$96.5 \pm 1.3$	$117.0 \pm 3.2$	$129.9 \pm 3.0$
$\beta_s$	$0.80 \pm 0.01$	$0.80 \pm 0.01$	$0.81 \pm 0.01$	$0.75 \pm 0.02$	$0.52 \pm 0.04$
$n$	$0.95 \pm 0.08$	$0.80 \pm 0.07$	$0.66 \pm 0.07$	$0.94 \pm 0.17$	$0.01 \pm 0.14$
$R$ [fm]	$27.9 \pm 1.8$	$30.4 \pm 2.4$	$31.2 \pm 2.0$	$14.3 \pm 1.6$	$14.4 \pm 1.2$

Table 5.1: Fit parameters obtained with blast-wave fit to  $m_T$  spectra. In the fit procedure it was required that  $T$  and  $n$  be positive and  $\beta_s$  was limited to the physically relevant range of  $[0, 1]$ .

common transverse surface velocity  $\beta_s$  and they are all thermally frozen out at the same temperature  $T$ . Therefore a fit procedure is developed in which the invariant spectra of  $\pi^\pm$ ,  $K^\pm$ ,  $p$  and  $\bar{p}$  leaving the reaction zone at the same rapidity are all fitted according to eq. 5.2. This entails a fit with 10 parameters, i.e.  $T$ ,  $\beta_s$ ,  $n$  and  $R$  from eqs. 5.1 and 5.2 as well as an overall normalization factor for each particle species involved.

As pointed out in [22] the decay contributions feeding into the various particle spectra obtained may alter the picture of only one possible fit pair  $(T, \beta_s)$ . Only corrections from feed-down of weakly decaying particles are included in this analysis. No strong or electromagnetic decay corrections have been applied which e.g. could take into account contributions from  $\rho$ s and  $\Delta$ s in the pion spectra. Hence the determination of the best  $(T, \beta_s)$  as well as the integrated rapidity densities may be affected by this discrepancy. The obtained extrapolated yields are on the low side of what one would obtain if the these additional corrections could be applied.

Fitting is performed in the ROOT software framework [125] using the minimum  $\chi^2$  method. The obtained fit results are shown in fig. 5.3 where the ranges of the shown functions indicate the applied fit ranges.

In an analogous manner the obtained  $p_T$  spectra may be fitted within the blast-wave context, with the same outcome as in the above parametrization.

The fit parameters  $T$ ,  $\beta_s$ ,  $n$  and  $R$  obtained in the fit procedure above are tabulated in tab. 5.1. The thermal freeze-out temperature is around 100 MeV for  $y < 2$  and increases to 130 MeV around rapidity 3. The surface expansion velocity is rather steady around 0.8 in the range from  $y = 0$  all the way up to  $y = 2$  before decreasing in the far forward region reaching  $\beta_s \sim 0.5$  at  $y \sim 3$ .

As pointed out in [135] the power law profile of the expansion velocity implicates that the geometric radius  $R$  does not influence on the shape of the spectra but only on the absolute normalization for a constant  $C_i$ . Consequently  $R$  is not well determined by the fit procedure. Different fixed values of  $R$  were attempted without significant change neither in the other fit parameters nor in extrapolated yields (sec. 5.3).

Also  $n$  in eq. 5.1 is not so well determined in blast-wave fits [135]. This may be argued from the obtained  $n$  whose relative fit uncertainty increases in significant manner with increasing rapidity. Hence, the spectra have been fitted with fixed values on  $n$ . The three remaining parameters that are tabulated in tab. 5.1 show little dependence on  $n$ , as listed in tab. 5.2. One exception here is at the very forward region around  $y = 3$ , where the value of  $\beta_s = 0.66$  obtained with fixed  $n$  is somewhat larger than the value of 0.52 for  $\beta_s$

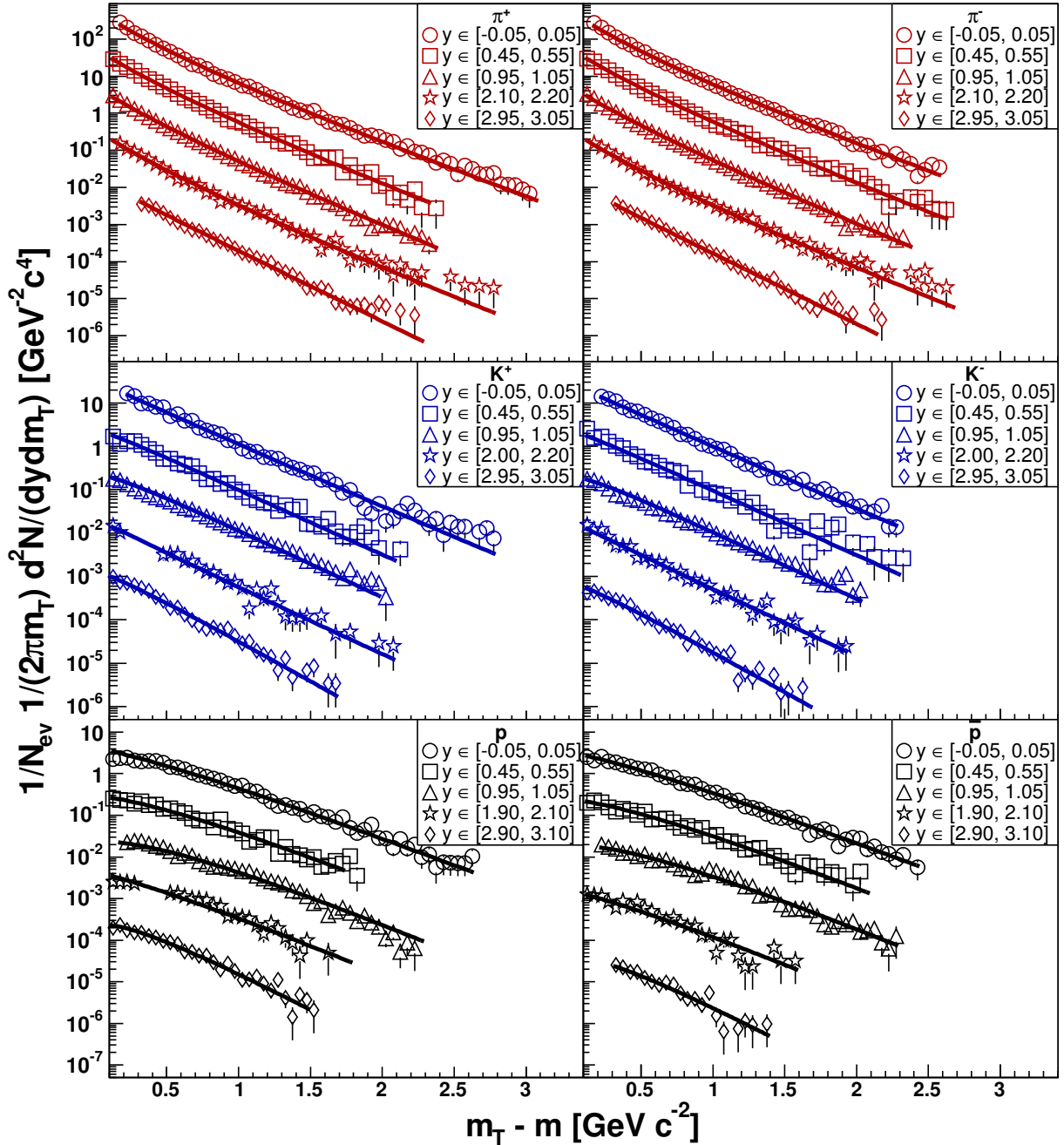


Figure 5.3: Invariant  $m_T$  spectra for the 10% most central Au+Au collisions at  $\sqrt{s_{NN}} = 200 \text{ GeV}$  fitted with blast-wave parametrization [22]. The ranges of the functions shown in the figure indicate the ranges applied in the fit procedure. Spectra and fit functions are scaled as in fig. 5.2.

y	0	0.5	1	2	3
$T$ [MeV]	$112.3 \pm 1.7$	$104.4 \pm 1.8$	$95.8 \pm 2.1$	$118.4 \pm 3.5$	$125.2 \pm 3.4$
$\beta_s$	$0.79 \pm 0.01$	$0.80 \pm 0.01$	$0.82 \pm 0.01$	$0.73 \pm 0.01$	$0.66 \pm 0.02$
$R$ [fm]	$27.0 \pm 1.9$	$30.3 \pm 2.6$	$18.4 \pm 2.1$	$16.0 \pm 2.0$	$15.7 \pm 1.9$

Table 5.2: Resulting blast-wave fit parameters after fixing  $n$  at 0.81. The requirement of positive  $T$  and  $\beta_s$  limited to the range of  $[0, 1]$  was applied in the fit algorithm.

with freely varying  $n$ . Note, however, that the discrepancy between the fixed value of  $n=0.81$  and the fitted value of  $n$  is largest at this rapidity.

The value of  $n$  does in particular affect the concavity of the blast-wave parametrization function at the low end and subsequently has significant impact on the integrated rapidity densities. The effect of  $n$  is illustrated in fig. 5.4 in terms of the obtained fit functions for positive pions, kaons and protons around  $y=1$ .

As can be seen the various values of  $n$  have different impact on the functional behavior depending on the particle species. In addition to modifications of the functional concavity the overall fit functions of the heavier particles are altered also at higher  $m_T - m$ . Fig 5.4 shows qualitatively that the proton fit function for  $n$  fixed at 1.5 is shifted to higher ordinate values relative to the other proton fits. The pion fit functions appears to have a more regular dependence on  $n$  than the protons.

The choice of fit function is in particular guided by its ability to describe the spectra in the low kinematic range containing the bulk of the particle population. Fig. 5.5 shows the various spectra obtained at  $y=1$  and an assortment of fit functions.

The pions are noticeably not well described by exponentials as they fail to reproduce the non-exponential rise at low values of  $m_T - m$ . Both the power law and the blast-wave fit functions are well fitted in this respect.

For the heavier particles the flow contribution becomes important as mentioned above. Exponentials in  $p_T$  do not reproduce the curving of the spectra in the low range, while exponentials in  $m_T$  reproduce the curved shape at least for kaons. Again the blast-wave parametrization does a good job in fitting the spectra of kaons and protons in the low end.

### 5.3 Yields

In order to obtain rapidity densities from integrated spectra the obtained parametrizations of  $p_T$  or  $m_T$  spectra are integrated over the full range. I.e.  $dN/dy$  may obtained either as

$$\frac{dN}{dy} = 2\pi \int_0^\infty p_T \left( \frac{1}{2\pi p_T} \frac{d^2 N}{dy dp_T} (p_T) \right) dp_T \quad (5.3)$$

or equivalently as

$$\frac{dN}{dy} = 2\pi \int_m^\infty m_T \left( \frac{1}{2\pi m_T} \frac{d^2 N}{dy dm_T} (m_T) \right) dm_T \quad (5.4)$$

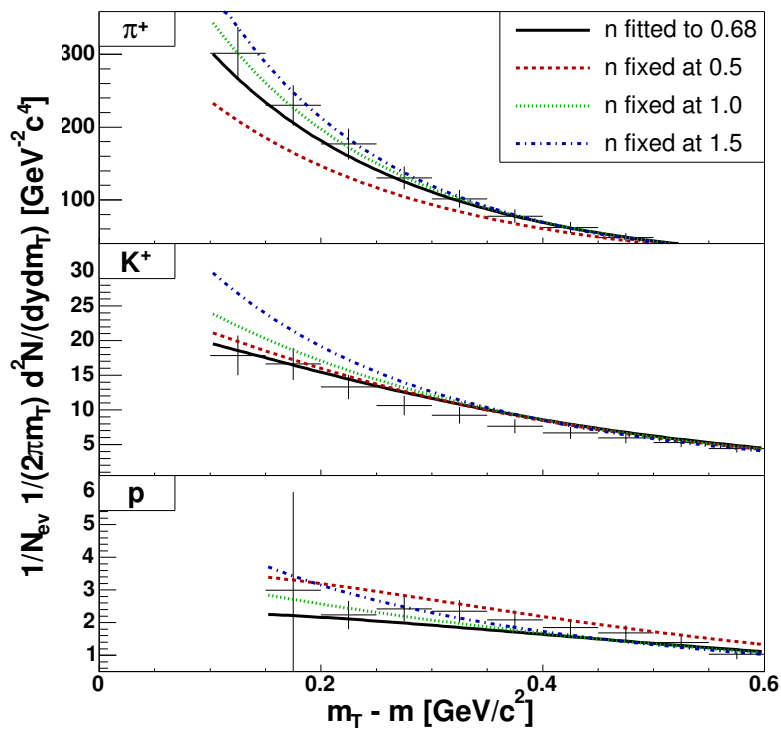


Figure 5.4: Obtained fit functions for positive particles around  $y = 1$ . The different functions for each species correspond to different values of  $n$ . Compared to the lighter particles the proton fit function is qualitatively more affected by the variations in  $n$  also at higher values of  $m_T - m$ .

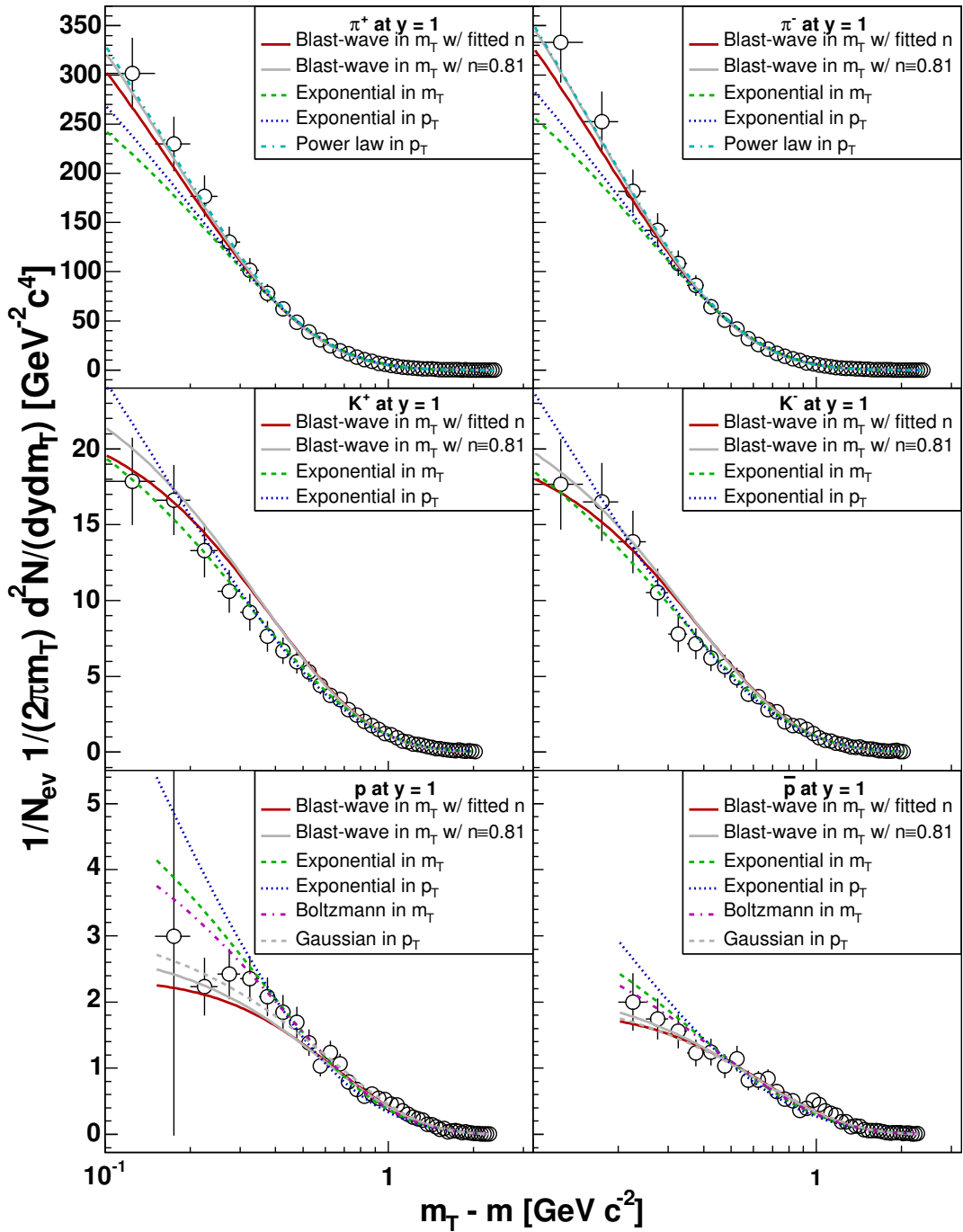


Figure 5.5: The blast-wave fit function compared to other possible fits at  $y = 1$ . The fitted value of  $n$  is the one in tab. 5.1, while the chosen  $n = 0.81$  is the average of the fitted  $n$  values for  $y \leq 2$ . The abscissa is logarithmic to show the differences in description in the low end of the spectra.

In the latter expression the lower limit of integration is  $m$  since the invariant  $m_T = m$  corresponds to  $p_T = 0$ . Nevertheless, the obtained fit functions are expressed in terms of  $m_T - m$  and hence they are integrated in the range  $(m_T - m) \in [0, \infty)$ .

By performing the integration according to eq. 5.4 for the chosen rapidities the obtained rapidity distributions in fig. 5.6 are obtained. The rapidity densities are also tabulated in C.1.

Also, corrections due to decay, absorption and multiple scattering are mostly dominant at low particle momentum. In [97] a momentum cut in the MRS is applied in which particles with  $p < 0.4 \text{ GeV}/c$  are removed. This way the extrapolated yields are less affected by possible systematic uncertainties in the correction factors applied in the low ends of the spectra. In order to allow a consistent comparison of the results presented in this analysis with the ones obtained in [97, 123] attempts have been made in which the blast-wave curves were only fitted for  $p > 0.4 \text{ GeV}/c$ . Limiting the fitting range in this way was found to have negligible impact on the obtained rapidity densities. The largest fraction of the spectra are discarded by the momentum cut at  $y = 0$ . In this rapidity bin  $dN/dy$  for pions, kaons and (anti-)protons are lowered by 5–6%, 2–3% and <1%, respectively, relative to the rapidity densities obtained when fitting also particles with  $p < 0.4 \text{ GeV}/c$ . The rapidity densities obtained in the MRS applying this cut on momentum are summarized in tab. C.2.

As mentioned in sec. 4.7 the obtained rapidity densities depend to some extent on the choice of fit functions. In tab. 5.3 are listed the extrapolated yields at  $y = 1$  obtained from blast-wave and exponential fits in  $m_T$  as well as power-law and Gaussian fits in  $p_T$ . The corresponding fit quality in terms of  $\chi^2$  per degree of freedom are also shown. The listed rapidity densities are comparable for fit functions that have reasonable correspondence to the spectra. E.g. it is obvious that Gaussian distributions are not consistent with the obtained pion spectra. Also the power-law fit to the  $p$  and  $\bar{p}$  spectra clearly deviate more than the other fit functions. Similar comparison of fit functions for the other selected rapidities are listed in tabs. C.3 through C.6.

The extrapolated regions account for significant fractions of the total ranges of integration. Tab. 5.4 summarizes the integrated areas within the spectrometer acceptance and fit ranges relative to the integral of the fit functions over  $(m_T - m) \in [0, \infty)$ .

The rapidity distributions for  $\pi^\pm$ ,  $K^\pm$  and  $\bar{p}$  are fitted with single Gaussian distributions whose centroids are fixed at  $y = 0$ . As can be seen qualitatively in fig. 5.6 the shape of the distributions are consistent with a such functional description. The Gaussians in fig. 5.6 are plotted in the rapidity range spanned by the two RHIC beams, i.e.  $y \in [-5.3, 5.3]$ .

By integrating the rapidity distributions the yield of identified particles over the full  $4\pi$  solid angle is determined. Tab. 5.5 summarizes the obtained integrated yield as well as the quality of the Gaussian fits.

The single Gaussian fits to the rapidity densities show that the widths of the rapidity distributions depend on the particle species. The widths are plotted in fig. 5.7 as a function of the mass of the particle. Positive and negative pions have the same width within errors. The widths of positive kaon distribution, however, exceeds the width of their negative counterpart. This difference may be attributed to the increase in baryochemical potential with increasing rapidity and hence greater production of  $K^+ = (u\bar{s})$  than  $K^- = (\bar{u}s)$ .

The rapidity distribution of net-protons is obtained by subtracting the number of

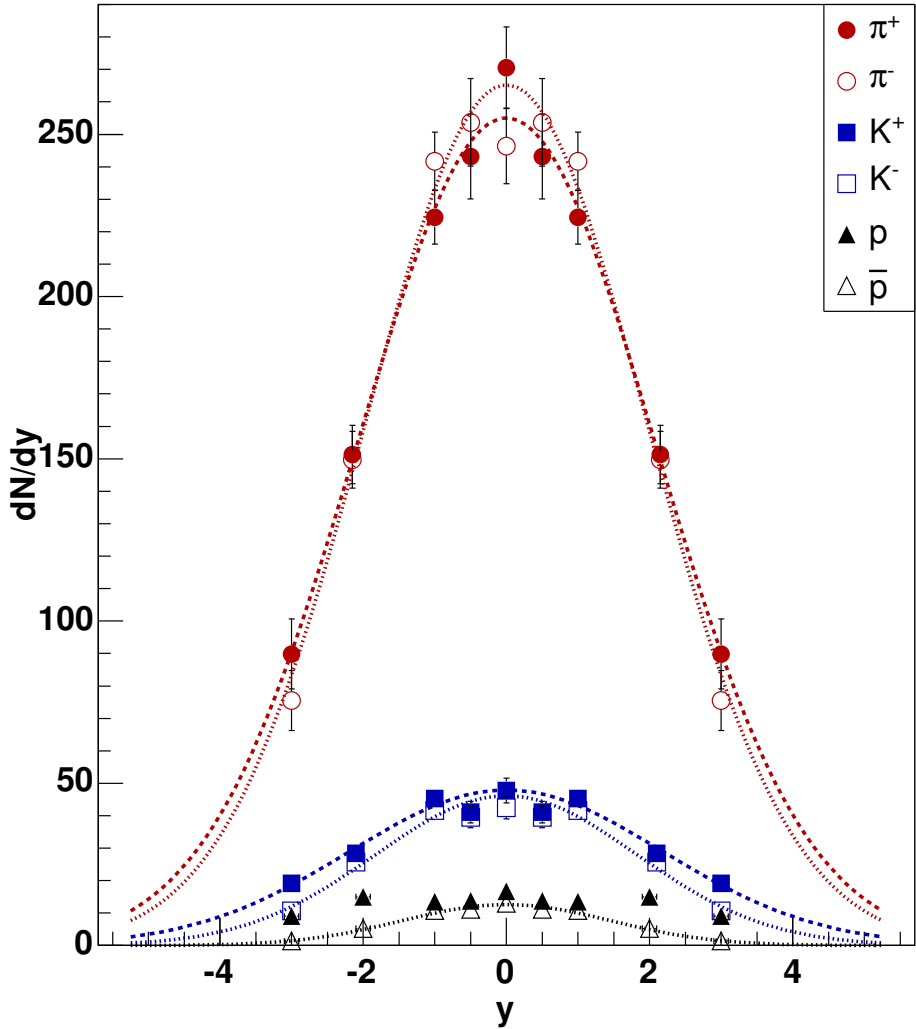


Figure 5.6: Obtained rapidity distribution for identified pions, kaons and (anti-)protons in the 10% ( $N_{part} = 328 \pm 6$ ) most central Au+Au collisions at  $\sqrt{s_{NN}} = 200$  GeV. Rapidity densities are obtained only for positive rapidities and subsequently mirrored around  $y = 0$ . All species except protons are fitted with a single Gaussian function in which the centroid is fixed at  $y = 0$ , where the dashed (dotted) curves represent the rapidity distribution of positive (negative) particles.

	blast-wave	power-law	exponential	Gaussian
$dN/dy (\pi^+)$	$224.4 \pm 8.0$	$242.8 \pm 12.5$	$207.2 \pm 8.6$	$135.7 \pm 9.1$
$\chi^2/n_{DOF} (\pi^+)$	20 / 45	18 / 45	33 / 45	300 / 45
$dN/dy (\pi^-)$	$241.7 \pm 8.6$	$259.1 \pm 13.6$	$220.3 \pm 9.1$	$139.8 \pm 9.4$
$\chi^2/n_{DOF} (\pi^-)$	22 / 45	20 / 45	35 / 45	300 / 45
$dN/dy (K^+)$	$45.3 \pm 1.6$	$48.1 \pm 2.0$	$43.3 \pm 1.7$	$38.8 \pm 2.0$
$\chi^2/n_{DOF} (K^+)$	34 / 39	13 / 39	9 / 39	65 / 39
$dN/dy (K^-)$	$41.6 \pm 1.6$	$45.7 \pm 2.0$	$40.6 \pm 1.8$	$35.2 \pm 1.8$
$\chi^2/n_{DOF} (K^-)$	35 / 39	20 / 39	17 / 39	66 / 39
$dN/dy (p)$	$13.5 \pm 0.6$	$20.0 \pm 0.25$	$18.2 \pm 0.8$	$14.3 \pm 0.7$
$\chi^2/n_{DOF} (p)$	47 / 41	94 / 41	58 / 41	25 / 41
$dN/dy (\bar{p})$	$10.7 \pm 0.5$	$15.4 \pm 0.8$	$12.9 \pm 0.6$	$10.1 \pm 0.5$
$\chi^2/n_{DOF} (\bar{p})$	30 / 42	59 / 42	42 / 42	30 / 42

Table 5.3: Comparison of extrapolated yields and  $\chi^2$  per degree of freedom at  $y=1.0$  using the parametrizations of blast-wave in  $m_T$ , power-law in  $p_T$ , exponential in  $m_T$  and Gaussian in  $p_T$ .

y	0	0.5	1	2	3
$\pi^+$	50%	62%	65%	50%	24%
$\pi^-$	53%	61%	66%	50%	26%
$K^+$	54%	72%	70%	42%	72%
$K^-$	54%	85%	72%	78%	71%
$p$	76%	93%	79%	56%	78%
$\bar{p}$	83%	91%	74%	85%	46%

Table 5.4: Fractions of the extrapolated yields which are within the acceptance of the spectrometer and the defined fit ranges.

	$\int(dN/dy)dy$	$\sigma_{dN/dy}$	$\chi^2/n_{DOF}$
$\pi^+$	$1331 \pm 59$	$2.08 \pm 0.08$	2.1 / 9
$\pi^-$	$1310 \pm 51$	$1.97 \pm 0.07$	6.4 / 9
$K^+$	$262 \pm 14$	$2.18 \pm 0.10$	10.2 / 9
$K^-$	$211 \pm 9$	$1.82 \pm 0.06$	13.1 / 9
$\bar{p}$	$46 \pm 2$	$1.45 \pm 0.05$	4.2 / 9

Table 5.5: Integrated yields, corresponding widths of the rapidity distributions and the single Gaussian fit quality. The results are obtained for the 10% most central Au+Au collisions.

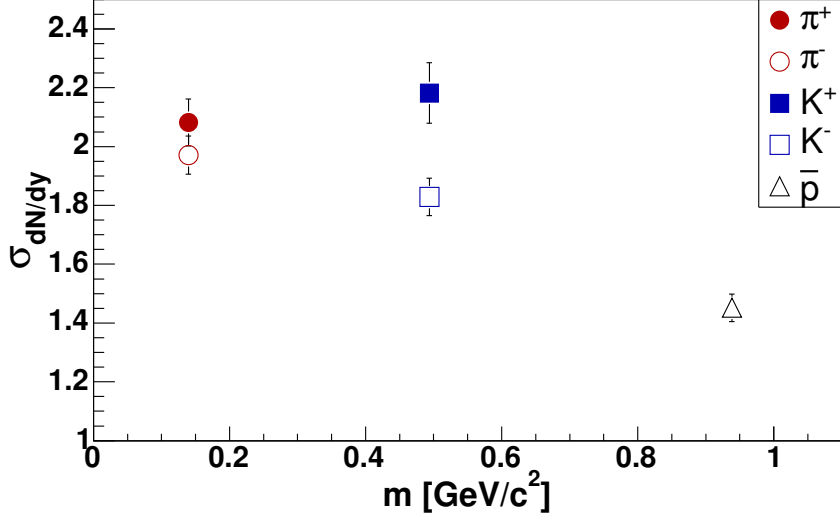


Figure 5.7: Width of the Gaussian fits to the rapidity distributions plotted as a function of the mass of the particle.

anti-protons from the number of protons at each rapidity bin. Fig. 5.8 shows the rapidity distributions of  $p$  and  $\bar{p}$  and the net-proton distribution obtained in this analysis for the 0 – 10% most central Au+Au collisions. It is clear that the net-proton distribution is lower at mid-rapidity than in the forward region. The bulk of the net-protons is located at rapidities above  $y=3$  which points to a high degree of transparency in central Au+Au collisions.

Previous results for the 0 – 5% most central collisions [136] were not corrected for feed-down. For the new 0 – 5% results shown in fig. 5.8 the following correction has been applied. Using mid-rapidity results from PHENIX [129] and STAR [137] we equal  $\Lambda/p = \bar{\Lambda}/\bar{p} = 0.93 \pm 0.11 (\text{stat}) \pm 0.25 (\text{syst})$  and use this fractional value also for  $(\text{net-}\Lambda)/(\text{net-}p)$ . From simulations of the BRAHMS experiment we estimate that 53% of the  $\Lambda$ s and  $\bar{\Lambda}$ s are identified as protons and anti-protons, respectively. This fraction includes both the 64% branching ratio of  $\Lambda$  ( $\bar{\Lambda}$ ) going to  $p$  ( $\bar{p}$ ) as well rejection of tracks not originating at the primary interaction vertex. Hence the published data points are each multiplied by a correction factor  $c_{FD} = 0.67 \pm 0.05 (\text{stat}) \pm 0.11 (\text{syst})$ .

When relaxing the centrality selection, i.e. going from the 0 – 5% to the 0 – 10% most central collisions, there is a slight decrease in net-proton at mid-rapidity while the picture is unchanged closer to the fragmentation region. This behavior seems reasonable since for less central collisions more of the protons are likely to end up in the fragmentation region.

Pions are by far the most abundant species produced in heavy ion collisions at RHIC. By looking at the number of pions produced per participant one may gain information on the amount of entropy created in the collision. It is believed that the entropy will increase at the onset of QGP creation as the partonic degrees of freedom outnumber the degrees of freedom in the hadronic stage. Fig. 5.9 shows the number of pions integrated over the full solid angle relative to the number of participants in heavy ion collisions as a

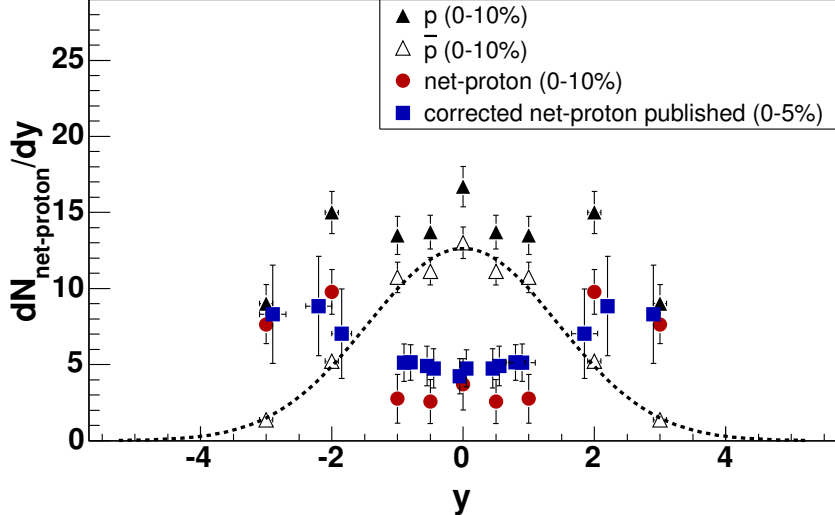


Figure 5.8: Rapidity distributions of  $p$ ,  $\bar{p}$  and net-protons for the  $0 - 10\%$  centrality selection. A single Gaussian function is fitted to the distribution of anti-protons. The published net-proton result for the  $0 - 5\%$  most central collisions [136] (which is almost identical to the BRAHMS graph in fig. 2.2) have been corrected for feed-down from  $\Lambda$  and  $\bar{\Lambda}$  and are shown for comparison. The points at  $y < -0.05$  are mirrored values as in fig. 5.6.

function of Fermi's variable  $F$ . This variable is related to the center of mass energy as

$$F = \frac{(\sqrt{s_{NN}} - m_N)^{3/4}}{\sqrt{s_{NN}}^{1/4}} \quad (5.5)$$

The number of pions in fig. 5.9 also include neutral pions and are estimated as  $\langle \pi \rangle = 1.5 \cdot (\langle \pi^+ \rangle + \langle \pi^- \rangle)$ . It is obvious that the obtained results from BRAHMS differ from the ones previously shown by PHOBOS.

## 5.4 Temperature and transverse expansion

From the fits shown in fig. 5.3 one may on the basis of eqs. 5.1 and 5.2 deduce the temperature and expansion velocity of the matter in the fireball. These two parameters are by nature anti-correlated. Hence the higher the temperature the lower the expansion velocity. Fig. 5.10 shows the obtained  $1$  and  $3\sigma$  contours at the selected rapidities.

Creating these contours the  $n$  and  $R$  parameters of the blast-wave parametrization had to be fixed at their fitted values. I.e. in the fit procedure  $n$  and  $R$  are allowed to vary freely, but in the calculation of contours their values are fixed.

The results obtained in the first unit of rapidity around  $y = 0$  all show similar expansion velocity. Going to more forward rapidities the transverse expansion velocity decreases but only by about 10% compared to  $\beta_s$  around mid-rapidity. The behavior of the temperature appears to be anti-correlated with the one of  $\beta_s$  and reaches its highest value in the most forward region investigated in this analysis.

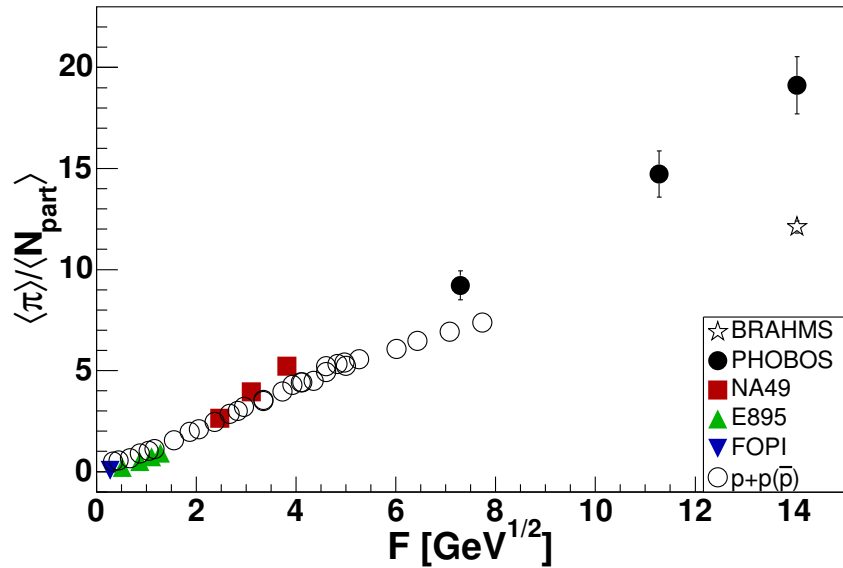


Figure 5.9: Excitation function for  $\langle \pi \rangle / \langle N_{part} \rangle$  in central heavy ion collisions plotted as a function of  $F$ . The obtained result from this analysis is compared to previously deduced results in [138] and references therein.

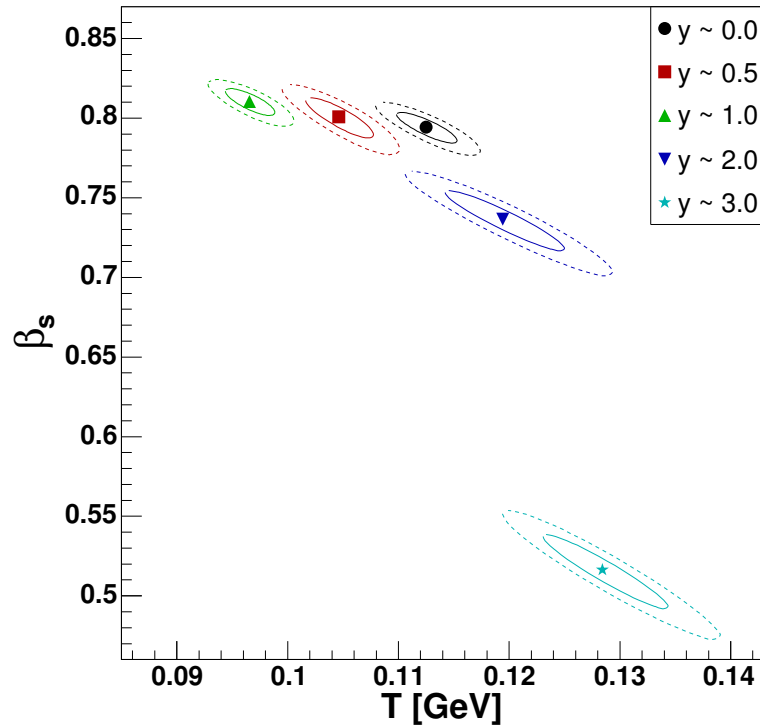


Figure 5.10: Transverse surface velocity in correlation with the thermal freeze-out temperature. Solid lines are indicate  $1\sigma$  confidence levels while the dashed lines represent the  $3\sigma$  levels.

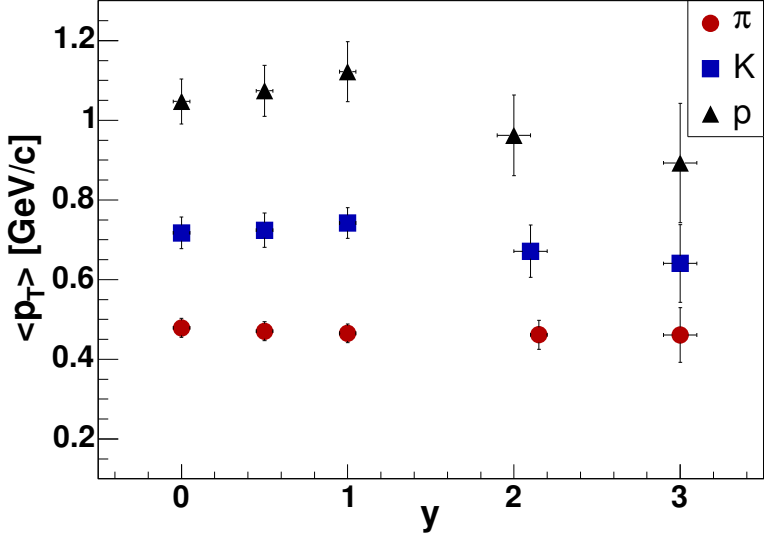


Figure 5.11: Rapidity dependence of mean transverse momentum for pions, kaons and protons. The errors of the charge conjugate species are added in quadrature to form the error on  $\langle p_T \rangle$  shown in the figure.

Inquiries into the transverse kinematics may also be performed by investigating the mean transverse momentum,  $\langle p_T \rangle$ , which may be expressed as

$$\begin{aligned}
 \langle p_T \rangle &= \frac{\int_0^\infty p_T \frac{d^2N}{dydp_T} dp_T}{\int_0^\infty \frac{d^2N}{dydp_T} dp_T} \\
 &= \frac{\int_m^\infty \sqrt{m_T^2 - m^2} \frac{d^2N}{dydm_T} dm_T}{\int_m^\infty \frac{d^2N}{dydm_T} dm_T} \\
 &= \frac{2\pi \int_m^\infty m_T \sqrt{m_T^2 - m^2} f(m_T) dm_T}{dN/dy} \tag{5.6}
 \end{aligned}$$

In the latter expression  $f(m_T)$  represents each species' function fitted to the spectra in fig. 5.3.

Considering that the spectra are fitted with fit functions according to the blast-wave parametrization the obtained  $\langle p_T \rangle$  is identical for charge conjugate particles, e.g.  $\pi^+$  and  $\pi^-$ . The normalization factor for each species has no effect since it cancels in the fraction of eq. 5.6. The resulting mean transverse momenta are plotted in fig. 5.11 as a function of rapidity.

As can be seen from fig. 5.11 the mean transverse momentum shows little dependence on rapidity, especially for the pions. The rapidity dependence increases with the mass of the particle.

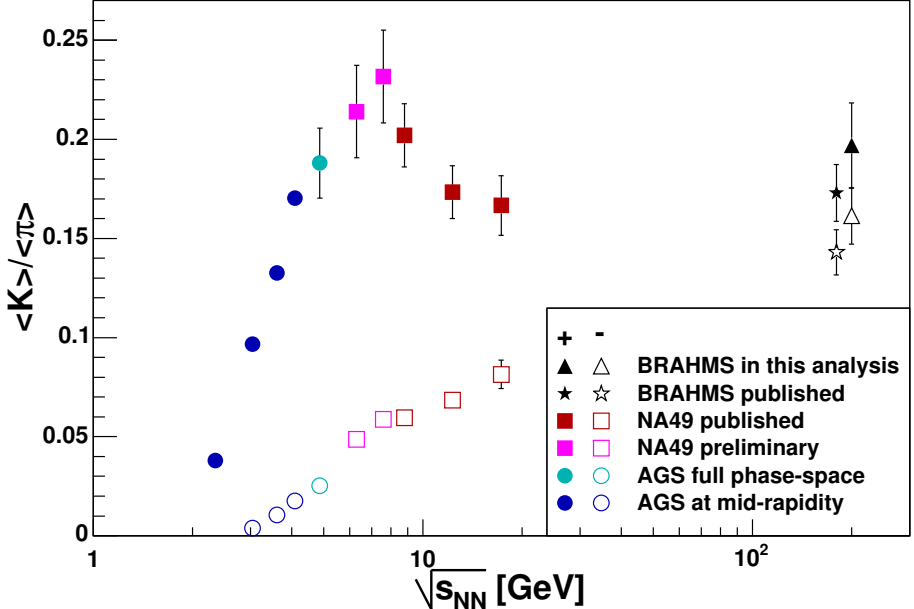


Figure 5.12:  $\langle K^+ \rangle / \langle \pi^+ \rangle$  and  $\langle K^- \rangle / \langle \pi^- \rangle$  as a function of the center-of-mass energy. The results from this analysis are compared to values obtained at the SPS and AGS ([140] and references therein) and other BRAHMS results presented in [141]. The data points corresponding to the numbers in [141] have been shifted to a slightly lower  $\sqrt{s_{NN}}$  for clarity.

## 5.5 Strangeness production

A large fraction of the strangeness produced in heavy ion collisions is carried by kaons. An increased production of strange particles was early proposed as a signature of QGP [55, 56]. Even so, since also statistical hadron models predict increased strangeness production [139] its significance as signature of the deconfined phase is questioned.

Nevertheless, previous measurements on the production of kaons relative to pions has shown an interesting behavior as a function of center-of-mass energy. Especially the  $\langle K^+ \rangle / \langle \pi^+ \rangle$  excitation function serves as a good means to distinguish between various models.

Fig. 5.12 shows the obtained results for the phase space integrated ratios  $\langle K^+ \rangle / \langle \pi^+ \rangle$  and  $\langle K^- \rangle / \langle \pi^- \rangle$  compared to results obtained at SPS and AGS and results previously deduced by the BRAHMS collaboration.

The results obtained in this analysis are consistent with the ratios in [141]. The positive ratio at  $\langle K^+ \rangle / \langle \pi^+ \rangle = 19.7 \pm 2.1\%$  is comparable to the value at the intermediate SPS energy regime while  $\langle K^- \rangle / \langle \pi^- \rangle = 16.1 \pm 1.4\%$  is higher than what was obtained at the lower energies.



# Chapter 6

## Discussion

The results shown in ch. 5 address various aspects of the scenarios presented in ch. 2. This chapter discusses the experimental outcome from this analysis in light of the previously presented collision scenarios.

### 6.1 Transverse characteristics

Invariant spectra of identified pions, kaons and protons are shown in sec. 5.1. A qualitative comparison between the various species reveal that there are non-thermal components in the transverse degrees of freedom. With increasing particle mass the flattening in the low end of the  $m_T$  spectra becomes more and more pronounced. This marked quality is typically attributed to the presence of transverse flow and strongly suggests fitting the spectra with functions that include collective motion.

When fitting the spectra with blast-wave functional parametrizations according to [22] the obtained surface expansion velocity is of the order of  $\beta \sim 0.8$  in the first unit around mid-rapidity. The corresponding temperatures are found to be in the range  $T \in [95, 115]$  MeV. Beyond  $y > 1$  the expansion velocity decreases slightly and the freeze-out temperature conformably increases. The obtained expansion velocities unveil the need for model descriptions that properly include collective flow. The transverse pressure gradients are high in the central rapidity region.

The obtained temperatures, expansion velocities and mean transverse momenta are more or less constant for  $|y| \lesssim 1$  with subsequent small changes at the higher rapidities. The Bjorken picture [106] predicts boost invariance for the thermodynamic observables around mid-rapidity. One may argue that the presented rapidity dependence of  $T$ ,  $\beta_s$  and  $\langle p_T \rangle$  neither qualify nor disqualify support for Bjorken's statement. It is true that the values of  $T$  and  $\beta_s$  do not seem to depend much on  $y$  for the first unit of rapidity. The mean transverse momentum, however, appears more or less constant throughout the measured rapidity window. The rapidity dependence of  $\langle p_T \rangle$  evaluated in Bjorken's context points to boost-invariance in a very wide window of rapidity. Such a wide window does, nevertheless, contradict the rapidity dependence of the  $dN/dy$  shown in fig. 5.6.

Bjorken's description also assumes that the expansion around mid-rapidity is longitudinal several fm/c after the collision, i.e. typically until the separation of the contracted nuclei exceeds their radii ( $R_{Au} \simeq 1.2A^{1/3} \simeq 7$  fm). This assumption is questionable in light

of the strong elliptic flow observed at RHIC [133] which suggests that thermalization and creation of strong transverse pressure gradients occurs within the first fm/c [142].

## 6.2 Longitudinal characteristics

The rapidity distributions of  $\pi^\pm$ ,  $K^\pm$ ,  $p$  and  $\bar{p}$  are shown in fig. 5.6. It is evident that the distributions of the species produced in the collision, i.e. excluding the (positive) protons, are all well described by single Gaussians. Scenario descriptions involving boost-invariance do at first not seem to be viable solutions for these particular species. Based on this characteristic Landau's description involving full stopping of the incoming baryons [100] is clearly more favored than a transparent collision according to Bjorken.

It may be that even though the final state rapidity distributions do not show signs of boost-invariance the underlying thermodynamic quantities are invariant in a limited window of rapidity. During the stage of one-dimensional spatial expansion in Bjorken's model the rapidity range in which boost-invariance persists is implicitly assumed to be infinite. When taking into account the finite size of the rapidity range in which boost-invariance may prevail it was shown a.o. in [23] that massless pions have Gaussian rapidity distributions even if the invariant region in the fundamental thermodynamic quantities stretches as far out as to  $y_0 \sim 2$ . The rapidity density is modified by the finite size of  $y_0$  such that

$$\frac{dN}{dy} \propto T^3 [\tanh(y + y_0) - \tanh(y - y_0)] \quad (6.1)$$

Boost-invariance in the underlying thermodynamic quantities should be more pronounced in the rapidity distributions of heavier particles such as  $\bar{p}$  than for the (close to) massless pions. The momentum distribution of pions created from a thermalized QGP is wider than for protons because of  $m_\pi < m_p$ . Thus, one may imagine that the rapidity distributions of identified particles depend on their mass in the following way: (1)  $\frac{dN}{dy}(y)$  of light particles such as pions appears to be Gaussian from the convolution of boost-invariant entropy density and wide Gaussian thermal momentum distributions, while (2) the narrow momentum distributions of anti-protons for each value of  $y$  maintain the boost-invariance of the thermodynamic quantities.

However, from the obtained rapidity distributions in fig. 5.6 it seems that rapidity distributions of anti-protons and pions are equally well described by single Gaussians. And the width of the fitted Gaussian rapidity distributions plotted as a function of particle mass in fig. 5.7 shows that  $\sigma_{dN/dy}^{\bar{p}} < \sigma_{dN/dy}^{\pi^\pm}$ . The narrow distribution of anti-protons does at least put very strong limits on the width of a possible boost-invariant region around mid-rapidity.

In addition the final state rapidity densities in Bjorken's model description are to a great extent guided by his assumption of negligible transverse expansion in the early stages, as was mentioned above. This assumption leads to the entropy density,  $dS/dy$ , being constant throughout the hydrodynamic expansion. Since it appears that the transverse expansion can not be neglected in the first fm/c after the collision it is not so obvious that the entropy density is conserved. Hence, the rapidity density of pions is not necessarily boost-invariant if the expansion is not only longitudinal.

Even though the rapidity distributions of the produced particles favors Landau's description over Bjorken, the distribution of protons does not fit into Landau's model. The rapidity distribution of  $p$  is clearly not described by the single Gaussian parametrization. The final proton outcome seem to be smeared out in the full rapidity window, a result which is difficult to describe in terms of a Landau type full stopping and subsequent expansion.

Still, even with leading protons at high rapidity one could expect that the remaining protons around mid-rapidity behave similarly to the produced particles, at least in the case of full stopping according to Landau. It has previously been shown that the mean rapidity loss in the 0 – 5% most central collisions at RHIC is around  $\langle y \rangle \sim 2$  [136]. With beam rapidities at  $y_{beam} = \pm 5.3$  the bulk of the leading protons end up around  $y \sim \pm 3.3$ . The flatness of the proton spectra for  $|y| \lesssim 3.3$  appears to be in contradiction to Landau's Gaussian prediction.

Neither do the experimental data fully support Bjorken's picture. The net-proton rapidity distribution, indicative of but not equal to the net-baryon distribution, as shown in fig 5.8 is not zero at mid-rapidity. The net-proton distribution points to partial transparency in heavy ion collisions at RHIC.

Hence, while the longitudinal distributions of produced particles suggest a scenario as described by Landau, protons indicate at least some degree of Bjorken style transparency. The picture is clearly mixed since these two descriptions are generally thought to exclude each other.

Landau's hydrodynamical model predicts that the width of the rapidity distributions increases logarithmically with the squared center-of-mass energy,  $s$ , according to eq. 2.2. I.e. the equation expresses a relation for the squared width of the Gaussian distribution,  $L = \sigma^2$ , which for central Au+Au collisions at RHIC amounts to  $L = 0.5 \ln(200^2/(2m_p^2)) \simeq 4.67$ . The width of the Gaussian rapidity distribution for pions is predicted in Landau's model to be of the order of  $\sigma \simeq 2.16$ .

Comparing to the obtained widths for  $\pi^\pm$  plotted in fig. 5.7 there is excellent agreement with Landau's prediction. The agreement may actually appear to be too good. In [102] it is suggested that roughly half of the center of mass energy is carried away by leading particles that are not found in the central rapidity region of a p+p collision. This value is contrasted by [143] in which a fraction of about 2/3 of the total energy in A+A collisions is used for production of new degrees of freedom. Additionally it was shown in [136] that a fraction of  $0.73 \pm 0.03$  of the incoming energy in Au+Au collisions at RHIC is used to create new particles.

These different numbers suggest that the energy term in eq. 2.2 should possibly be replaced by some effective energy per participant pair. This modified  $s = s_{eff}$  is clearly lower than the original squared center-of-mass energy and would predict correspondingly smaller values of  $L$ .

## 6.3 Conclusions

From the above sections one may be tempted to conclude that the evolution in a central collision of two heavy ions may be better described by Landau's hydrodynamic model than by Bjorken's expansion. The author clearly supports this view. But Landau's description

has some essential caveats. As was mentioned the rapidity distribution of protons do not fit into the picture of full stopping. And the prediction for the width of the pion rapidity distributions seems unclear. Finally, the results on  $\langle \pi \rangle / \langle N_{part} \rangle$  presented fig. 5.9 does not suggest a linear dependence of the ratio on the Fermi variable  $F$  as predicted in [143].

In summary it appears that both Landau and Bjorken pictures are not able to fully describe the full set of longitudinal distributions presented in this analysis and elsewhere. Additionally Bjorken does not describe the transverse characteristics observed at RHIC.

Yet, the models of both Bjorken and Landau involve crude approximations. Bjorken's assumption of boost-invariance as well as Landau's alleged full stopping are only phenomenological descriptions of the early stages of the collisions since no calculable theory of complex strong interactions in heavy ion collisions existed.

In this respect the three-dimensional hydrodynamic description in [23] is built on a firmer ground. Various experimental observables at RHIC, such as the dependence of charged hadron multiplicity on centrality, rapidity and energy are consistent with descriptions in which two slabs of CGC collide [144, 145, 146]. The characteristics of the incoming slabs are calculated on the basis of the McLerran-Venugopalan model [110] which provide the initial conditions for the subsequent hydrodynamic expansion. Hence the description of hydrodynamic evolution is closely connected to the representation of the state before the collision. From the results shown in [23] the model seems to be in agreement with the experimental data.

The rapidity distributions of charged hadrons are clearly reminiscent of the similarly shaped distributions of pions in fig. 5.6. In fig. 6.1 the rapidity distributions of identified particles from fig. 5.6 are shown in comparison with the distributions of pions, kaons and protons from the CGC+Hydro model [147]. The hydro calculations are done with the same centrality selection as in this analysis.

The model distributions are fairly close to Gaussian, but their overall normalizations are significantly above the results presented in this analysis. This may be attributed to initial model parameters were chosen in order to reproduce the multiplicity results presented by the PHOBOS collaboration [148]. As can be gauged from fig. 5.9 these experimental multiplicities are high compared to the ones obtained in this analysis. Also, the PHOBOS pseudo-rapidity distributions used for the model parameters in [23] carry a significant uncertainty that allows the model parameter to be altered.

Furthermore, the chemical freeze-out temperature in the model is set at  $T_{ch} = 170$  MeV. This may or may not be the right temperature. Since the relative yield of hadrons depend strongly on the chemical freeze-out temperature the relative difference in the model distributions are correspondingly uncertain.

Finally no baryon or isospin chemical potentials were taken into account in the model calculations. Therefore, there is no difference between particle and anti-particle. As can be seen in fig. 6.1 there is significant difference between the model curve for (anti-) protons and the corresponding results from this analysis.

With these model caveats in mind one may argue that the CGC+Hydro model fit the data qualitatively well. When properly taking into account the missing pieces mentioned above it is the belief of the author that the model may well describe the rapidity distributions from this analysis.

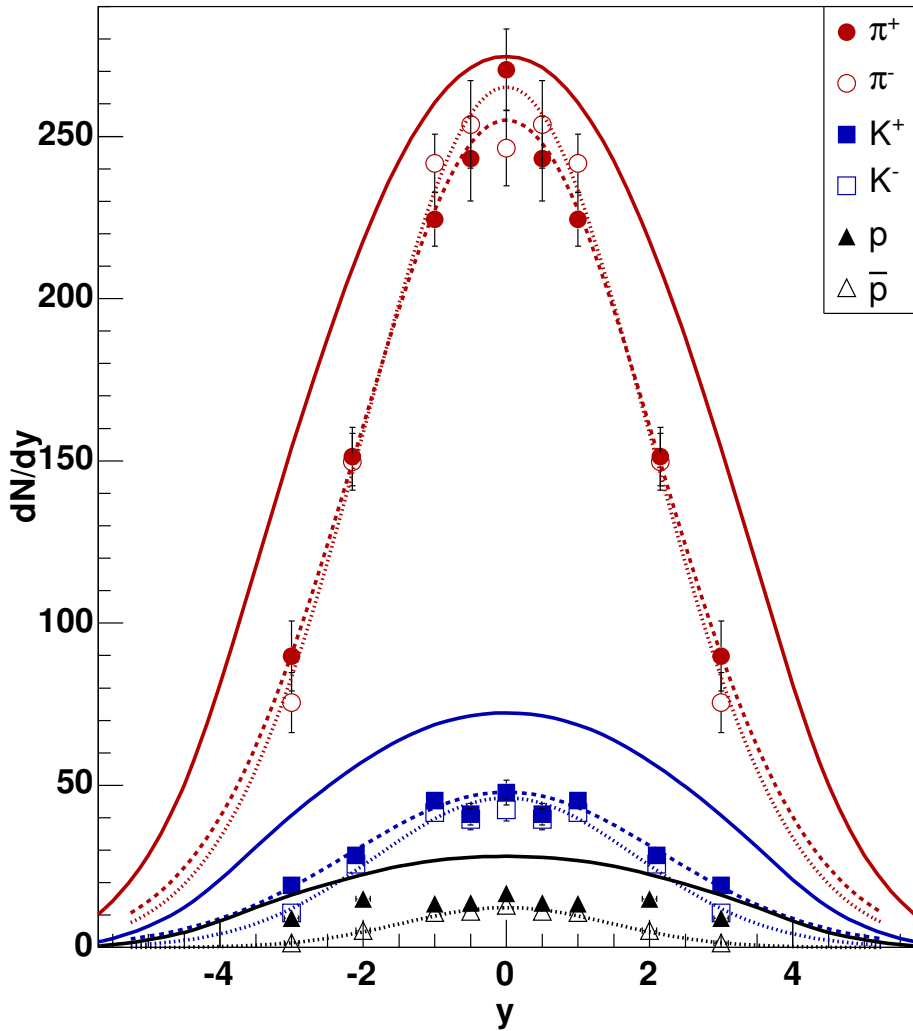


Figure 6.1: Rapidity distributions obtained in this analysis (fig. 5.6) in comparison with results obtained with the CGC+Hydro model drawn as solid lines [147]. The hydro calculations have been performed with impact parameter  $b = 3 \text{ fm}$  which corresponds to  $N_{part} = 328$ .



# Appendix A

## Kinematics

A number of kinematic terms and units are used when dealing with high energy heavy ion collisions. This appendix define an essential number of these. For the presentation here *natural units* are used in which  $\hbar = c = 1$ . When transforming from natural units one may apply the following equivalence:  $\hbar c = 197.3 \text{ MeV fm}$ .

### A.1 Lorentz transformations

Often multiple reference frames are used in the when describing collisions of heavy ions. E.g. in some case one refers to the *center-of-mass frame*, while in other case the *lab frame* may be the most pertinent<sup>1</sup>. Lorentz-transformations have to be applied when translating quantities measured in one frame to be used in another frame.

The energy and 3-momentum of a particle are combined in a 4-vector  $(E, \mathbf{p})$  where  $E$  and  $\mathbf{p}$  relate as  $E^2 - \mathbf{p}^2 = m^2$ . Here  $m$  is the mass of the particle whose possible values are positive including 0. Assume a transformation is required from frame  $S$  to frame  $S'$  whose velocity relative to  $S$  is  $\beta_f$  along the  $z$ -coordinate of  $S$ . In this case one may decompose  $\mathbf{p}$  into a longitudinal component along  $z$ ,  $p_L$ , and a transverse component orthogonal to  $z$ ,  $p_T$ . The transformation from  $(E, \mathbf{p})$  measured in  $S$  to the corresponding  $(E', \mathbf{p}')$  measured in  $S'$  is defined as

$$\begin{pmatrix} E' \\ p_L' \end{pmatrix} = \begin{pmatrix} \gamma_f & -\gamma_f \beta_f \\ -\gamma_f \beta_f & \gamma_f \end{pmatrix} \begin{pmatrix} E \\ p_L \end{pmatrix} \quad (\text{A.1})$$

$$p_T' = p_T \quad (\text{A.2})$$

The conversion matrix is fully determined by the kinematical quantities  $\beta_f$  and  $\gamma_f = (1 - \beta_f^2)^{-1/2}$ . This conversion assures that the scalar product of two 4-vectors is invariant, i.e.  $p_1 \cdot p_2 = p_1' \cdot p_2'$ .

The center-of-mass energy in a sample of particles is a customary quantity. It is defined as

$$E_{cm} = \sqrt{\left(\sum_i E_i\right)^2 - \left(\sum_i \mathbf{p}_i\right)^2} \quad (\text{A.3})$$

---

<sup>1</sup>When colliding equal nuclei with equal energy in a collider, as is the case for the colliding systems whose analysis is described in this dissertation, the center-of-mass and lab frames coincide. In fixed target experiments, however, these frames are separated typically by several units of rapidity.

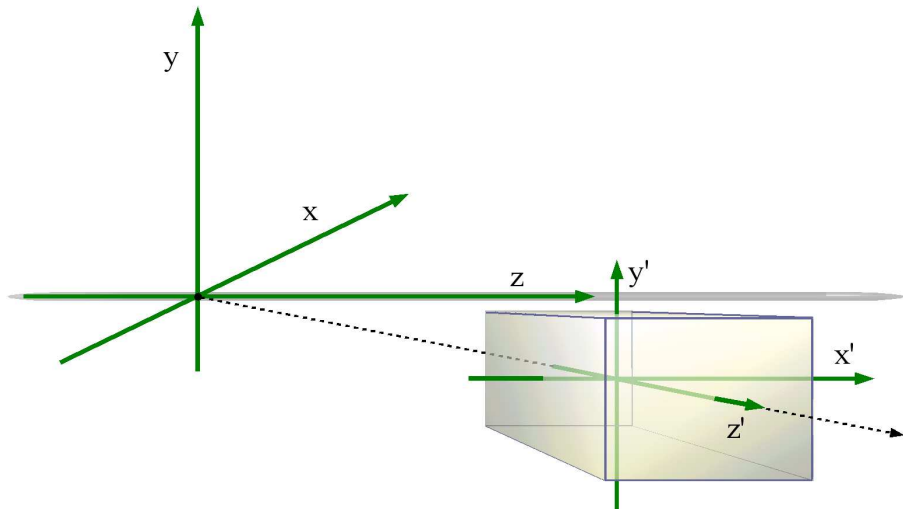


Figure A.1: Illustration of coordinate systems defined for the BRAHMS experiment. The global unprimed coordinate system has  $z$  direction along the beam pipe and is centered at the nominal interaction point. The primed system exemplify the local coordinates of a tracking detector in the forward arm.

where the index  $i$  refers to a particular particle in the sample. E.g. in the case of two particles colliding their center-of-mass energy is defined as

$$E_{cm} = \sqrt{(E_1 + E_2)^2 - (\mathbf{p}_1 + \mathbf{p}_2)^2} = \sqrt{s} \quad (\text{A.4})$$

Here  $s$  is one of the Lorentz-invariant Mandelstam variables. Hence when we in the context of heavy ion collisions at RHIC talk about  $\sqrt{s_{NN}} = 200 \text{ GeV}$  we refer to the center-of-mass energy per pair of nucleons, i.e. one nucleon from each of the colliding nuclei.

## A.2 Coordinate systems

In this dissertation, in particular in ch. 4, certain quantities are used in the context of the global coordinate system, while other quantities refer to local coordinates e.g. in a detector. The coordinate systems are illustrated in fig. A.1. The unprimed coordinate system is the global system. In this system the  $z$  direction coincides with the direction of the beam pipe, the  $y$  direction is vertical and the  $x$  direction is in the horizontal plane and orthogonal to  $z$ . The chosen  $(0, 0, 0)$  of the global system is at the nominal interaction vertex.

The primed system illustrates the choice for a tracking detector in the forward arm. Here  $z'$  points away from the nominal interaction point and thus in a typical direction of a penetrating particle. As seen in fig. A.1 the local  $z'$  is parallel to two of the walls of the box shaped detector cage. The local  $y'$  coordinate is parallel to  $y$  and  $x'$  is in the horizontal plane and orthogonal to  $z'$ .

### A.3 Kinematic variables

The decomposition of momentum in terms of a transverse and a longitudinal component in the kinematical description is often used. Above  $p_T$  and  $p_L$  were described. I.e. in terms of the global coordinate system one may express the transverse and longitudinal momenta as

$$p_T = \sqrt{p_x^2 + p_y^2} \quad (\text{A.5})$$

$$p_L = p_z \quad (\text{A.6})$$

If spherical coordinates  $p$ ,  $\theta$  and  $\phi$  are used one may calculate the components of the momentum as

$$p_T = |\mathbf{p}| \sin \theta \quad (\text{A.7})$$

$$p_L = |\mathbf{p}| \cos \theta \quad (\text{A.8})$$

Here  $\theta$  is the angle of the momentum vector of the particle relative to the  $z$  direction, while  $\phi$  describe the angle of the 3-momentum projected into the  $(x, y)$  plane.

In several occasions it is useful to use the *transverse mass* defined as

$$m_T = \sqrt{p_T^2 + m^2} \quad (\text{A.9})$$

Here  $m$  is the mass of the particle, sometimes referred to as its *rest mass*, i.e. the mass as measured in a coordinate system in which the particle momentum is 0.

Furthermore we define *rapidity* as

$$y = \frac{1}{2} \ln \left( \frac{E + p_L}{E - p_L} \right) \quad (\text{A.10})$$

The introduction of rapidity gives a benefit when translating quantities from coordinate system  $S$  to  $S'$  as the rapidity is additive under Lorentz transformations. That means that the shape of a rapidity distribution in reference frame  $S$  is the same as in frame  $S'$  and the centroid of the distribution is only shifted by an additive constant.

Sometimes it is useful to express the energy and longitudinal momentum of a particle in terms of its transverse mass and rapidity. The following relations are applicable.

$$E = m_T \cosh y \quad (\text{A.11})$$

$$p_z = m_T \sinh y \quad (\text{A.12})$$

Since the longitudinal component of velocity may be expressed as  $\beta_z = p_z/E$  the division of eq. A.12 by eq. A.11 yields the identity

$$\beta_z = \tanh y \quad (\text{A.13})$$

Often *pseudo – rapidity* is used instead of rapidity. In the case of massless particles these two quantities are equal. Pseudo-rapidity is defined as

$$\eta = \frac{1}{2} \ln \left( \frac{|\mathbf{p}| + p_L}{|\mathbf{p}| - p_L} \right) \quad (\text{A.14})$$

Comparing eqs. A.10 and A.14 one may also infer that for highly relativistic particles, for which  $|\mathbf{p}| \gg m$ , one substitute pseudo-rapidity where rapidity is used. Pseudo-rapidity is typically more readily available than rapidity since no particle identifications is required and it only depends on the polar angle  $\theta$  as

$$\eta = -\ln(\tan(\theta/2)) \quad (\text{A.15})$$

Yet the equality of  $\eta$  and  $y$  is only limited to the very high energy and/or massless particles. At mid-rapidity at RHIC the charged particles have a sufficiently low energy that their pseudo-rapidity and rapidity distributions clearly differ.

## Appendix B

# RICH correction for mis-identified particles

The detection efficiency of RICH was estimated in [85] using simulated tracks and RICH' response embedded into real data. An efficiency of  $\epsilon = 97\%$  was found with this method. When determining the RICH component of the PID probability the inefficiency of the detector will contribute to pollution of light particles into the samples of the heavier ones.

E.g. assume a pion goes through the RICH with momentum  $p \in [p_\pi + \delta_p, p_K]$ . Here  $p_i$  is the RICH momentum threshold for particle  $i$ . The momentum interval  $\delta_p$  added to the pion threshold illustrates the ranges in momentum around the particle's thresholds in which the efficiency of the RICH is not well determined, as discussed in sec. 4.5.2. In order to be on the safe side  $\delta_p = 1 \text{ GeV}/c$  for all particle species was used in this analysis.

In the indicated range 3% of the pions do not generate Cherenkov rings. That means that the pion probability output from the RICH is 0 for these particles. Hence, the ID of these pions is wrongly determined to be either kaon or proton based on the information from H1 and H2.

The true number of pions in a momentum bin in this range,  $N_\pi(p)$ , is thus determined from the recorded number of pions,  $n_\pi(p)$  as

$$N_\pi(p) = n_\pi(p)/\epsilon \quad (\text{B.1})$$

in which  $p$  is the momentum at the center of the momentum bin.

The true numbers of kaons and protons,  $N_K(p)$  and  $N_p(p)$  respectively, are also calculated. But in addition to depending on the recorded numbers of each species,  $n_K(p)$  and  $n_p(p)$ , they depend also on the feeding from mis-identified pions. The true number of kaons is given by

$$N_K(p) = n_k(p) - N_\pi(p)(1 - \epsilon)f_{\pi \rightarrow K}(p) \quad (\text{B.2})$$

The second term expresses the number of mis-identified pions ( $N_\pi(p)(1 - \epsilon)$ ) multiplied by the fraction of these ending up as kaons ( $f_{\pi \rightarrow K}(p)$ ). The fraction  $f_{\pi \rightarrow K}(p)$  can be estimated from the data as the recorded number of kaons divided by the summed numbers of kaons and protons. I.e.

$$f_{\pi \rightarrow K}(p) = \frac{n_k(p)}{n_k(p) + n_p(p)} \quad (\text{B.3})$$

Momentum range	$[p_\pi + \delta_p, p_K + \delta_p]$	$[p_K + \delta_p, p_p + \delta_p]$	$[p_p + \delta_p, \infty]$
$N_\pi =$	$n_\pi/\epsilon$	$n_\pi/\epsilon$	$n_\pi/\epsilon$
$N_K =$	$n_K \left[ 1 + \frac{n_\pi}{n_k + n_p} \left( 1 - \frac{1}{\epsilon} \right) \right]$	$n_K/\epsilon$	$n_K/\epsilon$
$N_p =$	$n_p \left[ 1 + \frac{n_\pi}{n_k + n_p} \left( 1 - \frac{1}{\epsilon} \right) \right]$	$n_p \left[ 1 + \frac{n_\pi + n_k}{n_p} \left( 1 - \frac{1}{\epsilon} \right) \right]$	$n_p/\epsilon$

Table B.1: Corrections applied to data recorded with the full FS to account for mis-identifications in the RICH.  $n_i$  is the recorded number of particle species  $i$ , while  $N_i$  is the true corrected number.

Using eq. B.1 we may express  $N_K(p)$  for in the momentum range  $[p_\pi + \delta_p, p_K]$  as

$$N_K(p) = n_k(p) - \frac{n_\pi(p)}{\epsilon} (1 - \epsilon) \frac{n_k(p)}{n_k(p) + n_p(p)} \quad (\text{B.4})$$

$$= n_k(p) \left[ 1 - \frac{n_\pi(p)}{n_k(p) + n_p(p)} \left( \frac{1}{\epsilon} - 1 \right) \right] \quad (\text{B.5})$$

$$= n_k(p) \left[ 1 + \frac{n_\pi(p)}{n_k(p) + n_p(p)} \left( 1 - \frac{1}{\epsilon} \right) \right] \quad (\text{B.6})$$

Analogously the true number of protons is calculated as

$$N_p(p) = n_p(p) \left[ 1 + \frac{n_\pi(p)}{n_k(p) + n_p(p)} \left( 1 - \frac{1}{\epsilon} \right) \right] \quad (\text{B.7})$$

Similar corrections are applied in other regions of momentum space. Table B.1 summarizes the various corrections due to mis-identification caused by the RICH.

For momenta below  $p_\pi + \delta_p$  no correction for feeding from mis-identification of leptons is applied. It is assumed that the hodoscopes remove most of the lepton contribution from the samples of hadrons.

# Appendix C

## Tabulated results

y	0	0.5	1	2	3
$dN/dy(\pi^+)$	$270.6 \pm 9.5$	$243.1 \pm 8.7$	$224.4 \pm 8.0$	$151.4 \pm 8.5$	$89.9 \pm 9.3$
$dN/dy(\pi^-)$	$246.4 \pm 8.9$	$253.7 \pm 8.9$	$241.7 \pm 8.5$	$149.7 \pm 8.2$	$75.5 \pm 8.0$
$dN/dy(K^+)$	$47.8 \pm 1.9$	$41.1 \pm 1.7$	$45.3 \pm 1.6$	$28.4 \pm 2.1$	$19.1 \pm 2.0$
$dN/dy(K^-)$	$42.4 \pm 1.6$	$39.5 \pm 1.7$	$41.5 \pm 1.6$	$25.6 \pm 1.7$	$10.6 \pm 1.1$
$dN/dy(p)$	$16.7 \pm 0.6$	$13.7 \pm 0.6$	$13.5 \pm 0.6$	$15.0 \pm 1.0$	$9.0 \pm 1.0$
$dN/dy(\bar{p})$	$13.0 \pm 0.5$	$11.1 \pm 0.5$	$10.7 \pm 0.5$	$5.2 \pm 0.4$	$1.4 \pm 0.1$

Table C.1: Extrapolated yields obtained from integration of fitted blast-wave parametrized functions.

y	0	0.5	1
$dN/dy(\pi^+)$	$256.4 \pm 12.8$	$239.9 \pm 12.2$	$219.8 \pm 8.2$
$dN/dy(\pi^-)$	$231.5 \pm 11.8$	$250.0 \pm 12.2$	$236.7 \pm 8.8$
$dN/dy(K^+)$	$46.6 \pm 1.8$	$40.9 \pm 1.5$	$44.9 \pm 1.6$
$dN/dy(K^-)$	$41.4 \pm 1.5$	$39.4 \pm 1.5$	$41.2 \pm 1.6$
$dN/dy(p)$	$16.6 \pm 0.8$	$13.7 \pm 0.8$	$13.4 \pm 0.6$
$dN/dy(\bar{p})$	$12.9 \pm 0.6$	$11.1 \pm 0.7$	$10.7 \pm 0.5$

Table C.2: Extrapolated yields obtained in the MRS from fits where particles with  $p < 0.4 \text{ GeV}/c$  are discarded.

	blast-wave	power-law	exponential	Gaussian
$dN/dy(\pi^+)$	$270.6 \pm 9.4$	$278.7 \pm 16.9$	$197.7 \pm 9.1$	$110.6 \pm 9.3$
$\chi^2/n_{DOF}(\pi^+)$	25 / 58	15 / 58	64 / 58	374 / 58
$dN/dy(\pi^-)$	$246.4 \pm 8.9$	$272.2 \pm 16.8$	$203.3 \pm 9.1$	$105.9 \pm 8.0$
$\chi^2/n_{DOF}(\pi^-)$	23 / 49	21 / 49	53 / 49	344 / 49
$dN/dy(K^+)$	$47.8 \pm 1.9$	$58.9 \pm 3.2$	$48.9 \pm 2.5$	$36.8 \pm 2.6$
$\chi^2/n_{DOF}(K^+)$	37 / 51	37 / 51	37 / 51	106 / 51
$dN/dy(K^-)$	$42.4 \pm 1.6$	$52.7 \pm 3.3$	$42.5 \pm 2.0$	$32.6 \pm 2.3$
$\chi^2/n_{DOF}(K^-)$	19 / 42	17 / 42	21 / 42	113 / 42
$dN/dy(p)$	$16.7 \pm 0.6$	$18.1 \pm 0.7$	$16.8 \pm 0.6$	$13.3 \pm 0.7$
$\chi^2/n_{DOF}(p)$	30 / 51	96 / 51	47 / 51	39 / 51
$dN/dy(\bar{p})$	$13.0 \pm 0.5$	$15.5 \pm 0.5$	$14.0 \pm 0.5$	$11.5 \pm 0.6$
$\chi^2/n_{DOF}(\bar{p})$	22 / 46	64 / 46	29 / 46	41 / 46

Table C.3: Comparison of extrapolated yields and  $\chi^2$  per degree of freedom at  $y=0.0$  using the parametrizations of blast-wave in  $m_T$ , power-law in  $p_T$ , exponential in  $m_T$  and Gaussian in  $p_T$ .

	blast-wave	power-law	exponential	Gaussian
$dN/dy(\pi^+)$	$243.1 \pm 8.7$	$247.5 \pm 12.9$	$218.9 \pm 9.5$	$179.8 \pm 13.5$
$\chi^2/n_{DOF}(\pi^+)$	20 / 45	20 / 45	29 / 45	224 / 45
$dN/dy(\pi^-)$	$253.7 \pm 8.9$	$261.4 \pm 13.9$	$214.5 \pm 9.7$	$169.9 \pm 13.5$
$\chi^2/n_{DOF}(\pi^-)$	19 / 50	15 / 50	41 / 50	262 / 50
$dN/dy(K^+)$	$41.1 \pm 1.7$	$45.0 \pm 2.3$	$40.4 \pm 2.0$	$39.7 \pm 2.8$
$\chi^2/n_{DOF}(K^+)$	29 / 39	33 / 39	28 / 39	75 / 39
$dN/dy(K^-)$	$39.5 \pm 1.7$	$50.9 \pm 2.8$	$44.2 \pm 2.3$	$44.5 \pm 3.1$
$\chi^2/n_{DOF}(K^-)$	45 / 41	39 / 41	39 / 41	81 / 41
$dN/dy(p)$	$13.7 \pm 0.6$	$14.1 \pm 0.6$	$13.9 \pm 0.5$	$13.0 \pm 0.6$
$\chi^2/n_{DOF}(p)$	23 / 36	58 / 36	31 / 36	20 / 36
$dN/dy(\bar{p})$	$11.1 \pm 0.5$	$11.4 \pm 0.5$	$11.2 \pm 0.4$	$10.0 \pm 0.5$
$\chi^2/n_{DOF}(\bar{p})$	18 / 39	53 / 39	27 / 39	18 / 39

Table C.4: Comparison of extrapolated yields and  $\chi^2$  per degree of freedom at  $y=0.5$  using the parametrizations of blast-wave in  $m_T$ , power-law in  $p_T$ , exponential in  $m_T$  and Gaussian in  $p_T$ .

	blast-wave	power-law	exponential	Gaussian
$dN/dy(\pi^+)$	$151.4 \pm 8.4$	$167.7 \pm 15.1$	$130.0 \pm 8.5$	$114.9 \pm 10.9$
$\chi^2/n_{DOF}(\pi^+)$	$19.3 / 47$	$16.5 / 47$	$29.1 / 47$	$113.8 / 47$
$dN/dy(\pi^-)$	$149.7 \pm 8.2$	$165.2 \pm 15.0$	$125.9 \pm 6.3$	$106.2 \pm 9.7$
$\chi^2/n_{DOF}(\pi^-)$	$17 / 47$	$14 / 47$	$28 / 47$	$119 / 47$
$dN/dy(K^+)$	$28.4 \pm 2.0$	$31.3 \pm 2.9$	$28.7 \pm 2.7$	$32.8 \pm 4.5$
$\chi^2/n_{DOF}(K^+)$	$18 / 28$	$19 / 28$	$18 / 28$	$30 / 28$
$dN/dy(K^-)$	$25.6 \pm 1.7$	$30.4 \pm 2.4$	$26.3 \pm 2.0$	$26.6 \pm 3.0$
$\chi^2/n_{DOF}(K^-)$	$13 / 34$	$11 / 34$	$13 / 34$	$35 / 34$
$dN/dy(p)$	$15.0 \pm 1.0$	$15.4 \pm 1.0$	$14.7 \pm 0.9$	$14.6 \pm 1.1$
$\chi^2/n_{DOF}(p)$	$16 / 25$	$31 / 25$	$20 / 25$	$10 / 25$
$dN/dy(\bar{p})$	$5.2 \pm 0.4$	$6.3 \pm 0.5$	$5.7 \pm 0.4$	$6.0 \pm 0.5$
$\chi^2/n_{DOF}(\bar{p})$	$23 / 27$	$29 / 27$	$22 / 27$	$17 / 27$

Table C.5: Comparison of extrapolated yields and  $\chi^2$  per degree of freedom at  $y=2.0$  using the parametrizations of blast-wave in  $m_T$ , power-law in  $p_T$ , exponential in  $m_T$  and Gaussian in  $p_T$ .

	blast-wave	power-law	exponential	Gaussian
$dN/dy(\pi^+)$	$89.9 \pm 9.3$	$87.7 \pm 9.4$	$78.8 \pm 5.3$	$65.1 \pm 5.6$
$\chi^2/n_{DOF}(\pi^+)$	$14 / 37$	$12 / 37$	$13 / 37$	$53 / 37$
$dN/dy(\pi^-)$	$75.5 \pm 8.0$	$89.1 \pm 12.1$	$76.4 \pm 5.9$	$63.1 \pm 6.1$
$\chi^2/n_{DOF}(\pi^-)$	$15 / 36$	$13 / 36$	$13 / 36$	$59 / 36$
$dN/dy(K^+)$	$19.1 \pm 2.0$	$22.6 \pm 1.7$	$19.8 \pm 1.3$	$23.0 \pm 2.1$
$\chi^2/n_{DOF}(K^+)$	$15 / 30$	$16 / 30$	$14 / 30$	$34 / 30$
$dN/dy(K^-)$	$10.6 \pm 1.1$	$12.3 \pm 0.9$	$11.0 \pm 0.7$	$14.0 \pm 1.2$
$\chi^2/n_{DOF}(K^-)$	$16 / 29$	$24 / 29$	$18 / 29$	$23 / 29$
$dN/dy(p)$	$9.0 \pm 1.0$	$11.1 \pm 0.7$	$9.8 \pm 0.6$	$10.3 \pm 0.7$
$\chi^2/n_{DOF}(p)$	$15 / 29$	$36 / 29$	$22 / 29$	$15 / 29$
$dN/dy(\bar{p})$	$1.4 \pm 0.2$	$2.6 \pm 0.4$	$1.9 \pm 0.2$	$1.9 \pm 0.2$
$\chi^2/n_{DOF}(\bar{p})$	$13 / 20$	$13 / 20$	$12 / 20$	$11 / 20$

Table C.6: Comparison of extrapolated yields and  $\chi^2$  per degree of freedom at  $y=3.0$  using the parametrizations of blast-wave in  $m_T$ , power-law in  $p_T$ , exponential in  $m_T$  and Gaussian in  $p_T$ .



# Appendix D

## Glossary

In the field of high energy nuclear physics a jargon with a multitude of acronyms and terms are used. Below follows a list of particular terms used in this thesis. The list includes also terms relating to the BRAHMS experiment in particular.

**ADC** Analogue-to-digital converter, used to sample the amplitude of a an electric pulse

**AGS** Alternating Gradient Synchrotron (at BNL)

**BB** Beam-beam counter in the BRAHMS experiment

**BEVALAC** Joint complex of the BEVATRON circular accelerator and the SuperHILAC linear accelerator (at LBL)

**BFS** Back-forward spectrometer, i.e. the rear part of the FS in the BRAHMS experiment

**BNL** Brookhaven National Laboratory, US

**BRAHMS** Broad Range Hadron Magnetic Spectrometers

**C1** Threshold Cherenkov detector in the FFS

**CERES/NA45** Experiment for the study of electron pair production in hadron and nuclear collisions (at SPS)

**CERN** Conseil Europén pour la Recherche Nucléaire, Switzerland/France

**CGC** Color glass condensate

**D1** Dipole magnet in front of T1

**D2** Dipole magnet between T1 and T2

**D3** Dipole magnet between T3 and T4

**D4** Dipole magnet between T4 and T5

**D5** Dipole magnet between TPM1 and TPM2

**DC** Drift Chamber

**Drell-Yan** The process in which a di-lepton pair is created in the collision of two hadrons

**DST** Data Summary Tree data structure

**DX** RHIC dipole magnet

**E866/E917** High baryon density study experiment (at AGS)

**E895** Multi-particle correlations experiment (at AGS)

**EoS** Equation of State

**FEE** Front-end electronic

**Feed-down** Referring to the fraction of a sample of particles that are decay products

**FFS** Front-forward spectrometer, i.e. the front part of the FS in the BRAHMS experiment

**Fireball** The matter right after the collision of two nuclei consisting of the participants and particles created in the collision

**FS** Forward spectrometer in the BRAHMS experiment

**GSI** Gesellschaft für Schwerionenforschung mbH, Germany

**H1** Time-of-flight wall/hodoscope in the FFS

**H2** Time-of-flight wall/hodoscope in the BFS

**HBT** Hanbury-Brown Twiss interferometry

**HIJING** Heavy Ion Jet Interaction Generator Monte-Carlo model

**IR** Interaction region, referring to the experimental halls along RHIC

**ISR** Intersecting Storage Rings (at CERN)

**LBL** Lawrence Berkely National Laboratory, US

**LHC** Large Hadron Collider (at CERN)

**Luminosity** Measure of beam intensity in dimensions of  $1/(time \cdot length^2)$ .

**MA** Multiplicity array centrality detector in the BRAHMS experiment

**Monte-Carlo** Referring to statistical randomness, e.g. in computer simulations

**MRS** Mid-rapidity spectrometer in the BRAHMS experiment

**MS** Multiple scattering

**NA49** Large acceptance hadron detector for an investigation of Pb-induced reactions (at SPS)

**NA50** Experiment for the study of muon pairs and vector mesons produced in high energy Pb-Pb interactions (at SPS)

**Participant** The nucleons in the colliding nuclei that interact in a nuclear collision

**PHENIX** Pioneering High-Energy Nuclear Interaction eXperiment (at RHIC)

**PHOBOS** Experiment at RHIC, named after one of the moons of planet Mars

**PID** Particle Identification

**PMT** Photo-multiplier tube

**pQCD** Perturbative Quantum Chromo-Dynamics

**PYTHIA** Event generator based on pQCD

**QCD** Quantum Chromo-Dynamics

**QED** Quantum Electro-Dynamics

**QGP** Quark Gluon Plasma

**QMD** Quantum Molecular Dynamics

**Reaction plane** The plane in three-dimensional space spanned by the momentum vectors of the incoming nuclei and the impact parameter (Fig. 1.6.)

**RF** Radio frequency

**RHIC** Relativistic Heavy Ion Collider (at BNL)

**RICH** Ring Imaging Cherenkov detector in the BFS

**RQMD** Relativistic Quantum Molecular Dynamics

**SIS** SchwerIonenSynchrotron (e.g. Heavy Ion Synchrotron at GSI)

**Spectator** The nucleons in the colliding nuclei that do not interact in a nuclear collision

**SPS** Super Proton Synchrotron (at CERN)

**STAR** Solenoidal Tracker at RHIC (experiment at RHIC)

**T1** First TPC in the FFS

**T2** Second TPC in the FFS

**T3** First DC in the BFS

**T4** Second DC in the BFS

**T5** Third DC in the BFS

**TDC** Time-to-digital converter, used to sample the timing of a an electric pulse

**TOF** Time-of-flight

**TOFW** Time-of-flight wall/hodoscope in the MRS

**TPC** Time Projection Chamber

**TPM1** First TPC in the MRS

**TPM2** Second TPC in the MRS

**UrQMD** Ultra-relativistic Quantum Molecular Dynamics

**WA97/NA57** Experiment for the study of strange and multi-strange baryon production in lead-lead collisions (at SPS)

**ZDC** Zero-degree calorimeter, in this thesis usually referring to calorimeters in the BRAHMS experiment

# Appendix E

## List of publications

### E.1 Publications in refereed journals

1. S. Sanders *et al.* (BRAHMS Collaboration),  
*Charged Particle Multiplicities at BRAHMS*,  
J. Phys. G**27** (2001) 671
2. I. G. Bearden *et al.* (BRAHMS Collaboration),  
*Rapidity dependence of anti-proton to proton ratios in Au+Au collisions at  $\sqrt{s_{NN}} = 130 \text{ GeV}$* ,  
Phys. Rev. Lett. **87** (2001) 112305
3. I. G. Bearden *et al.* (BRAHMS Collaboration),  
*Charged particle densities from Au+Au collisions at  $\sqrt{s_{NN}} = 130 \text{ GeV}$* ,  
Phys. Lett. B**523** (2001) 227
4. F. Videbæk *et al.* (BRAHMS Collaboration),  
*Results from the BRAHMS experiment at RHIC*,  
Nucl. Phys. A**698** (2002) 29c
5. I. G. Bearden *et al.* (BRAHMS Collaboration),  
*Particle Ratios at Forward Rapidity in  $\sqrt{s_{NN}} = 130 \text{ GeV}$  Au+Au Collisions*,  
Nucl. Phys. A**698** (2002) 667c
6. D. Röhrich *et al.* (BRAHMS Collaboration),  
*Results from the BRAHMS experiment at RHIC*,  
J. Phys. G**28** (2002) 1607
7. I. G. Bearden *et al.* (BRAHMS Collaboration),  
*Pseudorapidity distributions of charged particles from Au+Au collisions at the maximum RHIC energy*,  
Phys. Rev. Lett. **88** (2002) 202301
8. I. G. Bearden *et al.* (BRAHMS Collaboration),  
*Rapidity Dependence of Charged Antiparticle-to-Particle Ratios in Au+Au Collisions at  $\sqrt{s_{NN}} = 200 \text{ GeV}$* ,  
Phys. Rev. Lett. **90** (2003) 102301

9. P. Staszek *et al.* (BRAHMS Collaboration),  
*Results from the BRAHMS experiment at RHIC*,  
*Acta Phys. Polon. B***33** (2002) 1387
10. I. Arsene *et al.* (BRAHMS Collaboration),  
*Transverse-Momentum Spectra in Au+Au and d+Au collisions at  $\sqrt{s_{NN}} = 200 \text{ GeV}$  and the Pseudorapidity Dependence of High- $p_T$  Suppression*,  
*Phys. Rev. Lett.* **91** (2003) 072305
11. I. G. Bearden *et al.* (BRAHMS Collaboration),  
*Nuclear Stopping in Au+Au Collisions at  $\sqrt{s_{NN}} = 200 \text{ GeV}$*   
*Phys. Rev. Lett.* **93** (2004) 102301
12. I. Arsene *et al.* (BRAHMS Collaboration),  
*Evolution of the Nuclear Modification Factors with Rapidity and Centrality in d+Au collisions at  $\sqrt{s_{NN}} = 200 \text{ GeV}$*   
*Phys. Rev. Lett.* **93** (2004) 242303
13. J. H. Lee (for the BRAHMS Collaboration)  
*Rapidity Dependent Strangeness Measurements in BRAHMS*  
*J. Phys. G***30** (2004) S85
14. M. Murray (for the BRAHMS Collaboration)  
*Scanning the phases of QCD with BRAHMS*  
*J. Phys. G***30** (2004) S667
15. Z. Yin (for the BRAHMS Collaboration)  
*High  $p_T$  charged pion and proton production in  $\sqrt{s_{NN}} = 200 \text{ GeV}$  Au+Au and d+Au collisions*  
*J. Phys. G***30** (2004) S983
16. D. Ouerdane (for the BRAHMS Collaboration)  
*Rapidity dependence of charged hadron production in central Au + Au collisions at  $\sqrt{s_{NN}} = 200 \text{ GeV}$  with BRAHMS*  
*J. Phys. G***30** (2004) S1129
17. J. J. Gaardhøje *et al.* (BRAHMS Collaboration),  
*The new physics at RHIC. From transparency to high  $p_T$  suppression*  
*Nucl. Phys. A***734** (2004) 13
18. I. Arsene *et al.* (BRAHMS Collaboration),  
*High  $p_T$  Results for Au+Au Collisions at  $\sqrt{s_{NN}} = 200 \text{ GeV}$*   
*Eur. Phys. J. C***33** (2004) S603
19. I. Arsene *et al.* (BRAHMS Collaboration),  
*Quark-gluon plasma and the color glass condensate at RHIC? The perspective from the BRAHMS experiment*  
*Nucl. Phys. A***757** (2005) 1

20. I. Arsene *et al.* (BRAHMS Collaboration),  
*Centrality dependence of charged-particle pseudorapidity distributions from d+Au collisions at  $\sqrt{s_{NN}} = 200 \text{ GeV}$*   
*Phys. Rev. Lett.* **94** (2005) 032301
21. H Ito (for the BRAHMS Collaboration)  
*Towards measuring pseudorapidity dependence in elliptic flow at BRAHMS*  
*J. Phys. G: Nucl. Part. Phys.* **31** (2005) S23
22. I. G. Bearden *et al.* (BRAHMS Collaboration),  
*Forward and midrapidity like-particle ratios from p+p collisions at  $\sqrt{s} = 200 \text{ GeV}$*   
*Phys. Lett. B* **607** (2005) 42
23. D. Röhrlrich *et al.* (BRAHMS Collaboration),  
*Properties of matter at forward rapidities at RHIC*  
*Nucl. Phys. A* **749** (2005) 295
24. D. Röhrlrich (for the BRAHMS Collaboration)  
*Strangeness production at RHIC: recent results from BRAHMS*  
*J. Phys. G: Nucl. Part. Phys.* **31** (2005) S659
25. D. Ouerdane (for the BRAHMS Collaboration)  
*Rapidity dependence of strangeness production in central Au+Au collisions at RHIC*  
*J. Phys. G: Nucl. Part. Phys.* **31** (2005) S1019
26. I. Arsene *et al.* (BRAHMS Collaboration),  
*Centrality Dependent Particle Production at  $y=0$  and  $y \sim 1$  in Au+Au Collisions at  $\sqrt{s_{NN}} = 200 \text{ GeV}$*   
Accepted for publication in *Phys. Rev. C*

## E.2 Conference contributions

1. *Rapidity distributions of charged pions and kaons at  $\sqrt{s_{NN}} = 200 \text{ GeV}$ . From raw data to distributions*  
Poster presented at the XVI International Conference on Ultrarelativistic Nucleus-Nucleus Collisions,  
Nantes, France, July 18 - 24, 2002
2. *Rapidity dependence of strange particle ratios and spectra at  $\sqrt{s_{NN}} = 200 \text{ GeV}$  Au-Au collisions*,  
Parallel talk given at the XVI International Conference on Particles and Nuclei,  
Osaka, Japan, September 30 - October 4, 2002
3. *Strangeness production in  $\sqrt{s_{NN}} = 200 \text{ GeV}$  Au+Au Collisions at RHIC*,  
Parallel talk given at the International Europhysics Conference on High Energy Physics,  
Aachen, Germany, July 17 - 23, 2003

4. *Kaon production in central Au+Au collisions at  $\sqrt{s_{NN}} = 200 \text{ GeV}$*   
 Poster presented at the XVII International Conference on Ultrarelativistic Nucleus-Nucleus Collisions,  
 Oakland, California, US, January 11 - 17, 2004

### E.3 Publications as contributor or primary author

1. J. I. Jørdre *et al.* (BRAHMS Collaboration),  
*Rapidity dependence of strange particle ratios and spectra at  $\sqrt{s_{NN}} = 200 \text{ GeV}$  Au-Au collisions*,  
 Proceedings following the XVI International Conference on Particles and Nuclei,  
 Osaka, Japan, September 30 - October 4, 2002,  
 Nucl. Phys. A**721** (2003) 235c
2. M. Adamczyk *et al.* (BRAHMS Collaboration),  
*The BRAHMS experiment at RHIC*,  
 Nucl. Instrum. Meth. A**499** (2003) 437
3. J. I. Jørdre *et al.* (BRAHMS Collaboration),  
*Strangeness production in  $\sqrt{s_{NN}} = 200 \text{ GeV}$  Au+Au Collisions at RHIC*,  
 Proceedings following the International Europhysics Conference on High Energy Physics,  
 Aachen, Germany, July 17 - 23, 2003  
 Eur. Phys. J. C**33** (2004) S624
4. I. G. Bearden *et al.* (BRAHMS Collaboration),  
*Charged Meson Rapidity Distributions in Central Au+Au collisions at  $\sqrt{s_{NN}} = 200 \text{ GeV}$*   
 Phys. Rev. Lett. **94** (2005) 162301

# References

- [1] A. Einstein, Annalen Phys. **49** (1916) 769
- [2] G. S. Bali, Phys. Rept. **343** (2001) 1
- [3] B. Müller, *The Physics of the Quark-Gluon Plasma*, Lecture Notes in Physics **225** (1985)
- [4] M. Calderón de la Barca Sánchez, Ph.D. thesis, Yale University, USA (2001)
- [5] J. W. Harris, B. Müller, Annu. Rev. Nucl. Part. Sci. **46** (1996) 71
- [6] R. D. Pisarski, F. Wilczek, Phys. Rev. D **29** (1984) 338
- [7] K. Rajagopal, F. Wilczek, Nucl. Phys. B**399** (1993) 395
- [8] F. Karsch, Nucl. Phys. A**698** (2002) 199c
- [9] B. Friman, J. Phys. G: Nucl. Part. Phys. **30** (2004) S895
- [10] E. Braaten, R. D. Pisarski, Nucl. Phys. B**337** (1990) 569
- [11] S. Necco, R. Sommer, Nucl. Phys. B**622** (2002) 328
- [12] S. Datta *et al.*, Phys. Rev. D **69** (2004) 094507
- [13] O. Kaczmarek *et al.*, Phys. Lett. B**543** (2002) 41
- [14] K. Geiger, B. Müller, Nucl. Phys. B**369** (1992) 600
- [15] K. Eskola, X. N. Wang, Phys. Rev. D **49** (1994) 1284
- [16] K. Geiger, J. I. Kapusta, Phys. Rev. D **47** (1993) 4905
- [17] H. Sorge *et al.*, Phys. Lett. B**289** (1992) 6
- [18] J. Aichelin, K. Werner, Phys. Lett. B**300** (1993) 158
- [19] S. A. Bass *et al.*, J. Phys. G: Nucl. Part. Phys. **25** (1999) R1
- [20] R. Hagedorn, J. Rafelski, Phys. Lett. B**97** (1980) 136
- [21] H. Stöcker *et al.*, Z. Phys. A**303** (1981) 259

- [22] E. Schnedermann *et al.*, Phys. Rev. C **48** (1993) 2462
- [23] T. Hirano, Y. Nara, Nucl. Phys. A**743** (2004) 305
- [24] J. Adams *et al.* (STAR collaboration), Phys. Rev. Lett. **92** (2004) 112301
- [25] N. Herrmann *et al.*, Nucl. Phys. A**610** (1996) 49
- [26] J. Rafelski, J. Letessier, Nucl. Phys. A**715** (2003) 98c
- [27] H. Stöcker, W. Greiner, Phys. Rep. **137** (1986) 277
- [28] J. Y. Ollitrault, Phys. Rev. D **48** (1993) 1132
- [29] P. Danielewicz *et al.*, Phys. Rev. Lett. **81** (1998) 2438
- [30] P. J. Siemens, J. O. Rasmussen, Phys. Rev. Lett. **42** (1979) 880
- [31] A. M. Poskanzer, S. A. Voloshin, Phys. Rev. C **58** (1998) 1671
- [32] N. S. Amelin *et al.*, Nucl. Phys. A**544** (1992) 463c
- [33] C. Spies *et al.*, Phys. Rev. C **57** (1998) 908
- [34] J. Chance *et al.*, Phys. Rev. Lett. **78** (1997) 2535
- [35] H. Liu *et al.*, Nucl. Phys. A**638** (1998) 451
- [36] C. Ogilvie *et al.*, Nucl. Phys. A**638** (1998) 57
- [37] L. S. Wood, PhD thesis, University of California, Davis, USA (1998)
- [38] H. Sorge, Phys. Rev. Lett. **82** (1999) 2048
- [39] P. F. Kolb *et al.*, Phys. Rev. C **62** (2000) 054909
- [40] C. Adler *et al.* (STAR collaboration), Phys. Rev. C **66** (2002) 034904
- [41] E. Shuryak, Nucl. Phys. A**750** (2005) 64
- [42] F. Retiére, J. Phys. G: Nucl. Part. Phys. **30** (2004) S895
- [43] R. Hanbury-Brown, R. Q. Twiss, Phil. Mag. **45** (1954) 663
- [44] S. Pratt, Phys. Rev. D **33** (1986) 1314
- [45] G. Løvhøiden, UIO/PHYS/97-01
- [46] D. Flierl, PhD thesis, J. W. Goethe-Universitet, Germany (2002)
- [47] S. Pratt, Phys. Rev. D **33** (1986) 72
- [48] G. F. Bertsch, Nucl. Phys. A**498** (1989) 173c
- [49] F. Yano, S. Koonin, Phys. Lett B**78**, (1978) 556

- [50] M. Podgoretskii, Sov. J. Nucl. Phys. **37** (1983) 272
- [51] U. Heinz, B. Jacak, Ann. Rev. Nucl. Part. Sci. **49** (1999) 529
- [52] C. Adler *et al.* (STAR collaboration), Phys. Rev. Lett. **87** (2001) 082301
- [53] D. H. Rischke, M. Gyulassy, Nucl. Phys. A**608** (1996) 479
- [54] D. H. Rischke, Nucl. Phys. A**610** (1996) 88c
- [55] J. Rafelski, B. Müller, Phys. Rev. Lett. **48** (1982) 1066
- [56] P. Koch *et al.*, Phys. Rep. **142** (1986) 167 [check times]
- [57] C. Greiner, Nucl. Phys. A**715** (2003) 75c
- [58] P. Chung *et al.* (E895 collaboration), Phys. Rev. Lett. **91** (2003) 202301
- [59] F. Antinori, J. Phys. G: Nucl. Part. Phys. **30** (2004) S725
- [60] J. Adams *et al.* (STAR collaboration), Phys. Rev. Lett. **92** (2004) 182301
- [61] G. E. Bruno *et al.* (NA57 collaboration), *New results from the NA57 experiment*, Preprint: arXiv:nucl-ex/0305033
- [62] S. Soff *et al.*, Phys. Lett. B**471** (1999) 89
- [63] P. V. Ruuskanen, Nucl. Phys. A**544** (1992) 169c
- [64] C. Song, Phys. Rev. C **47** (1993) 2861
- [65] M. Strickland, Phys. Lett. B**331** (1994) 245
- [66] D. K. Srivastava *et al.*, Phys. Lett. B**276** (1992) 285
- [67] S. Chakrabarty *et al.*, Phys. Rev. D **46** (1992) 3802
- [68] M. C. Abreu *et al.* (NA50 collaboration), Eur. Phys. J. C**14** (2000) 443
- [69] D. Adamova *et al.* (CERES/NA45 collaboration), Nucl. Phys. A**715** (2003) 262c
- [70] M. M. Aggarwal *et al.* (WA98 collaboration), Phys. Rev. Lett. **85** (2000) 3595
- [71] J. Frantz, J. Phys. G: Nucl. Part. Phys. **30** (2004) S1003
- [72] D. Adamova *et al.* (CERES/NA45 collaboration), Phys. Rev. Lett. **91** (2003) 042301
- [73] G. E. Brown, M. Rho, Phys. Rept. **363** (2002) 85
- [74] R. Rapp, J. Wambach, Adv. Nucl. Phys. **25** (2000) 1
- [75] J. Adams *et al.* (STAR collaboration), Phys. Rev. Lett. **92** (2004) 092301
- [76] P. Braun-Munzinger, J. Stachel, Nucl. Phys. A**690** (2001) 119c

- [77] R. Baier, R. Rückl, Z. Phys. C**19** (1993) 251
- [78] T. Matsui, H. Satz, Phys. Lett. B**178** (1986) 416
- [79] P. Braun-Munzinger, K. Redlich, J. Stachel, *Particle production in heavy ion collisions*, Preprint: arXiv:nucl-th/0304013
- [80] M. C. Abreu *et al.* (NA50 collaboration), Phys. Lett. B**450** (1999) 456
- [81] M. C. Abreu *et al.* (NA50 collaboration), Phys. Lett. B**477** (2000) 28
- [82] J. Nagle *et al.* (PHENIX collaboration), Nucl. Phys. A**698** (2002) 599
- [83] R. Vogt in S. A. Bass *et al.*, Nucl. Phys. A**661** (1999) 205c
- [84] T. K. Hemmick, J. Phys. G: Nucl. Part. Phys. **30** (2004) S659
- [85] Z. Yin, Ph.D. thesis, Univ. of Bergen, Norway (2004)
- [86] K. Klein-Bösing, J. Phys. G: Nucl. Part. Phys. **30** (2004) S975
- [87] D. Kharzeev *et al.*, Phys. Lett. B**561** (2003) 93
- [88] J. Adams *et al.* (STAR collaboration), Phys. Rev. Lett. **91** (2003) 072304
- [89] W. Scheid *et al.*, Phys. Rev. Lett. **21** (1968) 1479
- [90] G. F. Chapline *et al.*, Phys. Rev. D **8** (1973) 4302
- [91] C. Hartnack *et al.*, Nucl. Phys. A**495** (1989) 303c
- [92] M. Berenguer *et al.*, J. Phys. G: Nucl. Part. Phys. **18** (1992) 655
- [93] W. Schmidt *et al.*, Phys. Rev. C **47** (1993) 2782
- [94] K. Ashktorab *et al.*, BRAHMS Conceptual Design Report 1994 (updated 1995)
- [95] Y. J. Kim, Ph.D. thesis, Korea University, South Korea (2004)
- [96] X. N. Wang, M. Gyulassy, Comput. Phys. Commun. **83** (1994) 307
- [97] P. H. L. Christiansen, Ph.D. thesis, NBI, Denmark (2003)
- [98] H. Sorge *et al.*, Phys. Lett. B**243** (1990) 7
- [99] A. von Keitz, Phys. Lett. B**263** (1991) 353
- [100] L. D. Landau, Izv. Akad. Nauk. SSSR **C47** (1953) 52
- [101] E. Fermi, Prog. Theor. Phys. **5** (1950) 570
- [102] P. Carruthers, M. Duong-van, Phys. Rev. D **8** (1973) 859
- [103] S. Z. Belenkij, L. D. Landau, Nuovo. Cim. Suppl. **3S10** (1956) 15

- [104] P. Steinberg, Nucl. Phys. A**752** (2005) 423
- [105] P. Carruthers, N. Y. Acad. Sci. **229** (1974) 91
- [106] J. D. Bjorken, Phys. Rev. D **27** (1983) 140
- [107] C. Alt *et al.* (NA49 collaboration), Phys. Rev. C **68** (2003) 034903
- [108] G. Agakichiev *et al.* (NA45/Ceres collaboration), Phys. Rev. Lett. **92** (2004) 032301
- [109] E. Iancu, R. Venugopalan, in *Quark Gluon Plasma 3*, World Scientific, Singapore (2004)
- [110] L. D. McLerran, R. Venugopalan, Phys. Rev. D **49** (1994) 2233, **49** (1994) 3352, **50** (1994) 2225
- [111] K. Golec-Biernat, M. Wüsthoff, Phys. Rev. D **59** (1999) 014017, **60** (1999) 114023
- [112] E. Iancu *et al.*, Phys. Lett. B**590** (2004) 199
- [113] T. Sjostrand *et al.*, Comput. Phys. Commun. **135** (2001) 238
- [114] K. Adcox *et al.* (PHENIX collaboration), Phys. Rev. Lett. **91** (2003) 072301
- [115] H. Hahn *et al.*, Nucl. Instr. and Meth. A**499** (2003) 245
- [116] T. Abbott *et al.*, Nucl. Instr. and Meth. A**290** (1990) 41
- [117] K. Shigaki *et al.*, Nucl. Instr. and Meth. A**438** (1999) 282
- [118] GEANT Detector Description and Simulation Tool, CERN Program Library Long Writeup W5013
- [119] M. Adamczyk *et al.*, Nucl. Instr. and Meth. A**499** (2003) 437
- [120] A. Kümichel, Nucl. Instr. and Meth. A**360** (1995) 52
- [121] J. I. Jørdre, Master thesis, Univ. of Bergen, Norway (2001)
- [122] S. V. Afanasiev *et al.* (NA49 collaboration), Nucl. Instr. and Meth. A**430** (1999) 210
- [123] D. Ouerdane, Ph.D. thesis, NBI, Denmark (2003)
- [124] R. Karabowicz, Master thesis, Jagiellonian University, Poland (2003)
- [125] R. Brun *et al.*, ROOT Users' Guide, <http://root.cern.ch/root/doc/RootDoc.html>
- [126] T. M. Larsen, Master thesis, Univ. of Oslo, Norway (2003)
- [127] P. Staszek, BRAHMS analysis note (2001)
- [128] S. Eidelman *et al.* (Particle Data Group), Phys. Lett. B**592** (2004) 1

- [129] K. Adcox *et al.* (PHENIX collaboration), Phys. Rev. Lett. **89** (2002) 092302
- [130] V. V. Anisovich, V. M. Shekhter, Nucl. Phys. B**55** (1973) 455
- [131] T. S. Tveter, BRAHMS analysis note (2005)
- [132] I. Arserne *et al.* (BRAHMS collaboration), *Centrality Dependent Particle Production at  $y=0$  and  $y \sim 1$  in Au+Au Collisions at  $\sqrt{s_{NN}} = 200$  GeV*, Preprint: arXiv:nucl-ex/0411039
- [133] K. H. Ackermann *et al.*, (STAR collaboration), Phys. Rev. Lett. **86**, (2001) 402
- [134] T. Abbott *et al.*, (E802 collaboration), Phys. Rev. Lett. **64** (1990) 847
- [135] G. E. Bruno *et al.*, (NA57 collaboration), J. Phys. G: Nucl. Part. Phys. **30** (2004) S717
- [136] I. G. Bearden *et al.*, (BRAHMS collaboration), Phys. Rev. Lett. **93** (2004) 102301
- [137] C. Adler *et al.* (STAR collaboration), Phys. Rev. Lett. **89** (2002) 092301
- [138] S. V. Afanasiev *et al.*, (NA49 collaboration), Phys. Rev. C**66** (2002) 054902
- [139] P. B. Munzinger *et al.*, Phys. Lett. B**465** (1999) 15
- [140] C. Blume, (NA49 collaboration), *Review of results from the NA49 collaboration*, Preprint: arXiv:nucl-ex/0411039
- [141] I. G. Bearden *et al.*, (BRAHMS collaboration), Phys. Rev. Lett. **94** (2005) 162301
- [142] U. Heinz, P. Kolb, Nucl. Phys. A**702** (2001) 269
- [143] M. Gazdzicki, M. I. Gorenstein, Acta Phys. Polon. B**30** (1999) 2705
- [144] D. Kharzeev, M. Nardi, Phys. Lett. B**507** (2001) 121
- [145] D. Kharzeev, E. Levin, Phys. Lett. B**523** (2001) 79
- [146] D. Kharzeev, E. Levin, M. Nardi, Nucl. Phys. A**730** (2004) 448
- [147] T. Hirano, Y. Nara, *Private communication*
- [148] B. B. Back *et al.*, (PHOBOS collaboration), Phys. Rev. Lett. **91** (2003) 052303

ISBN 82-497-0285-9